National Library
of Canada

Bibliothèque nationale
du Canada

Canadian Theses Service

Service des thèses canadiennes

Ottawa, Canada
K1A 0N4

NOTICE

The quality of this microform is heavily dependent upon the quality of the original thesis submitted for microfilming. Every effort has been made to ensure the highest quality of reproduction possible.

If pages are missing, contact the university which granted the degree.

Some pages may have indistinct print especially if the original pages were typed with a poor typewriter ribbon or if the university sent us an inferior photocopy.

Reproduction in full or in part of this microform is governed by the Canadian Copyright Act, R.S.C. 1970, c. C-30, and subsequent amendments.

AVIS

La qualité de cette microforme dépend grandement de la qualité de la thèse soumise au microfilmage. Nous avons tout fait pour assurer une qualité supérieure de reproduction.

S'il manque des pages, veuillez communiquer avec l'université qui a conféré le grade.

La qualité d'impression de certaines pages peut laisser à désirer, surtout si les pages originales ont été dactylographiées à l'aide d'un ruban usé ou si l'université nous a fait parvenir une photocopie de qualité inférieure.

La reproduction, même partielle, de cette microforme est soumise à la Loi canadienne sur le droit d'auteur, SRC 1970, c. C-30, et ses amendements subséquents.

NL-339 (r. 88/04) c

Canada

HOT DUCTILITY AND STRENGTH OF FIVE MICROALLOYED STEELS IN THE TEMPERATURE RANGE 800°C-SOLIDUS

by

Alain M. Guillet

A Thesis Submitted to the Faculty of Graduate Studies and
Research in Partial Fulfilment of the Requirements
for the Degree of Doctor of Philosophy

Department of Mining and Metallurgical Engineering
McGill University
Montreal, Province of Quebec, Canada

November 1989

ISBN 0-315-63547-9

ABSTRACT

Tensile testing was carried out on five microalloyed steels in order to investigate the hot ductility behaviour between 800 and 1300°C, and between 1400°C and the solidus temperature. The influence of an increase of the carbon content up to the peritectic composition ($\approx$0.14 wt%) in Nb-Ti-Al bearing steels, and the effect of microalloying additions (Al, Al-Nb-Ti and, Al-Nb-Ti-V-Cr) were examined.

Above 1400°C, intergranular embrittlement occurs by incipient melting at the grain boundary at temperatures between 0 and 30°C below the solidus. The increase in the carbon content from 0.07 to 0.14 wt% leads to a decrease of the grain boundary incipient melting temperature, although the bulk solidus temperatures for all the steels remain more or less constant at about 1500°C. This is explained by the grain boundary segregation behaviour of carbon. According to differential thermal analysis results, embrittlement occurs in the single δ ferrite phase for the low carbon steels (0.07 and 0.1 wt%) and in the $\gamma + \delta$ duplex region for the 0.14 wt% C steel. At 1480°C, for the 0.14 wt% C steel, the grain boundary segregation of carbon in the δ-ferrite and austenite phases is estimated to be 80 and 12 at%, respectively. It is concluded that the lower carbon content at austenite grain boundaries leads to the observed lower incipient melting temperature of the 0.14 wt% C steel. It has also been shown qualitatively that the Cr addition could increase the grain boundary incipient melting temperature by decreasing C, S and P segregation, via the effect of chemical interaction on segregation behaviour.

Above 1400°C, fractography reveals that the grain size in the steel with the peritectic composition (0.14 wt% C) is coarser than that of the low carbon grades (0.07-0.1 wt% C). This effect is attributed to: (i) the higher γ/δ transformation temperature in the steel with the peritectic composition, thus allowing more grain coarsening, and (ii) the lower amount of δ ferrite, which reduces the pinning effect of this phase on austenite grain growth. In the Cr containing steel the relatively low degree of segregation also produces a coarser structure than that of the Nb/Ti/Al steel, because the pinning effect of the segregating species is diminished.

In the temperature range 800-1300°C, the ductility is strongly dependent on prior heat treatment. For the Nb-Ti-Al bearing steels, an increase of the carbon content up to 0.14 wt% slightly affects hot ductility after direct heating and annealing at 1330°C. However, after sensitizing at 1480°C the width of the ductility trough is increased in the 0.14 wt% C steel. This effect is attributed to the coarser austenite structure inherited from the sensitizing treatment.

For the C-Mn-Al steel, the ductility is the lowest following the direct heat treatment because of the presence of a greater volume percent of AlN precipitates at the grain boundaries compared to the Nb-Ti-Al steels. In contrast, after annealing and sensitizing, the C-Mn-Al grade displays the highest ductility because of the sluggish rate of precipitation of AlN in austenite.

Finally, Ti additions to Nb containing steels improve the ductility because some of the Nb is combined with TiN particles both as complex TiNb(C,N) and by precipitating as NbC on existing particles. Such precipitation is less deleterious to ductility than the fine dispersion of NbCN which would otherwise takes place in the absence of TiN. The addition of V to the Nb-Ti-Al steels (which contains also Ni and Cr) increases the ductility because of the retardation of Nb(C,N) precipitation. However, after the sensitizing treatment, at low test temperatures, the V containing grade displays the lowest ductility because of the coarser grains.

RÉSUMÉ

Des tests de traction ont été éffectués sur cinq aciers microalliés afin d'étudier leur ductilité à des températures comprises entre 800-1300°C et entre 1400°C et la température de solidus. L'effet d'une augmentation de la teneur en carbone jusqu'à la composition péritectique (≈0.14 pds %) dans des aciers contenant du niobium et du titane a été étudié, ainsi que l'influence d'éléments de microalliage tels que Al, Al-Nb-Ti et Al-Nb-Ti-V-Ni-Cr.

Au dessus de 1400°C, la rupture intergranulaire est causée par la fusion des joints de grain à des températures comprises entre 0 et 30°C en dessous du solidus. Une augmentation de la teneur en carbone de 0.07 à 0.14 pds % diminue la température de fusion des joints de grain, quoique, pour tous les aciers, la température du solidus de la matrice est approximativement constante (≈1500°C). Ce phénomène est attribué à la ségrégation du carbone. Selon les résultats de l'analyse thermique différentielle, la rupture se produit en phase δ pour les aciers bas carbone (0.07 et 0.1 pds % C) et dans la région biphasée γ+δ pour l'acier contenant 0.14 pds % de carbone. A 1480°C, pour l'acier à 0.14 pds % de carbone, la ségrégation du carbone en phases δ et γ a été estimée à 80 et 12 at%, respectivement. Nous concluons que la plus basse teneur en carbone est la cause d'une température de fusion des joints de grain plus basse dans l'acier contenant 0.14 pds % de carbone. Nous montrons aussi, qualitativement, que l'addition de Cr augmente la température de fusion des joints de grain en diminuant la ségrégation de C, S and P par une intéraction chimique.

Au dessus de 1400°C, l'analyse fractographique a montré que pour l'acier de composition péritectique (0.14 pds% C), la taille des grains est plus importante que celle des aciers à niveau de carbone plus bas (0.07-0.1 pds % C). Cette observation s'explique d'une part par la température de transformation γ/δ plus élevée dans le cas de l'acier de composition péritectique, permettant une croissance des grains plus importante, et d'autre part, par le plus faible pourcentage de ferrite δ dont l'effet de retenue sur la croissance des grains austénitiques est ainsi diminué. Dans l'acier au chrome, le faible taux de

ségrégation permet aussi une croissance plus importante des grains que dans l'acier au Nb/Ti/Al parce que l'effet des éléments ségrégés sur le grossissement des grains décroit.

Dans le domaine de température 800-1300°C, la ductilité est fortement influencée par le traitement thermique. Pour les aciers au Nb, Ti et Al, suite à un chauffage direct à la température de test ou au traitement thermique de recuit à 1330°C, une augmentation de la teneur en carbone jusqu'a 0.14 pds % a peu d'effet sur la ductilité à chaud. Cependant, pour l'acier contenant 0.14 pds % de carbone, la largeur de la poche de ductilité augmente après le traitement de sensibilisation à 1480°C. Ce phénomène s'explique par la plus grande taille des grains austénitiques dans cet acier, hérités du traitement de sensibilisation.

La ductilité de l'acier C-Mn-Al est la plus basse lors du chauffage direct, ceci parce que le pourcentage volumique de précipités aux joints de grain est plus important que les aciers au Nb-Ti-Al. A l'opposé, après recuit ou sensibilisation, cet acier possède la ductilité la plus élevée car la reprécipitation des nitrures d'aluminium est très lente dans l'austénite.

Enfin, l'addition de titane dans les aciers au niobium améliore la ductilité car une partie du Nb est combinée avec les précipités de TiN à la fois sous forme de complexes TiNb(C,N) et par précipitation de NbCN sur les particules déja présentes. Ce réseau de précipités provoque une plus faible décroissance de la ductilité qu'une fine dispersion de NbCN qui existerait en l'absence de TiN. L'addition de vanadium aux aciers Nb-Ti-Al augmente la ductilité parce que la précipitation de Nb(C,N) est retardée. Cependant, après le traitement de sensibilisation, à basse température, la nuance contenant du vanadium possède une ductilité plus basse que celle des aciers au Nb, Ti et Al en raison d'une taille de grains plus importante.

ACKNOWLEDGMENTS

The author would like to express his gratitude to Professor M.G. Akben, director of this research, for her guidance and encouragement throughout the course of this study. I would like also to express my deep gratitude to Professor S. Yue for his co-supervision with Professor Akben and strong involvement, help and support during the writing of the thesis. Many thanks are also due to Professor J.J. Jonas who initially accepted me as a member in his dynamic and creative research team.

I am also indebted to Professor B. Mintz (City University, London, England), visiting professor at McGill University, whose expertise in the field of hot ductility of steel led to many significant insights.

For the preparation of the tests specimens, the author acknowledges the assistance received from E. Fernandez, technician of the hot deformation group, and M. Knoepfel, B. Grondin of the department of Mining and Metallurgical Engineering, and A. Clément of the department of Mechanical Engineering. The author also whishes to thank to Dr J.J. Hechler (Institute of Materials Research, Boucherville, Quebec) with whom the DTA experiments were carried out.

The author is indebted to the Metals Technology Laboratory of CANMET for providing the experimental materials and for financial support, and particularly to Dr G.E. Ruddle for his personal interest in the progress of the research and his involvement in the preparation of the test materials. The support of CSIRA (Canadian Steel Industry Research Association) and NSERC (Natural Science and Engineering Research Council) is gratefully acknowledged.

Many thanks are also due to my fellow graduate students who created a pleasant and friendly working environment during these years. The author is also grateful to Carol Rousseau, secretary of the department of Mining and Metallurgical Engineering, and Lorraine Mello, secretary of the research group, for their help in completing the various administrative formalities associated with this work.

The author wishes to thank all his friends from Quebec, especially Yves and Denise Dagenais, for their moral support and encouragement during the critical period of the writing of the thesis. Finally, last but not least, the

achievement of this thesis would not have been possible without my spouse, Anne Groboillot, who shares with me the busy life of graduate student. This thesis is dedicated to her.

TABLE OF CONTENTS

LIST OF FIGURES

Figure Page

LIST OF TABLES

CHAPTER 1

INTRODUCTION

In the last twenty years, the metallurgical community has seen the development of High Strength Low Alloy (or microalloyed) steels, in which small additions of carbonitride formers, such as Nb, V, and Ti, lead, through controlled rolling, to strong improvements in room temperature mechanical properties. At the same time, the development of continuous casting has been so great in certain countries that it has made the use of ingot casting obsolete. In order to save energy, current research is underway to link the continuous casting machine with the reheating furnace (Continuous Casting Hot Charging) or with the rolling mill (Continuous Casting Direct Rolling). The ultimate extrapolation of this process is the introduction of strip casting, with only one or two high temperature rolling passes required to produce strip.

However, since the inception of continuous casting, it is apparent that certain grades of steels are difficult to cast because of the formation of cracks in the interior and on the surface of the cast product. A defect free slab is an absolute prerequisite for the development of the Continuous Casting Hot Charging or Direct Rolling processes. The microalloyed steels containing Nb are amongst those problem grades, but plain carbon steels with a C content close to the peritectic composition ($\approx$0.14 wt% C) are also susceptible to cracking. Cracks are caused by a combination of poor mechanical properties of steels at high temperatures and mechanical stresses and strains applied on the strand during the continuous casting process.

The general objective of this work is to investigate, by tensile testing, the ductility and strength of five microalloyed steels, between 800°C and the solidus temperature. More specifically, the aims of this thesis are:

(i) To investigate the influence of carbon content (between 0.07 and 0.14 wt%) and microalloying (Al, Nb-Ti and Al-Nb-Ti-V-Ni-Cr) additions on the characteristics of grain boundary incipient melting, which occurs at temperatures below the solidus.

(ii) To determine the effect of carbon on the ductility of Nb-Ti-Al steels in the temperature range 800-1300°C under various prior heat treatments.

(iii) To establish the influence of Ti and V on ductility in the same temperature range and prior heat treatments.

A review on the technological causes of the cracks is given in Chapter 2, followed by an extensive analysis of the published literature concerning the hot ductility of steel, with respect to crack formation on slabs during continuous casting. The influence of the alloying additions commonly used in low carbon microalloyed steels is presented.

In Chapter 3, the experimental techniques employed in this work are described. Although tensile testing constitutes the core of the laboratory work, several other techniques have been used, such as differential thermal analysis, Auger electron spectroscopy, scanning electron microscopy and metallography.

The experimental results are given in Chapter 4, followed by the first part of the discussion in Chapter 5. Here, an attempt is made for the first time to analyse the results of the hot ductility investigations above 1400°C using equilibrium segregation theory.

In Chapter 6, the results of the tensile tests in the temperature range 800-1300°C are discussed; in particular, the role of carbon and microalloying additions under the various prior heat treatments is explained. Finally, the conclusions of this study are drawn in Chapter 7.

CHAPTER 2

LITERATURE REVIEW

2.1 CONTINUOUS CASTING

Techniques to produce semi-finished steel products (slabs, blooms or billets) without recourse to conventional ingot casting, have been proposed as early as 1891 [1]. In 1933, the working principles of the continuous casting machines now in service were first proposed by Junghans [2]. However, it is only during the last 30 years, and particularly since the first oil crisis, that steel production with this new method has developed significantly. In 1960, only 1% of the steel production of the western world was cast by this new route, compared to 56% in 1985 [3], but there are large disparities from country to country, some western countries producing 100% of their tonnage by continuous casting [4].

The main reasons for the worldwide popularity of continuous casting technology are obviously economical. The continuous casting process involves fewer operations than conventional ingot casting. This is because, starting from ingot, hot deformation must be performed to produce the semifinished product. Continuous casting eliminates much of this required hot deformation, thereby saving energy, labour costs per ton and capital investment in rolling mills, since reheating and slabbing are no longer necessary [5]. Steel produced by this method is 10 to 15% cheaper, and the product quality is often better than from ingots [4].

2.1.1 Stages of Continuous Casting

During the continuous casting operation the liquid steel is bottom poured from the ladle into a tundish. It is then poured from the bottom of the tundish into one or several watercooled copper molds located at the top of the CC machine. This is the so called primary cooling stage and it ensures the solidification of one centimeter of the skin strand. The mold oscillates vertically, thus exerting a stripping action of the steel strand from the mold. At the mold exit, the strand is supported and guided by top and bottom rolls, which also prevent the bulging of the slab due to ferrostatic pressure of the liquid core. Simultaneously, water sprays (secondary cooling) continue the solidification process.

What happens beyond this point depends on the type of the continuous casting machine [6]. If the machine is vertical (Fig. 2.1a) the strand can be cut without bending, or it can be curved when the solidification stage is completed and cut (Fig. 2.1b). Another variant of the vertical mould machines is to bend the strand whilst the core is still liquid (Fig. 2.1c). However, the most widely used machines are those with a curved mould, where the strand follows the path imposed by the supporting rolls to the point of straightening, i.e., where the movement becomes horizontal (Fig. 2.1d). At this stage the steel is completely solidified and the strand begins to exit the withdrawal section; it is then cut out into slabs, blooms or billets of the desired length. Finally, there is an increasing trend towards machines which use a curved mould, but where the straightening takes place whilst the strand still has a liquid core (Fig. 2.1e).

2.1.2 Quality of CC products

As can be seen from Table 2.1, defects such as inclusions, blowholes, and segregation can affect the quality of the final product [3]. However cracks have the most deleterious influence on quality and have significantly retarded the development of continuous casting. For example, if the skin slab tears and leads to a "break out" of the liquid steel, the cost can be as high as $100,000 [6]. Of course all cracks do not have such drastic consequences, but there are many other problems associated with their presence. Surface cracks are oxidized by air and can result in defects in the rolled products. They can be removed by scarfing or grinding, but the costs of inspection, surface treatment and yield loss affect the profitability of the operation.

Internal cracks lead to voids in the final product, and their vestiges in the rolled product can cause difficulties in subsequent manufacturing process. Moreover, the demands of high productivity require high casting speeds and

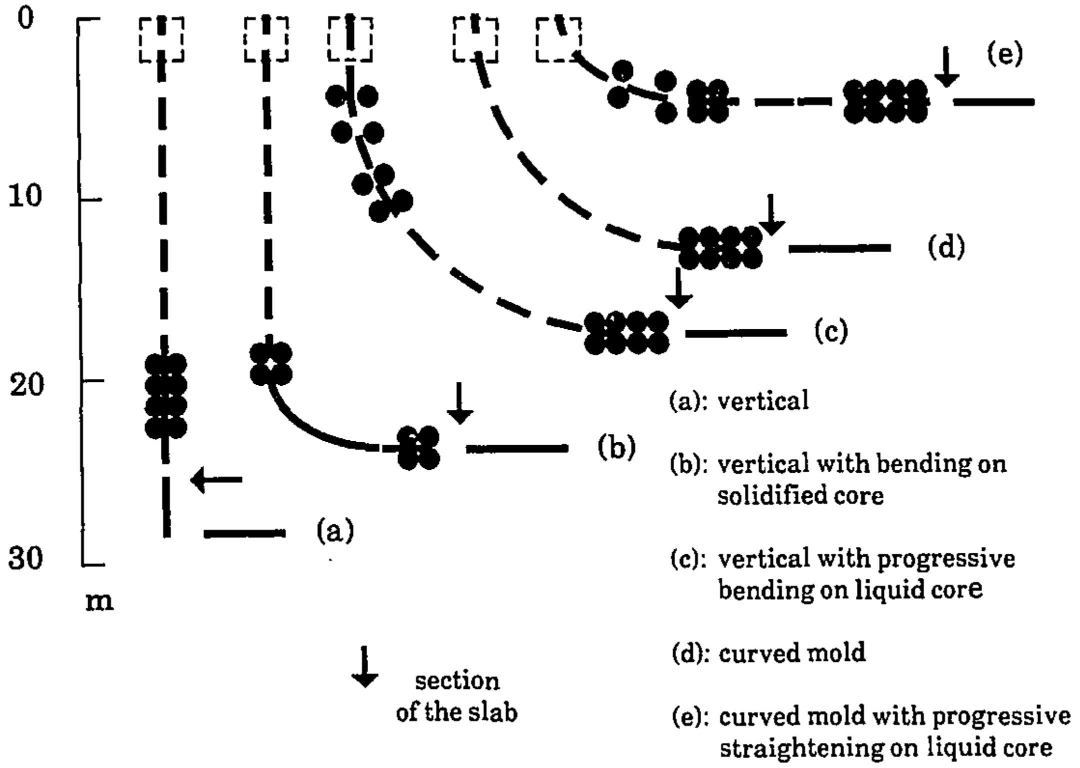

(a): vertical

(b): vertical with bending on solidified core

(c): vertical with progressive bending on liquid core

(d): curved mold

(e): curved mold with progressive straightening on liquid core

Figs. 2.1: Different kinds of CC machines [6].

Table 2.1

Classification of the main defects encountered during CC and influencing factors [3].

Defect classification	Defect type	Influencing factors
Surface and subsurface	1. Entrapped inclusions. 2. blowholes.	(a) Ladle treatment. (b) Stream protection. (c) Tundish size and design. (d)Use of weirs and dams in tundish. (e) Steel temperature. (f) Mould level control. (g) sub entry nozzle design.
Internal	1. Internal inclusions.	(a) Steel composition (C, Nb, V, Ni, N ...) (b) Mould geometry. (c) Mould powder type. (d) Mould level control. (e) Mould/top zone geometry and alignment. (f) Intensity and uniformity of secondary cooling. (g) Mold plating (star cracking).
	1. Intercolumnar cracking/segregation. 2. Centerline cracking/segregation. 3. Spot segregation.	(a) Ladle treatment. (b) Stream protection. (c) Tundish size and design. (d)Use of weirs and dams in tundish. (e) Steel temperature. (f) Mould level control. (g) Teeming conditions .
Shape	1. Rhomboidity (billets and blooms). 2. Edge shape (slabs).	(a) Mould geometry. (b) Mould taper. (c) Uniformity and secondary cooling.

this in turn results in a tendency towards an increase in internal cracking [7]. Finally, a defect free slab is an absolute necessity for the implementation of Continuous Casting Hot Charging (CC-HC) or Continuous Casting Direct Rolling (CC-DR) processes. In the former, slabs are directly charged into the reheating furnace before the onset of the γ-α transformation, whereas in the latter, they are directly rolled without reheating. In both cases, conditioning of slab surfaces by means of cold scarfing cannot be performed [8].

There are two broad categories of cracks: (i) internal and (ii) surface. For each category, subcategories have been defined [9] using the criteria of defect position on the slab (Fig. 2.2). In the following sections it is shown that these cracks correspond to different temperatures and mechanisms of formation.

2.1.2.1 Internal cracks

It is generally agreed that internal cracks are formed in the mould at temperatures close to the solidus [7,9-12]. It is also recognized that even small tensile stresses and strains within the solid plus liquid two phases region can lead to internal cracking in solid steel [13]. The critical values for the initiation of internal cracks vary with steel composition [7]. Following recent investigations, the critical strain required to produce internal cracking was calculated to be less than 1%, and the higher the difference between solidus and liquidus temperatures, the lower the critical strain [12].

The mechanism of internal cracking is a hot tearing process which occurs in the following manner. During solidification of the melt, primary dendrite arms grow and the remaining liquid steel is enriched with segregating elements such as S, P and C. If tensile strains exceed the separation strain value of the solid-liquid interface, a crack is formed along the intercolumnar dendritic region and liquid steel rich in segregants is sucked into part or all of the crack [11]. The formation of a such a structure, i.e. a liquid phase in a solid matrix, results in very poor mechanical properties, as demonstrated by Kamdar [14].

According to Morita et al. [7] internal cracks are mainly due to the strain and stresses generated by:

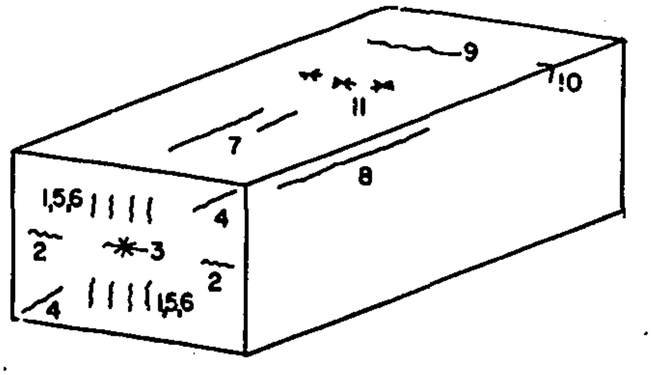

Internal cracks

1-Midway
2-Triple point
3-Centreline
4-Diagonal
5-Straightening/bending
6-Pinch roll

Surface cracks

7-Longitudinal, mid face
8- Longitudinal, corner
9-Transverse, mid face
10-Transverse, corner
11-star

Fig.2.2: Schematic drawing of strand cast section showing different types of cracks [9].

- bulging caused by ferrostatic pressure between the strand support rolls,
- roll squeezing,
- bending or unbending,
- thermal stresses due to the temperature difference between slab surface and solidification front,
- slab withdrawal.

Brimacombe and Sorimachi [9] classify internal cracks, based on the position on the slab, as shown in Table 2.2. For each category the causes and the influencing factors are given and some corrective actions in term of process and machine design are suggested.

2.1.2.2 Surface cracks

Surface cracks occur in the mould, with the noticeable exception of transverse cracks which are formed in the lower temperature range after solidification [9]. Transverse cracking, which occurs during the bending or straightening operation, has been associated with a coarse austenitic structure and/or precipitation of sulfides or carbonitrides [9]. The mechanism of embrittlement generally accepted is the nucleation and growth of voids at the grain boundary/precipitate interfaces and/or at thin ferrite film at austenite grain boundaries. Small deformations at slow strain rates, as experienced in the slab during the straightening operation [15], can be sufficient to produce surface defects. Precipitation takes place in the temperature range 1200-900°C for sulfides, and between 1000-700°C for the carbonitrides, the latter temperature range corresponding to the bending or unbending operation. The austenite to ferrite transformation begins at the Ar_3 temperature. The mechanisms of embrittlement associated with the major alloying elements are presented later in this chapter. Table 2.3 summarizes the type, causes and influencing factors of surface cracks and the proposed corrective actions [9].

Table 2.2

Type, cause and corrective action of internal cracks [9]*

Type	Cause	Influencing factors	Corrective action
Midway cracks	Surface reheating in or below spray chamber.	High casting temperature. S and P > 0.02 pct increase crack formation.	Adjust spray system to minimize reheating. Lower pouring temperature. Minimize P and S levels.
Triple-point cracks	Bulging of wide face slabs.	Cracking increases with decreasing Mn below 0.9 pct and with Mn/S < 30.	Regap rolls.
Centerline cracks.	In slabs, bulging of wide face. In billets, rapid cooling of center region below pool.	Spray water intensity, casting speed, roll alignment low in the strand. Severe secondary cooling and high pouring temperature.	Adjust secondary cooling near bottom of pool.
Diagonal cracks	Asymmetrical cooling in mold or sprays.	High pouring temperature and smaller billet sizes increase cracking.	Install corner rolls at bottom of mold. Check alignment between mold and roller apron
Straighten--ing/bending cracks	Excessive deformation near solidification front due to straightening or bending.	Bending on liquid center.	Reduce tensile strain at solidification front to less than 0.3 pct. Lower casting speed.
Pinch roll cracks	Excessive pinch roll pressure.	Squeezing on a liquid center.	Reduce pinch roll pressure.

*All internal cracks form in high temperature zone of low ductility, between 1340°C and the solidus temperature. Elements such as P, S and Cu worsen the cracks.

Table 2.3

Type, cause and corrective action of surface cracks [9]*

Type	Cause	Influencing factors	Corrective action
Longitudinal midface cracks	Tensile strain generated in the mold and upper spray zones.	Crack frequency increases with: -C levels of 0.12 pct -increasing S and decreasing Mn/S -increasing casting speed -high pouring temperatures -casting of wide slabs -mould conditions overcooling in upper spray zones -insufficient support below mold -poor alignment between mold and submold system.	Adjust mold conditions to insure uniform cooling. Reduce cooling in upper spray zones and check submold support system.
Longitudinal corner cracks	Nonuniform cooling in corner region.	Cracking associated with: -reversal of mold taper owing to distortion of wear -large corner gaps in plate molds -high tundish temperature -high casting temperature -high casting speed -incorrect foot roller settings -steel containing 0.17-0.25 pct C, S>0.035 pct, P>0.035 pct.	Plate mold walls with chromium. Reface the mold. Check alignment and lubrication.
	In slabs, off-corner cracks caused by bulging of narrow face in mold.	Long molds and steel with 0.15 to 0.23 pct C give rise to increase cracking tendency.	Check mold support conditions.
Transverse, midface corner cracks	Large surface temperature gradients in the spray zone. Straightening within an unfavorable range of temperature between 700 and 900°C.	Strongly influenced by steel composition, Al, V, Nb, Mn>1 pct being the most important elements.	Reduce spray cooling and make it uniform in order to maintain surface temperature above 900°C through to straightener.
Star cracks	Scraping of copper from mold.	Secondary cooling.	Plate mold walls with chromium. Adjust machine alignment

*With the exception of transverse cracks, surface cracks probably form in the high temperature zone of ductility.

2.2 ORIGIN OF CRACKS IN CONTINUOUSLY CAST PRODUCTS

Cracks appear within or on the surface of a strand due to the presence of tensile stresses. The analysis of the stresses that exist in a strand during the continuous casting process is extremely complex, being a combination of thermal and mechanical effects. Lankford [16] described both kinds of stresses qualitatively, and these are summarized in the following section.

2.2.1 Mould friction forces

The upward and downward mould oscillation, which strips out the strand and prevents sticking, generates frictional forces on the solidified skin. This force is a maximum at the surface and decreases to zero at the solid-liquid interface resulting in a bending force in machines with a vertical mould. This bending force is in tension at the surface and becomes progressively compressive. When the mould moves downward, the combined effects of the bending and friction forces lead to a tensile stress across the entire solidified thickness.

2.2.2 Thermal stresses

During the continuous casting operations, the strand exhibits two thermal gradients, one through the thickness of the solidified skin and the other along the axis of the strand. The general rule is that tensile stresses occur in the cooler region because of the contraction restraint provided by the adjacent hotter regions, and compressive stresses occur in the hotter region. Therefore, on a *vertical* cross section of the slab, the thermal stress resulting from a through thickness gradient is tensile (hoop tensile stress) at the slab surface and compressive near the solidification front (Fig. 2.3). On a *horizontal* cross section of the skin, the axial temperature gradient, in combination with the through thickness gradient, generally causes an axial tensile stress at the skin and an axial compressive stress near the solidification front.

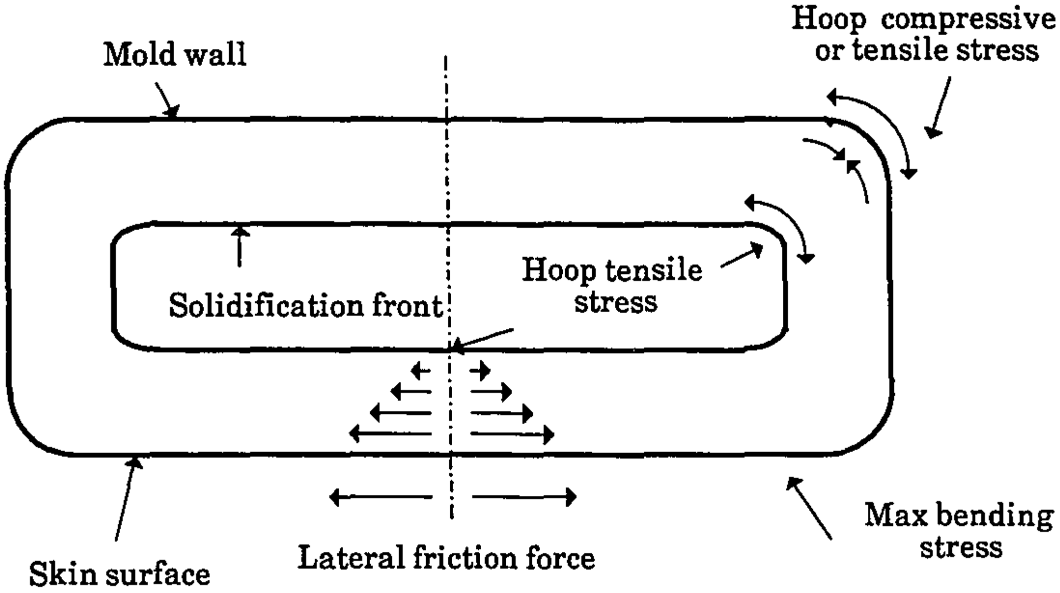

Fig. 2.3: Representation of lateral stresses in the solidifying skin in the mold [16].

However, due to non uniform secondary cooling using water sprays, the surface temperature along the strand does not decrease monotonically, but varies between upper and lower values about a gradually decreasing mean temperature. This cyclic cooling alters the stress distribution so that the stresses near the solidification front may become tensile, instead of compressive, eventually leading to internal cracks.

2.2.3 Ferrostatic pressure

In the mould, the casting shrinks and at the same time the liquid steel exerts a pressure on the solidified skin, which then generates bend stresses. Thus, hoop tensile stresses are developed by ferrostatic pressure of the solidification front [16].

As the casting progresses from the mould, the slab core is not completely solidified, and if the rolls are too widely spaced, the ferrostatic pressure can cause bulging and result in tearing. The bulging strain caused by ferrostatic pressure can be calculated using the following formula [7]:

$$\varepsilon_B = (P/3800) \times (l/d)^3 \qquad (2.1)$$

where P is the ferrostatic pressure (kgf/mm2), l the roll spacing (mm) and d the solidified thickness (mm). Using P~0.11 kgf/mm2, l~350 mm and d~95 mm, leads to a bulging strain of $\varepsilon_B = 0.0014$, thus demonstrating that relatively low strains can produce cracking.

2.2.4 Weight of casting and tractive effort

The weight of the strand contributes to axial stresses in the skin and, if the traction of the driving rolls is too high, this is also added to the weight of the slab. This combined force is particularly high in the vertical machines (Fig. 2.1-a) and is one of the reasons why the design of the machines has evolved into the configurations presented in Figs. 2.1-d and 2.1-e.

2.2.5 Bending forces

The greatest strains to which the strand cast is subjected during continuous casting are those due to bending and/or straightening of the strand. The total strain and average strain rate due to bending was calculated by Bernard et al.[15]. In the case where the slab exits vertically from the mould and is bent, the internal face is in compression and the external is in tension. The average tensile strain ($\Delta\varepsilon$) is given by:

$$\Delta\varepsilon=\frac{e}{2R} \tag{2.2}$$

where e is the thickness of the slab and R the radius of the curvature. The strain rate is calculated using the following equation:

$$\dot{\varepsilon}=\frac{\Delta\varepsilon}{\Delta t} \tag{2.3}$$

here, Δt is the time taken to bend the slab, and is calculated by:

$$\Delta t=\frac{2\pi R}{8V} \tag{2.4}$$

where $2\pi R/4$ is the length of a quarter circle deformed during bending and V is the extraction speed. Thus,

$$\dot{\varepsilon}=\frac{0.64eV}{R^2} \tag{2.5}$$

For e=200 mm, R=10 m and V=1 m/min the strain is 0.02 and the strain rate is $2\mathrm{x}10^{-5}\mathrm{s}^{-1}$.

At the solidification front, the *un*bending strain (in the case of machines with a curved mould) can be calculated using the following equation [7]:

$$\varepsilon=(e/2-d)\times((R_I-\frac{e}{2})^{-1}-(R_{I+1}-\frac{e}{2})^{-1}) \tag{2.6}$$

Deformation is assumed to take place over a series of incremental stages. Each of these stages corresponds to I in the equation. R_I and R_{I+1} are the slab radius at the stages I and I+1 respectively, e is the slab thickness and d is the solidified shell thickness. The calculation gives $\varepsilon \approx 8\text{x}10^{-5}$, for e=0.22 m, d=0.096 m, $R_I = 14$ m and $R_{I+1} = 15$ m.

2.2.6 Other sources of stresses

There are also other sources of stresses and strains which are due to operating irregularities, such as non concentric roll cages, misalignment between rolls cages, non uniform cooling in secondary cooling zones, eccentric mould distortion. For example, Bernard [15] calculates that a misalignment between two succeeding rolls can lead to a strain of 0.05 and a strain rate of 0.07s^{-1}. The strain due to misalignment can be calculated in the following manner [7]:

$$\varepsilon=1.15\times(\frac{3d}{l^3})\times\delta \tag{2.7}$$

Where d and l have the same meaning as above (Eq. 2.1) and δ is the amount of misalignment [7]. However, all these irregularities have relatively straightforward solutions.

2.3 HOT DUCTILITY BEHAVIOR OF STEELS UNDER CC CONDITIONS

Once the technological origins of cracks on steel slab have been established, the metallurgical aspects of this problem must be investigated. Defects appear on a strand, not only because of the continuous casting conditions, but also because of poor mechanical properties of the cast material.

To complement the previous overview, the parameters influencing the hot ductility of steel are discussed in this section.

2.3.1 Hot ductility test methods

With very few exceptions, hot ductility investigations have been carried out by tensile testing, where the reduction of area at fracture is taken as the appropriate ductility parameter. In order to obtain relevant results for the continuous casting operation, the experiments must simulate as closely as possible the conditions encountered during the process. The ideal test thus involves prior melting of the sample, followed by controlled cooling to the test temperature and deformation at low strain rates. However, the use of a prior heat treatment at temperatures close to the solidus (1460-1480°C) has proved to give similar results compared to prior melting [17]. Nevertheless, many hot ductility investigations have been carried out after annealing in the temperature range 1300-1350°C and cooling to test temperature [18-24]. Two broad categories of testing system have been used to determine hot ductility:

- The Instron [19,20,23-26] or MTS [27-29] mechanical testing machines to which a radiant [20,23,24,29] or a high frequency induction furnace [25,27,30,31] are attached, or
- the Gleeble apparatus [16,27,32-36].

In both systems, local melting of the sample is possible.

The Gleeble machine is the most widely used tool for hot ductility studies. It is a completely integrated system where the heating and cooling rates, holding time and deformation parameters can be precisely controlled. This apparatus, which was developed to investigate casting, welding and hot working problems, allows local melting of the specimen over a well defined gauge length. The sample is heated by electrical resistance heating; this system has an intrinsic longitudinal thermal gradient, but it is highly reproducible from one test to another. The newer models (Gleeble 1500) are computer interfaced for control and data acquisition. Tests can be performed in vacuum or in an inert atmosphere.

2.3.2 Influence of test parameters

This section reviews the effect of (i) temperature, (ii) thermal history of the material, and (iii) strain rate, these being the major parameters which affect hot ductility.

2.3.2.1 Temperature

Much of the hot ductility work pertaining to crack formation on continuously cast products deals with temperature range 600-1300°C, although some workers have investigated the behaviour up to the melting point.

It is generally accepted [9,32] that there are three temperature zones where, under continuous casting conditions, the steel ductility is poor (Fig. 2.4):

-Zone I : high temperature zone, (1340 °C to solidus),
-Zone II : intermediate zone, (800 to 1340 °C),
-Zone III: low temperature zone, (700 to 900 °C).

The exact location of the zones and the extent of the ductility loss depend critically on the aforementioned test parameters, as well as the steel grade.

Zone I

When steels are cooled from the melt and deformed, they exhibit, at a temperature *below, but close to the solidus temperature (Ts)*, a steep ductility drop over a 10°C range (Fig. 2.4). During the course of solidification, the remaining liquid phase between dendrites is highly concentrated with segregating elements like S, P, C, giving rise to an alloy with a solidification temperature lower than the matrix [9,12,32,33]. This residual liquid can embrittle a solid matrix [14]. The zero ductility temperature (ZDT) corresponds to the temperature at which an interconnected dendritic matrix is formed (i.e. after extensive solidification has occurred) and begins to be deformed. This is

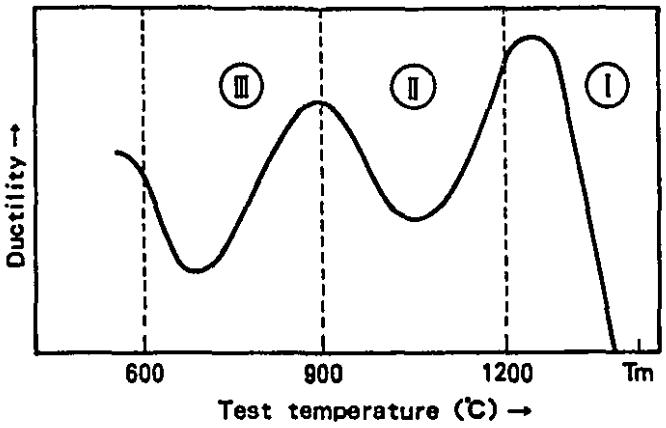

Fig. 2.4: Schematic presentation of ductility troughs appearing in hot tensile testing of steels [33].

confirmed by fracture surface analysis which reveals smooth rupture along dendrite interfaces.

Specimens reheated without prior melting and deformed below the solidus show a zero ductility temperature behavior [25], however, compared to samples cooled from the melt, the temperature is higher [33]. In this case the cause of embrittlement is still due to the presence of a liquid film in a solid matrix, but here, the decohesion is intergranular rather than interdendritic. Melting of the grain boundaries occurs below the solidus temperature because of the segregation of S, P, C (or other elements such as boron). The discrepancy beween the two ZDT temperatures (melting and reheating) may be ascribed to different segregation pattern. It is concluded by Brimacombe et al. [9] that most of the internal cracks are due to embrittlement at very high temperatures (zone I). The possibility of controlling this behaviour has been considered by Matsumiya et al. [12], but their findings indicate that this type of cracking cannot be eliminated by adjusting chemical composition and/or secondary cooling alone.

Zone II

The ductility loss in the intermediate zone is strongly dependent on the S content, Mn:S ratio and thermal history [9,17]. Experimental evidence has shown that the lower the Mn:S ratio, the lower the ductility [24]. In this case (i. e. for a high S content or low Mn level), S does not completely combine with Mn to form the stable phase MnS. Instead, iron sulfides (Fe,Mn,S) or oxysulfides (Fe,Mn,O,S), more or less enriched with Mn, can precipitate at the austenite grain boundaries and embrittle the material [27,33]. A deleterious influence of segregated sulfur alone has also been observed [23,24], and the findings are presented in the section concerning the effect of chemical composition on hot ductility.

Zone III

The low temperature zone between 700-900°C is associated with the precipitation of carbonitrides such as AlN or Nb(C,N) at the austenite grain boundaries and in the duplex α-γ region [9,15,28]. The details concerning zone III behaviour are also presented as part of the review on the effect of chemistry. In plain carbon steels which do not contain significant amounts of Al, the presence of zone III is attributed to proeutectoid ferrite nucleation at the austenite grain boundaries. This phase is softer than austenite and deformation takes place preferentially at the austenite grain boundaries [34,37].

The poor ductility in both the intermediate and low temperature zones is the origin of transverse surface cracks [9,15,28]

2.3.2.2 Thermal history

As mentioned previously, laboratory investigations of hot ductility must be performed using heating and cooling cycles which simulate the thermal history of the slab as closely as possible. Since the early work of Wilber et al. [17], the strong influence of the thermal history has been repeatedly demonstrated [20,27,28,32,38,39,40].

It has already been noted that in zone I, the difference in the ZDT values corresponding to heating up and cooling down have been attributed to changes in segregation patterns.

In zone II, the critical dependence of hot ductility on thermal history was demonstrated by performing tensile tests involving either melting the sample or annealing at a high temperature and then cooling to test temperature [17,32]. From Fig. 2.5 it can be seen that increasing the annealing temperature decreases the ductility, the worst case being when the sample is melted prior to testing [32]. In other words, the closer the test is to the thermal history of a continuously cast slab, the worse the ductility. However, Fig. 2.5 also indicates that annealing at temperatures close to, but below the solidus, is similar to melting in terms of hot ductility behaviour. This is an important observation, with respect to experimental procedure, because it demonstrates that it is not always necessary to melt the sample in order to investigate hot ductility in the intermediate temperature zone.

Prior heat treatment also has a significant effect on region III. For example, Maehara et al. [20], in their investigations on the role of carbon, found that embrittlement due to carbon in the range 0.10-0.14 wt% cannot be seen without prior melting of the material. Moreover, the harmful influence of

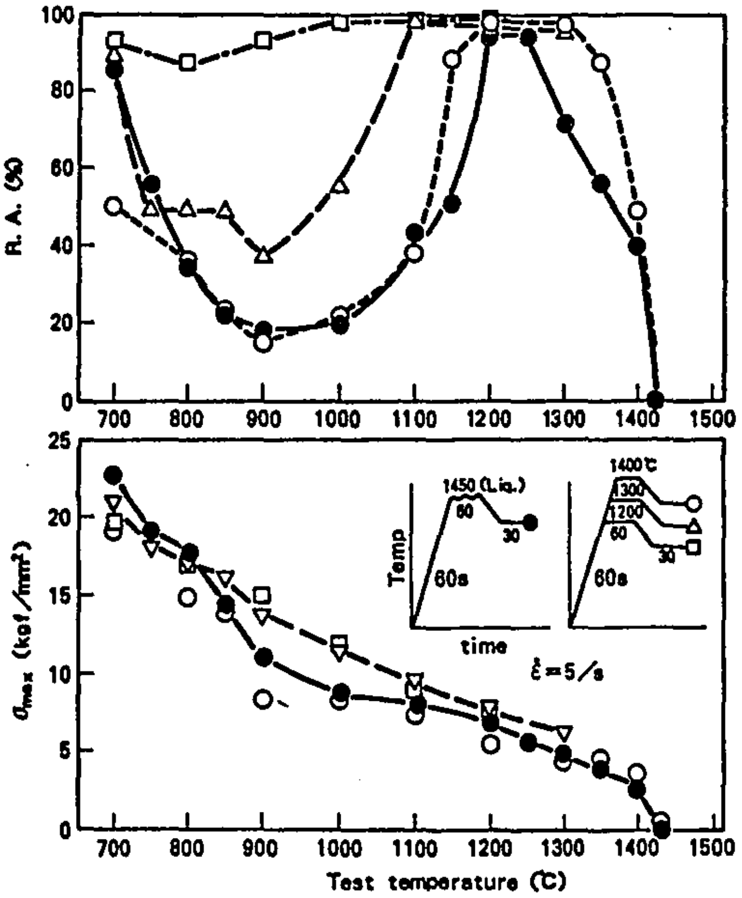

Fig. 2.5: Hot ductility and strength curves for low carbon aluminum killed steel subjected to various thermal cycles, $\dot{\varepsilon} = 5$/s, C.R. = 20°C/s, Mn/S = 31.7 [33].

phosphorus on a 0.4 wt% C steel is observed only after remelting of the sample and then cooling to test temperature [32].

Where carbonitride formation is involved in zone III, thermal history will affect the precipitation characteristics during testing. Hot ductility investigations of the low temperature zone are generally carried out after annealing around 1300°C, a temperature which is largely sufficient to dissolve most of the precipitates (see for example 19,22,35,39,41-46); followed by controlled cooling to test temperature. Depending on the type of microalloying additions and on the thermomechanical history of the specimen, precipitation can occur either statically and/or dynamically [83]. The mode of precipitation can significantly influence hot ductility.

The latest refinements in test technique for investigations for zone III, with respect to a closer simulation of the thermal history of a steel slabs, involve *cyclic* cooling between annealing and test temperature [47] or *prior melting* of the sample before cooling to test temperature [30,38]. Cyclic cooling more closely simulates the cooling pattern during strand casting where the surface temperature rebounds to higher values when it passes under the rolls [47]. Prior melting and/or cyclic cooling significantly affect hot ductility results via precipitation. A more detailed description of these effects is described in the chemical composition section.

2.3.2.3 Strain rate

At temperatures above 0.5 T_m (T_m = the melting point) the ductility, and other mechanical properties of steel, are strain rate sensitive. As noted above, the deformation rate associated with continuous casting is in the range 10^{-2}-$10^{-4}s^{-1}$ [15], and most investigations have been carried out at these levels. However, some work has been performed at strain rates of 5 s^{-1} or greater [32] and, more recently, up to 200 s^{-1} in order to study the effect of crack tip propagation on ductility [48].

Since the high temperature region (zone I) embrittlement is due to the presence of a liquid film along the grains boundaries or dendrite interfaces, it follows that the ZDT does not depend on strain rate [33].

In the intermediate temperature region (zone II), the hot ductility increases with decreasing strain rate (Fig. 2.6). This improvement is attributed to the coarsening of (Fe,Mn)S precipitates during deformation at low strain rate, this being less deleterious to hot ductility than small precipitates [17,32].

In the low temperature region (zone III) the opposite has been observed (Fig. 2.7) in the strain rate range 10^{-2}-10^{-4} s^{-1} [see for example:15,28,34,49,50]. However, recently Sakai and Ohashi [51] have noted that the hot ductility of microalloyed steels is distinctly improved by deformation at very low strain rates ($<10^{-4}s^{-1}$), a behaviour which is again attributed to the coarsening of the precipitates.

In order to explain the strain rate dependence of hot ductility in zone III, a qualitative model has been developed by Norstrom and Johanson [29]. They suggest that, with respect to strain rate, two possible "low ductility" regions may be defined, i.e. (i) a very low strain rate region or "creep embrittlement region" where high temperature mechanisms operate and weaken the grain boundaries through e.g. grain boundary sliding and cavitation; and (ii) a high strain rate region of strain hardening embrittlement, where recovery is strongly impeded, leading to early fracture due to high stresses within the grains. At strain rates between these two regions, recovery and eventually dynamic recrystallization takes place and the ductility is improved. Dynamic recrystallization is beneficial because if grain boundary migration occurs any the nucleated cracks remain isolated in a new dislocation free matrix. Therefore, the cracks can neither propagate nor coalesce.

Although precipitates in microalloyed steels affect dynamic recrystallization the hot ductility-strain rate dependence of such steels follows the Norstrom model.

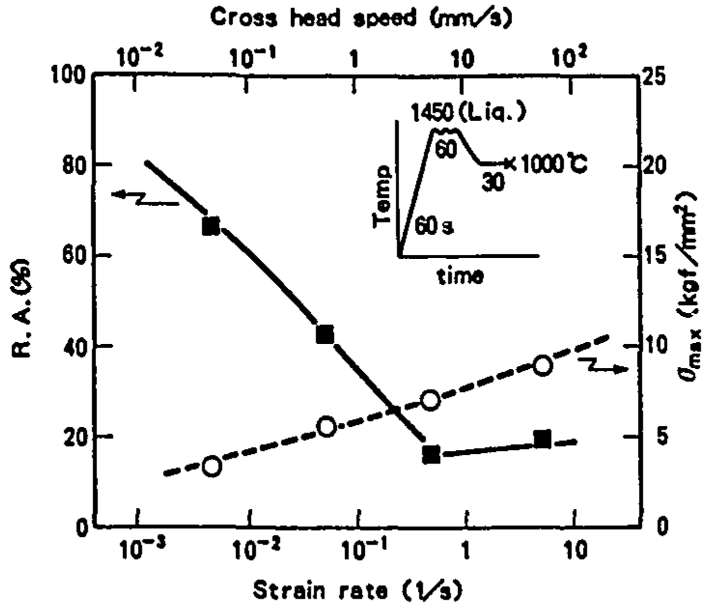

Fig. 2.6: Strain rate dependence of ductility at 1000°C (zone II) for low carbon aluminum killed steel subjected to melting treatment [33].

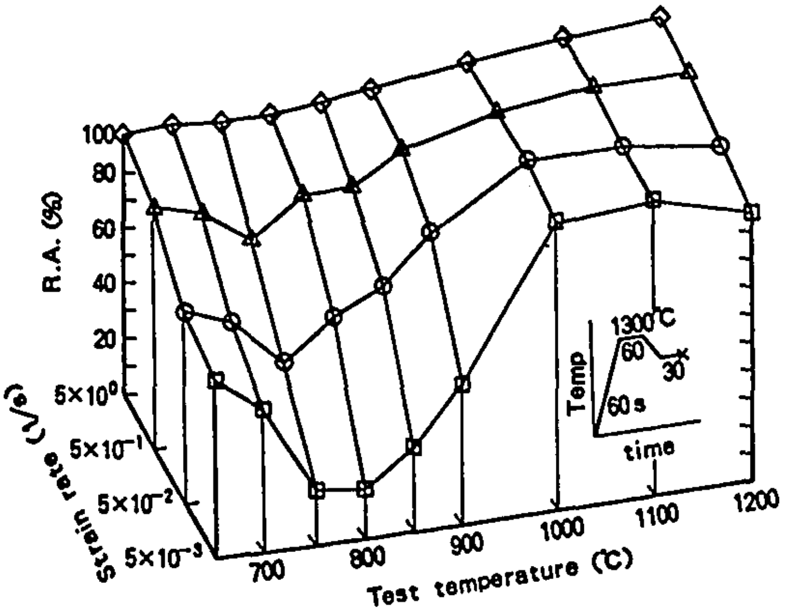

Fig. 2.7: Strain rate and temperature dependence of hot ductility (zone III) for Nb bearing steel [33].

2.4 EFFECT OF CHEMICAL COMPOSITION

Pure iron is reportedly ductile at all temperatures up to the melting point [52,53]. The ductility loss observed in the aforementioned temperature zones I, II, III, is due to the presence of impurities (e.g. S, P, N, O...), carbon, or elements added either to process the liquid steel (e.g. Al in killed steels) or to improve the mechanical properties of classical plain carbon steels. The last fifteen years have seen the development of microalloyed steels in which elements such as Nb, V, Ti or Al have been added to low carbon steels in order to improve their strength and toughness through controlled rolling and precipitation hardening. Such steels are increasingly produced by the continuous casting route and are known to be difficult to cast.

The purpose of this section is to describe the respective influence of impurities, carbon and microalloying elements on the hot ductility of steels, in relation to crack formation during continuous casting process. Thus, the results described here pertain to the temperature region, strain rate, and prior heat treatment relevant to the continuous casting operation.

2.4.1 Phosphorus

Phosphorus has been observed to promote internal cracking when the level exceeds 0.03% [9,13], and in fact, Fuji et al. have detected higher P (0.18 wt%) in the region of an internal crack than in the matrix (0.02 wt%) [54]. Other workers have calculated P segregation levels during cooling of between 0.1-0.2 wt%, relative to a matrix concentration of 0.025 wt% [55]. In laboratory studies, these observations have been supported by Adams, who detected a P concentration at the austenite grain boundaries of 0.2 to 0.5%, where the matrix concentration was 0.02% [56].

Several years before these findings, the harmful influence of P was noted by Sopher [57] (with respect to weld cracking) and other researchers [58]. His conclusions were that P in the range of 0.004-0.017 wt% P has little influence on the high temperature brittleness of a 0.4% C steel. However, a further increase to 0.039wt% strongly reduces ductility and strength in the temperature zone I.

The embrittlement is attributed to P segregation along dendrite interfaces during solidification [54,57], the P enriched liquid phase remains stable below the solidus temperature and increases cracking frequency. An alternate possibility is due to the formation of Fe-Fe_3P eutectic, which has a melting temperature of 1021°C [57]. The deleterious influence of phosphorus in zone I has been confirmed by Suzuki et al. who demonstrated that the zero ductility temperature of almost pure iron (99.997 wt%) decreased from 1530°C to 1475°C when 0.038 wt% of P was added [36].

Concerning the *surface* quality of slabs (i.e. in zone III), statistical observations by Mintz and Arrowsmith reveal a *beneficial* influence of raising the P content in low carbon ($C<0.25$ wt%) steels [49]. They claim that P improves the hot ductility of low soluble-Al bearing steels, but appears to have little effect when the Al content exceeds 0.04 wt%. This has been confirmed by Hannerz in his statistical observations and laboratory investigations [21]. The origins of this beneficial effect have not been rigorously explained, but the occupation of AlN precipitation sites by phosphorus segregation at the austenite grain boundaries is a possibility [49]. However, in the case of low carbon Nb-V bearing steels, Ouchi found no influence of P on hot ductility in zone III [28].

At C levels greater than 0.25 wt%, strong embrittlement takes place when the P content reaches 0.03 wt% [36]; the poor ductility domain covers the temperature range 900-1400°C. Embrittlement is seen only in prior melted specimens. Hot ductility is improved by a low rate of cooling ($<1°Cs^{-1}$), holding at test temperature (the amount of time depends on temperature) before deformation and a low rate of deformation ($\dot{\varepsilon}<10^{-2}s^{-1}$). Here again, no explanation has been given to rationalise this behavior.

In sulfur free steel containing 0.02 wt% C, the presence of P alone does not increase ductility loss of the alloys containing Nb(C,N) precipitates even if segregation of P to austenite grain boundaries has been established. However, in the presence of segregated sulfur, phosphorus further diminishes the ductility [24].

2.4.2 Nitrogen

Few studies have been made on the influence of free nitrogen on hot ductility and these deal only with the temperature range 700-1100°C, which covers temperature zones II and III. Suzuki et al. have demonstrated that greater than 0.005 wt% free N increases the depth of the ductility trough between 700-1100°C after solution treatment at 1300°C [34]. Ouchi and Matsumoto [28] have reached similar conclusions, but the actual influence of *free* N in their work is difficult to assess because the steels also had relatively high aluminum contents and therefore the nitrogen is combined with this element to form AlN. To further complicate matters, in C-Mn-Al-Nb steels, an increase of N from 0.0042 to 0.011 wt% only slightly deteriorates the ductility [44]. At present no embrittlement mechanisms have been proposed to explain any of these effects.

2.4.3 Carbon

Statistical analysis of slab defects have revealed a greater tendency towards internal cracking when the C level is increased [18,54]. The critical carbon content above which the percentage of internal cracks rises steeply is around 0.12 wt% C [54,59].

Hot ductility measurements have shown that an abrupt change in ZDT vs C concentration behaviour takes place at about 0.12 wt% C (Fig. 2.8) [60]. Above 0.12 %C the difference between the liquidus (T_L) and solidus temperature (T_S) becomes higher. As a consequence, for high carbon steels, the probability of the incidence of internal cracking is increased because the temperature range over which the liquid plus solid two phases region exists is larger. Thus, the possibility for a tensile stress to occur in the solid plus liquid state increases [12]. These findings are roughly comparable to the results of Morozenski et al. [61] and Guessier and Castro [58]. However, Suzuki et al. [36], in steels with C ranging between 0.003 % and 1.6 wt%, found the following linear relationship between ZDT and Ts in C steels with no singularities between 0.1-0.2 wt%C:

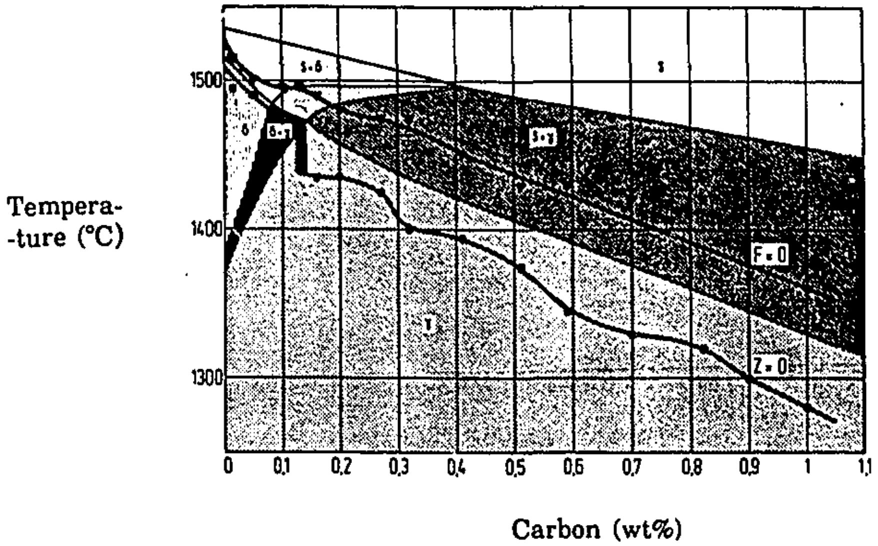

Fig. 2.8: The effect of C content on the temperatures of zero reduction of area (Z=0) and zero strength in relation to the phase diagram for Fe-C-Mn alloys containing 1.6 % Mn [74].

$$ZDT=1.14Ts-231\ (^{\circ}C) \tag{2.8}$$

As implied above, the remaining liquid phase due to carbon segregation seems to be the cause of poor hot ductility. Fractographic analysis [32] has shown approximately 10% of residual liquid steel at ZDT, thus confirming the liquid phase embrittlement theory. Among all the elements that can segregate during solidification (S, P, B), C has the smallest effect on ZDT [32].

Longitudinal cracking, which occurs at very high temperatures, has been linked with the peritectic reaction. Shrinkage away from the mould wall, due to the δ to γ transformation, leads to a lowering of the heat transfer between the mould and the slab resulting in a uneven solidified shell and the possibility of fracture at the thinner part of the solidified shell [18,62-64].

Carbon levels between 0.10-0.15 wt% not only increase the frequency of *internal* cracking, but also increase the susceptibility to *transverse surface* cracking [25,49,53,61]. Such carbon content leads to coarse austenite grains [65], which arise from the peritectic reaction. Here, grain growth is uninhibited because of the absence of δ phase, and the higher temperature of the delta ferrite-to-austenite transformation allows increased grain coarsening [20], Fig.2.9. Such grain coarsening may be a problem. However, other researchers have not observed any differences with increasing carbon content in terms of hot ductility due to grain coarsening. This in turn may be because, in hot ductility testing, grain coarsening is observed only after melting and solidification. A high temperature anneal around 1300°C is not sufficient to reveal significant differences in terms of microstructure between the various compositions examined [20, 21,28,34,65].

Clearly, there is been a certain amount of controversy concerning the influence of grain size on hot ductility [30,32,34,38,42-44,46,50,65-67]. However, Maheara et al. have proved that the decrease in ductility is inversely proportional to the grain size [20]. The increase of strain concentration at grain boundaries due to the lower grain boundary area per unit volume is one explanation of this phenomenon [68].

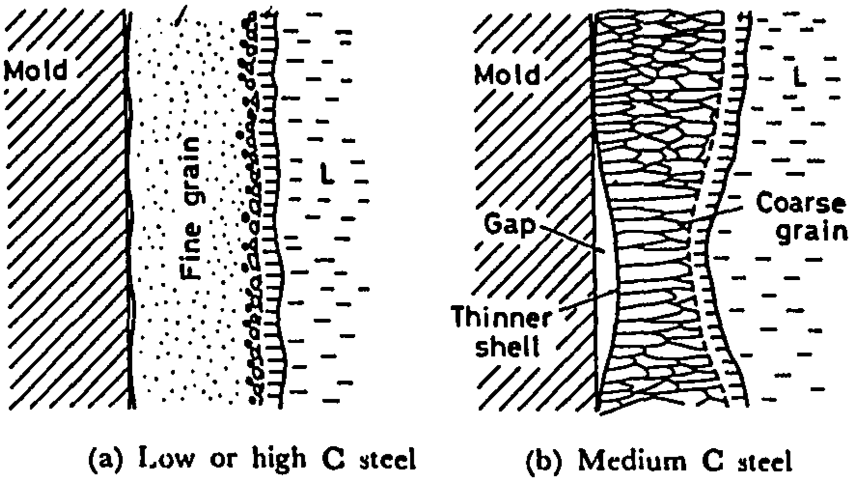

(a) Low or high C steel (b) Medium C steel

Fig. 2.9: Schematic illustration showing austenite structure in solidified shell [20].

Hannerz on the other hand, has noted generally that an increase in C level diminishes the incidence of surface cracking, but with no particular emphasis on a carbon range [21]. In carbon steels, the existence of a ductility trough between 600-900°C, even in the absence of prior remelting has been confirmed [34,69,70]. Suzuki et al. have shown that the width and the depth of the ductility trough diminishes with increasing carbon content, and dilatometric measurements have confirmed that the higher temperature side of the ductility trough corresponds to Ar_3 temperature [34]. This led the authors to propose a mechanism based on embrittlement due to the presence of proeutectoid ferrite along γ grain boundaries at Ar_3. The flow stress of ferrite is 1/4 that of the austenite at 900°C, and the work hardening rate of ferrite is small. Therefore, plastic deformation will occur preferentially in the grain boundary leading to a decrease in ductility. This hypothesis is supported by investigations on electrolytic iron where the narrow dual phase region precludes the formation of grain boundary ferrite, resulting in the absence of an embrittlement region [34].

Another study agrees with this mechanism for steels where the carbon level ranges from 0.04-0.28 wt% [69]. Above this concentration, the temperature for the start of the trough does not decrease with increasing C levels, but is raised by 100°C, and fracture occurs in the austenite phase by grain boundary sliding. This unexpected behaviour is attributed to the absence of dynamic recrystallization in high carbon steels due to the higher activation energy for dynamic recrystallization.

In addition to the influence of grain boundary ferrite, Crowther and Mintz have observed an influence of the austenite grain size in the α/γ duplex region, for carbon levels around 0.20 wt% [70]. Coarsening the grain size causes the temperature for the start of the ductility trough to increase up to the Ae_3 because of the production of long thin films of deformation induced ferrite around the grain boundaries. In fine grained material the ductility is better because the greater grain boundary surface area allows introduction of a greater volume fraction of ferrite reducing the relative strength difference between α and γ. Another possibility is that the high grain boundary surface area requires a greater volume of ferrite to be formed for complete delineation of the prior austenite grain boundaries. Hence the ferrite film becomes continuous at a temperature significantly lower than that for coarse grained material [71].

Finally, for very high carbon steels (0.65 wt%) the grain size refinement leads to even a better ductility because grain boundary sliding is impeded [70].

Ouchi et al did not observe any influence of C concentration on hot ductility in the range 0.081-0.20 wt% [28]. In the opinion of the present author, this could be explained by the presence of Nb in their steels; the precipitation of carbonitrides masking any carbon effect. Finally, Hannerz has revealed that decreasing the carbon level *diminishes* ductility [21]. Here it is difficult to explain why these results differ from those of Suzuki [34], although the presence of Al could be the cause.

2.4.4 Sulfur

Along with phosphorus and carbon, sulfur has long been linked with both internal and surface crack formation on continuously cast slabs [9,54,62]. For example, it has been shown that greater than 0.005 wt% S considerably increases the frequency of internal cracks [54]. Statistical analysis of one year's production of continuously cast products have revealed strong indications that S is associated with transverse surface cracks and therefore increases scarfing losses [21,54]. The seriousness of the problem is reflected by the extensive literature that exists concerning this problem [9,16,17,21,32,34,40,54,72-78].

Sulfur causes two ductility troughs; one some tens of degrees below the solidus (zone I), and the other between 800-1200 °C (zone II). As already noted the former is related to the onset of internal cracks, and the latter is associated with transverse surface cracks [16,73,74].

The results of an early study concerning the influence of S on the cracking resistance of weld metal, revealed that an increase of S concentration led to a decrease of the zero ductility temperature (zone I) [57]. At that time, the embrittlement phenomenon was attributed to S segregation leading to the formation of the Fe-FeS eutectic or FeS which have melting temperatures of 988 and 1190 °C respectively [75]. However, even with a relatively high sulfur level, ductility is regained below 1350°C, raising some doubts about this mechanism. Nevertheless, increasing the S content in almost pure iron (99.997 wt%) from 0 to 0.019 wt% decreases the ZDT from 1530 to 1450 °C, in tests carried out after solidification from the melt [36].

The ductility loss in zone II is associated with intergranular fracture and dense precipitation of fine (Fe,Mn)S particles enriched in iron at the austenite grain boundaries [76]. This, plus the results from many investigations undertaken on this subject [9,16,17,32,34,57,74,76], indicate that the lowest ductility results from high S levels, low Mn:S ratios, high preheat temperatures (the worst case being with prior melting of the sample) and high cooling rates [76]. All of these tend to increase fine precipitation. On the other hand, ductility is improved by a low annealing temperature followed by a slow cooling rate, as well as long holding times at test temperature prior to deformation. These factors all lead to a decrease in the density and an increase in the average size of precipitates [76]. Furthermore, high levels of Mn produce (Fe,Mn)S particles which are enriched in Mn. Such precipitates nucleate preferentially in the matrix and not at austenite grain boundaries [9]. In Fig. 2.10 the relationship between sulfur, manganese and ductility indicates that above a manganese content of 0.7 wt%, ductility is high, regardless of the sulfur level.

Another aspect of the effect of S which has been recently clarified, is the influence of segregated free sulfur at the austenite grain boundaries. At 900°C, it can be as much as 200 times larger than in the matrix [40]. Using quantum mechanics, Messmer and Briant [77] have demonstrated that segregated S exerts an attractive force on the electrons associated with the bonding of Fe atoms, thus reducing their strength. Their calculations support the experimental findings concerning hot ductility behaviour of zone refined iron doped with various levels of sulfur in the temperature zone 700-1200°C [24,78]. Above 50 ppm of S, voids nucleate at austenite grain boundaries because of sulfur segregation, and significant intergranular hot embrittlement takes place in the range 850-1100°C [78]. The void growth rate is higher than the rate of dynamic recrystallization, thus promoting earlier fracture.

In the next few sub-sections the influence of Al, Nb, Ti and V on hot ductility in zone III are presented. All these elements are carbonitride formers and, under certain conditions, can cause ductility problems by precipitation.

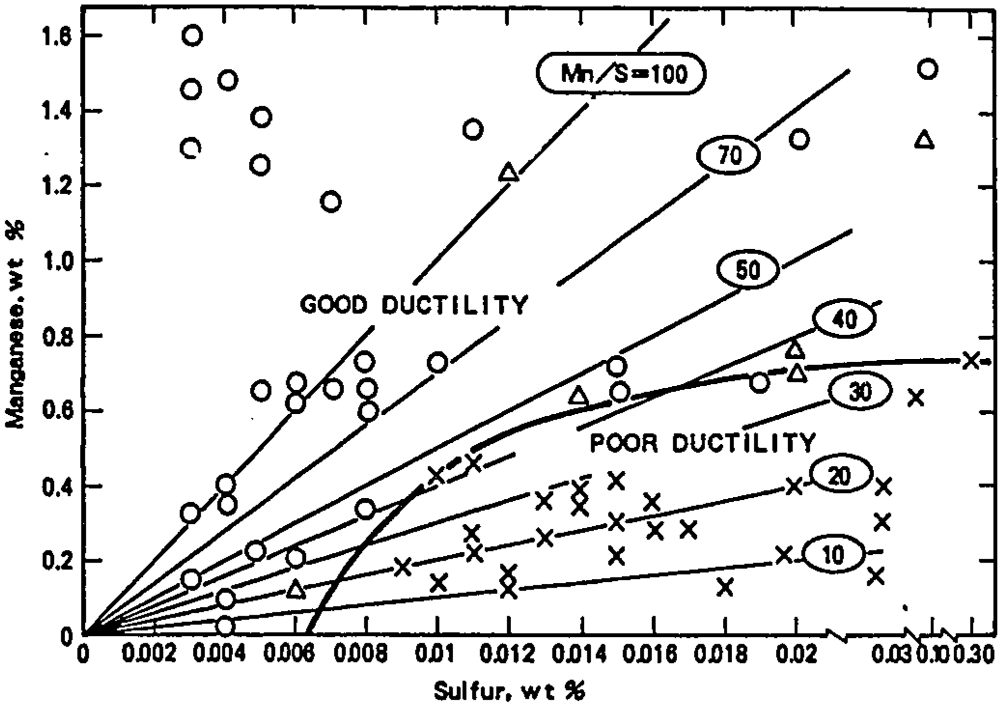

Fig. 2.10: Effect of Mn and S on the embrittlment in the temperature range 900-1200°C in low carbon steels (C<0.3%). 'Poor' ductility means RA<40% (X), 'good' ductility is RA>60% (○), and (Δ) are values between 40 and 60%, tested at 5 s^{-1}, C.R. = 20°C/s in the melted specimen [33].

But, it has been demonstrated [23,24,78] that these elements *do not create* any ductility trough when added to a 0.020 wt% carbon steel completely free of sulfur and other impurities. Increasing the sulfur content increases the depth and width of the ductility trough caused by the precipitates. Typically, the sulfur level above which the trough appears is between 0.0025-0035 wt%. In other words precipitates embrittle steel *only* if the grain boundary strength is lowered by segregated S.

2.4.5 Aluminum

To the knowledge of the present author, no investigation has been undertaken to study the effect of *free* Al on hot ductility. Aluminum is traditionally added as a deoxidant (Al-killed steels) or to refine grain size through AlN precipitation [79].

There is a high degree of certainty that AlN precipitation can cause transverse cracking in slab casting [15,21,28,34,41,49]. For common levels of Al and N ($Al \leqq 0.08$ wt% and $N \leqq 0.010$ wt%) the ductility trough is typically between 700-900°C. Increasing the product $Al_S.N$ (where Al_S is the soluble Al content) deepens the trough and widens it to higher temperatures [21,28,80]. It should be noted that the temperature zone of embrittlement covers the low austenitic range (typically 850-900°C) and the α-γ duplex region ($T \leqq 850°C$). The fracture model to explain the hot ductility behaviour in the α-γ duplex region (Fig. 2.11-a) resembles the one given for plain carbon steels. AlN, which can precipitate in the grain boundary ferrite, act as nuclei for void formation and as deformation proceeds at grain boundaries, rupture occurs by voids coalescence [45]. However, Ouchi and Matsumoto [28] claim that the primary factor controlling ductility is not AlN precipitation, but the thickness of ferrite around austenite grain boundaries.

A slight variant of this mechanism of embrittlement is illustrated in Fig. 2.11-b. It involves precipitation at the austenite grain boundary, nucleation of cavities at the interface grain boundary-precipitate, nucleation of ferrite induced by deformation [15,19] and coalescence of cavities [32]. The mechanism

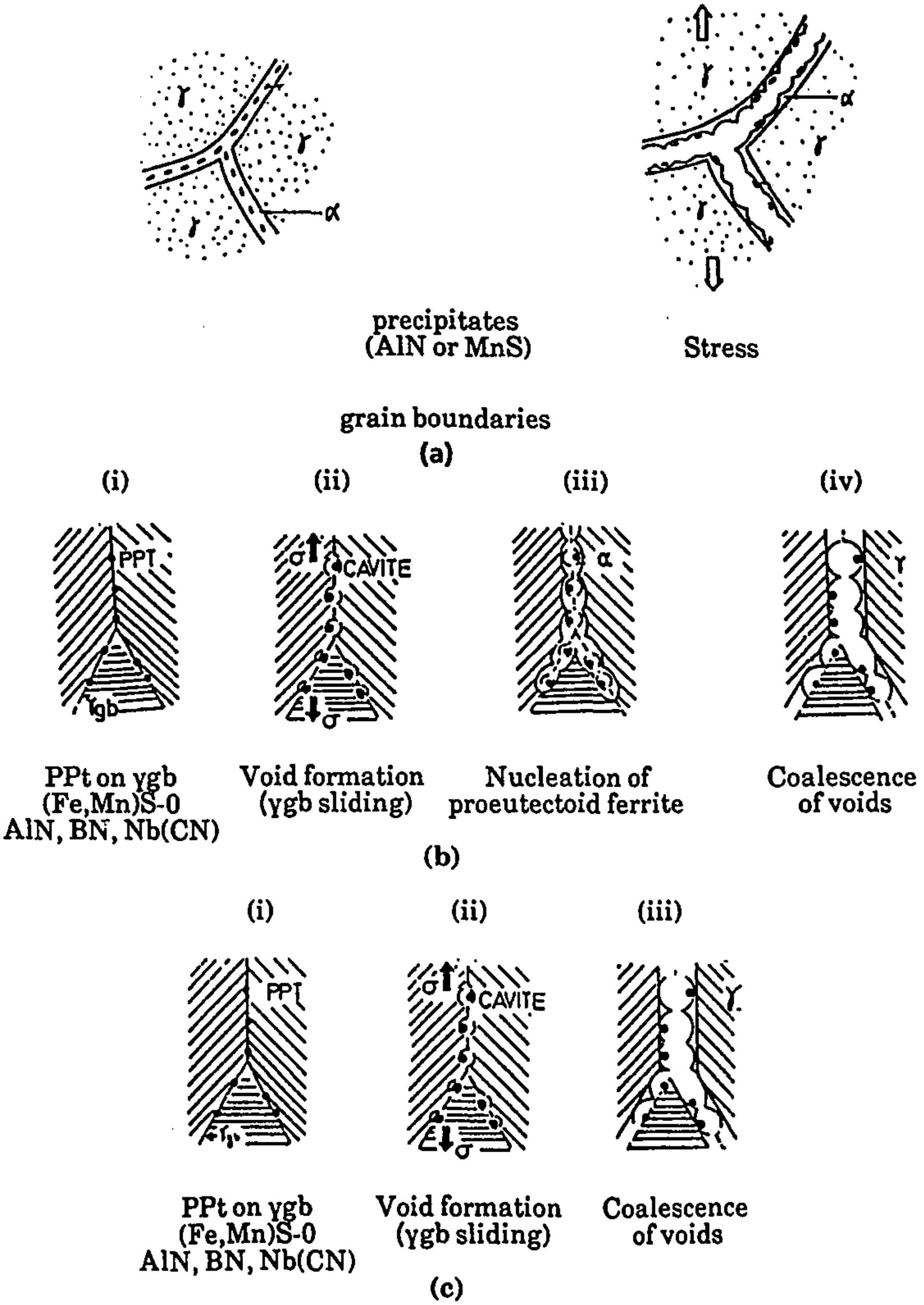

Figs 2.11: Models for the embrittlement in the austenite region due to AlN or Nb(C,N) precipitation: a [45], b [32,34], c [34,42].

in the low austenitic temperature region (Fig.2.11-c) is essentially the same, but with no influence of ferrite [34,42].

The heat treatment applied prior to testing can affect the precipitation behaviour of AlN and in turn influence hot ductility. For example, it has been demonstrated that rapid continuous cooling (>50°Cs^{-1}) from the solution treatment temperature produces fine and dense precipitation of AlN at the austenite grain boundaries, which results in very poor hot ductility [42,81]. In fact Funnel and Davies [42,43] found that an increase in the AlN particle size from 0.09 µm to 0.21 µm (by an appropriate heat treatment) led to an approximate doubling of the reduction of area at the test temperature of 850°C, all other testing conditions remaining constant. Similar results have been reported by Maheara et al. [19].

The mechanism preventing grain coarsening (AlN precipitation) is the same as the one that contributes to embrittlement in the temperature zone III [68]. It is therefore possible that any beneficial effect which could arise from grain refinement (as seen in plain carbon steels) may be offset by the effect of precipitates on the reduction of ductility [42,43]. However, it has been seen [66] that fine grained microalloyed steel obtained by prestraining of the material at 1050°C is effective in improving hot ductility.

For the same Al and N levels, hot ductility is worse in the as-cast condition than in the reheated case [30,82]. This is because, on cooling from the melt, highly segregated conditions favour AlN precipitation at the austenite grain boundaries. In the reheated case the AlN precipitates are taken back into solution and because of the sluggishness of precipitation in the austenite phase, fewer nitrides precipitate on cooling to test temperature. In addition to this, the coarsest austenite grain size is found in the as cast state [34].

In continuous casting, the strand surface does not follow monotonic cooling from the liquidus to the straightening temperature, but undergoes a cyclic rising and falling of temperature, although the *mean* temperature continuously decreases. The amplitude of the cycle can be as high as 100°C [47]. A simulation of a single cycle of a such cooling pattern, where the temperature was decreased to around 800-900°C and then increased to the test temperature of 1100°C, produced a deterioration of the ductility [39]. Conversely, a specimen held at 1100°C, on cooling from the solution temperature, and then deformed between 800-900°C exhibited improved ductility because of AlN particle coarsening [19].

Noting that an increase in prior holding time at test temperature in the 800-900°C temperature range is detrimental to hot ductility [19,80,83], it may be concluded that the hot ductility problem in Al bearing steels is mainly influenced by static (i.e. before deformation) rather than by dynamic (i.e. during deformation) precipitation [38,83,84]. However, some authors have not observed any precipitation before deformation [48,80,85]. These results indicate an influence of both static and dynamic precipitation on hot ductility. Prior deformation at high temperature ($T \geqq 1000$°C) and high strain rate ($\dot{\varepsilon} \geqq 10^{-2}s^{-1}$) leads also to improved ductility in the range 800-900°C, because strain induced precipitation and coarsening of AlN has occured [85].

From these studies, the following methods have been proposed that may reduce surface cracking frequency due to Al:

- reduce Al and N as much as possible and/or add an element which preferentially combines with nitrogen (e.g. Ti), thus limiting AlN precipitation [21,35],
- reduce temperature oscillations during secondary cooling [47]
- if applicable to the continuous casting operation, use a slow rate of cooling, and hold at a high temperature ($T \simeq 1100$°C) [85],
- reduce S level [21],
- predeform the material above 1000°C, at a relatively high strain rate [85].

2.4.6. Niobium (Columbium)

In continuously cast Nb bearing steels slabs, extensive precipitation of Nb(C,N) was observed in the area of transverse cracks [21,34,49]. This corresponds well to observations that Nb causes a ductility trough between 650-1100°C in hot ductility tests [15,28,44]. In general, increasing the Nb content widens and deepens the trough. Precipitation of Nb(CN) is the major cause of embrittlement and its effect in many ways resembles that of AlN.

The temperature zone where embrittlement occurs covers the low temperature austenite region and the γ-α temperature duplex range. The embrittlement mechanisms described in the previous section have also been suggested for Nb steels, but for intergranular embrittlement in the low γ temperature range, an alternative model has been proposed [19]. The previous mechanisms (Figs. 2.11 a-c) involved precipitation at the austenite grain boundaries followed by void nucleation at the grain boundary-precipitate interface [34,49]. The alternative model (Fig. 2.12), which is supported by other workers [15,39,83], involves matrix strengthening due to dynamic precipitation of Nb(C,N), leading to a strain concentration in the vicinity of austenite grain boundaries, where much softer precipitate free zones exist. The resulting strain concentration leads to fracture. Furthermore, in the austenite plus ferrite region, Nb(C,N) matrix precipitation suppresses the growth of grain boundary ferrite, causing a higher strain concentration in the narrow soft region. Bernard et al. [15] suggest that the main cause of poor hot ductility is retardation of dynamic recrystallization by precipitation. However the strain to fracture is smaller than that required to nucleate dynamic recrystallization. Furthermore, with respect to cracking in continuous casting, the strains generated during the straightening operation are also too small to nucleate dynamic recrystallization [28,46].

Heat treatments applied before deformation play a very important role in the hot ductility of Nb bearing steels. Once again it is observed that fast cooling rates from the solution temperature of the carbonitrides (around 1300°C) and the test temperature give a significantly finer and denser precipitation than slow cooling. This leads to a deterioration of hot ductility because small particles are more effective in pinning grain boundaries. Thus facilitating grain-boundary cavity growth by grain boundary sliding much easier [42,49]

The effects of thermal cycling to low temperatures (950°C) [47] and predeformation at high temperatures (1050°C), [68,85] are similar to that of AlN. The former deteriorates ductility by increasing precipitation of Nb(C,N) whilst the latter is beneficial due to precipitate coarsening. Similar results are found in tests performed above 1000°C following a solution treatment at 1300°C and intermediate treatment between 800-900°C [15,28,39,86].

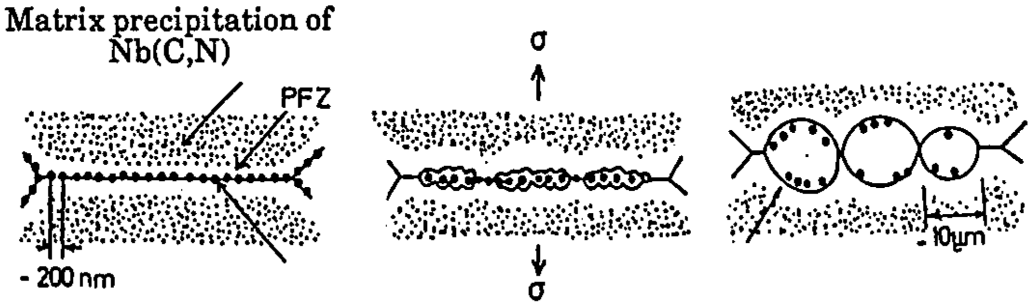

(a) grain boundary precipitation (b) Nucleation of microvoids (c) Microvoids coalescence

Fig 2.12 Models for the embrittlement in the austenite region due to Nb(C,N) precipitation (PFZ = Precipitation Free Zone) [19].

The respective influence of static and dynamic precipitation on hot ductility is unclear. Some workers claim that poor hot ductility is mainly due to dynamic precipitation [15,19,49], whilst others conclude that there is an influence of both types of precipitation [28,86]. Crowther et al. [83] have investigated this problem in depth by performing tensile tests at 950°C (following solution treatment) after holding for various times at test temperature. They have observed that, although increasing the holding time before deformation reduces embrittlement, even after 10,000 s of holding time the reduction of area is still lower than 50%. They conclude that both static and dynamic precipitation are effective in reducing hot ductility. However, dynamic precipitates have smaller size ($d = 15nm$) than static ones ($d = 60nm$), rendering them more deleterious to hot ductility. Furthermore, dynamic precipitation was observed either at the austenite grain boundaries or in the matrix (in agreement with the last embrittlement model presented above), whereas static precipitation is observed only at the austenite grain boundaries.

Unlike Al containing steels, it has been recently observed that Nb bearing steels tested after melting and cooling to the test temperature are more ductile than specimens which have been melted, cooled down to 100°C and, solution treated at 1330°C [30,38]. There is also an 80°C decrease in the upper temperature side of the ductility trough in the case of the as-cast material. The reduced ductility in reheated samples is attributed to dense, finely dispersed precipitation of Nb(C,N) along austenite grain boundaries and in the matrix. In the as-cast samples marked segregation occurs, resulting in the production of coarse Nb(C,N) eutectics at the austenite grain boundaries and fine precipitation in the matrix [33].

The effect of niobium carbonitrides on hot ductility can also depend on the chemical composition of the precipitates [28]. At a constant Nb level (0.015 wt%) it was found that an increase of the nitrogen level from 0.0020 to 0.0063 wt% markedly reduces plasticity. Low nitrogen levels promote the formation of $NbC_{0.85}$ type particles, whereas for high N concentrations $NbC_{0.60}N_{0.25}$ precipitation occurs. The better ductility observed with the former precipitates was ascribed to its lower rate of precipitation in austenite, leading to a lower volume fraction of precipitates. Mintz and Arrowsmith found only a slight influence of N concentration on hot ductility of C-Mn-Nb-Al steel, but here the lowest nitrogen level was 0.0042 wt% [44].

Suggestions to reduce the incidence of cracks in Nb bearing steels largely follow those for Al i.e.:

- lower the Nb level as much as possible and/or reduce the nitrogen level [28]
- perform the straightening operation above 1000°C [15],
- reduce the cooling rate and the amplitude of the temperature cycles, [47]
- apply a given amount of deformation above 1000°C allowing precipitation and coarsening of carbonitrides [85].

It is clear that the effect of Nb in steels is similar to that of Al. In fact the two troughs are approximately in the same temperature range, although, for Nb bearing steels, the ductility drop initiates at higher temperatures than for Al steels. This is consistent with the temperatures corresponding to the maximum precipitation rates which are 950°C for Nb(C,N) [82] and 815°C for AlN [87]. In steels where both Al and Nb are present, an interaction has been observed in that an increase in the soluble Al level diminishes both the mean particle size and interparticle spacing of Nb(C,N), consequently further reducing ductility [49]. This phenomenon has not yet received any physical interpretation.

2.4.7 Titanium

The benefits of using Ti additions to avoid *ingot* casting crack problems in Al killed steels have been reported [26,88,89]. However, no comprehensive statistical evaluations concerning the influence of this element on the quality of continuously cast products were found, although several laboratory investigations have been conducted on the role of Ti in hot plasticity of steels [21,24,25,26,28,42,43,49,90-93].

It is generally accepted that a Ti addition to Al bearing steels regains the ductility [26,42,49,92,90-93]. This may be due to the preferential precipitation of TiN, preventing the formation of AlN. TiN precipitates more uniformly in austenite, which is perhaps less damaging to hot ductility than AlN, which preferentially nucleates at the austenite grain boundaries. There is an alternative possibility that the improvement is *not* related to the prevention of AlN precipitation but to the smaller austenite grain size produced by TiN particles [93]. However, if the heat treatment employed is such that the TiN particles are small, a ductility trough can be observed [43]. In iron alloys containing AlN and S, Ti only improves hot ductility if $Ti/N > 3.4$ (stoichiometric ratio) which is attributable to the formation of titanium sulphides reducing S segregation at the austenite grain boundaries [24,91].

Mintz and Arrowsmith have noted only a slight improvement of hot ductility when Ti is added to Nb-Al steels [44]. On the other hand, Ouchi et al. [28] observe a beneficial effect of a Ti addition and, as noted above, explain this by the preferential formation of $NbC_{0.85}$ as opposed $NbC_{0.60}N_{0.25}$ due to N being taken up by Ti. Grain refinement is also regarded as contributing to the beneficial effect of Ti in this case.

All the aforementioned experiments were carried out after annealing around 1300°C. When tested in the as cast condition, C-Mn-Nb-Al steels were found to be more ductile with the addition of Ti [30]. The improvement was attributed to the removal of Nb(CN) precipitation at the austenite grain boundaries and its replacement by coarser NbTi(CN) precipitates. The same Ti bearing steels tested after annealing at 1330°C have a greater reduction of area than in the as cast state because of grain refinement after solution treatment.

Finally, it was recently shown that Ti in pure iron doped with S but *free* of N greatly improves hot ductility because the formation of Ti *sulphides* impedes S segregation [90].

2.4.8 Vanadium

V can form either V_4C_3 and VCN. The former precipitates from the Ar_3 to 500°C [94] and is not considered in this section; the latter shows a maximum precipitation rate at about 885°C [95]. There is no clear evidence that V is associated with surface defects in continuous casting [21], but Coleman and

Wilcox [35] have found a deleterious influence of this element on surface cracks of the product.

Hot ductility investigations by Hannerz [21] have revealed a ductility drop roughly proportional to the V concentration in the temperature range 700-950°C [21], but if the V level is limited to 0.07 wt% the depth of the trough is small and, below this value, the ductility is comparable to plain carbon steels. Coleman and Wilcox [35] have also reported a ductility trough due to V, but a comparison with the data of Hannerz [21] is difficult because they do not give the chemical composition of their steels. However, from their work it appears that addition of Al to the V bearing steels *improves* hot ductility [35]. The formation of AlN reduces the VN precipitation and the resultant increase in stress relaxation more than compensates for the detrimental effect of increased of AlN precipitation at the grain boundaries.

2.4.9 Molybdenum

This element has no deleterious influence on slab quality, but it has been shown to slightly improve ductility when it is added to levels of about 0.6 wt% [21].

2.4.10 Boron

No data exist regarding the effect of this element on the surface cracking frequency, but it may contribute to *internal* quality problems because it strongly reduces the zero ductility temperature of steels [33] via its strong tendency towards segregation. However, production statistics have clearly pointed out the beneficial influence of 'minute' additions of boron on *surface* quality [21]. This is reflected in hot tensile tests where boron largely increases hot ductility in zone III. This improvement can be ascribed to several factors: preferential boron nitride precipitation, retardation of the γ/α transformation which presumably avoids ferrite film formation at the austenite grain boundaries, and increasing the resistance to grain boundary sliding, which results in better creep ductility [21].

2.4.11 Other alloying elements

Elements which readily dissolve in iron (Ni, Cr, Cu) are not reported to be detrimental, but star cracks on continuously cast products were found to be caused by contamination from the copper mould, indicating a hot shortness problem [15]. However, no influence in the range 600-1000°C has been seen in laboratory tests, with the noticeable exception of a ductility decrease occurring below 650°C in steels containing more than 1% Cu. This cannot be related to hot shortness which is observed at much higher temperatures [21].

Cerium and calcium are used to improve the cleanliness of steels by reducing the S level [21,35]. Cerium is reported to have no influence on hot ductility [21] but calcium increases the reduction of area values of C-Mn-Al steels [96]. This enhancement has been attributed to the removal of sulphur by Ca [96]. Finally, Zr improves the hot ductility of Nb-Al containing steels, via preferential formation of zirconium nitrides (analogous to the influence of Ti).

CHAPTER 3

EXPERIMENTAL EQUIPMENT AND METHODS

As seen in the previous chapter, many hot ductility studies have been performed by hot tensile testing, with reduction of area at fracture taken as the relevant ductility criterion for hot ductility measurements, in the majority of cases. In the present study, tensile testing was also employed to investigate the hot ductility and strength behaviour of five microalloyed steels. The experimental work can be divided into two temperature domains; (i) 1400°C-solidus, and (ii) 800-1300°C. The first range clearly corresponds to zone I, whilst the second range encompasses zones II and III. The latter zones are associated with precipitation of sulfides and carbonitrides, respectively. However, due to the high Mn:S ratio, no Mn-Fe sulfides are expected to precipitate, therefore eliminating the cause of a zone II ductility trough. Thus, effectively, only zones I and III were investigated.

The hot deformation behaviour was examined under various conditions of strain rate and prior heat treatment. Apart from hot ductility, the hot strength behaviour was also analysed in order to assess any possible interrelationship between ductility and strength.

3.1. MATERIALS AND SPECIMEN PREPARATION

The chemical compositions of the materials examined are given in wt% and at% in Table 3.1. Grades P, A, B, and C are laboratory compositions which were prepared at the Physical Metallurgy Research Laboratories (CANMET, Ottawa), in the following manner. Air induction was employed to produce the four steels from a base alloy which contained low concentrations of nitrogen, carbon and residuals; deoxydation was achieved using aluminum. The liquid steel was then top poured into a permanent cast iron mold of dimensions 0.127 x 0.152 x 0.305 m^3, which corresponds to a 50 kg heat. The cooling rate during solidification was about 140 to 150°C/min between 1500 and 1100°C, and an average of 90°C/min down to room temperature. The cast material was then

Table 3.1

Chemical composition (in atomic and weight %) of the steels investigated.

		C	Mn	Si	P	N	S	Al	Nb	Ti	V	Ni	Cr
STEEL P	at%	0.364	1.40	0.690	0.0179	0.0309	0.0156	0.0411					
	wt%	0.078	1.39	0.35	0.010	0.0078	0.009	0.02					
STEEL A	at%	0.323	1.55	0.573	0.0215	0.0396	0.0156	0.0615	0.0179	0.015			
	wt%	0.072	1.54	0.29	0.012	0.01	0.009	0.03	0.03	0.013			
STEEL B	at%	0.462	1.56	0.572	0.0215	0.0396	0.0156	0.0615	0.0179	0.015			
	wt%	0.1	1.55	0.29	0.012	0.01	0.009	0.03	0.03	0.013			
STEEL C	at%	0.645	1.55	0.571	0.0215	0.0396	0.0156	0.0616	0.0179	0.015			
	wt%	0.14	1.54	0.29	0.012	0.01	0.009	0.03	0.03	0.013			
STEEL S	at%	0.323	1.41	0.572	0.0108	0.0316	0.0087	0.0926	0.0119	0.0139	0.087	0.236	0.266
	wt%	0.07	1.4	0.29	0.006	0.008	0.005	0.045	0.02	0.012	0.08	0.25	0.25

reheated at 1210°C and rolled into 0.017 m thick plates in 17 passes executed between 1200°C to 880°C.

Steel S, an experimental grade used with the consent of Stelco, was received in the as cast condition as a piece sectioned from a continuously cast slab with a cross section of 0.21x 2.2 m.

The five steels investigated can be divided into two groups. Group I refers to steels P, A and S in which the carbon level was kept constant but the microalloy additions were varied. In this grouping, the reference was steel P, a C-Mn Al-killed grade. Steel A was used to determine the effect of Nb and Ti on hot ductility, and grade S enabled the influence of Ni and Cr additions (0.25 wt% each), to a Nb-Ti bearing, steel to be assessed. (However, since steel S was received in the as cast condition and not as-hot rolled, the difference in flow curve shape between steels S and A may be due to the differing thermomechanical histories.) Nb and Ti are, of course, classical microalloying elements; the former is added for ferrite grain refinement via pancaking, and/or precipitation hardening, the latter for grain growth inhibition. Ni and Cr are used in carbon steel to increase matrix strengthening by solid solution.

Group II is comprised of grades A, B and C. In these grades, the amount of Al, Nb and Ti is constant (0.03 wt%, 0.03 wt% and 0.013 wt%, respectively), but the level of carbon increases from 0.07 wt% to 0.14 wt%, this latter value corresponding approximately to the peritectic composition.

For steels A, B, C and P, tensile specimens with shouldered ends were machined from the rolled plates, with the longitudinal axis parallel to the rolling direction (Fig. 3.1-a). In the case of the as-cast grade S, sections were cut out from the slab, as shown in Fig. 3.1-b, from which specimens were machined with their axes parallel to the casting direction. The shape and dimensions of the specimens used in this work are given in Fig 3.1-c. The dimensions do not rigidly follow the conventional standards for tensile specimens [97], and in the hot ductility literature the specimen size varies greatly. Typically, diameters from 5 to 10 mm and gauge lengths from 20 mm to 120 mm have been used. Thus, the dimensions adopted here were based on the constraints of accuracy of

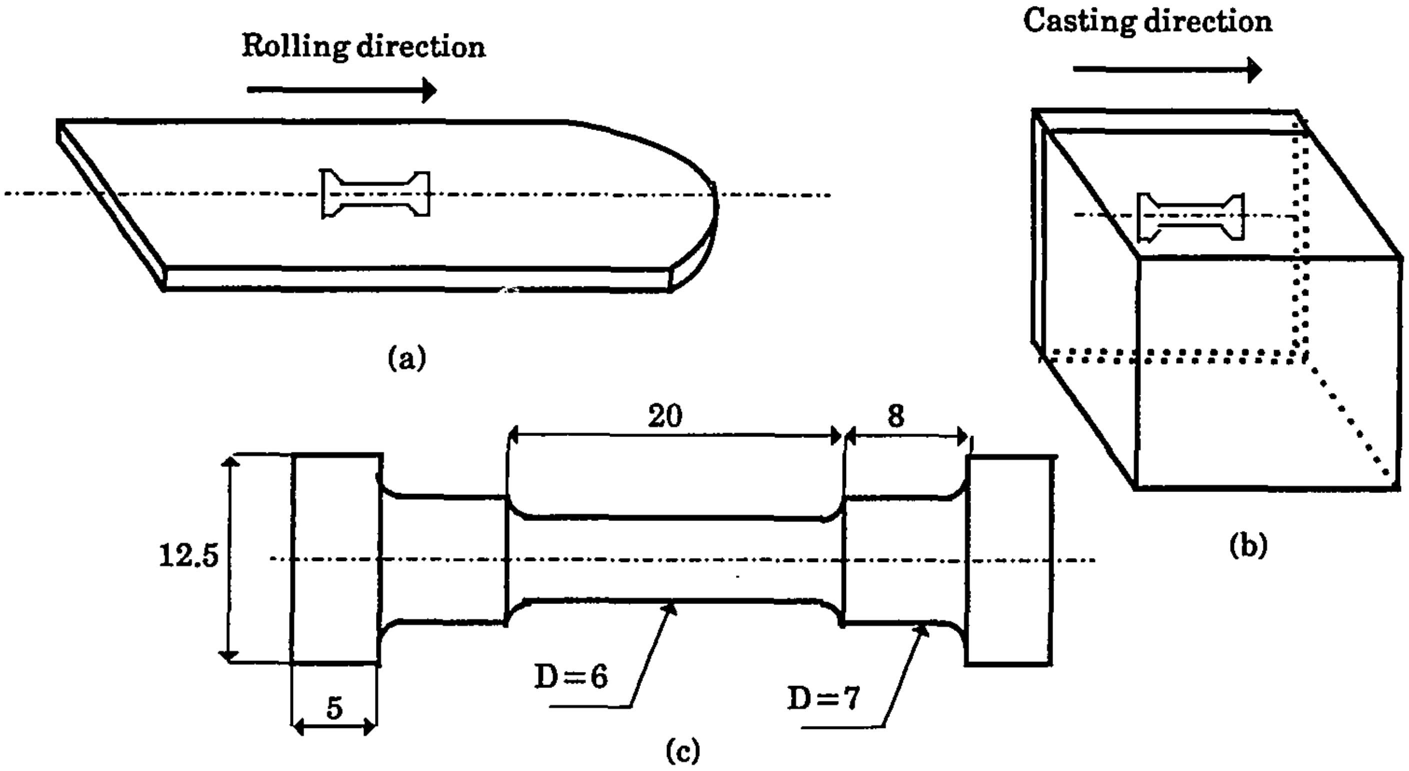

Fig. 3.1: (a) Tensile specimen orientation with respect to rolling direction of the rolled plates (steels P, A, B, and C).
(b) Tensile specimen orientation with respect to casting direction (steel S).
(c) Specimen configuration (dimensions in mm).

reduction of area measurements and limitations in the tensile testing machine and heating system configuration.

3.2. EXPERIMENTAL EQUIPMENT

3.2.1. Servohydraulic Tensile Test Apparatus

The experimental apparatus, which includes an MTS testing machine, Centorr furnace, PDP 11/04 computer, Tektronix terminal and hard copy device is shown in Fig. 3.2. The high temperature tensile tests were performed on a 100 KN closed loop MTS servohydraulic mechanical testing apparatus. In the temperature range 800-1300°C, load measurements were performed using a 453 kg (1000 lb) capacity load cell; above 1400°C a 113.5 kg (250 lb) capacity load cell was used. Machine control and data acquisition were achieved using a PDP-11/04 computer via a 433 processor interface unit. Thrcugh computer control, deformation at constant true strain rate was possible in the region of uniform elongation i.e. up to the onset of necking.

A program written in MTS RT 11 basic language, created for compression testing [98], was modified for tensile experiments. After the end of each experiment the load and actuator displacement information was recorded on floppy disk and converted into true stress-strain curves. The tensile flow curves were analysed to determine the maximum true stress and the occurrence of dynamic recrystallization. The programs for testing, data acquisition, data analysis and flow curve plotting are given in appendices I, II and III, respectively.

The final diameter of the fractured sample was measured with an accuracy of ±.1 mm using a projection microscope. The reduction of area (RA) at fracture was defined in the following way:

$$RA = 100(1 - D_f^2/D_0^2) \quad (\%) \tag{3.1}$$

Where D_0 and D_f are the initial diameter and diameter at fracture, respectively.

Fig. 3.2: View of the tensile testing system: (A) Furnace and vacuum system. (B) Heating and vacuum console. (C) Computer PDP 11 (D) Tektronix 4010 console.

3.2.2. Tensile Grip Design

From the literature, two alloys were selected that met the requirements of high strength and creep resistance at very high temperatures (above 1400°C): TZM and tungsten [99,100]. TZM, a molybdenum based alloy containing about 0.5 wt% Ti and 0.08 wt% Zr alloy (hence the initials TZM), that can be used up to 1600°C in vacuum or in an inert atmosphere, was chosen over W because of much better machinability and lower cost. However, at 20% Mo, the iron-molybdenum phase diagram displays an eutectic, with a melting point of 1450°C [101]. If the sample is in direct contact with the grips at a high temperatures, significant iron-molybdenum interdiffusion could take place at the sample-grip interface, and the eutectic composition may be attained. To avoid this possibility, both the grips and the specimen shoulders were covered with a layer of very pure (99.999%) alumina powder. For experiments of increased duration, the use of an alumina ring between grip and sample may be a better alternative.

The tensile grip design is shown in Fig. 3.3 and the grip/specimen configuration is displayed in Fig. 3.4.

3.3.3. Vacuum Furnace

The tests were performed in a Centorr M60 vacuum furnace (Fig. 3.5), which, under ideal conditions, can reach temperatures up to 1650°C. The heating elements are made of tungsten mesh and are surrounded by several layers of molybdenum shields, which insure thermal protection of the water cooled chamber walls and efficient specimen heating. Tests were carried out in a vacuum which was typically around $6x10^{-5}$ Torr. Compared to the heating systems mentioned in the literature review, the Centorr M60 furnace exhibits a very low thermal gradient (which decreases with increasing temperature), i.e. ±5°C over a 75 mm heat zone length. Since the specimen length is 46 mm, a very low thermal gradient in the specimen can be expected.

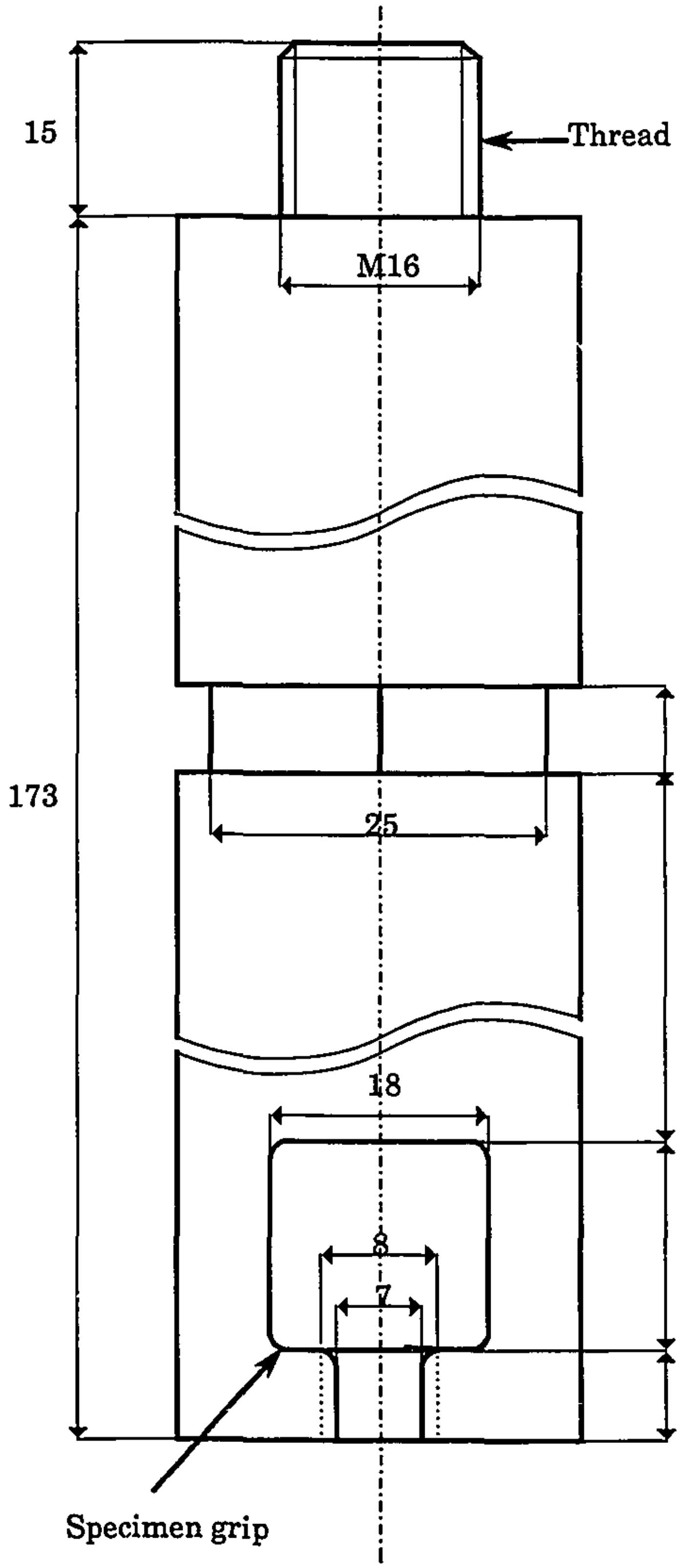

Fig. 3.3: Shape and dimensions (mm) of the tensile grip.

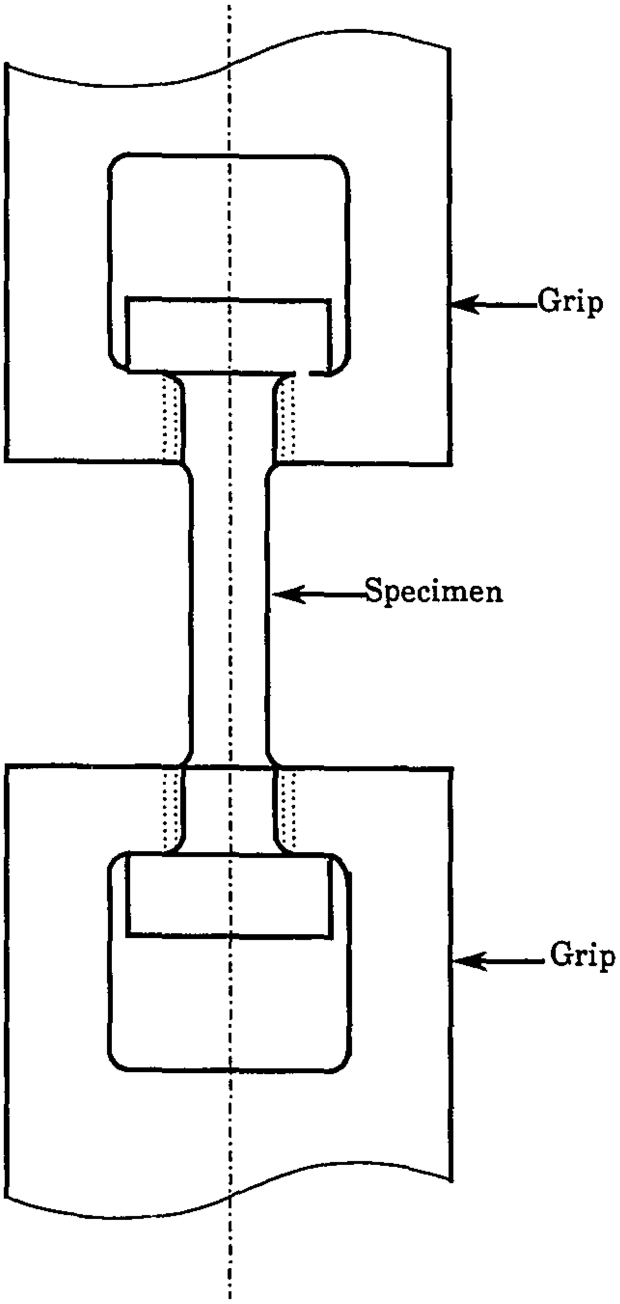

Fig. 3.4: Specimen gripping configuration.

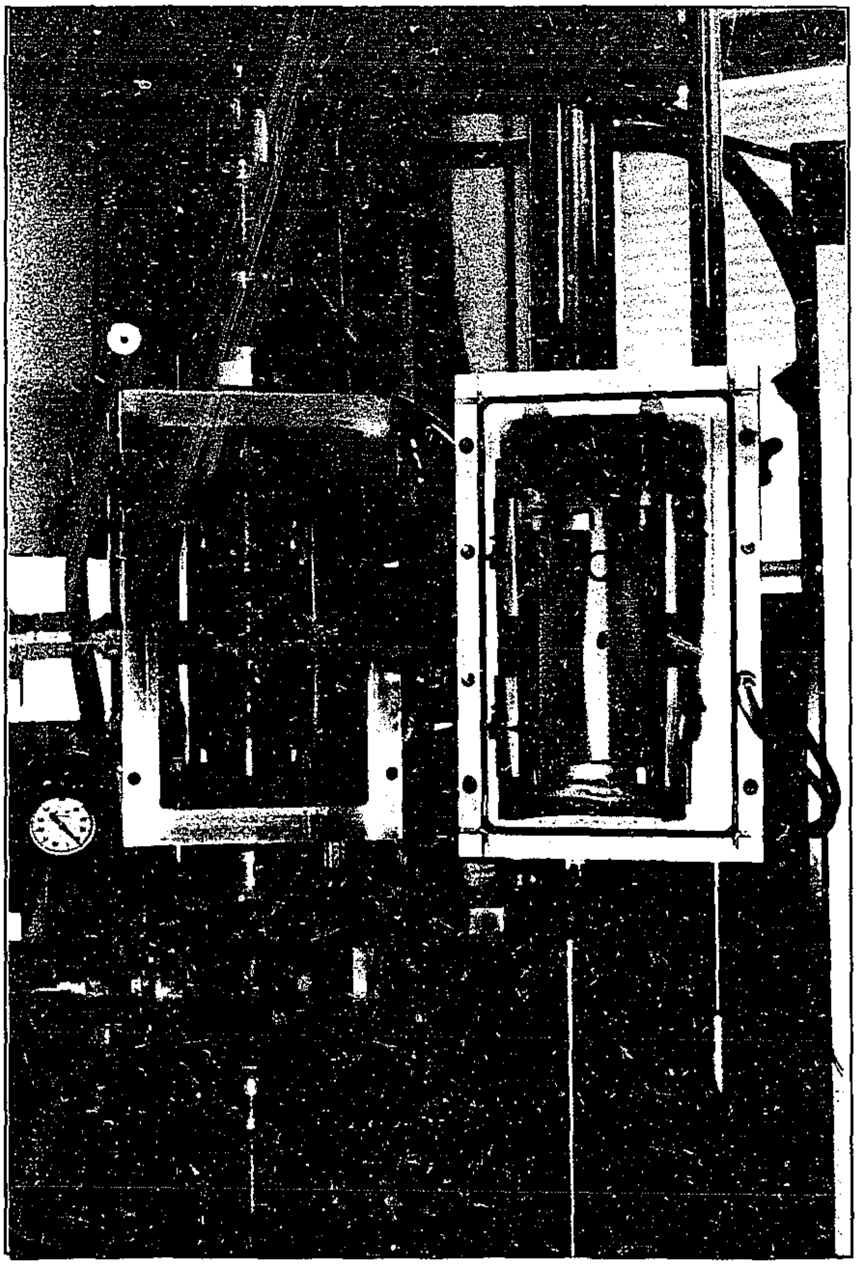

Fig. 3.5: Internal view of the heating chamber: (A) Specimen. (B) Grips. (C) Heating elements (tungsten mesh). (D) Molybdenum shields.

Although the testing configuration used in this study did not permit local melting of the sample, the mechanical properties of the material could be determined at a uniform and precisely controlled temperature. The temperature measurement was made by contacting two thermocouples on the specimen surface at the middle of the gauge length. The error in the temperature measurement, which has been estimated to be ±5°C, includes several factors: (i) non-ideal furnace operating conditions, leading to a higher thermal gradient, (ii) deteriorating contact between the surface of the sample and the thermocouple during testing.

Temperature measurements above 1350°C were initially performed with Pt/Pt-10%Rh (S type) or Pt/Pt-13% Rh (R type) thermocouples. However, it became apparent that these thermocouples deteriorated after several tests above 1400°C in vacuum. This could be attributed to Pt or Rh sublimation in vacuum, which led to a change in the characteristics of the thermal junction. Thus, in this work, W/W-5%Rh (C type) thermocouples were subsequently employed, since these remain stable at high temperatures in vacuum.

3.4 TENSILE TESTING CONDITIONS AND PROCEDURE

As mentioned at the beginning of this chapter, hot ductility investigations were performed in the two temperature domains corresponding to the two zones of poor ductility observed in steels with high manganese-sulfur ratios:

- Zone I; between 1400°C and the zero ductility temperature.
- Zone III; between 800 and 1300°C.

Although no hot ductility problems were expected to arise from (Mn-Fe)S precipitation (zone II) because of the high Mn:S ratios, the investigated zone III temperature range was extended up to 1300°C. Usually, zone III is only considered to occur between 800 and 1100°C. However, early experiments indicated, that in some cases, the ductility trough was not completely recovered at 1100°C. The zone III investigation was thus extended to 1300°C.

Three strain rates, 10^{-2}, 10^{-3} and, $2x10^{-4}s^{-1}$, were used to examine the tensile behavior in zone I. As noted earlier, strain rate variations do not affect the zero ductility *temperature*. In this work, interest was generally centred on the influence of strain rate variations on strength. Here, because the test temperatures were above 1400°C, no sensitization (i.e. prior heat treatment) was necessary. In other words, the specimens were heated directly to test temperature, held for 5 min. and then deformed (Fig. 3.6-a).

For zone III, the following heat treatments were used (Figs. 3.6-a, b, and c):

a) Direct heating; heat from room temperature to test temperature; 10 min. hold at test temperature prior to deformation to fracture.
b) Annealing; heat up to 1330°C; 10 min hold; furnace cool to test temperature; hold 3 min and then deformation to fracture.
c) Sensitization; heat up to 1480°C; 5 min hold (higher temperature requires shorter time for equilibration); furnace cool to test temperature; 3 min hold and then deformation to fracture.

For all tests, the rate of heating was between 60 and 80°C/min. In the case of the annealing and sensitizing treatments, the cooling patterns from the reheat to the test temperatures are given in Fig. 3.7. After fracture, the specimens were cooled to ambient temperature in 15 min using helium to increase the cooling rate (therefore increasing the rate of testing). For the direct and sensitizing treatments, deformation was carried out under the strain rates used for zone I. This range of strain rates largely encompasses those used in the majority of the published hot ductility/continuous casting data. However, any effects of chemistry and heat treatment were generally emphasized with decreasing the strain rate. Thus, in the case of the annealing treatment, only the lowest strain rate was employed.

3.5. DIFFERENTIAL THERMAL ANALYSIS

Phase transformations can influence, to a large degree, the ductility behaviour. In zone III, much work has been done to correlate the $\gamma \rightarrow \alpha$

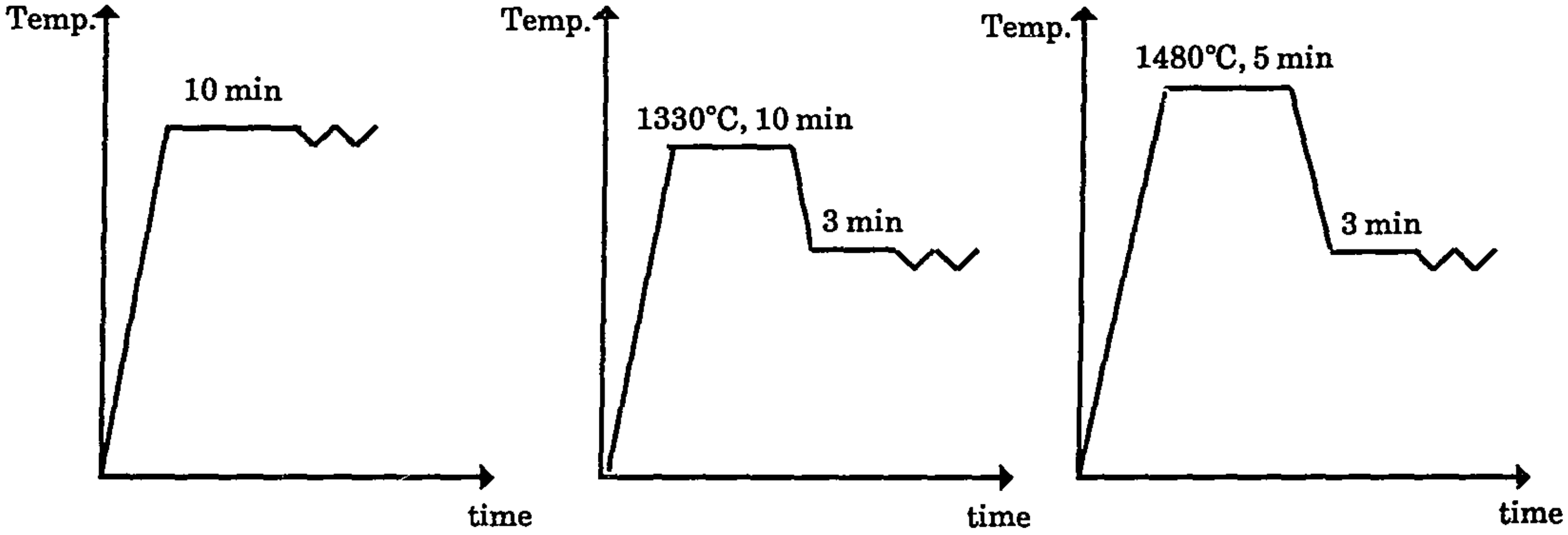

(a): Direct heating (b): Annealing (c): Sensitizing

Fig. 3.6: Heat treatments applied prior to deformation between 800 and 1300°C.

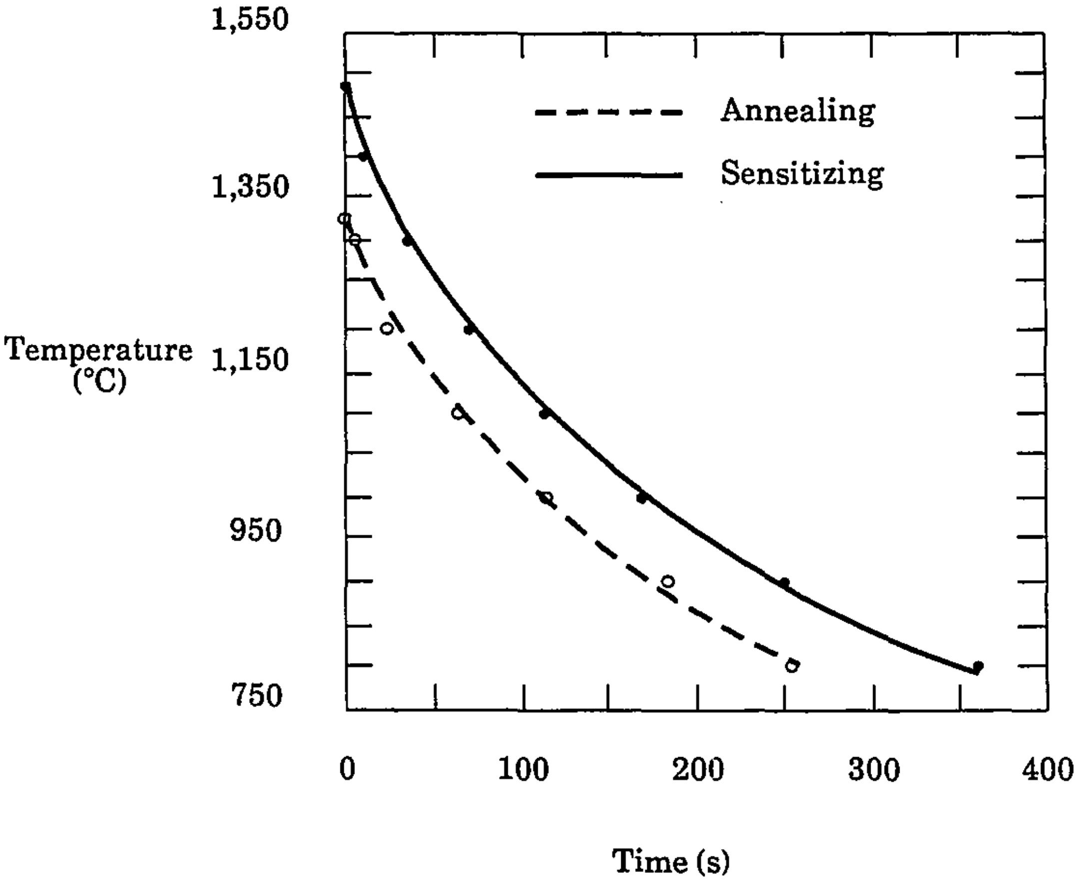

Fig. 3.7: Cooling patterns from reheating to test temperature for annealing and sensitizing heat treatments.

transformation with the chemical composition. Appropriate equations were used here to define this lower temperature transformation. In this study the various transformation temperatures in zone I were measured by using Differential Thermal Analysis (DTA). The main advantages of this technique over others (e.g. dilatometry) are that high temperatures can be attained, thus the solid to liquid transformation can be readily accommodated. Although differential thermal analysis is a widely used technique to follow transformations (or chemical reactions) in polymers, it has been rarely used for steels. In fact, only one such publication was found, giving phase transformation details of low carbon steels above 1400°C [59]. Unfortunately, no experimental or analytical details concerning DTA were presented in this paper. Because of the lack of information regarding the application of DTA to transformation in steel, new methods were developed in this thesis to analyse the DTA curves. The transformation temperatures, which are of interest in zone I, are the beginning and the end of the γ-to-δ transition and, most importantly, the solidus temperature.

3.5.1 Principle of the Technique

DTA is based on a comparison of the thermal properties of the sample, with those of a reference substance which undergoes no chemical reaction, or phase transformation, in the temperature range of interest. The reference and sample are simultaneously heated in the same furnace from room temperature to the desired temperature at a constant heating rate (typically 10°C/min). During heating, the sample temperature (T_S) and the temperature difference ($\Delta T = T_r - T_S$) between reference and specimen are recorded. If the sample does not undergo a reaction or a transformation over the temperature range involved, the differential temperature curve should be a line which is parallel to the sample temperature axis, i.e. the baseline, Fig. 3.8. Ideally $\Delta T = 0$, but even a small thermal gradient in the furnace, or differences in the characteristics of the thermocouples, will result in a shift of the baseline above or below $Tr - Ts = 0$. The important point is that the baseline must be parallel to the sample temperature axis.

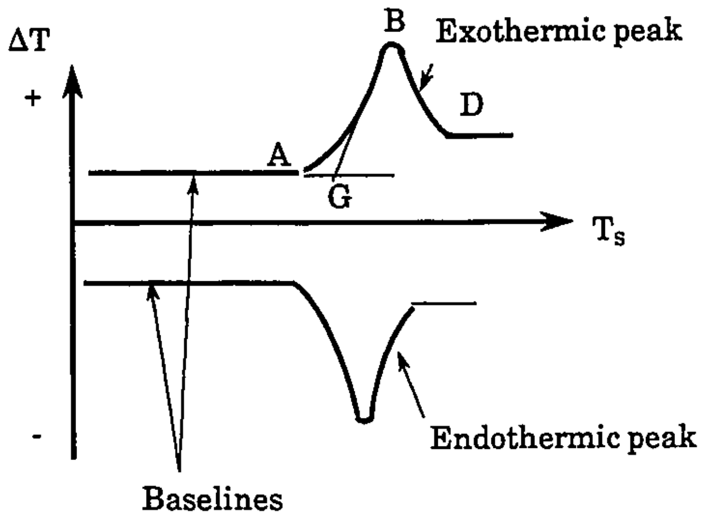

Fig.3.8: Schematic diagram of endothermic and exothermic DTA peaks [102].

However, if the sample experiences a phase transformation this will be accompanied by either a change in heat capacity, or an endothermic or exothermic reaction. In either case, the reference temperature will continue to rise at the programmed rate, while the sample temperature will increase at a different rate. On the ΔT versus T_S curve, this is revealed as a discontinuity or peak. For a pure substance, the phase transition takes place at a single temperature, and therefore appears on the curve as a spike. In steels, however, phase transitions generally occur over a temperature range and this, together with a slow heating rate, leads to a broad peak. On completion of the reaction, the temperature of the sample should rapidly change, so that the baseline ΔT is re-established.

In practice, DTA curves are difficult to analyse. One of the most common problems is defining the point at which a deviation from the baseline occurs, i.e. the temperature of the onset of the phase transformation. This temperature is not always clear, especially when the transformation occurs over a significant temperature range. When the reaction is endothermic or exothermic the DTA peak displays a shape as illustrated in Fig. 3.8, and the transformation start temperature (G), is usually defined by the intersection of the tangent BG, drawn at the point of greatest slope, with the extrapolated base line AG [102]. For the steels under investigation, however, the application of this technique to determine the solidus temperatures gives unrealistic results. However, for all the steels but grade C, closer examination of this peak (Fig. 3.9) reveals two curves. The solidus temperature determined using the initial maximum slope A'G' gives a temperature which is very close to the observed point of deviation from the baseline.

An endothermic (or exothermic) reaction leading to DTA curves, such as is illustrated in Fig. 3.9, is observed only for phase change involving relatively high enthalpy changes e.g. solid-liquid transformations. However, for solid-solid transformations, enthalpy changes are small and two other types of DTA behaviour can be identified. In Fig. 3.10-a, the two phases have different heat capacities, but negligible heat is involved in the reaction, thus the discontinuity is solely due to the change in heat capacity. In this case, the beginning of the transformation is determined as shown in the Fig. 3.10-a [102,103] and the end is assumed to be attained when the differential temperature reaches another

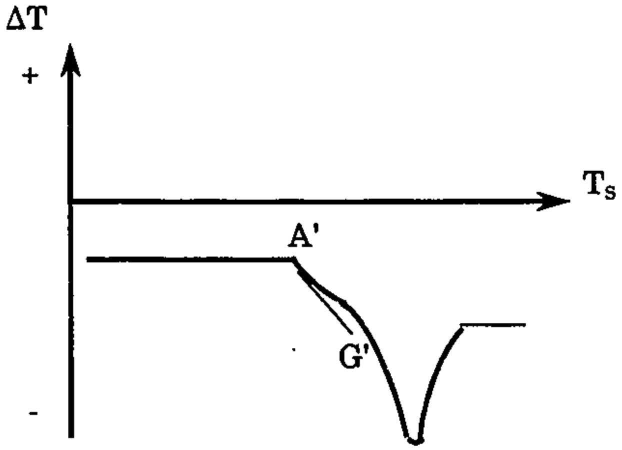

Fig.3.9: Typical DTA peak associated with the solid to liquid transformation in the steels used in this work. The solidus temperature is taken to be the point at which the baseline and the 'initial' maximum slope, A'G', intersect.

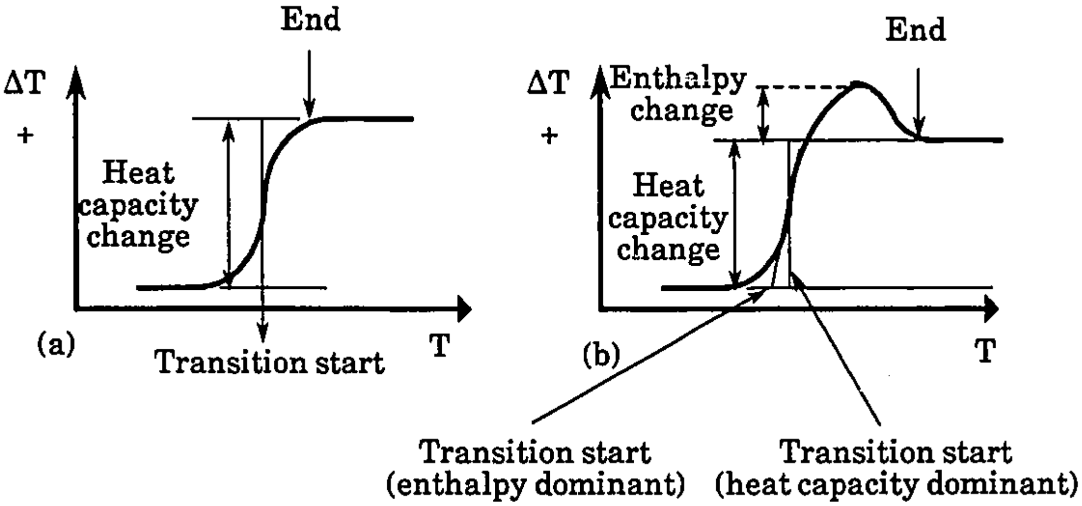

Fig.3.10: Solid-solid phase transition (a) heat capacity change only (b) heat capacity *and* small exothermic reaction [102,103].

'baseline'. This construction is used because it gives the most consistent results. When the transition involves a small endothermic or exothermic reaction, as well as a change in heat capacity, the former appears as a small peak superimposed on the baseline drift (Fig. 3.10-b). This type of curve can be analyzed by both techniques, i.e. assuming that either heat capacity or enthalpy dominates. The end of the transformation is still assumed to be where the new baseline begins.

3.5.3 DTA Equipment

The differential thermal analyser used for this investigation, which was developed by the Setaram Company, is schematically presented in Fig. 3.11. The sample and reference material holders (Al_2O_3 crucibles) are suspended in a furnace which has a very small thermal gradient. The reference material is platinum. The heating cycle is accurately followed by an RT 3000 controller and the apparatus is computer interfaced to allow data acquisition.

To avoid oxidation, all the measurements were carried out in argon using a flow rate of 50 cm^3/min. The furnace temperature was first rapidly increased from room temperature to 1200°C, at which point the heating rate was stabilized at 10°C/min up to 1600°C, thus completely melting the steels. This is a typical heating cycle for DTA experiments.

3.6. FRACTOGRAPHY

After rupture, selected fracture surfaces obtained were examined under a JEOL type T300 scanning electron microscope, using an accelerating voltage of 25 kV. In order to improve resolution, some of the fracture surfaces were plasma coated with a gold layer. The identification of the fracture mode (brittle, ductile) was identified from these. The grain size could be inferred from surface observations.

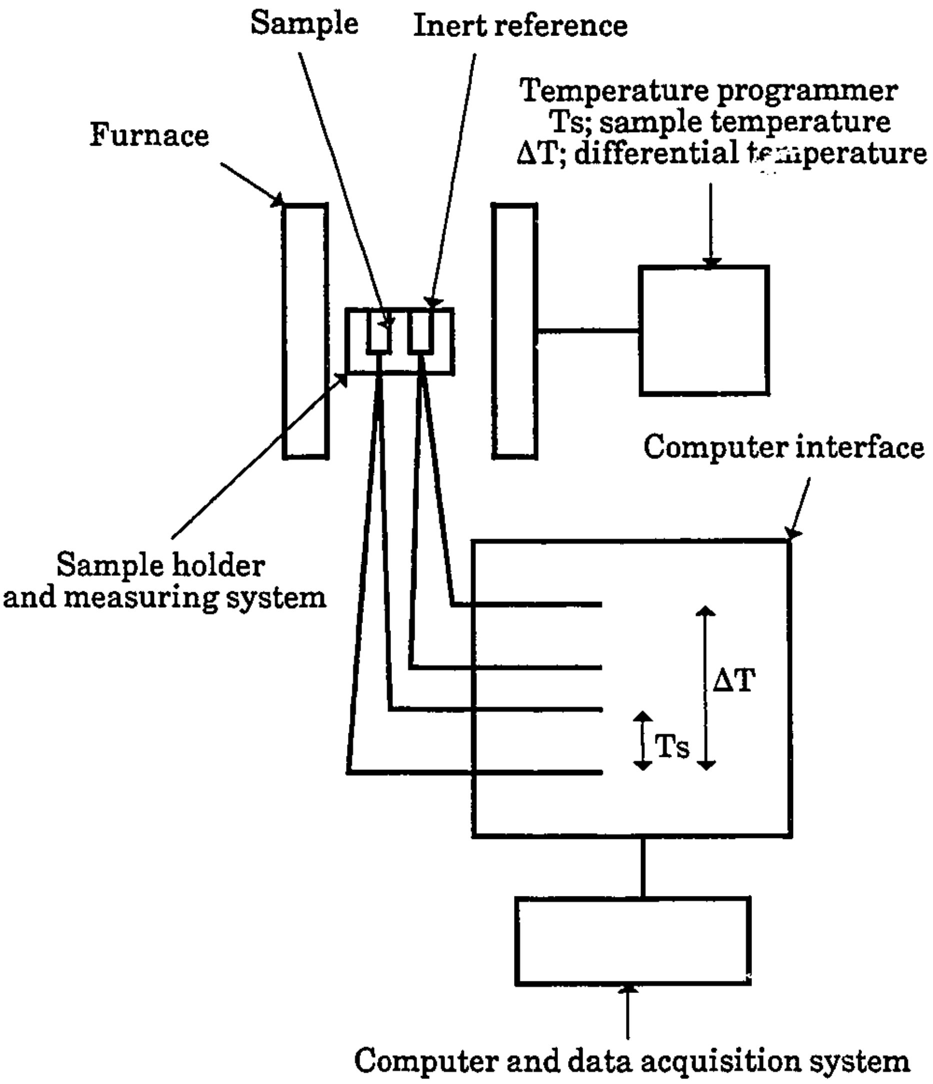

Fig. 3.11: DTA assembly

3.7. METALLOGRAPHY

The effect of reheat temperature on prior austenite grain size was determined for all the steels by metallography. Cylindrical specimens, 10 mm long and 6 mm in diameter, were austenitized in an argon atmosphere or a vacuum, at temperatures between 900 and 1330°C for 10 min, then rapidly quenched in a water plus ice bath to form martensite. The prior austenite grain boundaries were then revealed by etching the martensite in the following manner [104]:

(i) The specimens were heat treated at 235°C for 15 min to temper the martensite in order to improve delineation of the prior austenite grain boundaries.

(ii) They were then sectioned, mounted in bakelite and polished in the usual way from 180 to 600 grit silicon carbide, through to 6 and 1μm diamond paste.

(iii) Etching was performed by immersion in hot (70-80°C) saturated aqueous picric acid solution, containing some drops of a wetting agent, sodium tricyclobenzene sulfonate (Teepol 601).

The mean grain boundary diameter was measured by the 'three circles' method of Hilliard [105] where the number of grain boundary intersections with the circumferences of three concentric circles, having a total circumferential length of 500 mm, is counted. The magnification selected is such that the number of intersections must be between 75 and 150.

Sections of fractured samples exhibiting low ductility were also examined for selected specimens. Some fractured halves were sectioned longitudinally with a slow diamond cut-off wheel. This was then mounted in bakelite and polished using the previously described procedure. The specimens were observed under an optical microscope without prior etching in order to observe crack formation just below the fracture surface.

3.8 AUGER ELECTRON SPECTROSCOPY

Auger electron spectroscopy (AES) is a commonly used surface sensitive analytical technique [106], which is capable of providing the elemental composition of a surface layer of a solid. In this work, AES was used to examine the elemental composition of the fracture surface of a sample deformed in temperature zone I.

Auger electrons are produced when an incident radiation (an electron beam, in this case) interacts with an inner shell of an atom of the sample, resulting in the ejection of an electron, and thus leaving the atom in an excited state with a vacancy in the electron shell (Fig. 3.12-a). De-excitation occurs by the emission of the so called Auger electron (Fig.3.12-b). The kinetic energy (E_{KE}) of the ejected Auger electron (Figs. 3.12) is given by the following equation:

$$E_{KE}=E_K-2E_{KL_{2,3}}-\phi \qquad (3.2)$$

Where E_K is the energy of the K level, $E_{KL_{2,3}}$ is the energy difference between levels K and $L_{2,3}$, and ϕ, the work function of the sample, represents the kinetic energy lost by the electron in escaping out of the sample surface into the vacuum. Thus, the energy of an Auger electron peak is characteristic of a specific atom, and because of the low energy of these electrons, they are only emitted from the surface. In the energy range of interest (50 to 2500 eV) the electron escape depth is from one to ten monolayers.

An Auger electron spectroscopy system (Fig. 3.13) consists of an ultrahigh vacuum system, an electron gun for specimen excitation, and an energy analyzer for detection of Auger electron peaks in the total secondary electron energy distribution [107,108]. Experiments are normally performed in a high vacuum of $2\text{x}10^{-8}$ Torr, but in this case a micro-leak in the apparatus lowered the vacuum to $7\text{x}10^{-8}$ Torr and led to contamination of the sample surface with nitrogen and oxygen. This does not make a difference in terms of detection, but can play a role in the calculation of the atomic composition of the

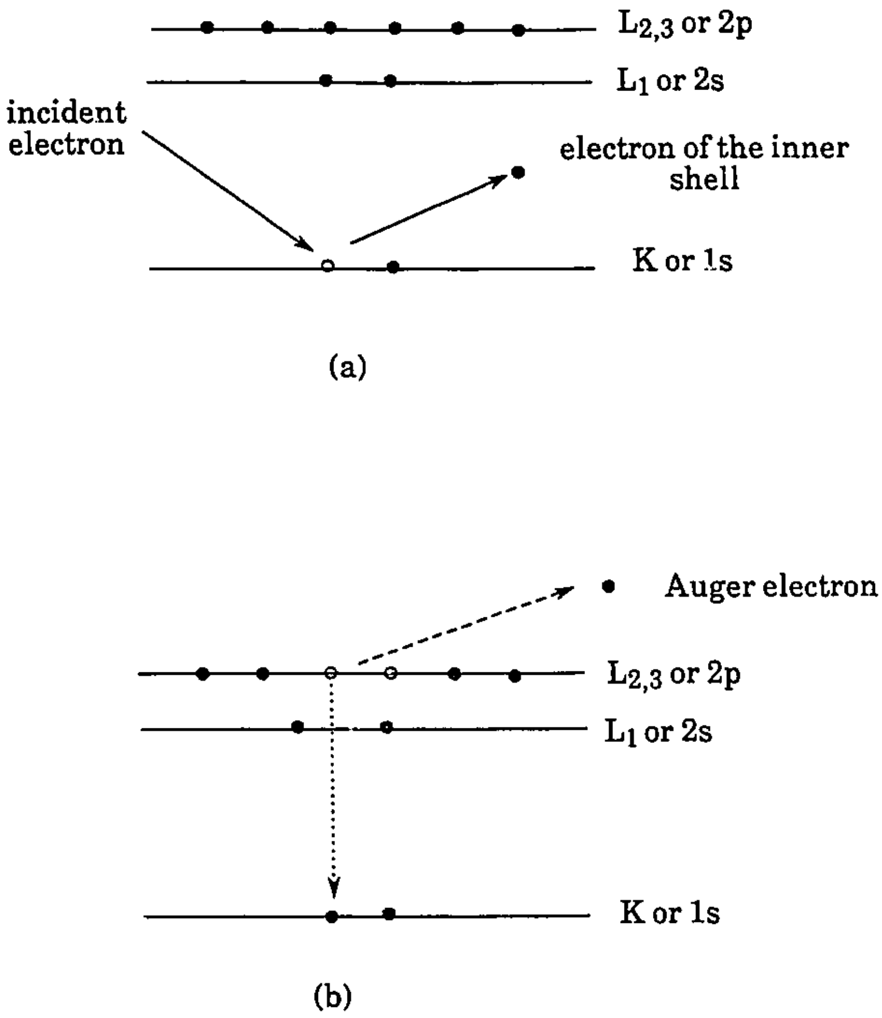

Fig. 3.12: Energy level diagrams describing the emission of an Auger electron [104,105].

surface. However, the relative error for Auger measurement is typically 20% [109]. Therefore, the errors involved with this contamination are relatively unimportant.

The accelerating voltage of the electron beam was 5keV and the beam current intensity was 5×10^{-8} A. All AES systems are coupled with an ion (generally argon) gun which sputters the sample surface. This cleans the specimen surface as well as enabling the variation of chemical composition with depth to be determined.

A tensile specimen of steel C was fractured in a brittle manner by holding at 1485°C for 5 min and then deforming to fracture at a strain rate of $10^{-2}s^{-1}$. The specimen was then cooled to room temperature in the furnace at the average rate of 115°C/min (Fig. 3.7). AES examination was performed on the fracture surface for different sputtering times (up to 69 min.) in order to assess the grain boundary segregation of sulfur, phosphorus and carbon.

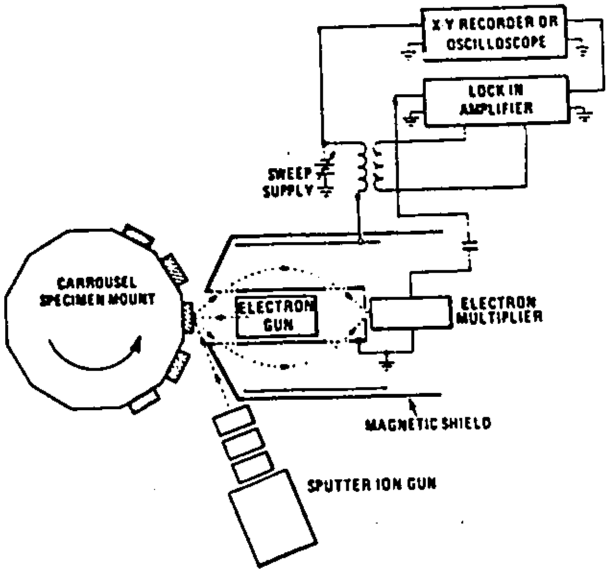

Fig. 3.13: Schematic of the experimental arrangement used for obtaining Auger spectra [106].

CHAPTER 4

EXPERIMENTAL RESULTS

The general objective of this study was to investigate the combined effect of carbon and microalloying elements on the hot ductility and strength of steel in the temperature range 800°C-solidus. In particular, the work was centered around the following aspects of hot ductility:

1) The influence of carbon level in the range 0.07-0.14 wt% on the hot strength and ductility of Nb-Ti bearing steels in the temperature range 800-1300°C.
2) The effect of the combined addition of Nb-Ti and V-Ni-Cr on the hot strength and ductility of C-Mn Al-killed steels.
3) The influence of carbon and microalloying elements on the occurrence of hot tearing (i.e. zone I) and, the correlation of the results with γ-δ-L transformations
4) The effects of temperature, strain rate, chemical composition and prior heat treatment on strength.

As mentioned previously, many aspects of hot ductility depend on the phase transformation during testing. The results section thus begins with analysis of the phase transformation behaviour of the steels investigated.

4.1. PHASE TRANSFORMATION IN STEELS

On heating from room temperature, in low carbon steels, three phase transitions are expected to occur; α→γ, γ→δ, and δ→L. Each transformation is characterised by the temperatures of the beginning and end of the transformation. The temperatures of the onset and the end of the α→γ transitions were calculated from the formulae derived by Andrews [110]. For the $\gamma \rightarrow \delta$ and $\delta \rightarrow L$ transitions, the temperatures were obtained from DTA measurements.

4.1.1. Austenite-to-Ferrite Transformation

The temperatures for the onset (Ac_1) and end (Ac_3) of the $\alpha \rightarrow \gamma$ transformation on heating are calculated from the equations 4.1 and 4.2., respectively [110]:

$$Ac_1\,(^\circ C) = 723 - 10.7Mn - 16.9Ni + 29.Si + 16.9Cr + 290As + 6.38W \tag{4.1}$$

$$\begin{aligned} Ac_3\,(^\circ C) = {} & 910 - 203\sqrt{C} - 15.2Ni + 44.7Si + 104V + 31.5Mo + 13.1W \\ & -(30Mn + 11Cr + 20Cu - 700P - 400Al - 120As - 400Ti) \end{aligned} \tag{4.2}$$

The concentration of the alloying elements is expressed in wt%. These equations were used to calculate Ac_1 and Ac_3 of steels P, A, B, C and S. The results of the calculation are given in Table 4.1. The *equilibrium* temperature (Ae_1) for the onset of the $\alpha \rightarrow \gamma$ transformation is also given by equation 4.1 [110], whereas the equilibrium temperature for the end of the $\alpha \rightarrow \gamma$ (Ae_3) can be calculated (for carbon levels between 0 and 0.2 wt%) from the following equation [110]:

$$\begin{aligned} Ae_3\,(^\circ C) = {} & 913 - (3.2 + 400(C + Ni/10) + 60Si + 100V + 60Mo + 40W \\ & - 25Mr - 11Cr - 20Cu + 700P - 250Al - 120As - 400Ti \end{aligned} \tag{4.3}$$

The results of the calculation are reported in Table 4.1

4.1.2. Differential Thermal Analysis

The change in differential temperature associated with the solid-liquid transformation is far greater than those of the solid-solid transitions, as can be seen in Fig. 4.1 (representative of steels P, A, B and, S) and Fig. 4.2 (steel C). Thus, all the transformation temperatures were obtained using the magnified

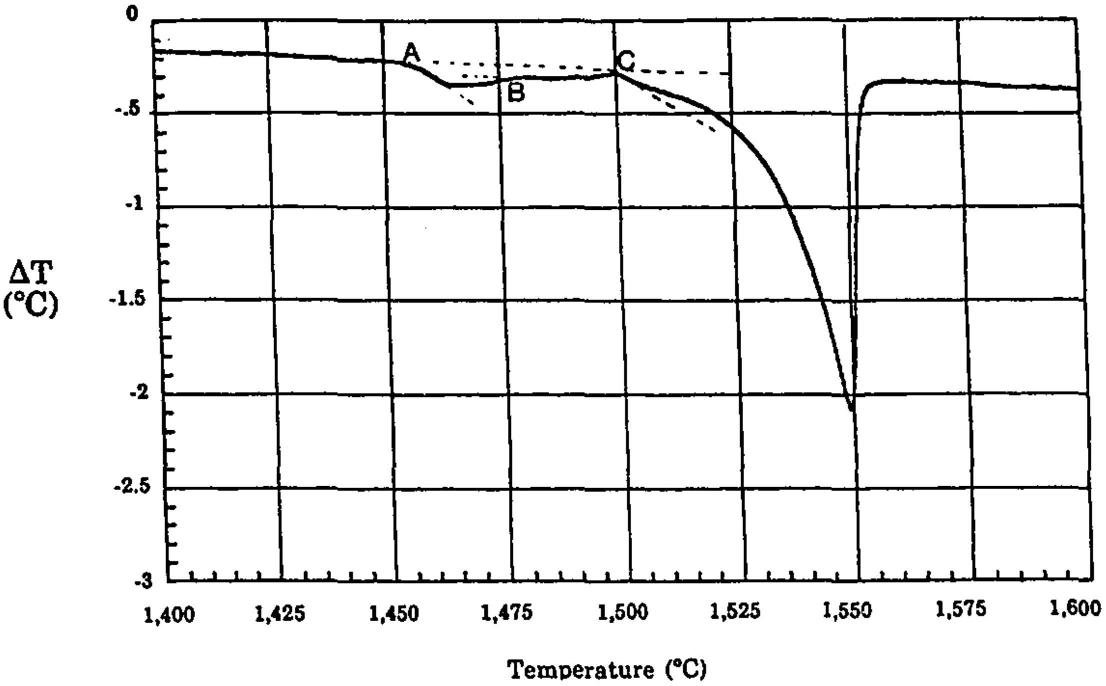

Fig.4.1: Typical DTA curve of steel P, is also representative of steels A, B and S.

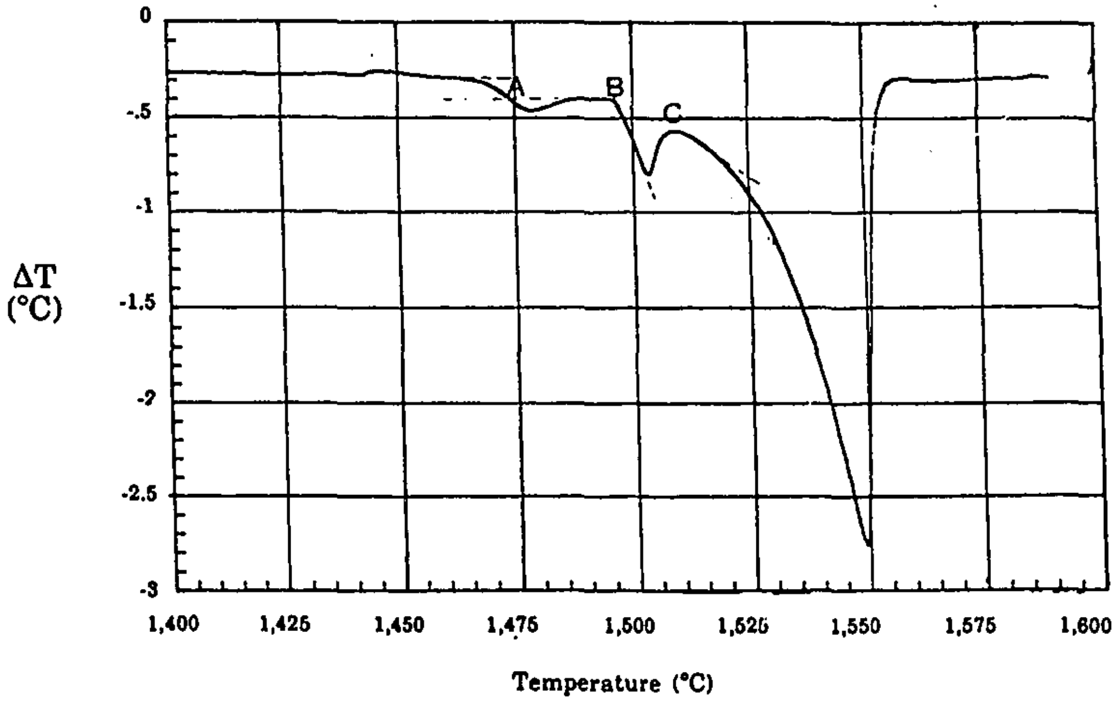

Fig.4.2: DTA curve of steel C.

curves of Figs.4.3 to 4.7 corresponding to steels P, A, B, C and S, respectively.

Table 4.1

Calculated values of Ac_1 and Ae_3.

Steel	$Ac_1 = Ae_1$ (°C)	Ac_3 (°C)	Ae_3 (°C)
P	718.5	842.5	867
A	715	848	855.5
B	715	838	844
C	715	826	828
S	720.5	856	847.5

These curves have been interpreted with the rules established in the section 3.5.2 and with the help of the Fe-C binary diagram [111] (Fig. 4.8). However, because of the many other additions to the steels used in this investigation, Fig. 4.8 can not be used to directly define the phase transformation temperatures.

It has been mentioned above that at high temperatures, in the proximity of the melting point, two phase transitions are observed, (i) $\gamma \rightarrow \delta$ and (ii) $\delta \rightarrow L$, characterised by four temperatures which define the beginning and the end of these transformations. For the present DTA study, only three temperatures are of interest, namely the beginning and the end of the γ/δ transformation and, most importantly, the solidus temperature. On each graph, for all the grades but C, these temperatures are referred to as A, B and C respectively. For steel C, transformation A corresponds to the beginning of the transition $\gamma \rightarrow \delta$, and B to the onset of melting. The results of the analysis are summarized in Table 4.2, and described in more detail below.

Steel P (Fig. 4.3):

The onset of the $\gamma \rightarrow \delta$ transformation (A) is accompanied by a change in heat capacity and a small enthalpy change. As can be seen in Fig. 4.3, the onset of the transformation was determined by the intersection of the slope with the extrapolated baseline (i.e. enthalpy is dominant, Fig.3.8) and by the method

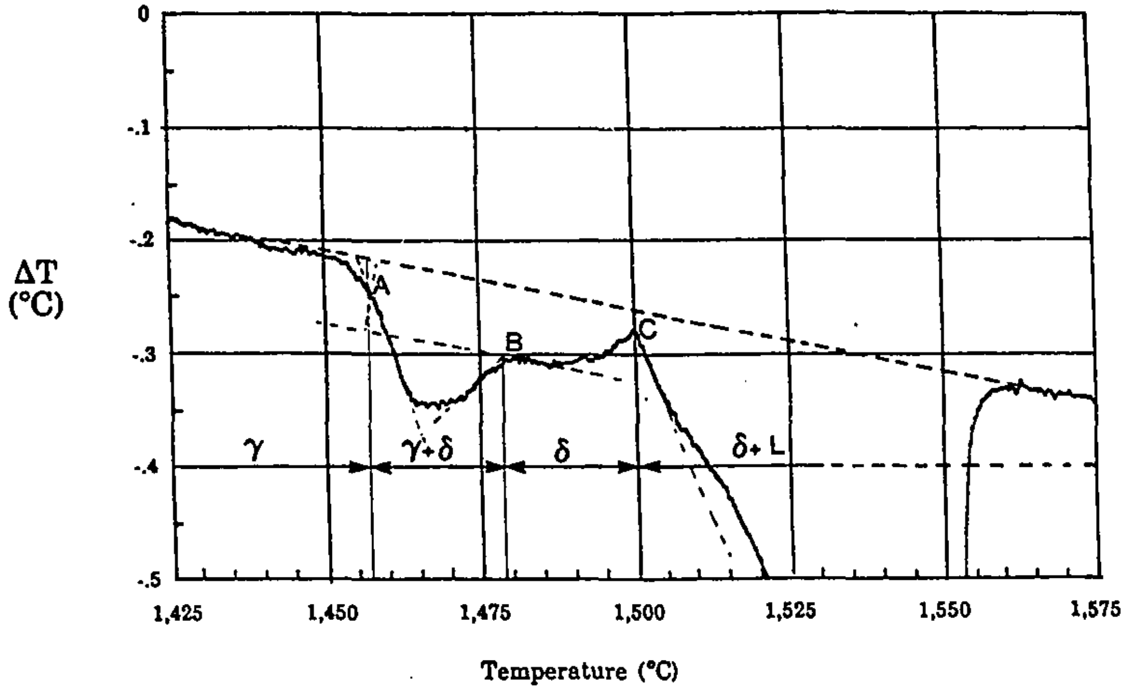

Fig.4.3: DTA curve of steel P.

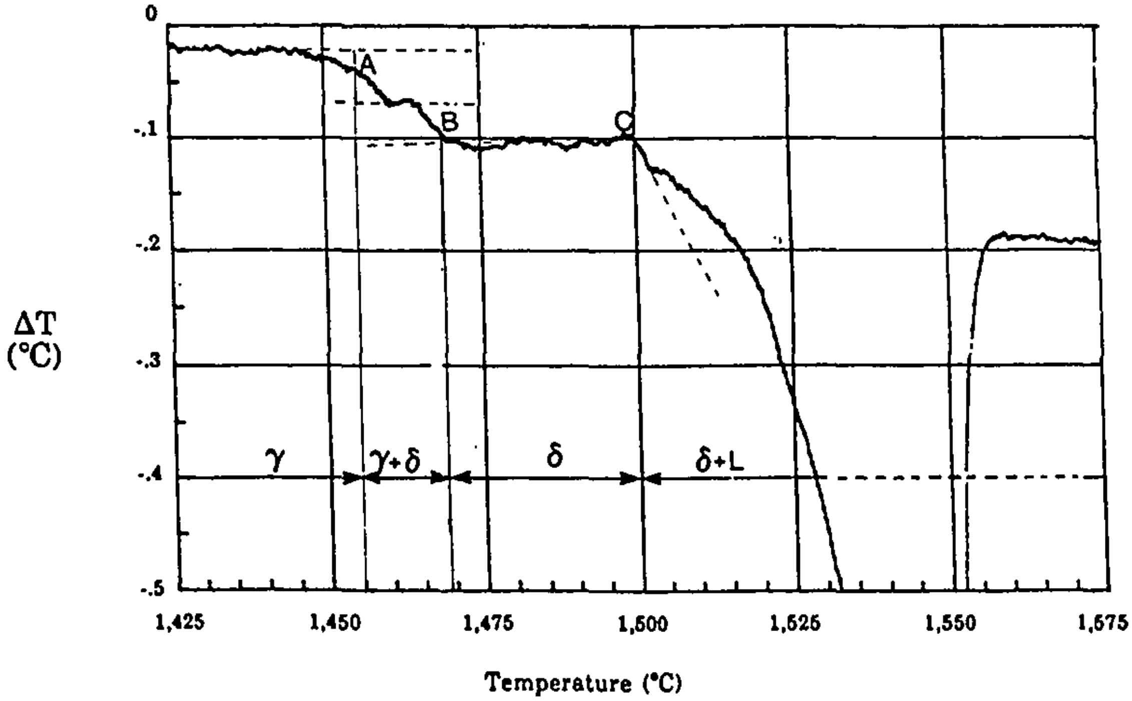

Fig.4.4: DTA curve of steel A.

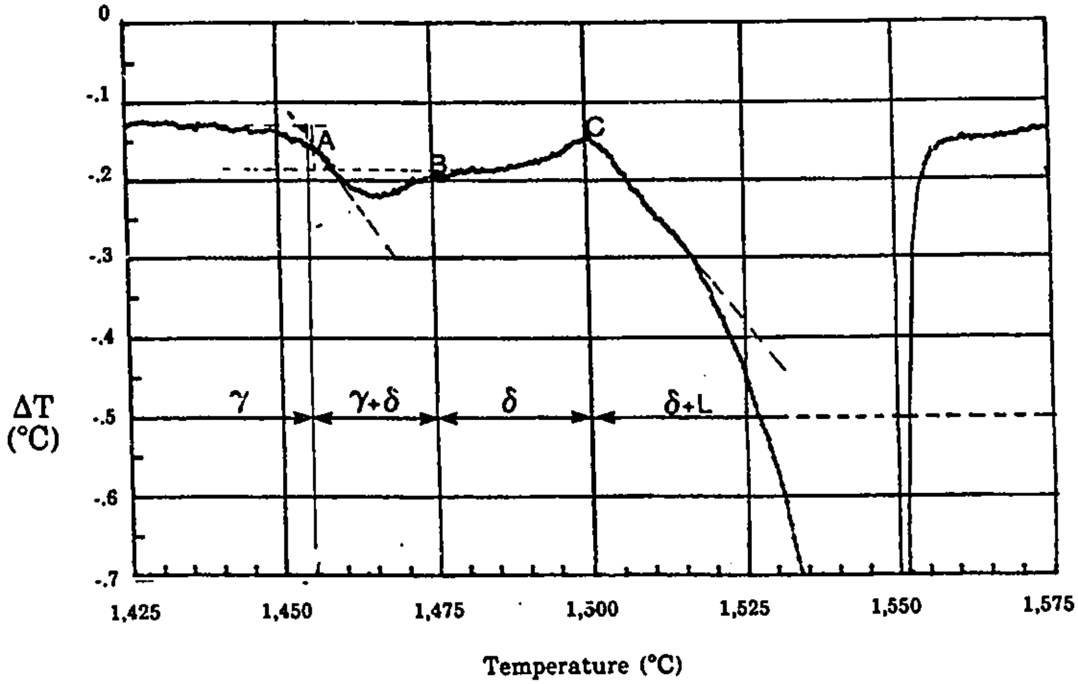

Fig.4.5: DTA curve of steel B.

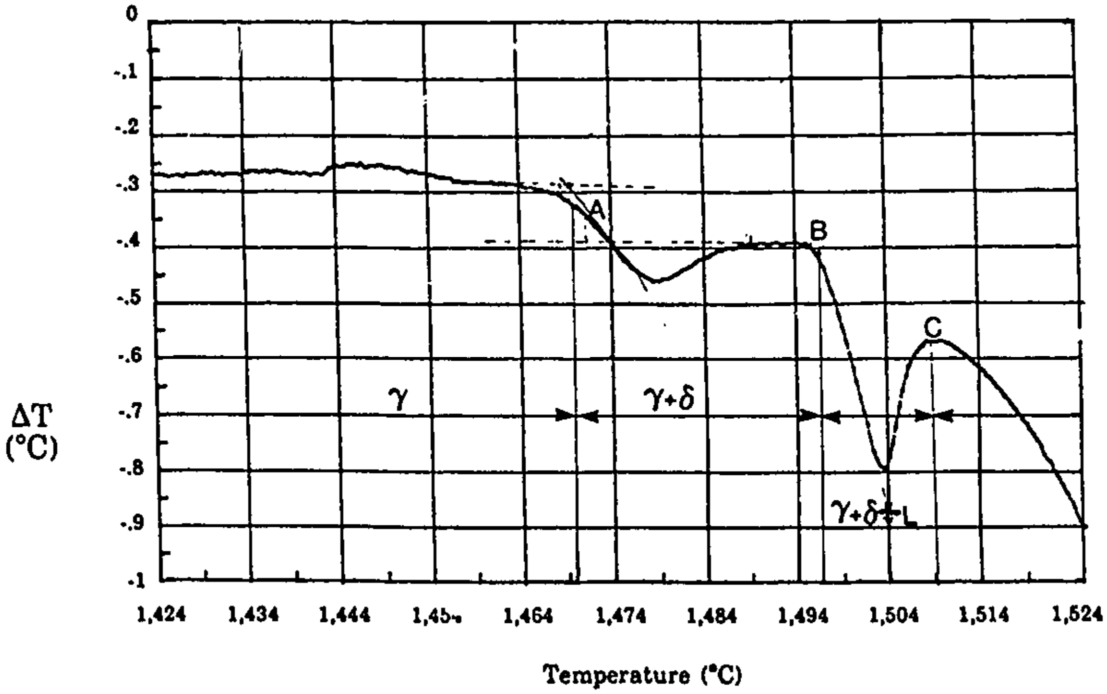

Fig.4.6: DTA curve of steel C.

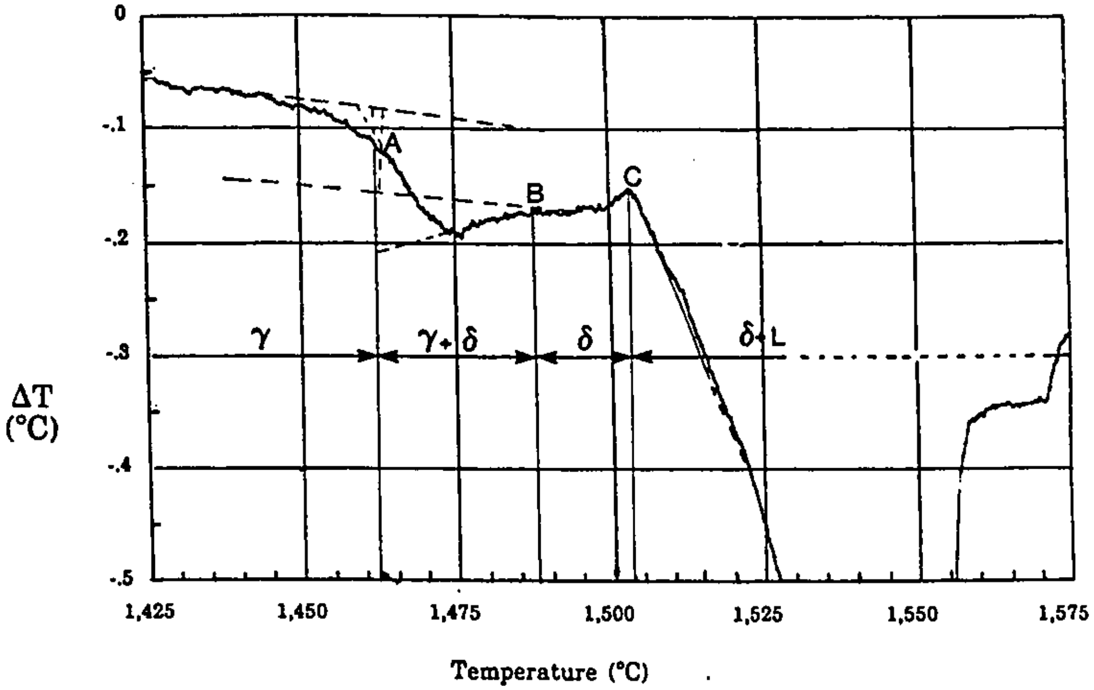

Fig.4.7: DTA curve of steel S.

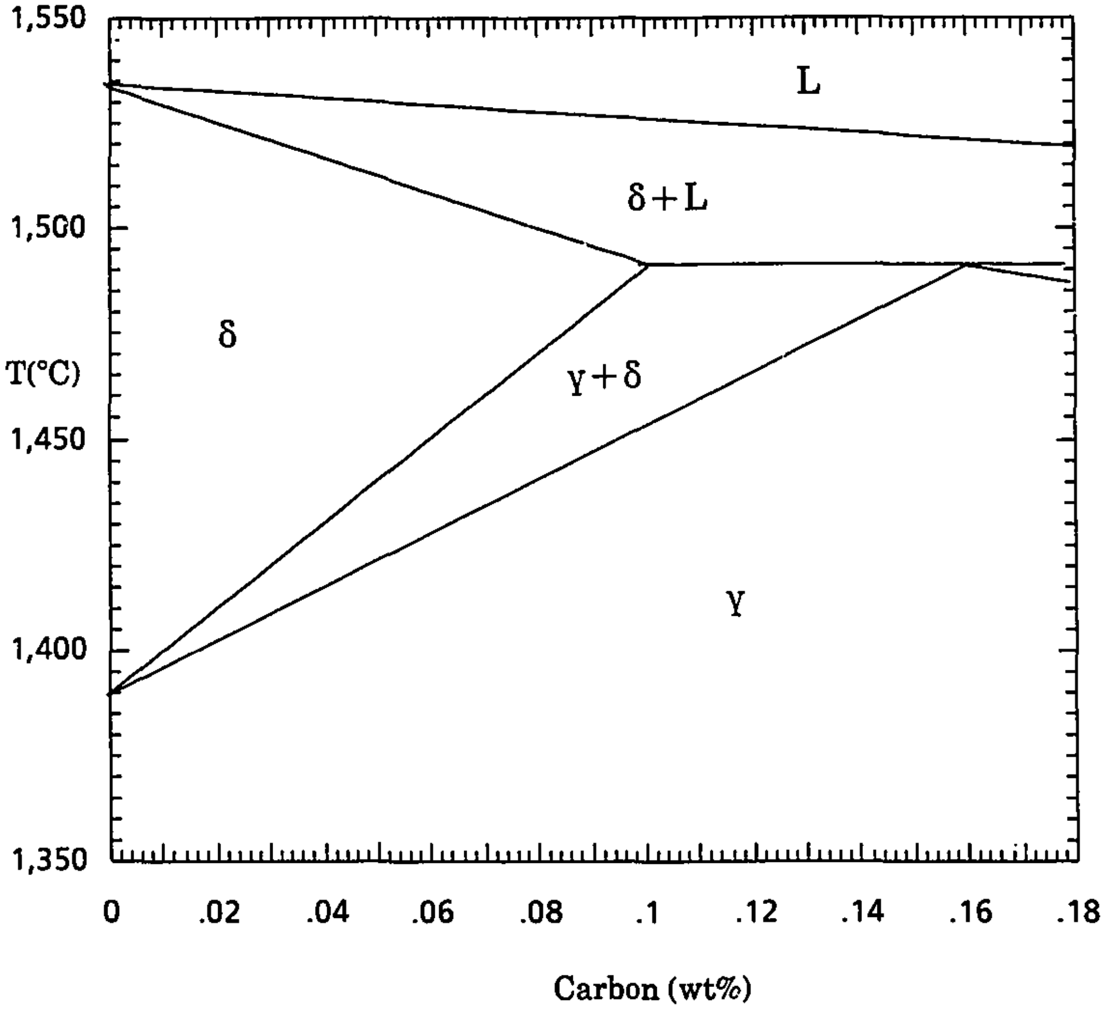

Fig.4.8: Pure Iron-Carbon phase diagram of the peritectic region [111].

described in Fig. 3.10-b (i.e. heat capacity change is dominant). The temperatures evaluated from these two techniques differ by only 2°C. Thus, the onset of the $\gamma \rightarrow \delta$ transformation can be precisely defined as 1456 ± 1°C. The end of the transition, i.e. $\gamma + \delta \rightarrow \delta$, at point B, is determined by the end of the endothermic peak, i.e. the intersection of the new baseline with the slope of the increasing curve.

After point B, the new baseline persists through 10°C. At this point the differential temperature starts to increase somewhat up to point C, where it then rapidly decreases, coinciding with the onset of melting. The change in concavity is clearly seen, thus allowing the solidus temperature to be determined using the initial maximum slope, as demonstrated in Fig. 3.9. The baseline drift from B to C suggests a transformation, but cannot be satisfactorily explained on this basis. It does *not* coincide with grain boundary melting, which is an endothermic reaction, nor does it coincide with any known phase transformation.

Steel A (Fig. 4.4)

The $\gamma \rightarrow \delta$ transformation appears on the curve as a baseline drift, corresponding to a change in heat capacity, only. The onset of the transformation (point A) was thus determined as in Fig. 3.10-a. The end of the transformation was taken to be at the start of the new baseline (B). However, during the transformation, (between temperatures A and B), a short (5°C) plateau appears. Although this plateau indicates the end of a transformation, it is not significant enough to be the single phase δ region. An alternative hypothesis is that the $\gamma + \delta$ region over this temperature range posesses a constant heat capacity. This is a possibility, but cannot be easily confirmed in this study.

Between points B and C, the differential temperature remains constant over 25°C, corresponding to the δ region. Point C, the solidus temperature, is determined in the usual manner.

Steel B (Fig. 4.5)

The DTA spectrum is similar to the ones obtained for steel P. The same analysis has therefore been applied to define the characteristic temperatures.

Table 4.2

Transition temperatures of the five steels and corresponding phase transformation.

STEEL		A	B	C
STEEL P	Temperature (°C)	1456±1	1473.5	1500
	Transformation	$\gamma \rightarrow \gamma + \delta$	$\gamma + \delta \rightarrow \delta$	$\delta \rightarrow \delta + L$
STEEL A	Temperature (°C)	1455	1469	1500
	Transformation	$\gamma \rightarrow \gamma + \delta$	$\gamma + \delta \rightarrow \delta$	$\delta \rightarrow \delta + L$
STEEL B	Temperature (°C)	1455±2	1475±5	1500
	Transformation	$\gamma \rightarrow \gamma + \delta$	$\gamma + \delta \rightarrow \delta$	$\delta \rightarrow \delta + L$
STEEL C	Temperature (°C)	1469.5± 1.5	1497.5	1509±5
	Transformation	$\gamma \rightarrow \gamma + \delta$	$\gamma + \delta \rightarrow \gamma + \delta + L$	$\gamma + \delta + L \rightarrow \delta + L$
STEEL S	Temperature (°C)	1461.5± 2	1488± 5	1503.5
	Transformation	$\gamma \rightarrow \gamma + \delta$	$\gamma + \delta \rightarrow \delta$	$\delta \rightarrow \delta + L$

Steel C (Fig. 4.6)

Of the five steels investigated, the DTA curve for steel C most clearly reveals the various phase transformations. Temperatures of the transitions at A and B have been determined with the help of Figs. 3.10-a and b, and 3.8, respectively. The phase diagram shown in Fig. 4.8 suggests that this carbon level (0.14 wt%) corresponds to a composition which is on the left side of the peritectic composition (0.16 wt%), indicating that temperature A corresponds to the $\gamma \rightarrow \gamma + \delta$ reaction. This is confirmed by the low heat of reaction at this point which indicates a solid-solid transformation. As will be seen later, the presence of a duplex structure at high temperatures can be also inferred from the fractographic observations.

The first transformation A ($\gamma \rightarrow \delta + \gamma$) is followed by transformation B which corresponds to the reaction $\delta + \gamma \rightarrow \delta + \gamma + L$. The plateau observed after this peak suggests that the relative fractions of δ and γ, in this temperature range, do not change greatly. It cannot, however, correspond to a single phase δ region, according to the phase diagram of Fig. 4.8.

The $\delta + \gamma + L \rightarrow \delta + L$ transformation start is probably somewhat masked by B, but was assumed to correspond to the temperature at C, as shown in Fig. 4.6. The precise definition of this temperature is not of any great consequence, since it occurs after the solidus. Note that in contrast to the other grades, steel C apparently does not exhibit a temperature region where only the δ phase exists.

Steel S (Fig. 4.7)

The DTA graph of steel S is similar to those obtained for steels P and B and has been interpreted in the same way.

From the results presented in Table 4.2, it can be seen that the solidus temperatures are virtually the same. An increase the carbon content from 0.07 to 0.10 wt% (steels A and B) has a negligible effect on the transformation temperatures. However, a further increase of the carbon content to 0.14 wt% (steel C) causes an increase of the $\gamma \rightarrow \delta$ start temperature (15°C).

The addition of Nb and Ti (steel A) to the C-Mn-Al steel (steel P) slightly decreases the temperature corresponding to end of the $\gamma \rightarrow \delta$ transformation, but otherwise has no influence. Finally the addition of Ni-Cr and V to steel A (steel S) along with a lower sulfur level, leads to a 5°C and 19°C of increase in the temperatures of the beginning and end, respectively, of the $\gamma \rightarrow \delta$ transformation.

4.2. HOT TENSILE TESTING RESULTS

The tensile testing results constitute the core of the experimental investigation. In this section the results are of course divided in two parts: (i) 800-1300°C (zone III), (ii) 1400°C-solidus (zone I).

4.2.1 Temperature Range 800-1300°C

4.2.1.1 Typical tensile flow curves

At high temperatures, steels deformed in tension exhibit different flow curve behaviours depending on the temperature, strain rate, prior heat treatment and chemical composition. Schematic diagrams of the types of flow curves observed in this work are shown in Fig. 4.9. All curves display a region of elastic deformation, followed by uniform plastic deformation, where the rate of stress increase diminishes with strain. For all the curves, the deformation ends by localization of the deformation (necking) and fracture. Two types of flow behaviour can be identified: (i) curves showing no stress oscillations (curves a and b), and (ii) those with one or more stress oscillations (curves c and d). Such behaviour can be correlated with the absence and presence of dynamic recrystallisation, respectively [112]. Two variants of each type can be defined:

> Type (i) variants: Uniform plastic deformation is followed either by a peak (onset of necking), as displayed in curve (a), or by a quasi-plateau as shown in curve (b). The quasi plateau corresponds to the case where dynamic recovery takes place over an extensive strain range.
>
> Type (ii) variants: As was indicated above, after uniform plastic deformation, the peak stress is followed by one (curve (d)) or more (curve (c)) stress oscillations. The oscillations correspond to cycles of dynamic recrystallization. One stress oscillation is associated with grain refinement, whereas several oscillations corresponds to grain coarsening [113].

The type of curve was generally not altered by the changes in strain rate that were used in this investigation. The C-Mn-Al steel (P) was an exception when tested at 900°C after direct heating, where a strain rate increase from $2x10^{-4}s^{-1}$ to 10^{-3} or 10^{-2} s^{-1} led to a change from type (i) to (ii).

Before considering the specific effects of temperature, strain rate, heat treatment and chemical composition, it should be noted that the flow curves

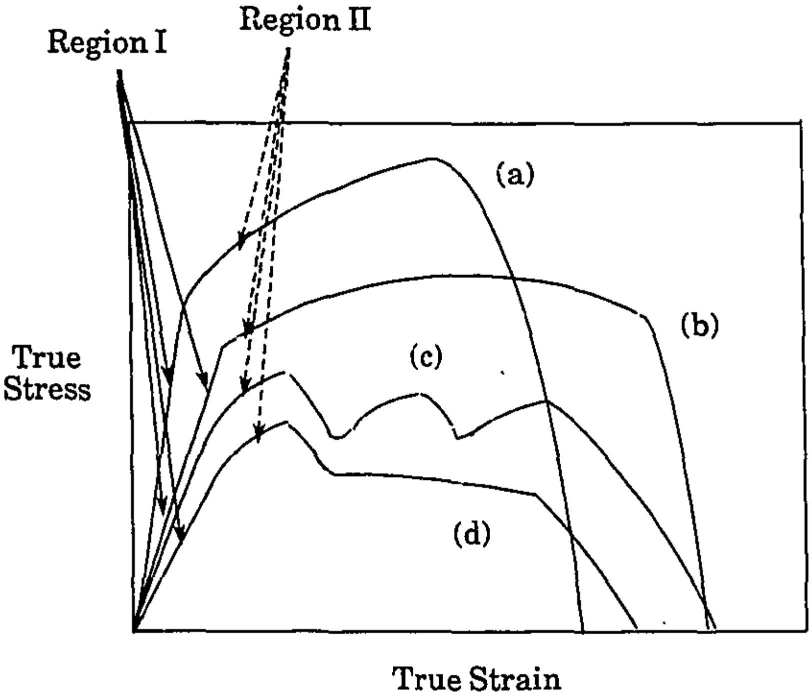

Fig.4.9: Schematic representation of different tensile flow curves.

reproduced in this thesis are in the form of *true*-stress-strain curves, and show the complete deformation behaviour up to and including fracture. However, these curves are only valid up to the onset of necking or plastic instability. The flow behaviour of the specimens beyond this strain is included in all the curves shown in this thesis, but without correction for necking. This latter part of the curve has no fundamental meaning. However, some workers have adopted such presentation to illustrate the flow behaviour, and it is used here to enable comparisons with results in the literature to be made [34].

For high temperature testing, an accurate measure of the strain which corresponds to the onset of necking is difficult to ascertain. However, an approximate value can be obtained by assuming that the diameter outside the necked region of the fractured specimen corresponds to the start of plastic instability. On each curve, this estimated value of the strain at the onset of necking is indicated by an arrow. For type (i) curves showing a peak stress, the strain at the peak coincides with the onset of necking. Where a plateau is observed, the strain at instability appears to occur just after the peak stress. However, because of the plateau region, the exact strain at which the peak stress occurs is difficult to define. Finally for curves exhibiting dynamic recrystallization (type (ii)), it is clear that that the strain at the maximum stress does not correpond to the onset of necking.

The effects of the deformation variables of temperature and strain rate are described below. The curves shown are those pertaining to steel B, but the trends are the same for all the steels.

<u>Temperature</u>

Increasing the test temperature (Figs. 4.10 and 11):

(i) decreases the maximum stress

(ii) increases the tendency for dynamic recrystallization.

Comparing the effect of temperature on directly heated and sensitized specimens, it can be seen that the sensitized specimens (Fig. 4.11) display greater maximum flow stresses and require much higher temperatures for dynamic recrystallization to occur. The effect of the annealing treatment is not illustrated but is similar to that of sensitization.

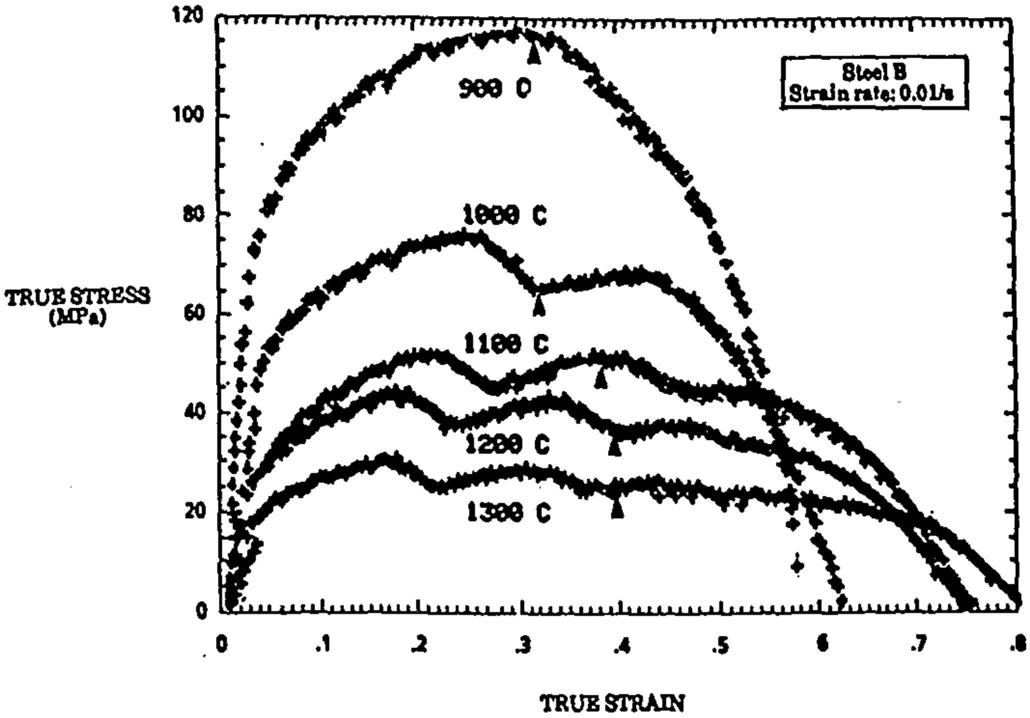

Fig. 4.10: Influence ot temperature on the flow curve behavior after after direct heating.

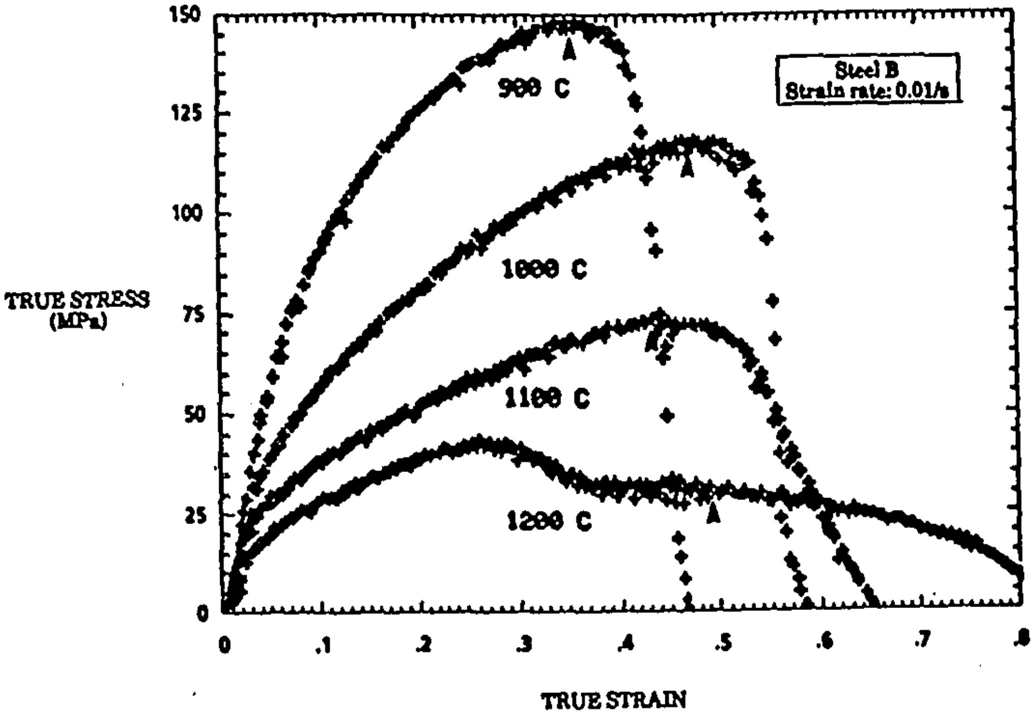

Fig. 4.11: Influence of temperature on the flow curve behavior after after sensitization.

Strain rate

The influence of strain rate on the flow curves is displayed for the two types of curves, i.e. (i) corresponding to low ductility and the absence of dynamic recrystallization, (Figs. 4.12 and 4.13) and, (ii) where high ductility and dynamic recrystallization are exhibited (Figs. 4.14 and 4.15). In general, a decrease in strain rate leads to decreases in:

(i) the maximum stress
(ii) the strain to the onset of dynamic recrystallization (in the case of type (ii) curves)
(iii) the fracture strain.

This general behavior is seen for both directly heated and sensitized specimens. However, for type (i) curves, the effect of strain rate on fracture strain is much greater for the sensitized specimens (i.e., those curves exhibiting peak stress rather than plateau behaviour), especially when decreasing from 0.01 to 0.001 s^{-1}. In fact for steel B, in the directly heated condition, there appears to be no effect of decreasing the strain rate from 0.01 to 0.001 s^{-1}, (Fig. 4.12) whereas, for the sensitized specimen, the fracture strain decreases from 0.47 to 0.3 (Fig. 4.13).

Heat treatment

The effect of prior heat treatment can be generalised on the basis of the occurrence of dynamic recrystallization. Annealed and sensitized specimens exhibit dynamic recrystallization only at very high test temperatures, whereas such behaviour is observed at much lower temperatures in the case of direct heating. After direct heating, dynamic recrystallization is observed at 1000°C for grades P, A, B and C and at 1100°C for steel S. Annealing reduces the temperature (900°C) at which dynamic recrystallization is observed for steel P, but increases it to 1100°C for the other steels. After sensitizing, dynamic recrystallization occurs between 1100 and 1200°C for the microalloyed steels and at 900°C for steel P. Note that for steels A, B and C the ductility is high at 1000°C, but without the appearance of dynamic recrystallization.

Furthermore, in all steels except P, the annealing and sensitizing treatments produce a high rate of work hardening, leading to a relatively high maximum flow stress, whereas the direct heating (Fig. 4.16) treatment produced a quasi plateau behaviour, in the temperature range 800-1000°C, (in

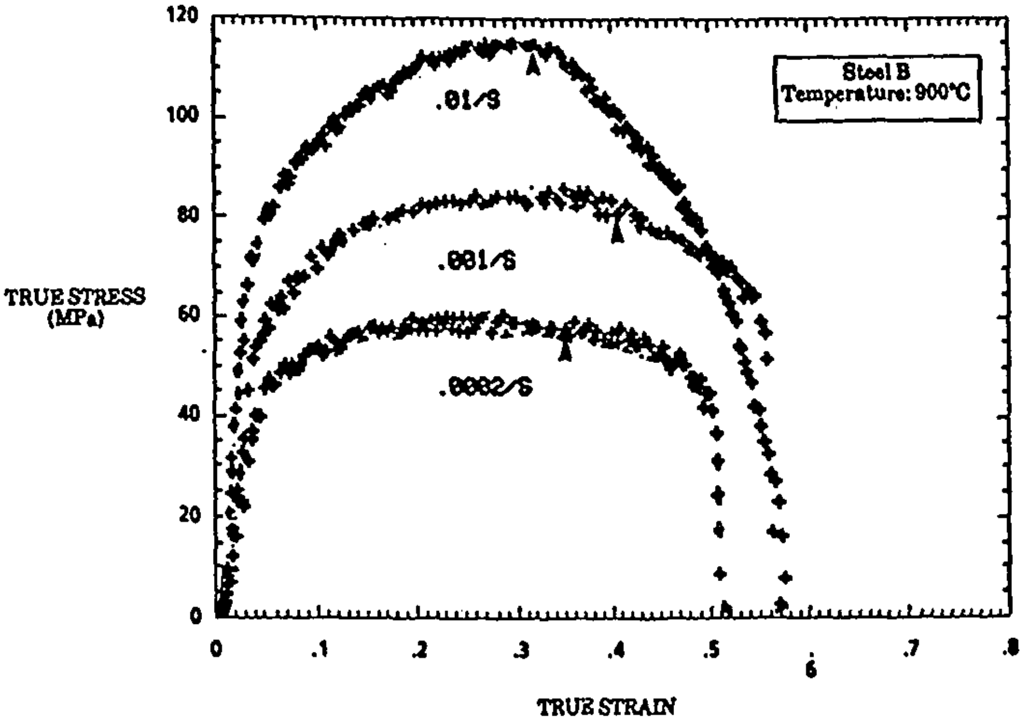

Fig. 4.12: Influence of strain rate on the flow curve behavior after direct heating.

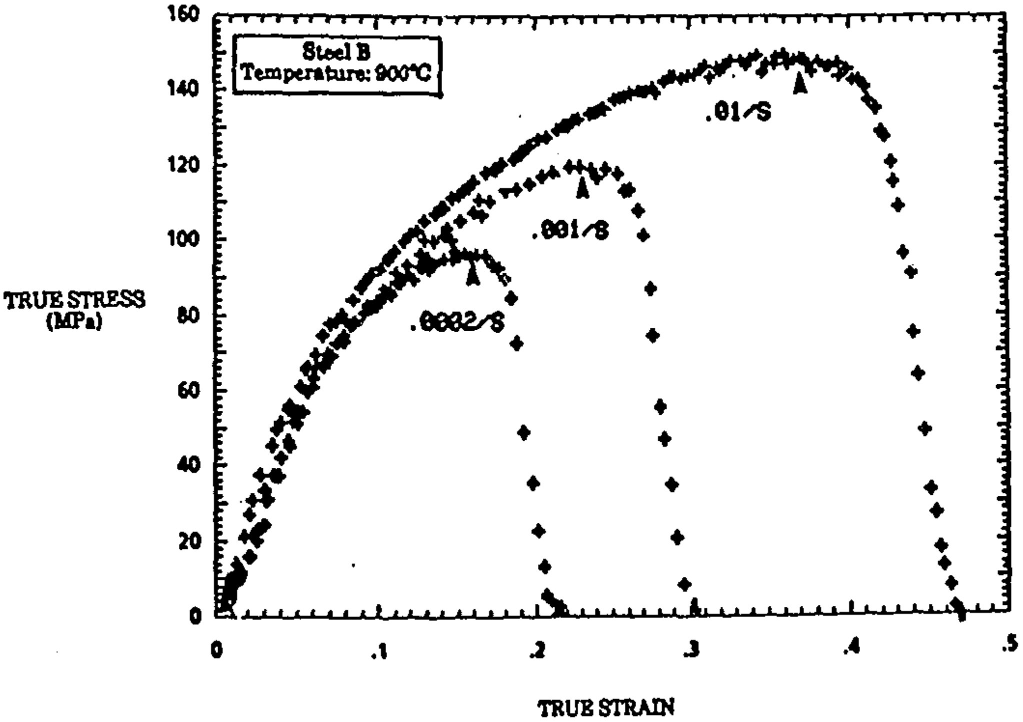

Fig. 4.13: Influence of strain rate on the flow curve behavior after sensitization.

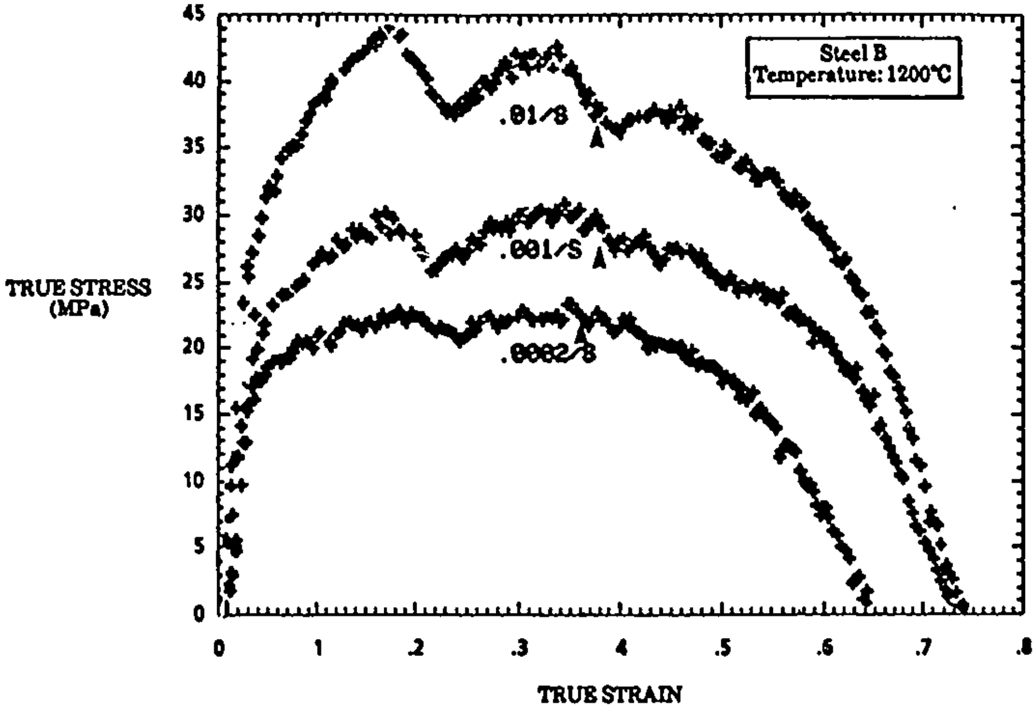

Fig. 4.14: Influence of strain rate on the flow curve behavior after direct heating.

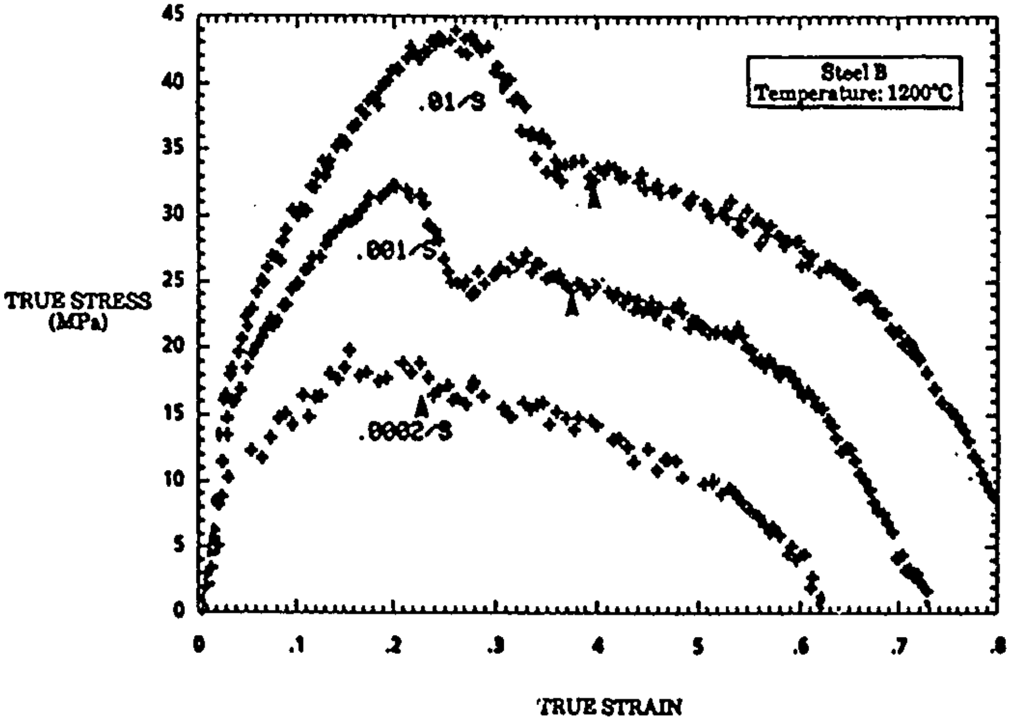

Fig. 4.15: Influence of strain rate on the flow curve behavior after sensitization.

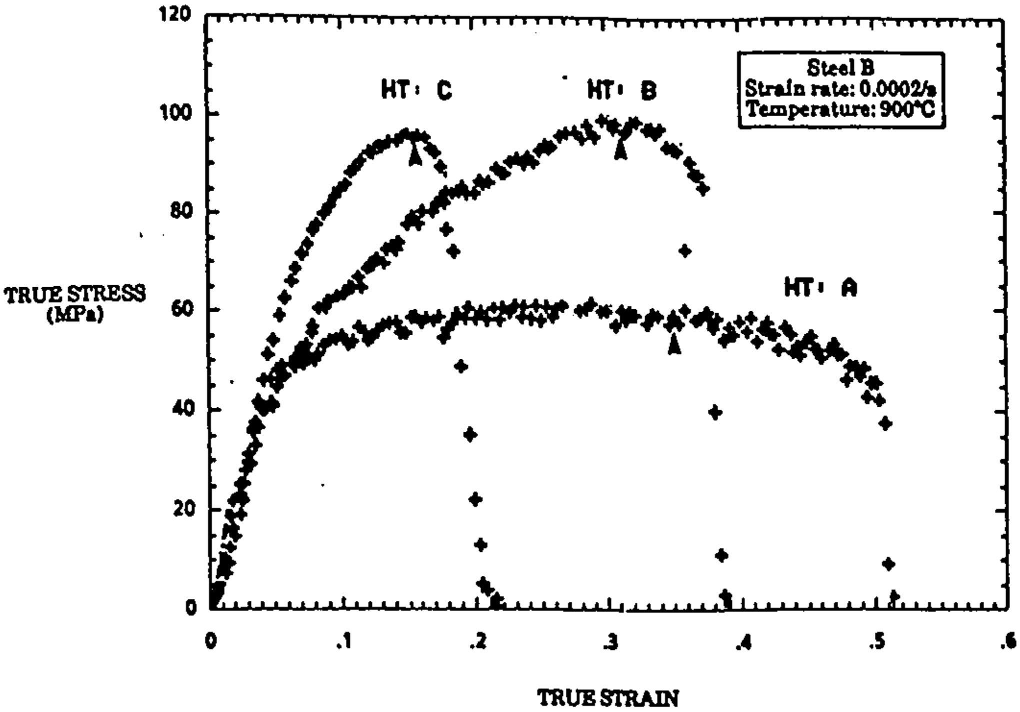

Fig. 4.16: Influence of prior heat treatment on the flow curves behavior. HT A: Direct heating. HT B: Annealing. HT C: Sensitizing.

the absence of dynamic recrystallization). For steel P, the maximum flow stress differential between direct heating and annealing or sensitizing is much smaller.

Increasing the carbon level

The influence of increasing the carbon level from 0.07(steel A) to 0.10 wt % (steel B) on the flow behaviour of type (i) curves, which exhibit low ductility is shown in Figs. 4.17 and 4.18 corresponding to the direct heating and sensitizing heat treatments, respectively. After direct heating, increasing the carbon content from 0.07 to 0.1 wt% significantly diminishes the fracture strain and the maximum flow stress. However, a further C increase to 0.14 wt% does not change the flow behaviour at all. In the case of sensitization changing the carbon content does not affect the flow curve shape. Finally, it is note worthy that for a given heat treatment, the carbon content does not affect the temperature at which dynamic recrystallization is first observed. Dynamic recrystallization is detected at 1000°C and 1200°C following direct heating and sensitizing treatments, respectively.

Microalloying additions

The effect of microalloying additions on type (i) curves is shown in Figs. 4.19 and 4.20, corresponding to direct heating and sensitizing treatments, respectively. In the case of direct heating, the addition of Nb and Ti (steel A) to the C-Mn-Al steel (P), causes an increase of the maximum stress and fracture strain. The addition of Ni and Cr (steel S) to Nb-Ti steels appears to further increase the maximum stress, but diminishes the fracture strain and changes the shape from plateau to peak behaviour.

The influence of microalloying additions in the case of the sensitizing treatment is somewhat different. The addition of Nb and Ti to plain carbon steels doubles the maximum flow stress, but drastically reduces the fracture strain. The addition of Ni and Cr further decreases the fracture strain and increases the maximum flow stress, but only to a small degree. For type (ii) curves, i.e. at high deformation temperatures, in general there is no marked effect of microalloying additions observed for either heat treatments. One general observation that can be made, however, is that, after the direct heat treatment, steel P exhibits the lowest maximum flow stress compared to steels A or S (see section 4.2.1.5).

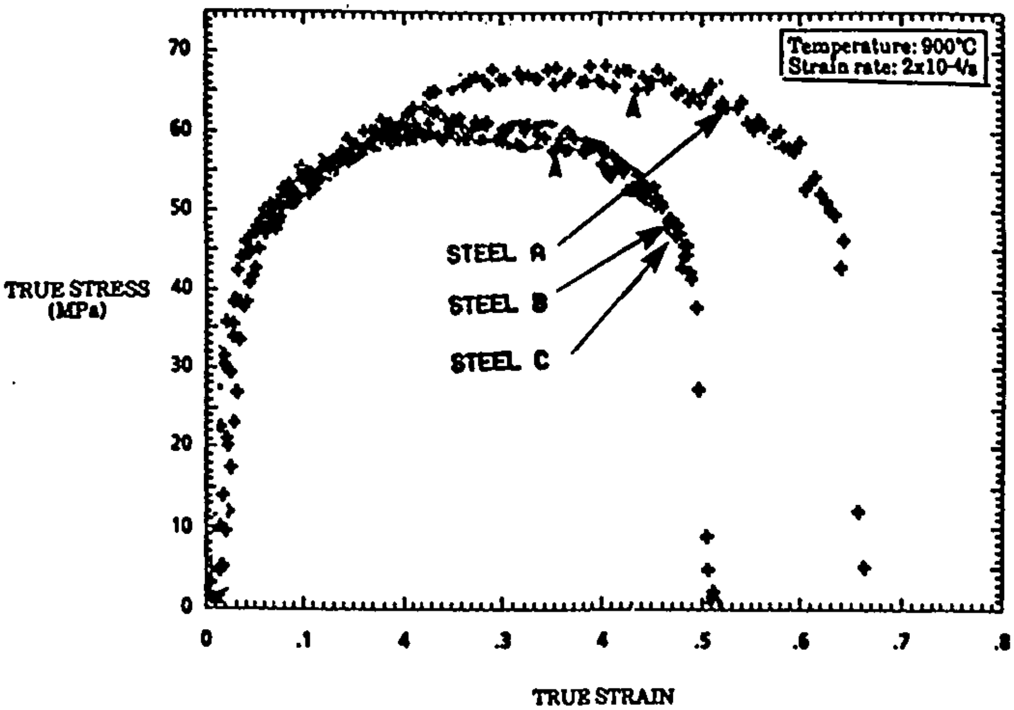

Fig. 4.17: Infuence of carbon content on the flow curve behavior after direct heating .

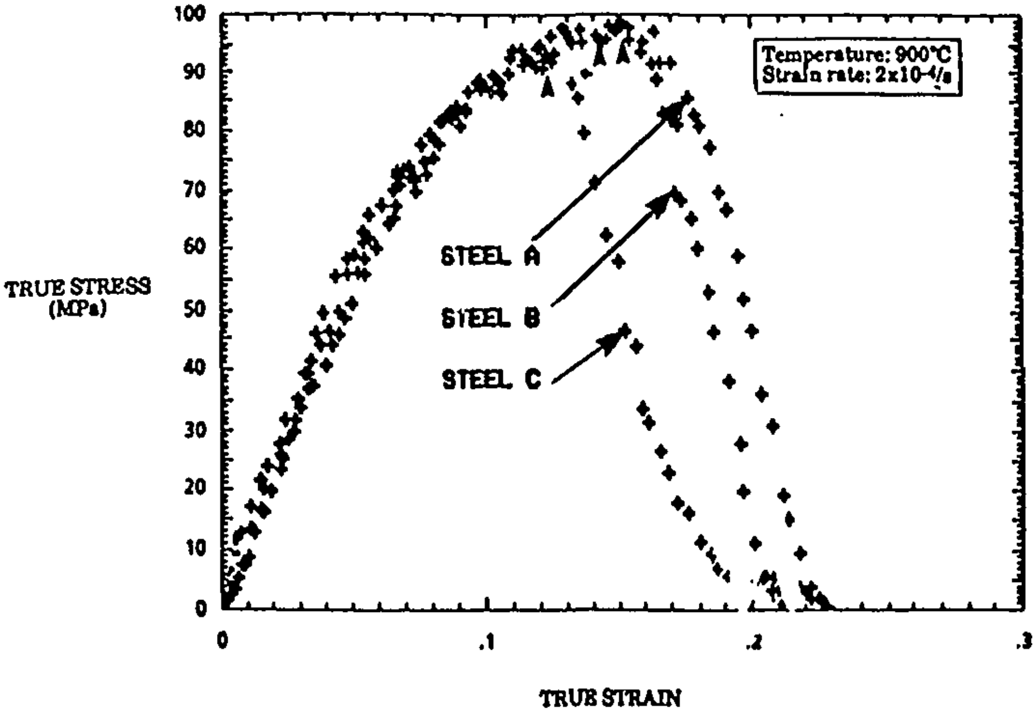

Fig. 4.18: Influence of the carbon content on the flow curve behavior after sensitization

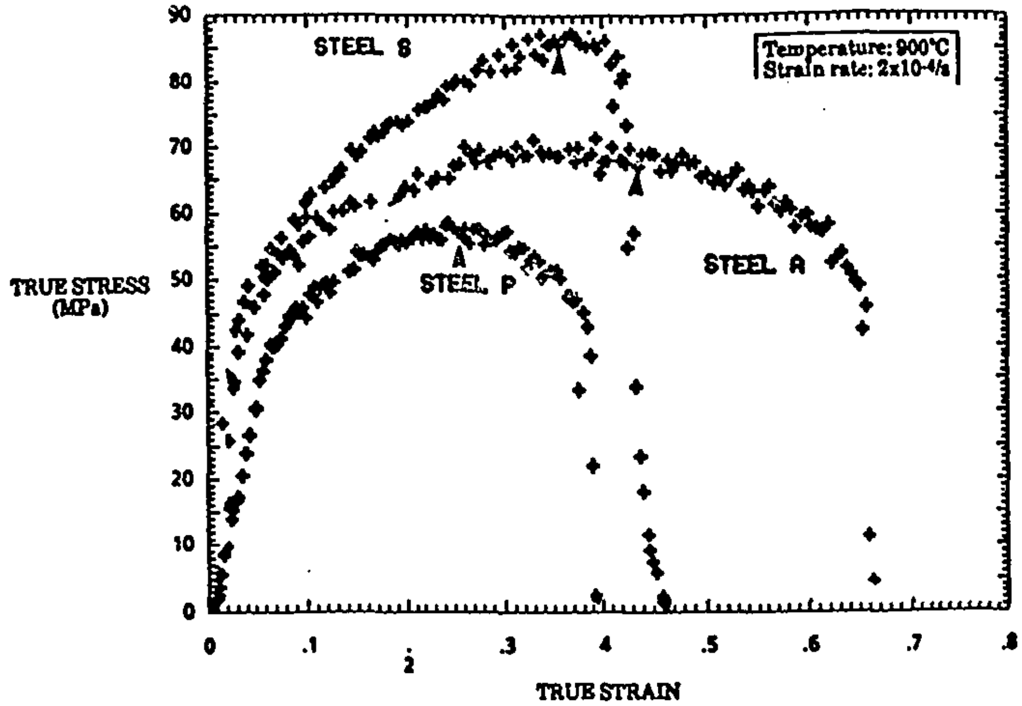

Figs. 4.19: Influence of the microalloying additions on the flow curve behavior after direct heating.

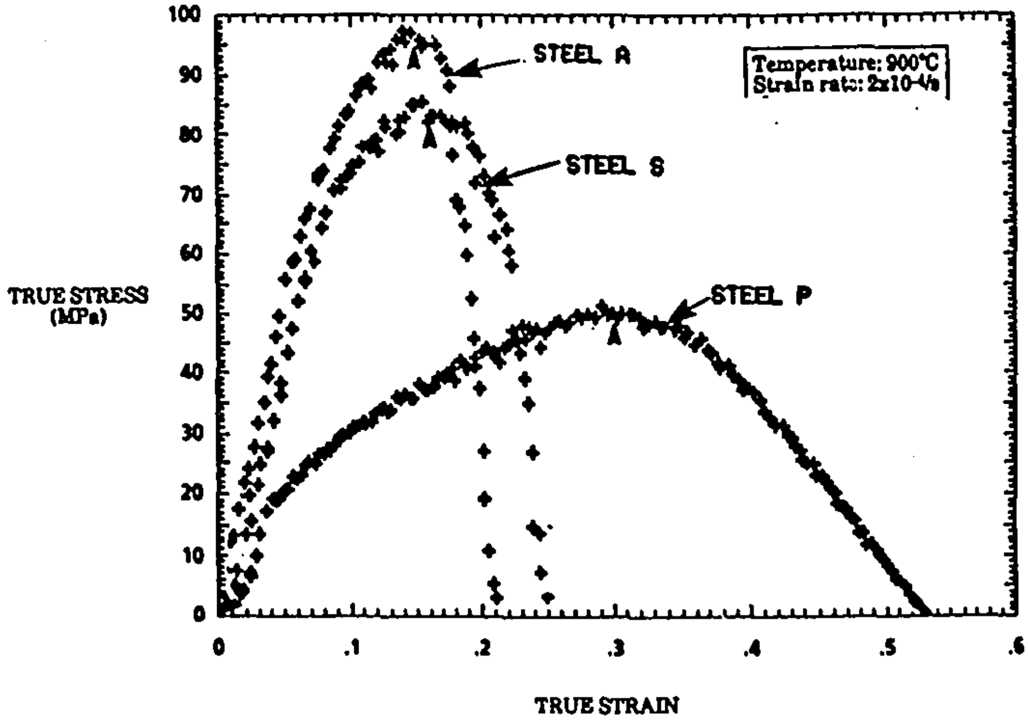

Figs. 4.20: Influence of the microalloying additions on the flow curve behavior after sensitization.

4.2.1.2 Hot ductility-temperature curves

Typical reduction of area (RA) vs temperature curves illustrating the effect of strain rate are shown in Fig. 4.21. On the hot ductility curves shown in this section, unless specified otherwise, the reduction of area refers to the reduction of area at fracture, and the arrows indicate the lowest temperature at which dynamic recrystallization takes place (i.e. when one or more stress oscillations are seen).

The width and depth of the ductility trough depend strongly on the chemical composition and thermal history of the material, as described in detail in the following sections. However, some general observations can be made regarding the hot ductility curves.

Decreasing the strain rate broadens and deepens the ductility trough, but does not change the ductility minimum. In the following sections, because the lowest strain rate ($2 \times 10^{-4} s^{-1}$) shows the most marked effect and is most closely related to the continuous casting process, only the results pertaining to this strain rate are presented.

Finally, it is interesting to note that dynamic recrystallization is always associated with a good ductility (i.e. RA>60%) but, as will be seen, dynamic recrystallization is not an absolute prerequisite for good ductility. At temperatures lower than the ductility minimum, dynamic recrystallization is not observed. However, the RA can be as high as 70%, e.g. in the case of direct heating at 800°C.

4.2.1.3 Influence of heat treatment on the hot ductility-temperature curves

The effect of the prior heat treatment on the hot ductility behaviour depends, to some extent, on the steel chemistry. In steel P, (Fig. 4.22) the pronounced ductility trough at 900°C observed for the directly heated specimens is not seen for the annealed or sensitized specimens. It is almost certain that

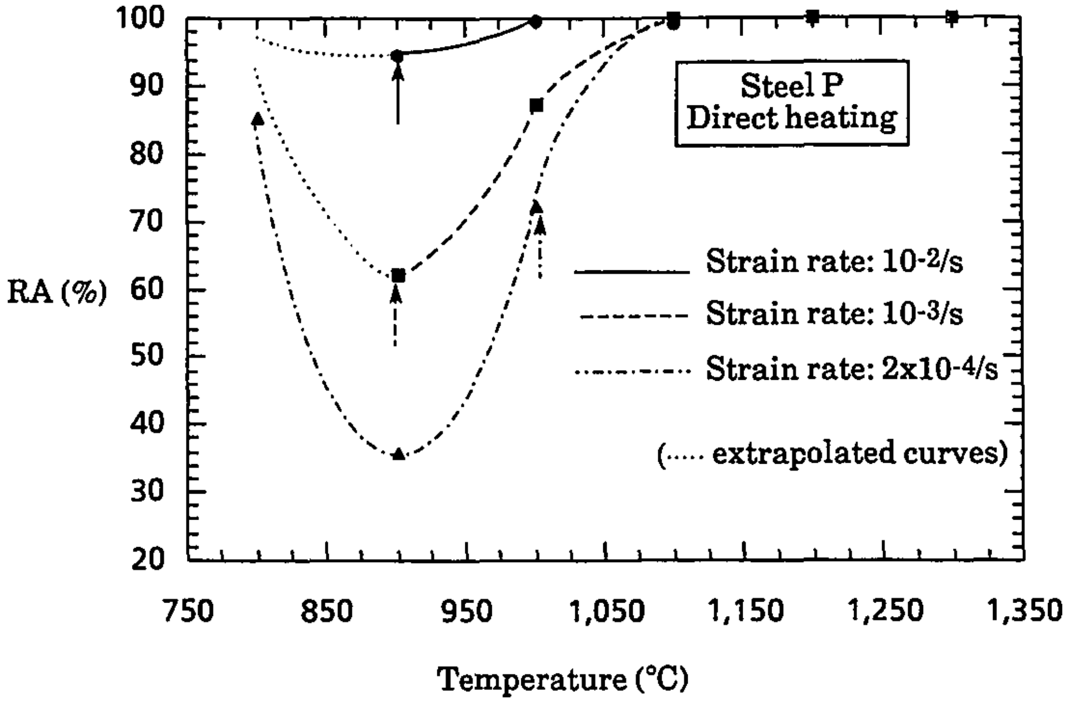

Fig. 4.21: Effect of strain rate on hot ductility curves.

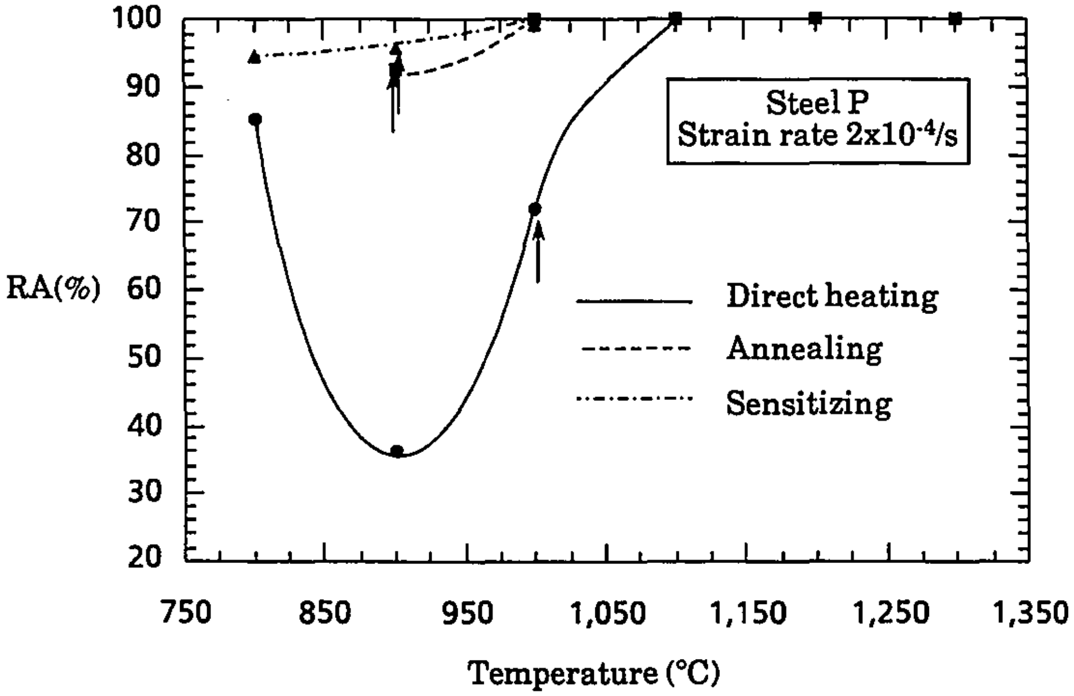

Fig. 4.22: Influence of prior heat treatment on the reduction of area versus temperature curves, steel P.

these latter treatments have shifted the trough to lower temperatures, i.e. between 700 and 850°C [114]. By contrast, for the Nb-Ti steels, (grades A, B, and C) increasing the heat treatment temperature (i.e. going from direct heating, through annealing to sensitizing) generally widens and deepens the trough (Figs 4.23 to 4.25). However, note that the width of the trough never extends to temperatures greater than 1000°C for annealed specimens. For the other two heat treatments, the high temperature side of the trough is 1100°C, except for the high carbon steel (C), where this temperature, in the sensitized condition, is 1200°C (Fig. 4.25).

Steel S (Fig. 4.26) shows a different behavior compared to the Nb-Ti steels after annealing, in that the ductility is observed to be higher than for the directly heated conditions. Sensitizing still leads to the deepest and widest trough, however.

4.2.1.4 Influence of the carbon content on the ductility behaviour of Nb-Ti steels

After direct heating, an increase of the carbon level from 0.07 to 0.10 wt% leads to a slight decrease of the ductility minimum and a small broadening of the trough (Fig. 4.27). There is no difference between the 0.10 and 0.14 wt% grades.

In the case of the annealing treatment, an increase of the carbon content to either 0.10 or 0.14 wt% more strongly deepens and broadens the trough compared to direct heating. The widening of the trough is somewhat greater for the 0.10 wt% C steel (Fig. 4.28).

The width and depth of the trough are considerably bigger for specimens subjected to the sensitizing treatment (Fig. 4.29). Increasing the C content from 0.07 to 0.10 wt% does not significantly affect the ductility minimum, but widens the trough (Fig. 4.29). The 0.14 wt% C steel exhibits a much wider and deeper trough than the steels with the lower C concentrations.

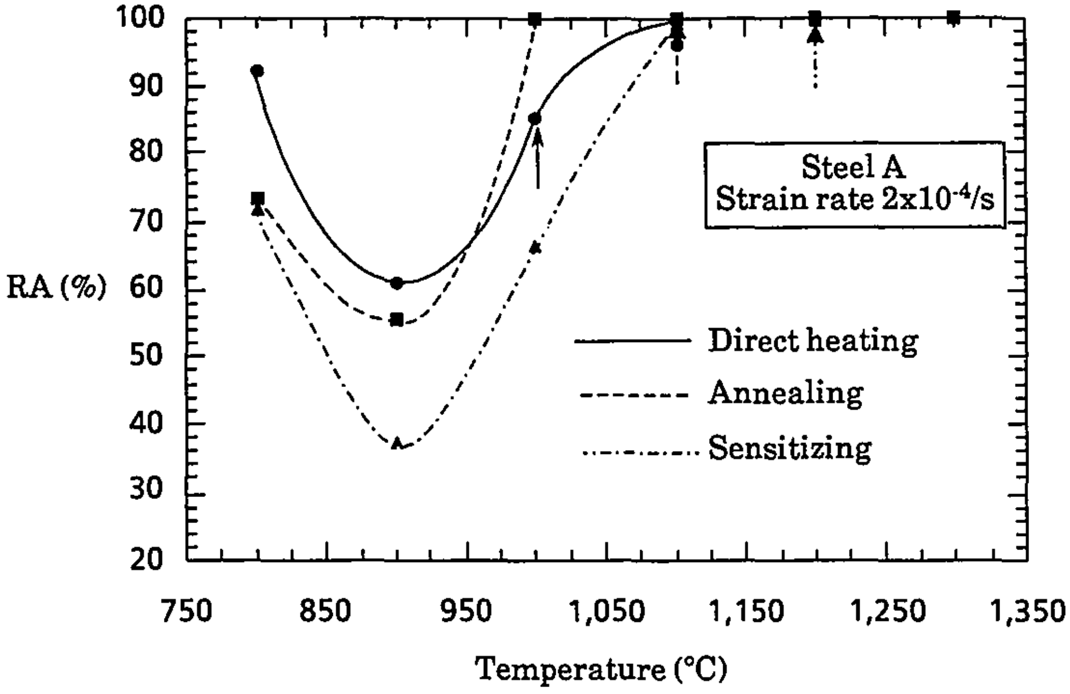

Fig. 4.23: Influence of prior heat treatment on the reduction of area versus temperature curves, steel A.

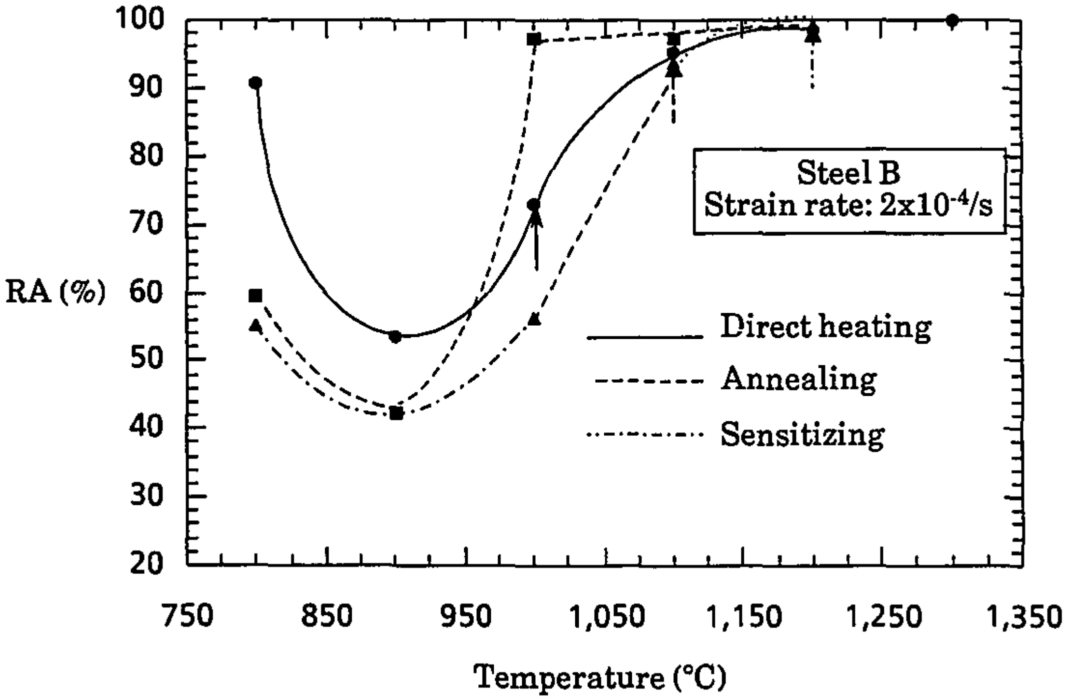

Fig. 4.24 : Influence of prior heat treatment on the reduction of area versus. temperature curve. Steel B.

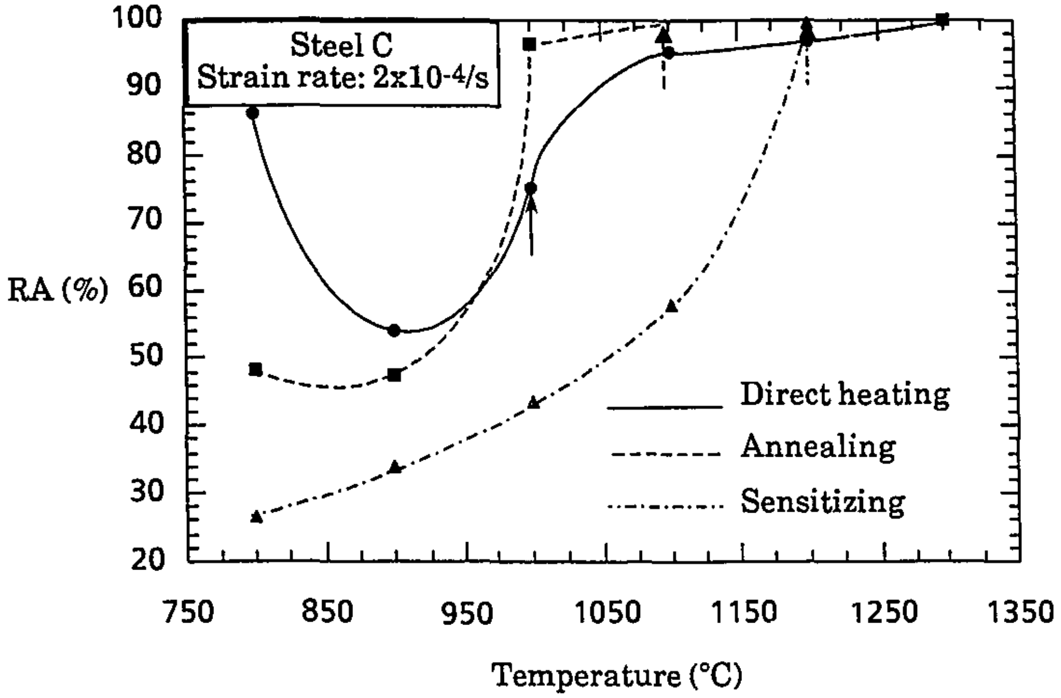

Fig. 4.25 : Influence of prior heat treatment on the reduction of area versus. temperature curve. Steel C.

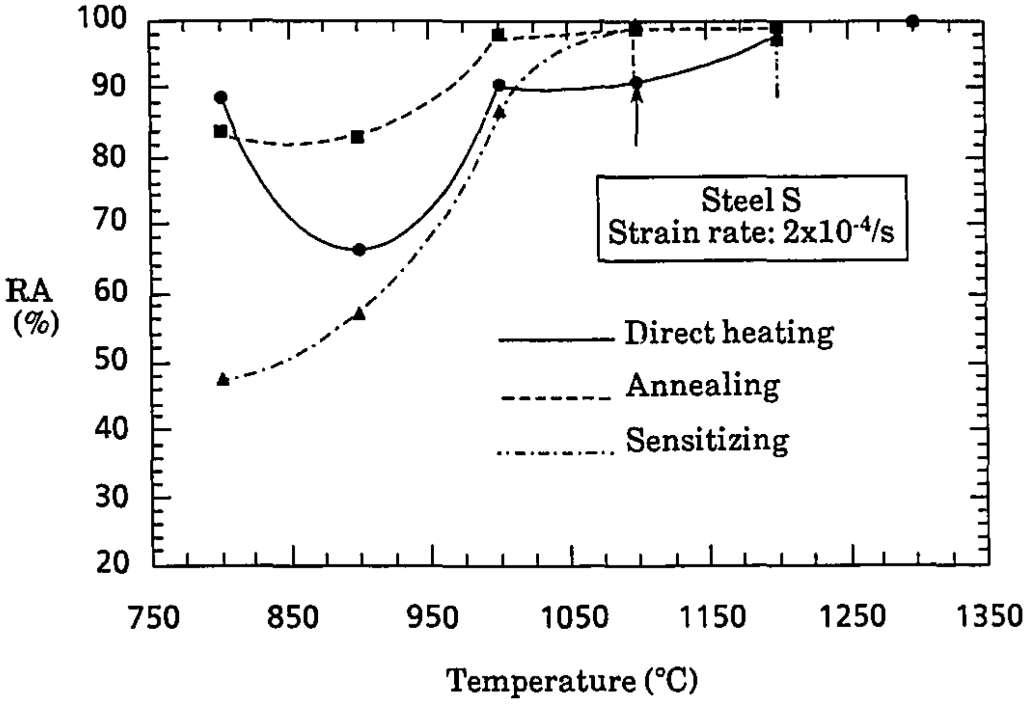

Fig. 4.26: Influence of prior heat treatment on the reduction of area versus temperature curve, steel S.

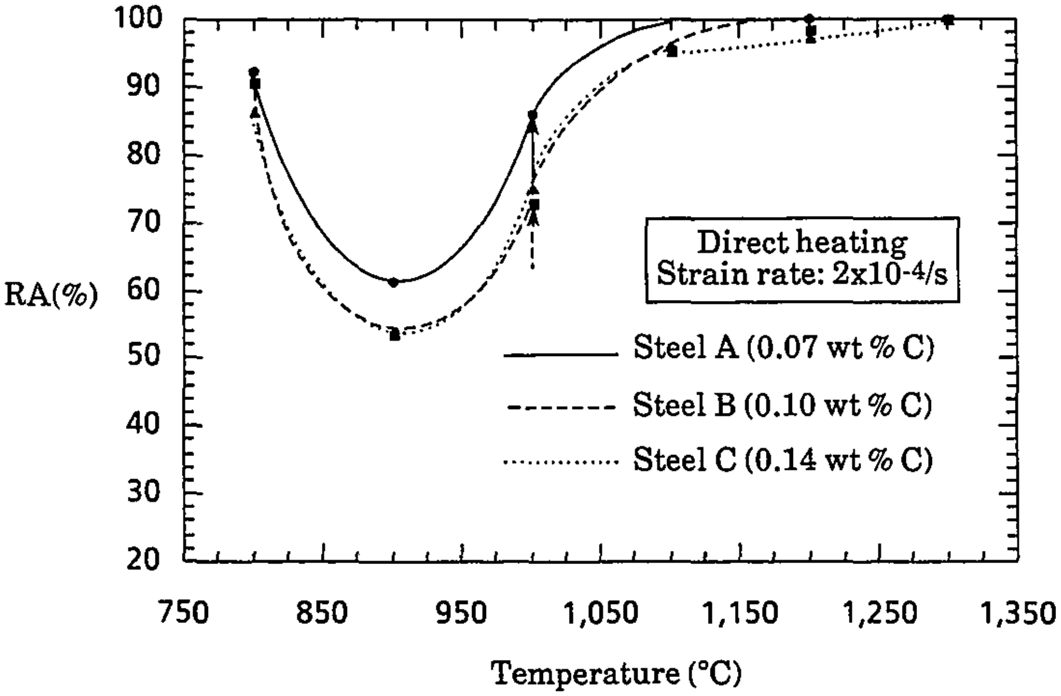

Fig. 4.27: Influence of carbon level on ductility following direct heating.

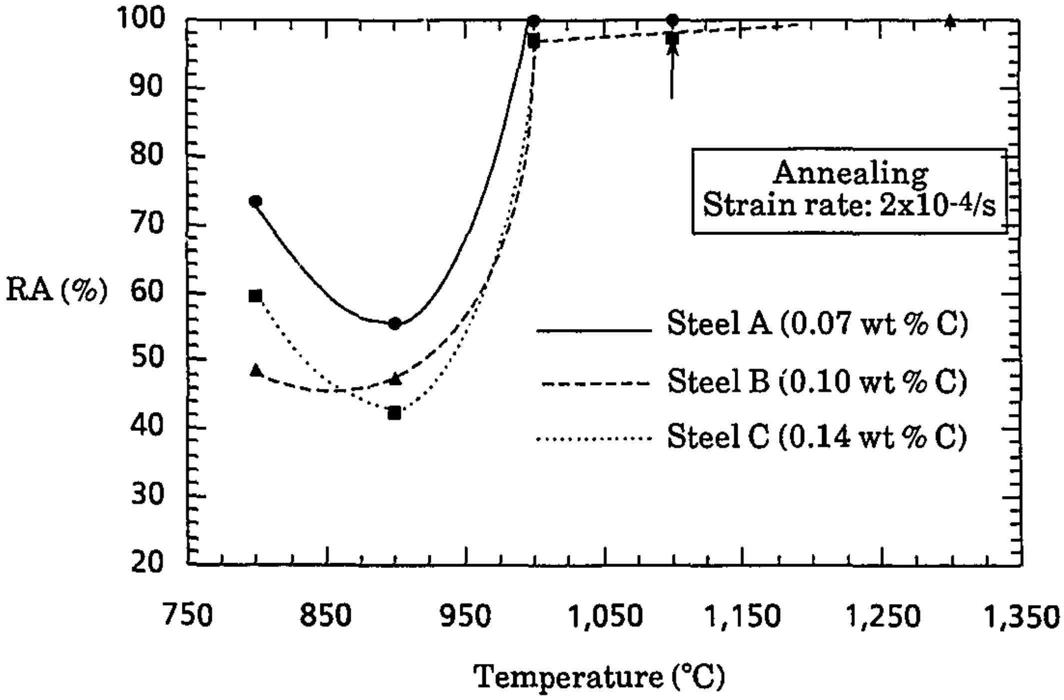

Fig. 4.28 : Influence of carbon level on ductility following annealing.

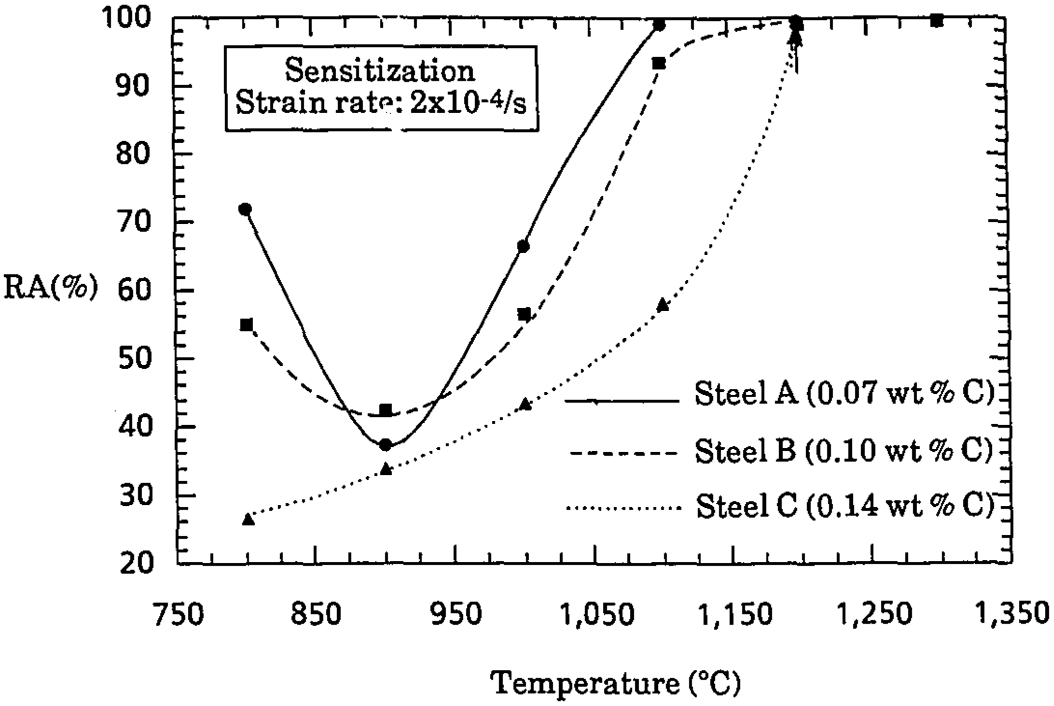

Fig. 4.29 : Influence of carbon level on ductility following sensitizing.

The effect of carbon on ductility is thus strongly dependent on the thermal history of the specimen. Essentially, a direct heating treatment does not reveal any great influence of C, but sensitization reveals a strong and adverse effect of increasing the carbon content.

4.2.1.5 Influence of microalloying elements on hot ductility

Direct heating leads to a well defined ductility trough between 800 and 1100°C with a minimum at 900°C for the plain C-Mn steel (Fig. 4.30). The addition of Nb-Ti (steel A) improves the ductility minimum from a reduction of area of 37.5 to 62.5 %, but does not change the width or the temperature of the trough. The addition of Ni-Cr-V (steel S) does not further affect the hot ductility behaviour.

After annealing (Fig. 4.31), the plain C-Mn steel shows no ductility trough in the test temperature range examined. The addition of Nb and Ti (steel A) leads to a decrease in ductility between 900 and 1000°C. The presence of Ni, Cr and/or or V in steel S improves the ductility of the Nb-Ti from 56 to 83% at 900°C and 73 to 84% at 800°C.

The behaviour of these steels after sensitizing is similar to the annealing treatment in that no ductility trough is seen in steel P, and the addition of Nb and Ti reveals a trough (Fig. 4.32). However, the trough is much deeper and wider compared to the annealed case. Moreover, the effect of the Ni-Cr-V addition to the Nb-Ti steel differs considerably from the annealed specimens in that the minimum ductility is not strongly improved and the temperature of the trough is shifted to a much lower value.

As in the case of carbon concentration, the influence of microalloying elements on hot ductility is strongly dependent on thermal history. The main point to note is that after direct heating, steel P, which contains the lowest amount of microalloying elements, displays the lowest ductility of the three grades, whereas, after annealing or sensitizing, the ductility of this steel is the highest in the temperature range investigated. In other words, the addition of Nb-Ti is adverse in the case of the annealing and sensitizing, but beneficial after

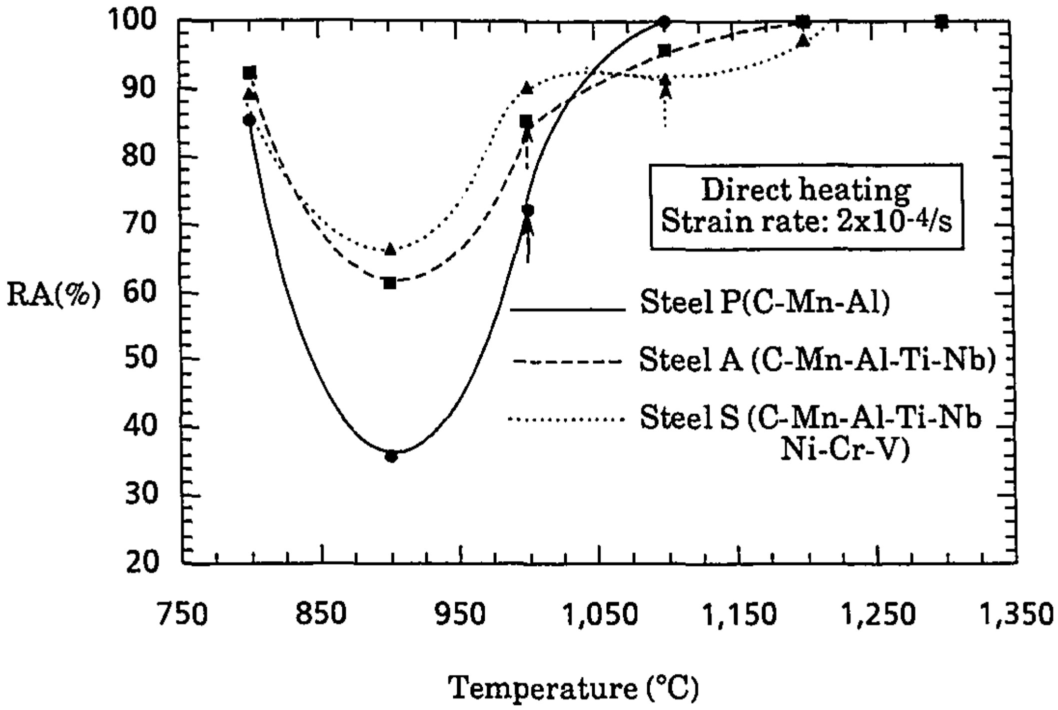

Fig. 4.30: Influence of the microalloying elements on ductility following direct heating.

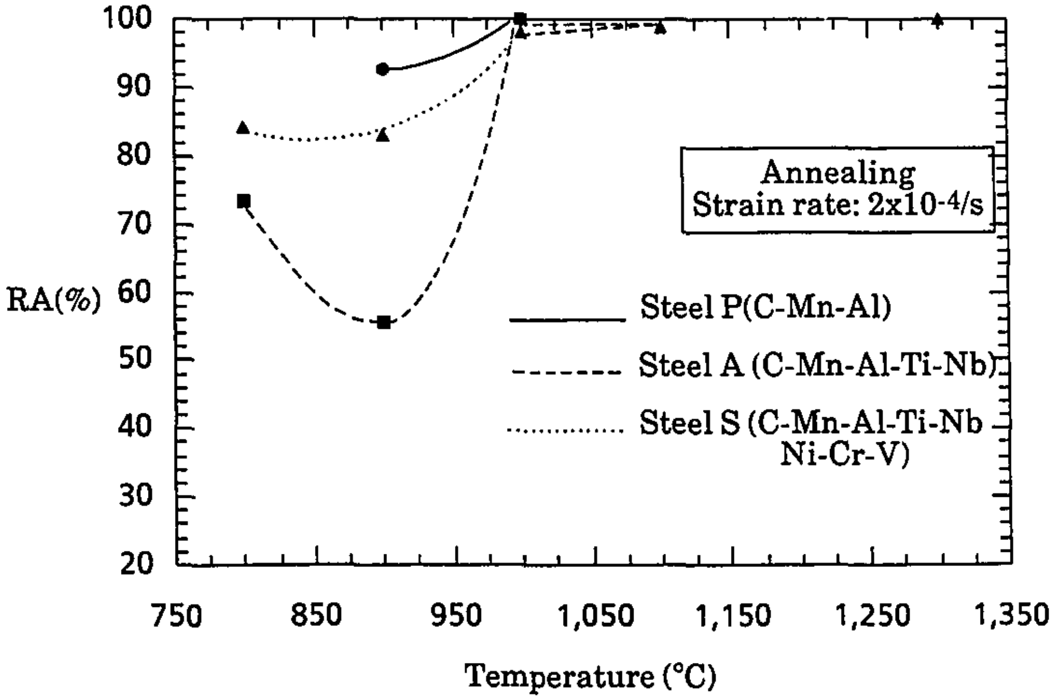

Fig. 4.31: Influence of the microalloying elements on ductility following annealing.

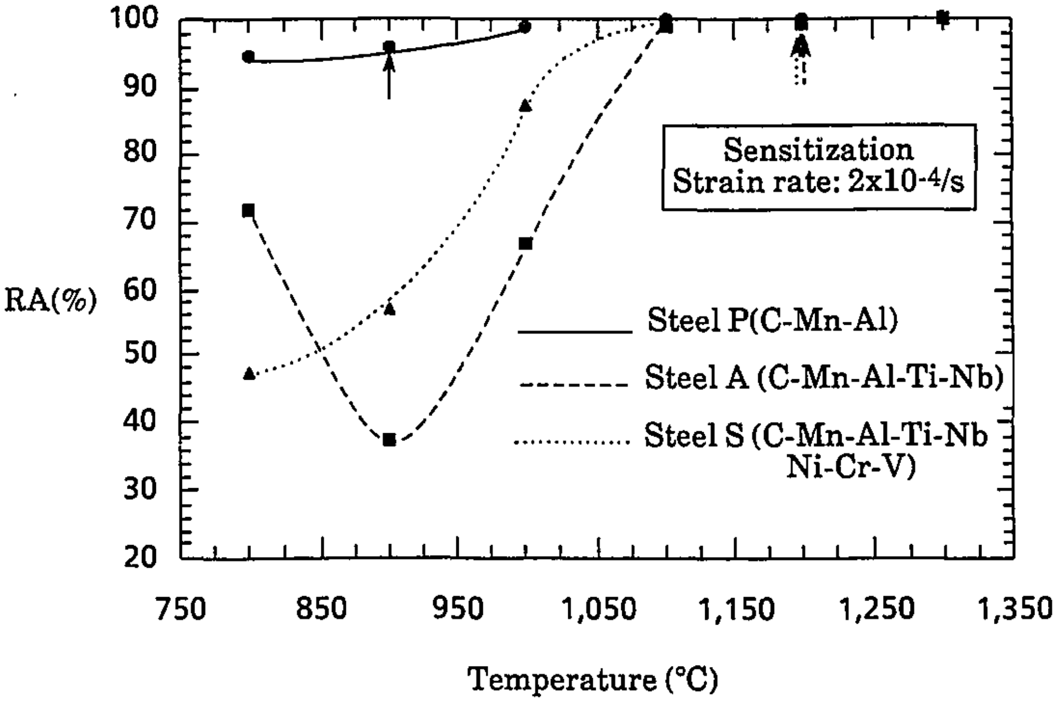

Fig. 4.32: Influence of the microalloying elements on ductility following sensitizing.

direct heating. The further addition of Ni-Cr-V is beneficial in the annealed case but only moves the trough to lower temperatures after sensitization. Only a slight effect of this addition is observed in the directly heated specimens.

4.2.1.6 Hot strength-temperature curves

Typical maximum stress vs temperature curves after direct heating and sensitizing treatments are displayed in Figs. 4.33 and 4.34, respectively. On each graph the influence of strain rate is also shown. As expected, the maximum stress increases with decreasing temperature and increasing strain rate. Note also that following direct heating, at the lowest strain rate, the *rate* of stress increase diminishes from 900°C to 800°C and can be equal to or lower than the stress at 900°C (Fig. 4.33).

There is little effect of heat treatment on the maximum stress at the lowest strain rate for steel P (Fig. 4.35), although, at 800°C, the maximum stress is slightly higher after direct heating than after sensitizing. In steels A, B, and C, (Figs. 4.36-4.38), above about 1000°C, the maximum stress is only weakly dependent on the heat treatment. Below this temperature, however, increasing the temperature of prior annealing (i.e. going from direct heating to sensitizing) leads to a higher flow stress increase with temperature for the annealed and sensitized specimens. From 900°C to 800°C, the rate of flow stress increase is maintained for the sensitized specimen, but decreases in the annealed case. For steel S (Fig. 4.39), heat treatment has no effect except at 800°C where the maximum stress decreases after the direct heating and annealing treatments, but continues to rise in the sensitized condition.

The influence of carbon on the hot strength at the lowest strain rate is shown in Figs. 4.40 and 4.41 for direct heating and sensitizing, respectively. It appears that increasing the level of carbon results in virtually no variation of the maximum stress, although at 800°C, after sensitizing, the maximum stress of steel A is somewhat lower than the other two. These figures also show that the rate of stress increase is much higher after sensitization, compared to direct heating, which is generally true of all the steels tested, except for steel P.

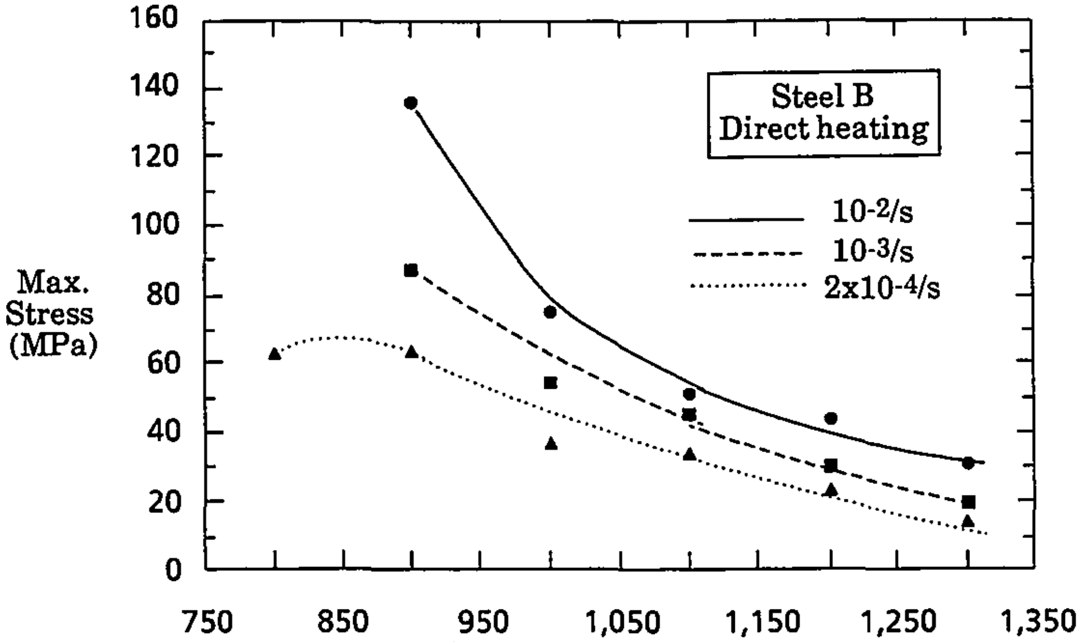

Fig. 4.33: Influence of temperature and strain rate on the maximum true stress of steel B after direct heating.

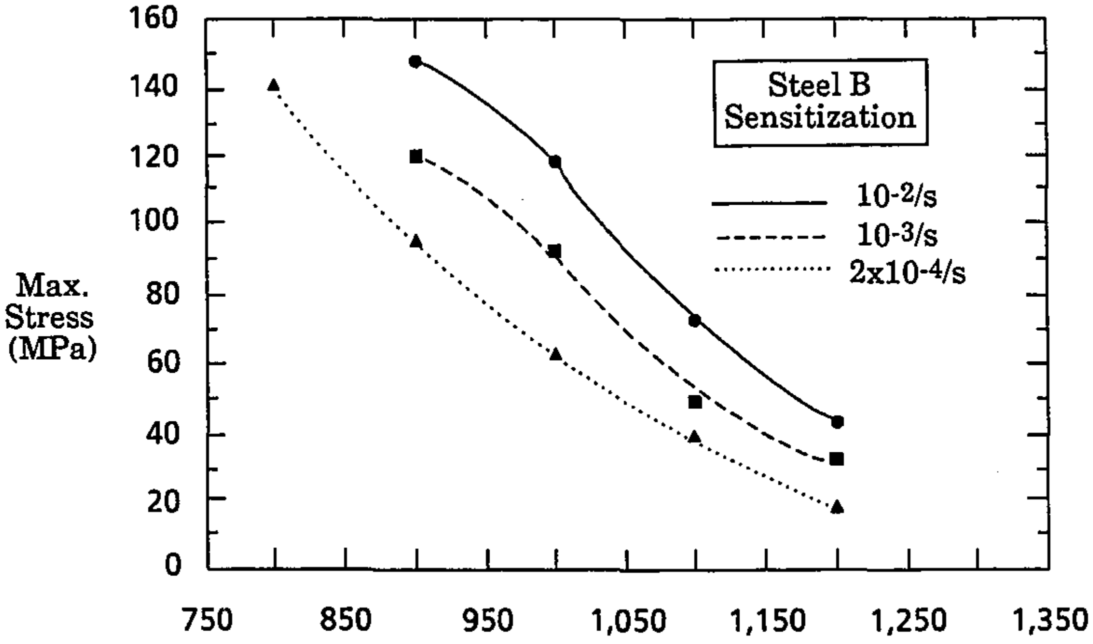

Fig. 4.34: Influence of temperature and strain rate on the maximum true stress of steel B after sensitizing.

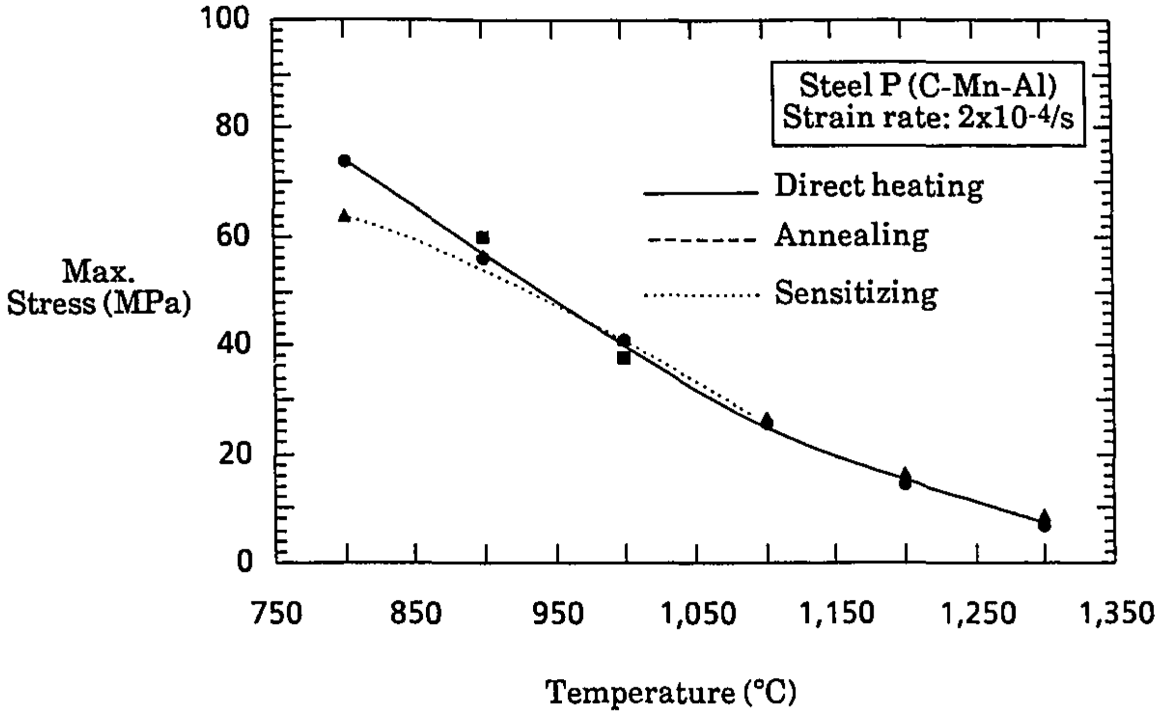

Fig. 4.35: Influence of temperature and prior heat treatment on the maximum true stress of steel P.

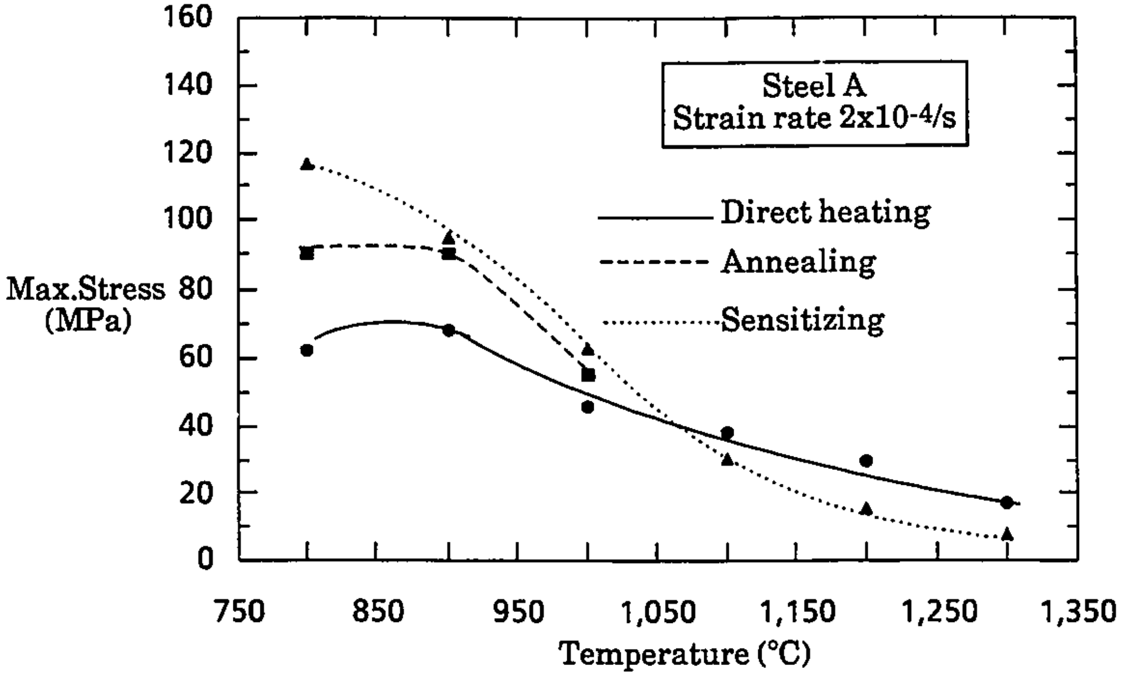

Fig. 4.36: Influence of temperature and prior heat treatment on the maximum true stress of steel A.

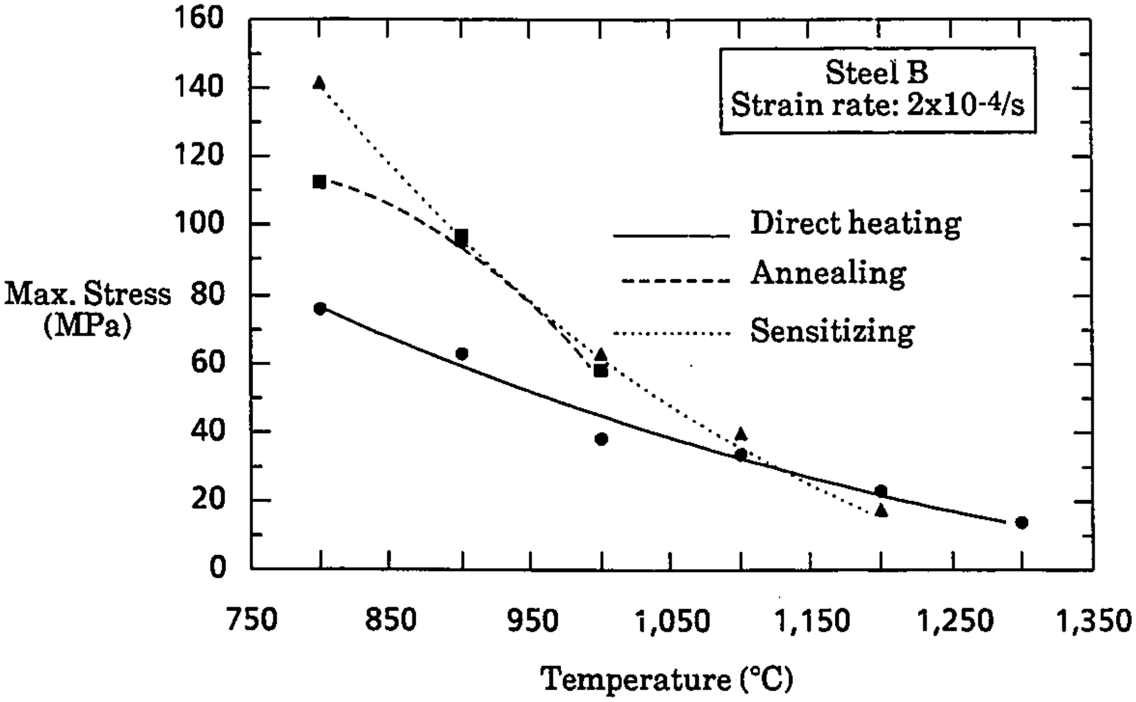

Fig. 4.37: Influence of temperature and prior heat treatment on the maximum true stress of steel B.

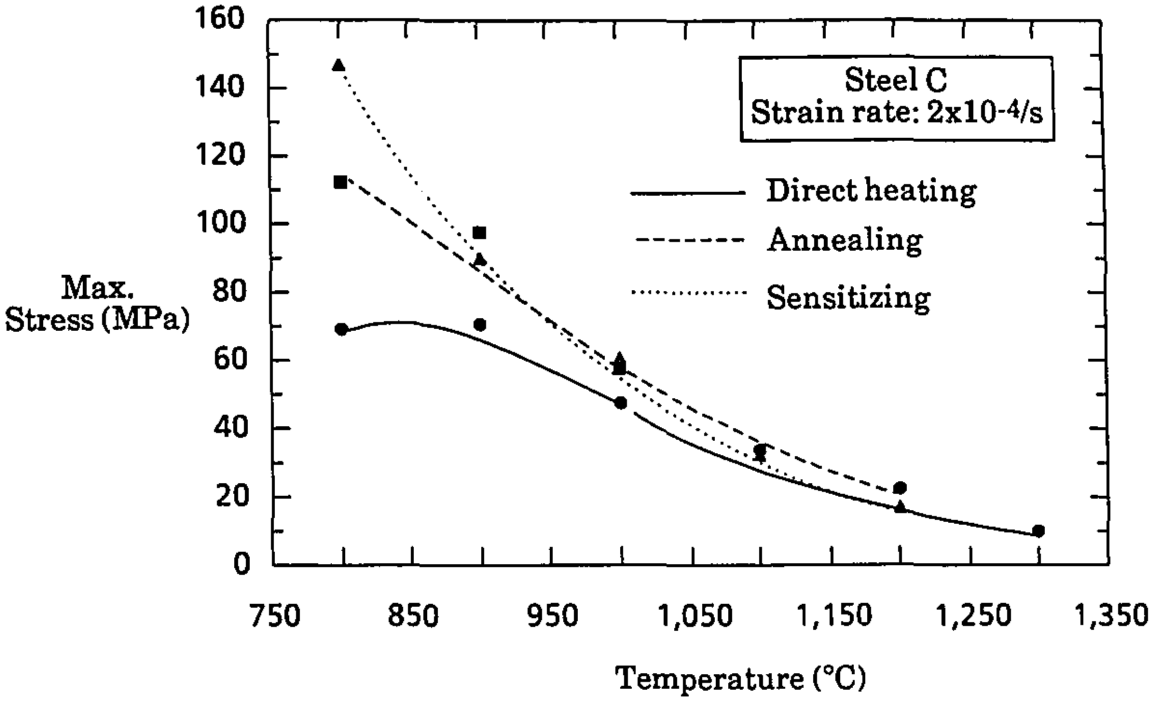

Fig. 4.38: Influence of temperature and prior heat treatment on the maximum true stress of steel C.

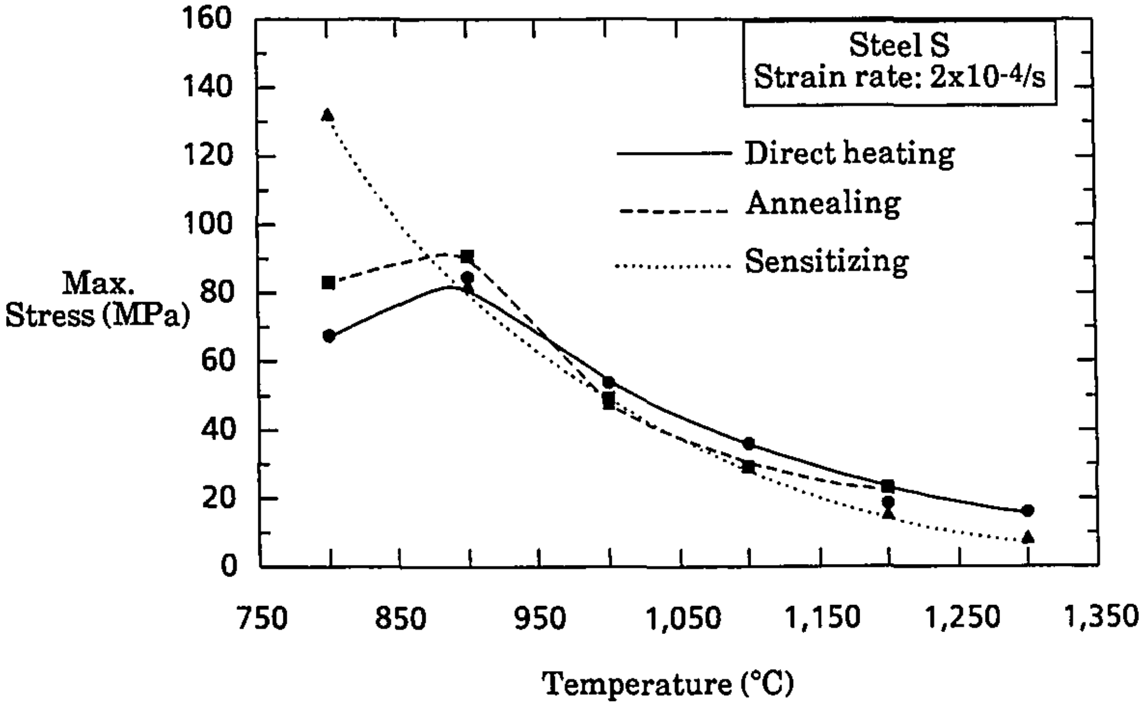

Fig. 4.39: Influence of temperature and prior heat treatment on the maximum true stress of steel S.

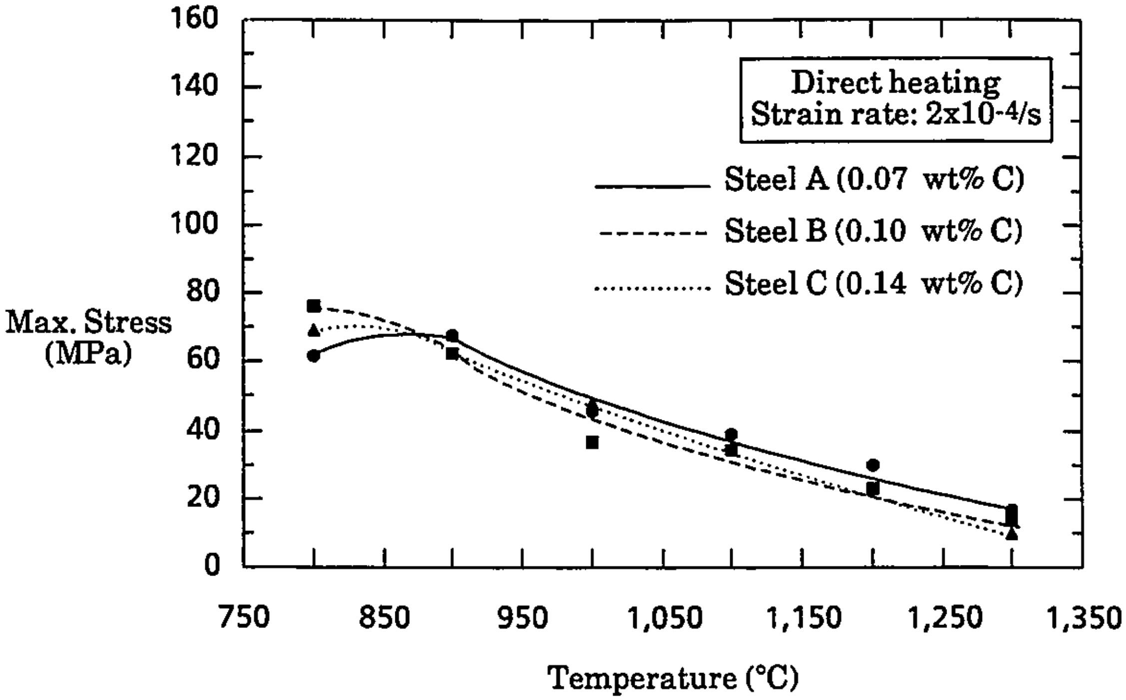

Fig. 4.40: Influence of carbon content on the maximum true stress versus temperature curves after direct heating.

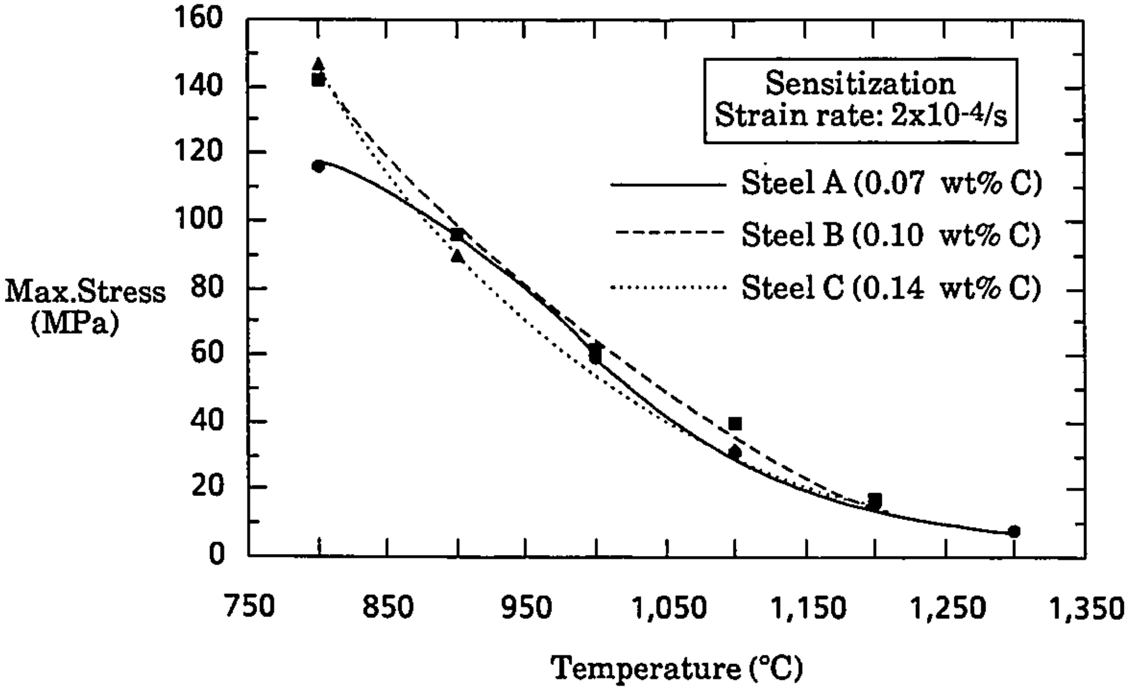

Fig. 4.41: Influence of carbon content on the maximum true stress versus temperature curves after sensitization.

The effects of microalloying elements on hot strength at the lowest strain rate are shown in Figs 4.42 and 4.43 for direct heating and sensitizing treatments, respectively. After direct heating, all the steels show a continuous increase of the stress over almost the entire temperature range. However, steel S and, to a lesser extent, grade A, display a peak stress at 900°C. The C-Mn steel generally exhibits the lowest stress but, apart from the values at 900°C, the difference is quite small.

The maximum stresses are the same for the three steels above 1100°C after the sensitizing treatment (Fig. 4.43). Below this temperature, the addition of Nb and Ti leads to an increasingly higher maximum stress, the difference increasing with decreasing temperature. The Ni/Cr/V addition leads to lower the stress in the range 900-1100°C (compared to the Nb-Ti steel), but at 800°C, the maximum stress of steel S is the highest. However, the observed differences between steels S and A are relatively small.

4.2.2 Temperature Range 1400°C-Solidus

4.2.2.1 Typical tensile flow curves

An example of the influence of temperature on the shape of flow curves is displayed in Fig. 4.44. As before, the approximate strain at which necking occurs is indicated by an arrow. Again, it is possible to classify the curves into two categories: (i) curves showing one or more stress oscillations (i.e. dynamic recrystallization) and (ii) those exhibiting no stress oscillations.

The effects of increasing the temperature on the flow curve behaviour are to decrease:

(1) the maximum stress
(2) the tendency towards dynamic recrystallisation

The general influence of strain rate on the flow curve behaviour is displayed in Fig. 4.45, it can be seen that a decreasing strain rate leads to a decrease in:

(1) the maximum stress

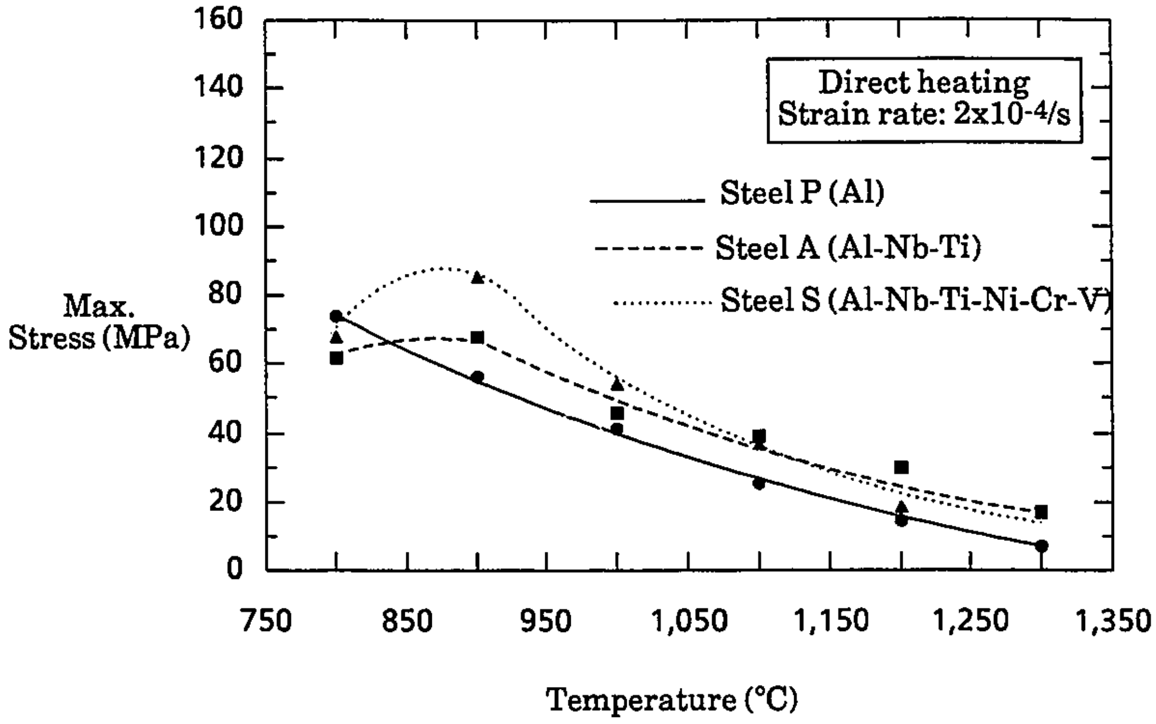

Fig. 4.42: Influence of microalloying elements on the maximum true stress versus temperature curves after direct heating.

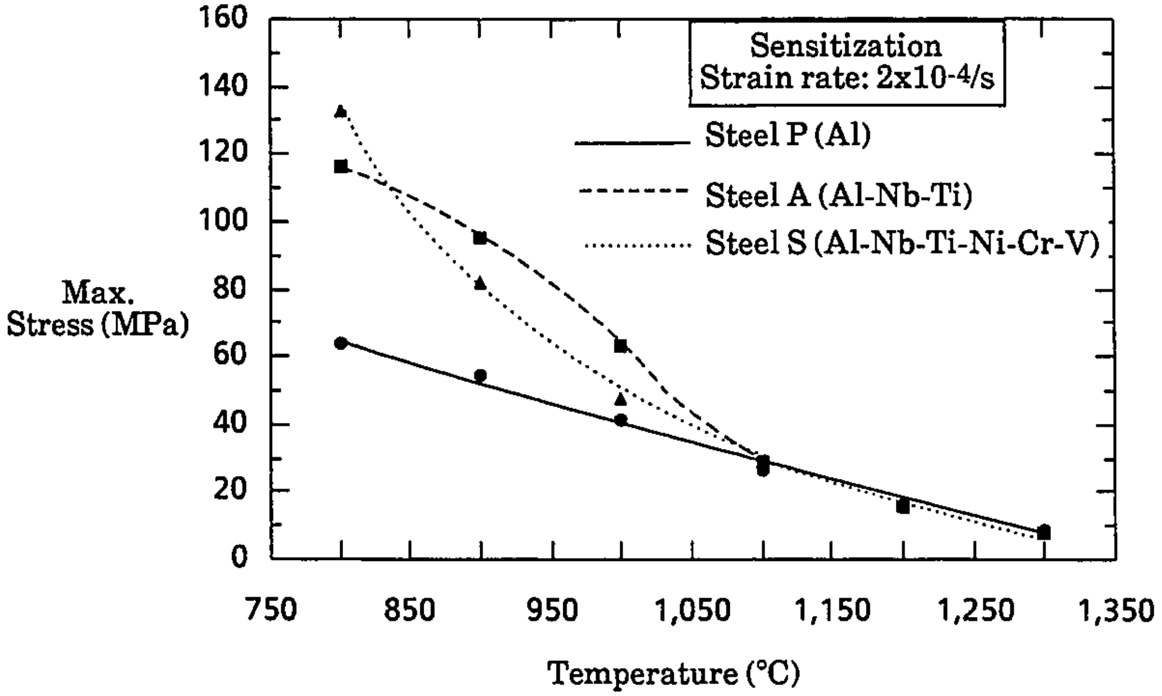

Fig. 4.43: Influence of microalloying elements on the maximum true stress versus temperature curves after sensitization.

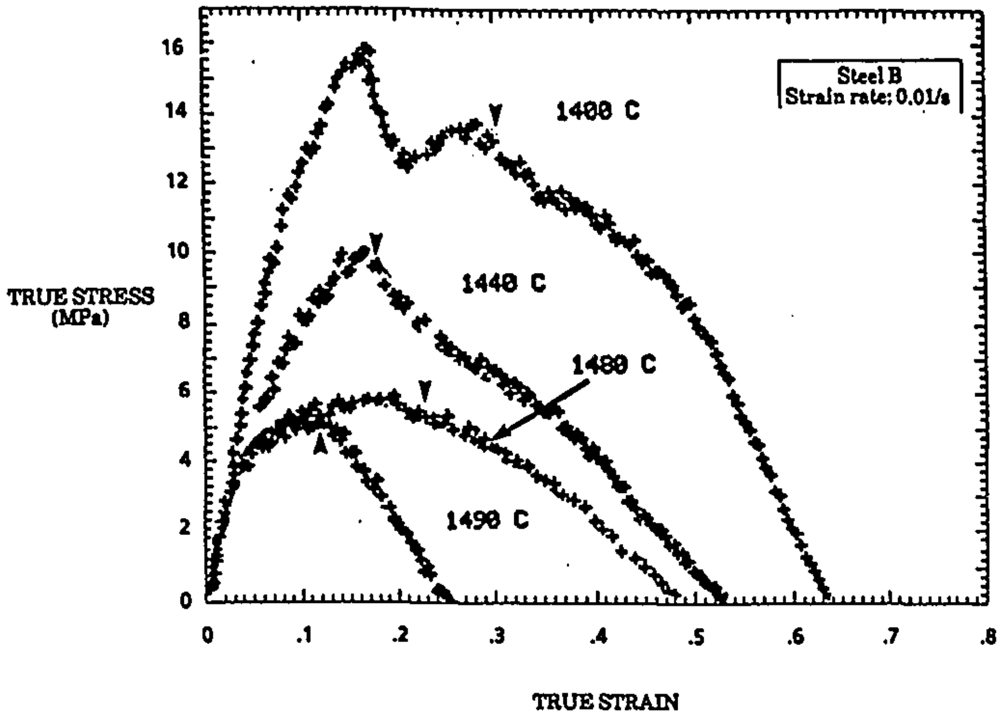

Fig. 4.44: Influence of temperature on the flow curve behaviour, steel B.

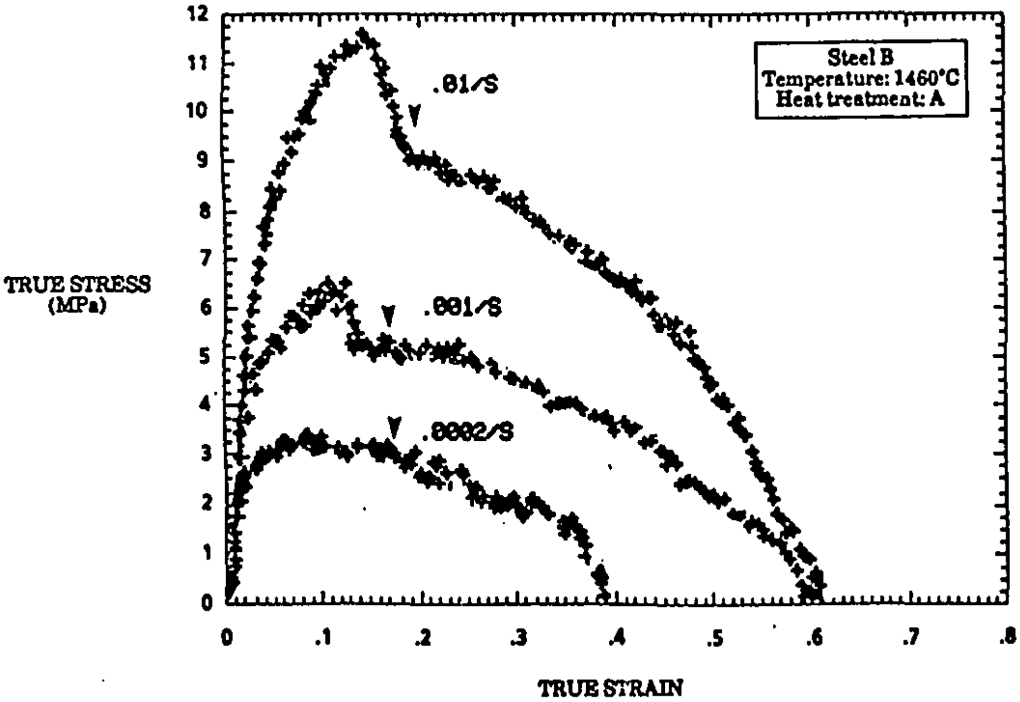

Fig. 4.45: Influence of strain rate on the flow curve behaviour, steel B.

(2) the strain to the onset of dynamic recrystallization.

4.2.2.2 Hot ductility-temperature curves

The reduction of area versus temperature curve for steel A is illustrated in Fig. 4.46 and is representative of all the grades except steel S, for which the curve is shown in Fig. 4.47. On these graphs the temperature zones in which the various phases exist are also indicated. It can be seen that, in the temperature range 1400-1460°C, ductility is very high (close to 100%) regardless of the grade. There is no effect of the $\gamma \rightarrow \gamma + \delta$ transformation. However at higher temperatures the ductility decreases to zero over a temperature range of about 20°C. The exact temperature depending on the chemical composition. Note that for steel S the ductility drop from 100% to 0% RA effectively occurs over a *zero* temperature range. In Table 4.3 the ductility drop start (DDS), and finish (DDE) temperatures are presented, along with the corresponding phase(s) which is (are) present. In addition, the temperature at which the RA is 50% ($T_{50\%}$) and the temperature differences between the solidus (from DTA measurements) and DDS (ΔT_1) and solidus and DDE (ΔT_2) are given. The main observation is that the DDS and DDE both occur before liquid phase is detected by DTA (i.e.ΔT_1 and ΔT_2 are always positive).

The influence of strain rate on the reduction of area vs temperature curves was investigated up to 1480°C for steels P and C and up to 1460°C for steels A, B and S. As anticipated no effect was detected.

4.2.2.3 Influence of carbon on the reduction of area versus temperature curves

Figure 4.48 shows that an increase of the carbon content reduces the temperatures for the onset and the end of ductility drop. Nominally, the DDS and DDE depend on the solidus temperature. However, from Table 4.3, there is no effect of C on the solidus temperature. Thus, the difference between DDS and solidus temperatures increases by $\simeq$50% (from 24°C to 35.5°C) when the carbon content is increased from 0.07 wt% (steel A) to 0.14 wt% (steel C). The same

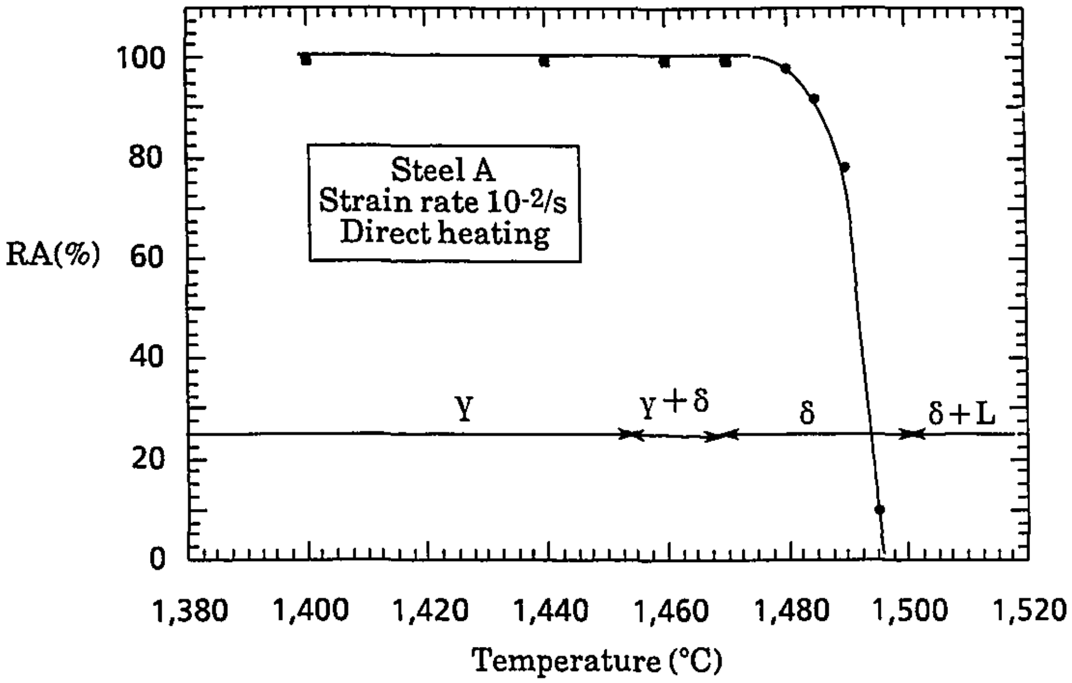

Fig. 4.46: Influence of temperature on the reduction of area between 1400°C and the solidus temperature, steel A.

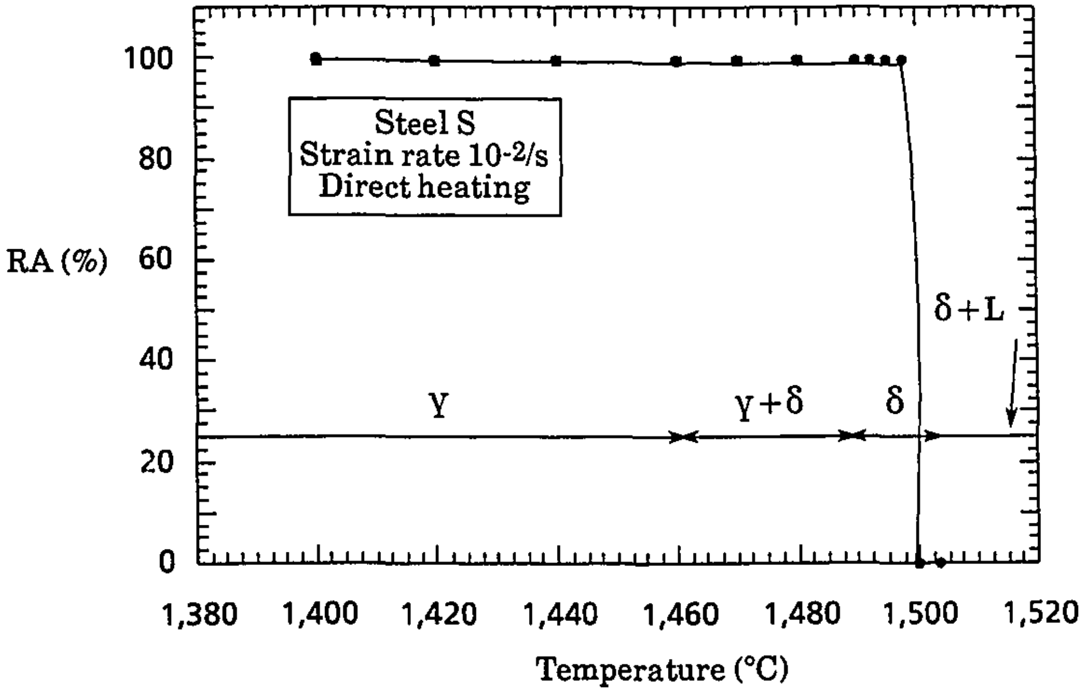

Fig. 4.47: Influence of temperature on the reduction of are between 1400°C and the solidus temperature, steel S.

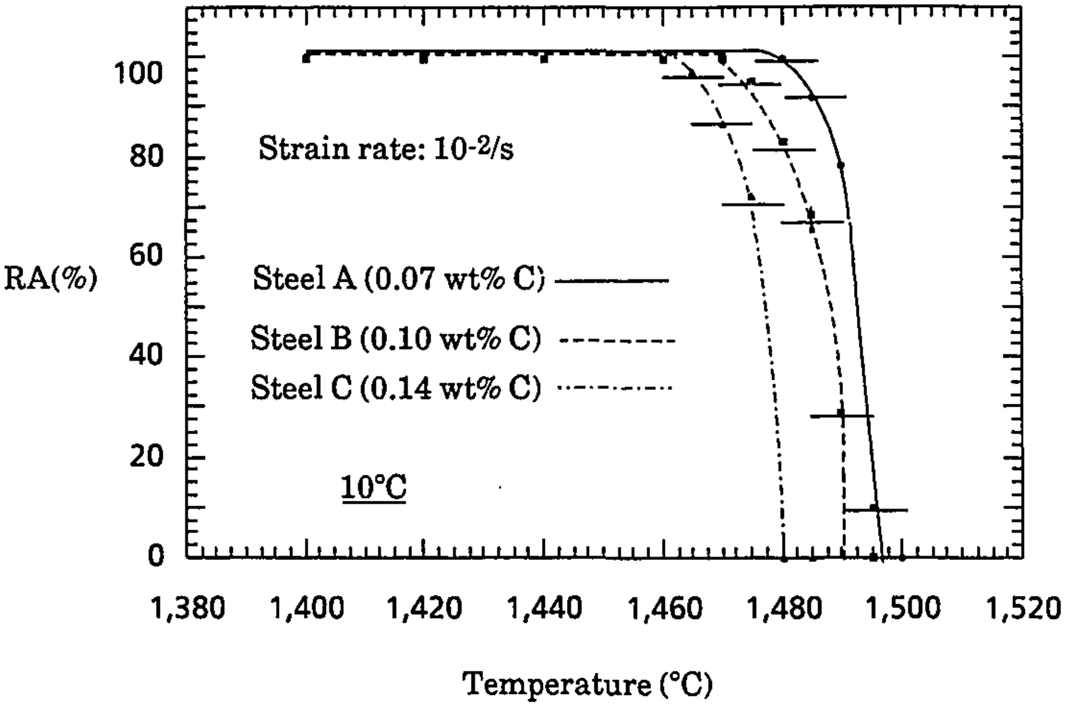

Fig. 4.48: Influence of the carbon content on hot tearing temperature. Strain rate $10^{-2}s^{-1}$, direct heating.

trend is observed when considering the DDE and the solidus temperature differential.

Table 4.3

Ductility drop start (DDS) and ductility drop end (DDE) temperatures correlated with the phase transitions.

Steel	Solidus (°C)	DDS (°C)	ΔT_1 (°C)	Phase	DDE (°C)	Phase	ΔT_2 (°C)	$T_{50\%}$ (°C)
P	1500	1476	24	δ	1492.5	δ	7.5	1488.5
A	1500	1476	24	δ	1496	δ	4	1492.5
B	1500	1470	30	δ	1490	δ	10	1490
C	1497.5	1462	36	$\gamma+\delta$	1480	$\delta+\gamma$	18	1477.5
S	1503.5	1499	4	δ	1500	δ	4	1499.5

4.2.2.4 Influence of microalloying elements on the hot ductility curves

Comparing the results of steels P and A in Fig. 4.49 and Table 4.3, it appears that there is no significant effect of Nb or Ti on zone I. The presence of Ni/Cr/V and/or the lower sulfur level in steel S leads to a decrease of ΔT_1 by 75% (Table 4.3). Furthermore, the temperature zone over which embrittlement occurs is much reduced (from 20°C to effectively zero).

4.2.2.5 Influence of temperature and strain rate on the maximum stress

The variation of the maximum stress with temperature and strain rate is shown in Figs. 4.50 to 4.54 for steels P, A, B, C and S respectively. On each graph the temperature range over which the various phases are observed are shown. As for the 800-1300°C temperature zone, the maximum stress decreases with increasing temperature and decreasing strain rate and reaches zero at a given temperature (Zero Strength Temperature). It can be seen that the rate of decrease in stress is relatively low between 1400 and 1460°C, but it increases

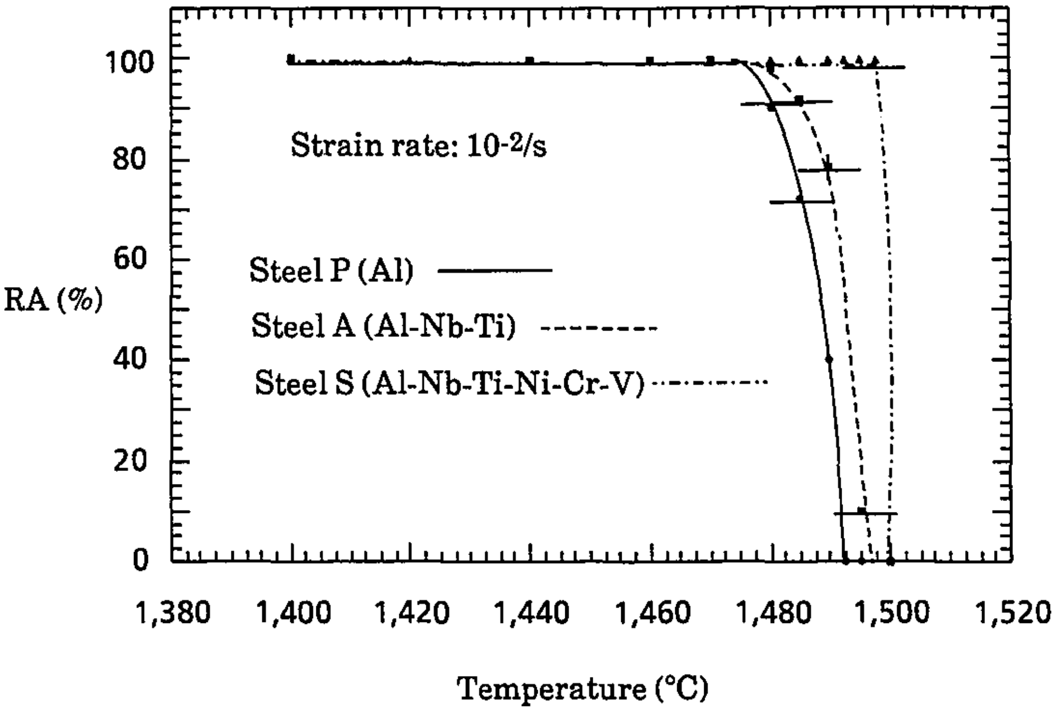

Fig. 4.49: Influence of the microalloying elements on the hot tearing temperature. Strain rate $10^{-2}s^{-1}$, direct heating.

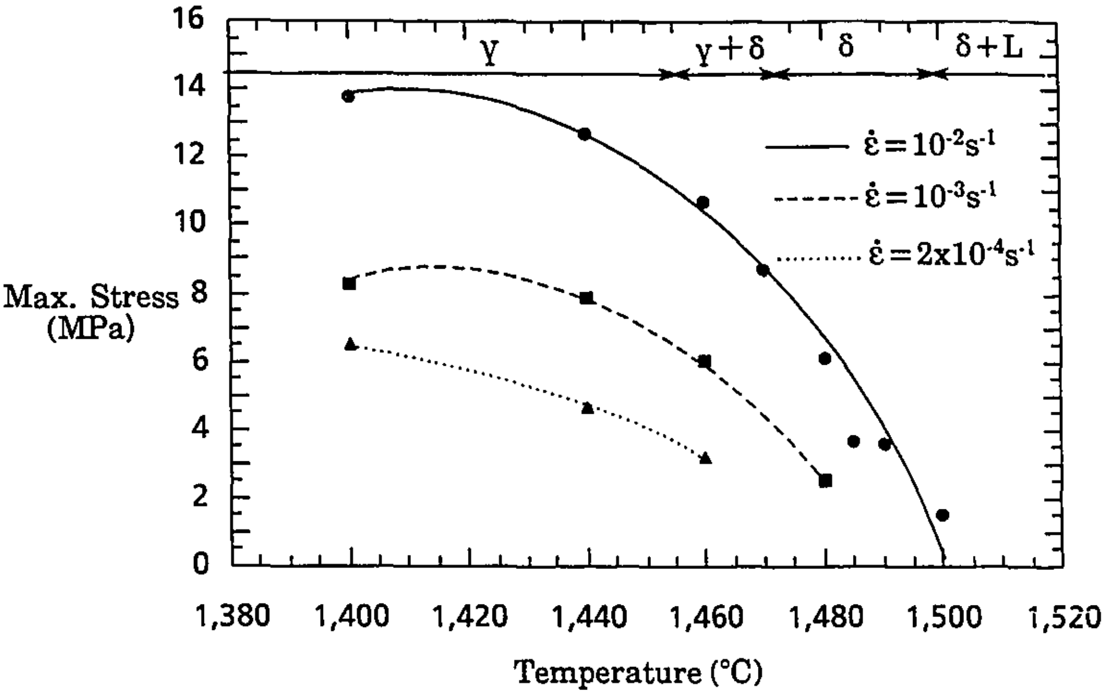

Fig. 4.50: Influence of temperature and strain rate on the maximum stress after direct heating, steel P.

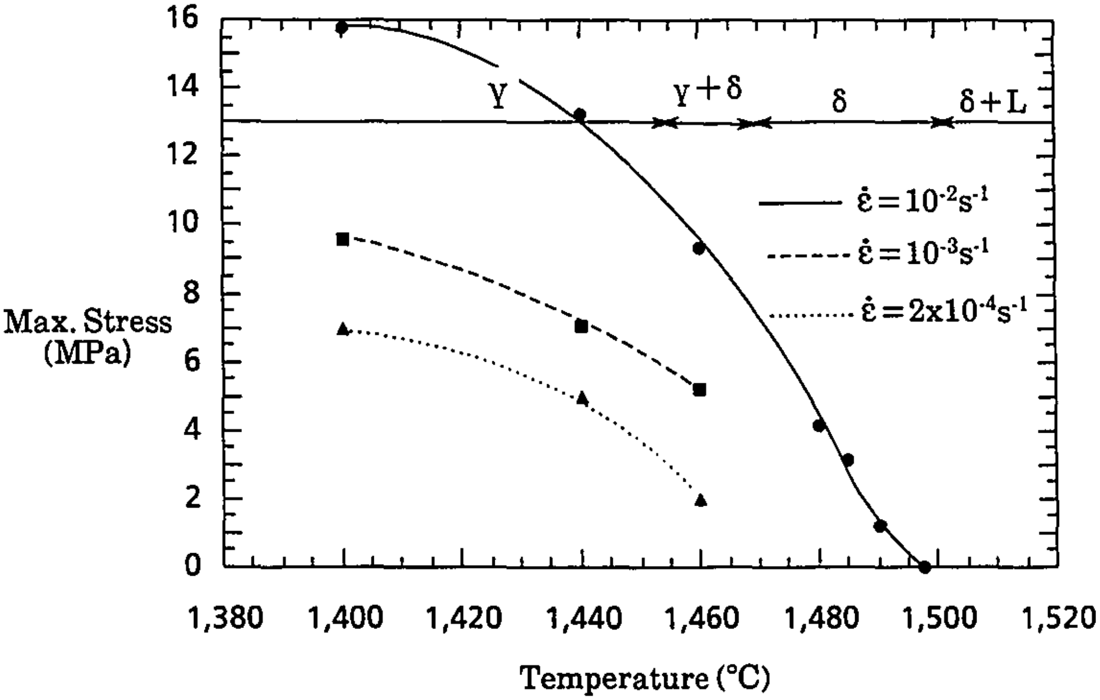

Fig. 4.51: Influence of temperature and strain rate on the maximum stress after direct heating, steel A.

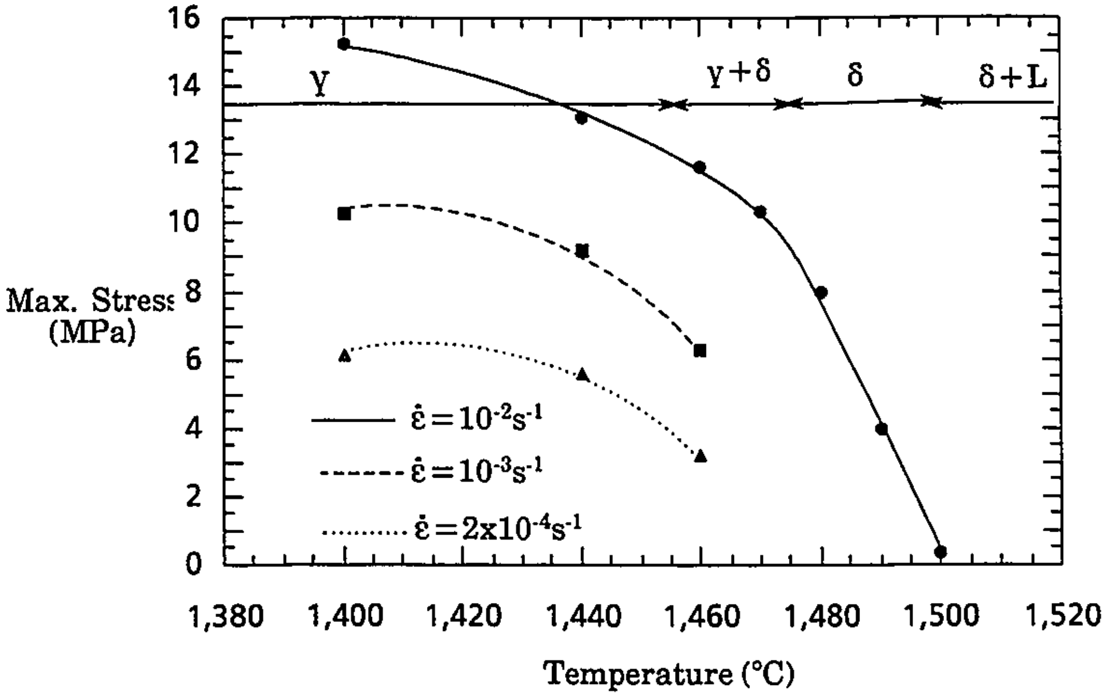

Fig. 4.52: Influence of temperature and strain rate on the maximum stress after direct heating, steel B.

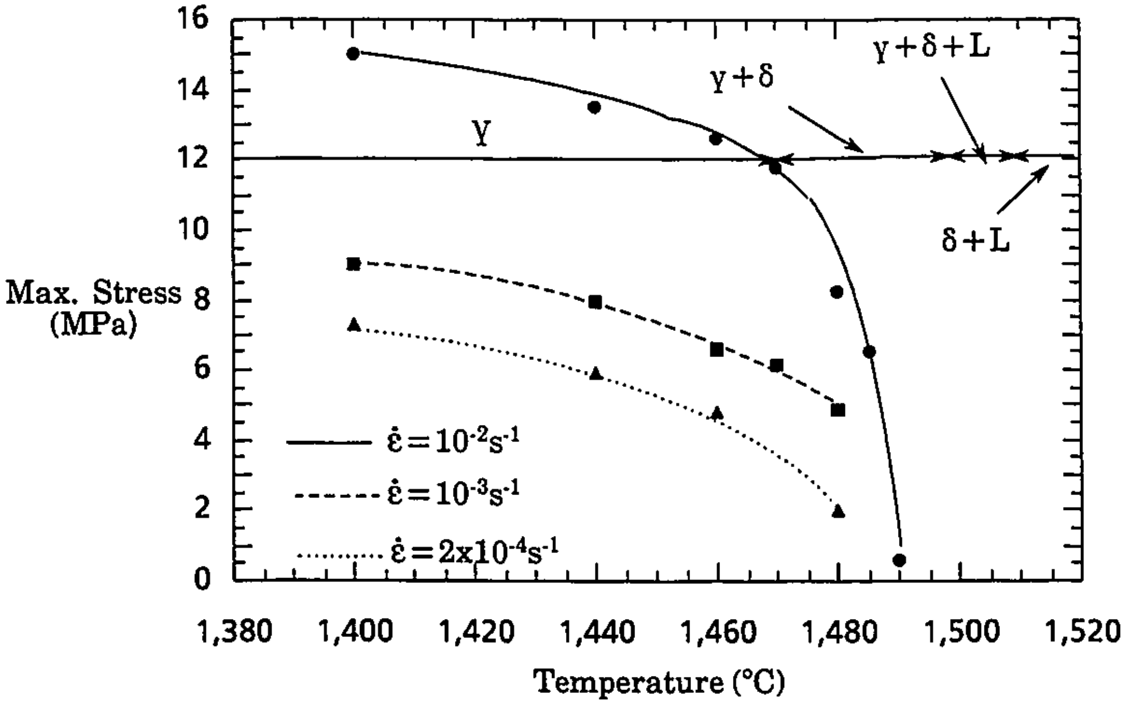

Fig. 4.53 : Influence of temperature and strain rate on the maximum stress after direct heating, steel C,

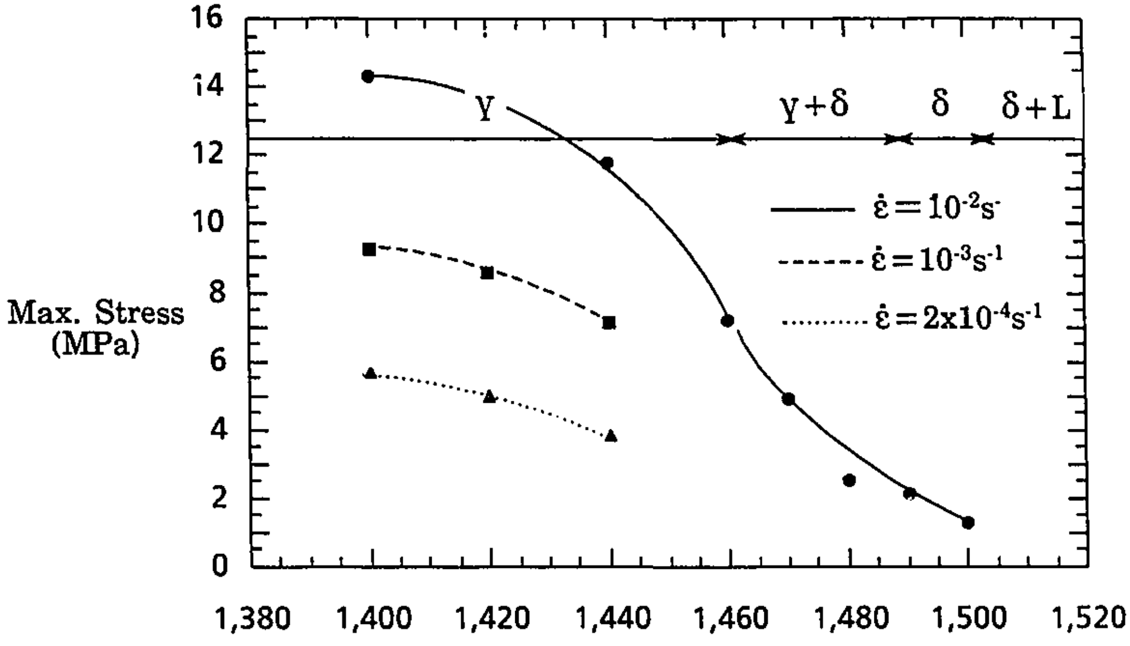

Fig. 4.54: Influence of temperature and strain rate on the maximum stress after direct heating, steel S.

steeply above this temperature. This behaviour is particularly pronounced for steel C (Fig. 4.53), where a sudden drop occurs around 1470°C.

In Table 4.4 the zero stress temperature (ZST) of each material is given and the phases which are present are also listed. It can be seen that ZST is higher than the DDS and DDE temperatures, more or less coinciding with the solidus temperatures. In Table 4.5 the maximum stress at the start and finish of embrittlement, σ_{DDS} and σ_{DDE} repectively, are listed. Note that the specimen is still load-bearing even at the temperature at the end of embrittlement (DDE).

4.2.2.6. Influence of carbon level and microalloying elements on the maximum stress

Slight differences can be seen on varying the C levels (Fig. 4.55), but no general rule can be identified at the low strain rates of 10^{-3} and $2x10^{-4}$ s^{-1} since the observed differences are within the load measurement error. However, at 10^{-2} s^{-1}, between 1430°C and 1490°C, a real stress increase is observed with increasing carbon content. Below 1430°C, there is little variation with C concentration.

The influence of microalloying elements (Fig. 4.56) is also difficult to detect, particularly for the lowest strain rates. In general it can be seen that steel S exhibits the lowest stress between 1400 and 1480°C.

4.3 METALLOGRAPHY

Typical micrographs showing the austenite grain structures revealed by hot picric acid etching are shown in Figs. 4.57 and 58 for steel P, on direct heating to 900°C and 1100°C, respectively. This grain size increase with temperature is also apparent for steel B in Figs 4.59 to 4.62. The behaviour of all the other steels is similar to steel B. Comparing P with B, it is clear that the grain size of steel P is considerably larger at all temperatures. This is probably mainly due to the presence of Ti in all steels except P. However, at low

Table 4.4

Comparison between the solidus temperature, DDS, DDE, and the zero stress temperature.*(extraploated value)

Steel	Solidus (°C)	DDS (°C)	DDE (°C)	ZST (°C)	Phase
P	1500	1476	1492.5	1500	δ+L
A	1500	1476	1496	1497.5	δ
B	1500	1470	1490	1500	δ+L
C	1497.5	1462	1480	1490	γ+δ
S	1503.5	1499	1500	1505*	δ+L

Table 4.5

Maximum stresses corresponding to DDE and DDS temperatures.

Steel	Solidus (°C)	DDS (°C)	σ_{DDS} (MPa)	DDE (°C)	σ_{DDE} (MPa)
P	1500	1476	8	1492.5	3.5
A	1500	1476	6	1496	.25
B	1500	1470	10.5	1490	4
C	1497.5	1462	12.6	1480	10
S	1503.5	1497.5	1.5	1500	1

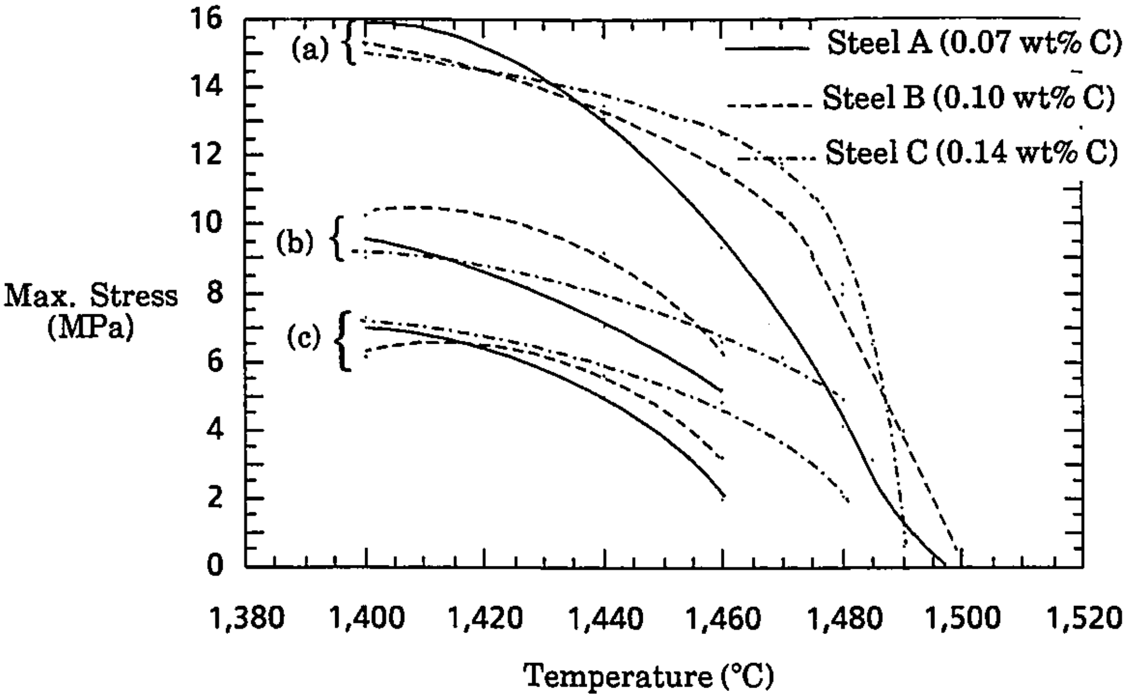

Fig. 4.55: Influence of the carbon content and strain rate on the maximum stress. (a): $\dot{\varepsilon} = 10^{-2}s^{-1}$, (b): $\dot{\varepsilon} = 10^{-3}s^{-1}$, (c): $\dot{\varepsilon} = 2x10^{-4}s^{-1}$

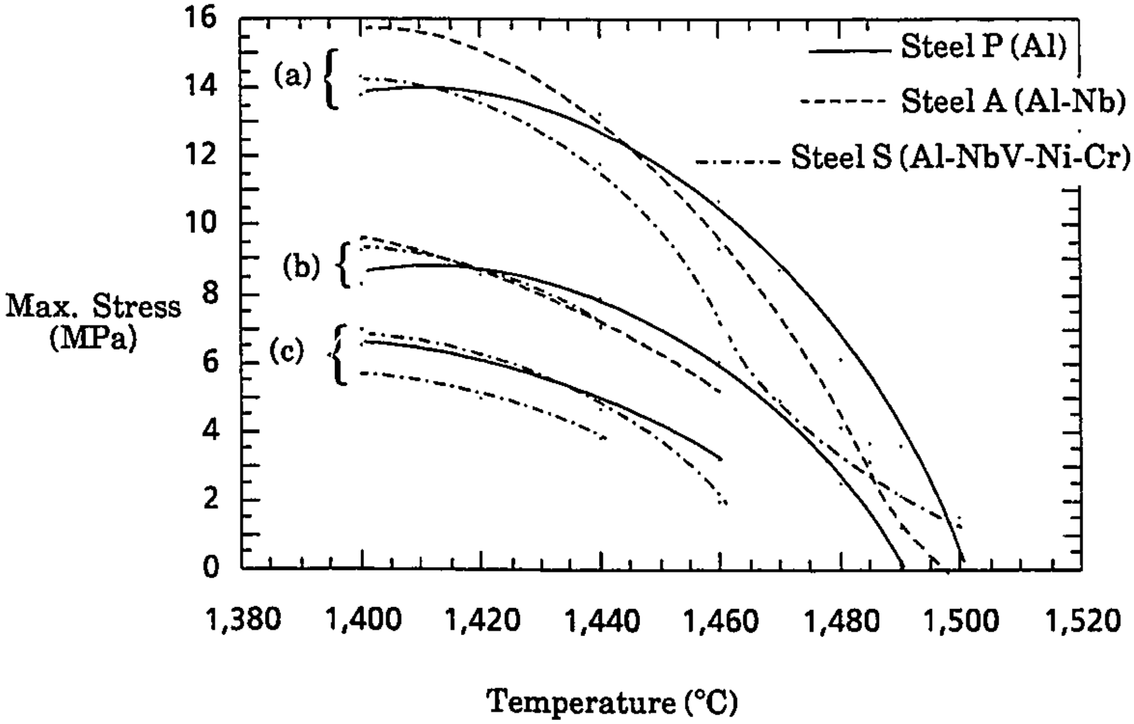

Fig. 4.56: Influence of temperature and strain rate on the maximum stress. (a): $\dot{\varepsilon} = 10^{-2}s^{-1}$, (b): $\dot{\varepsilon} = 10^{-3}s^{-1}$, (c): $\dot{\varepsilon} = 2x10^{-4}s^{-1}$

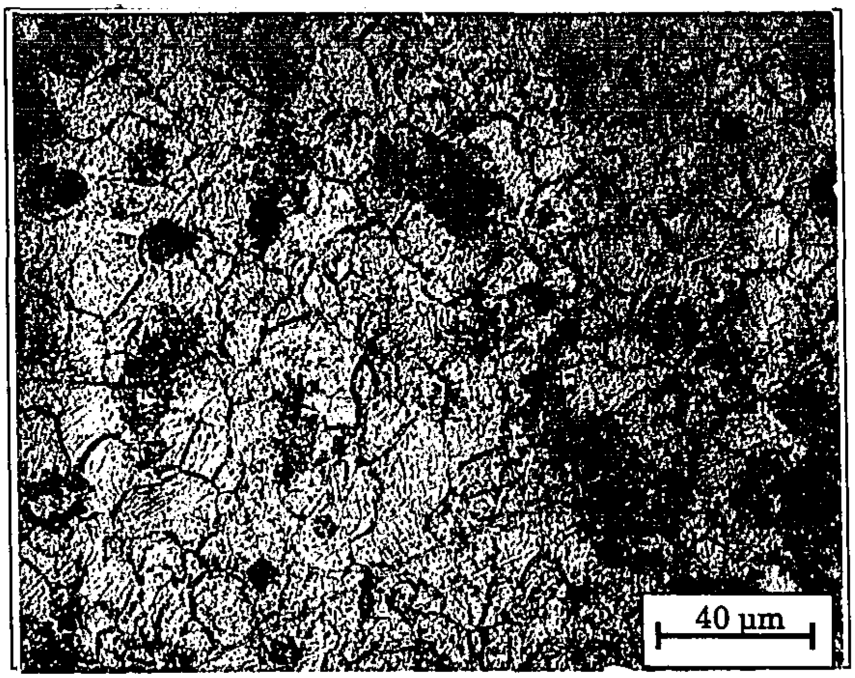

Fig. 4.57: Austenite grain size at 900°C, steel P.

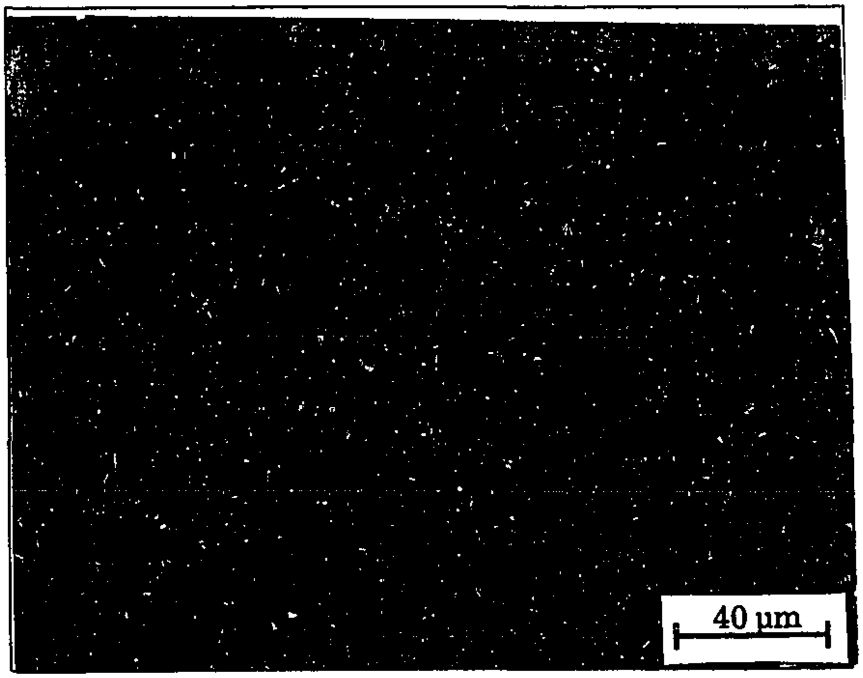

Fig. 4.58: Austenite grain size at 1100°C, steel P.

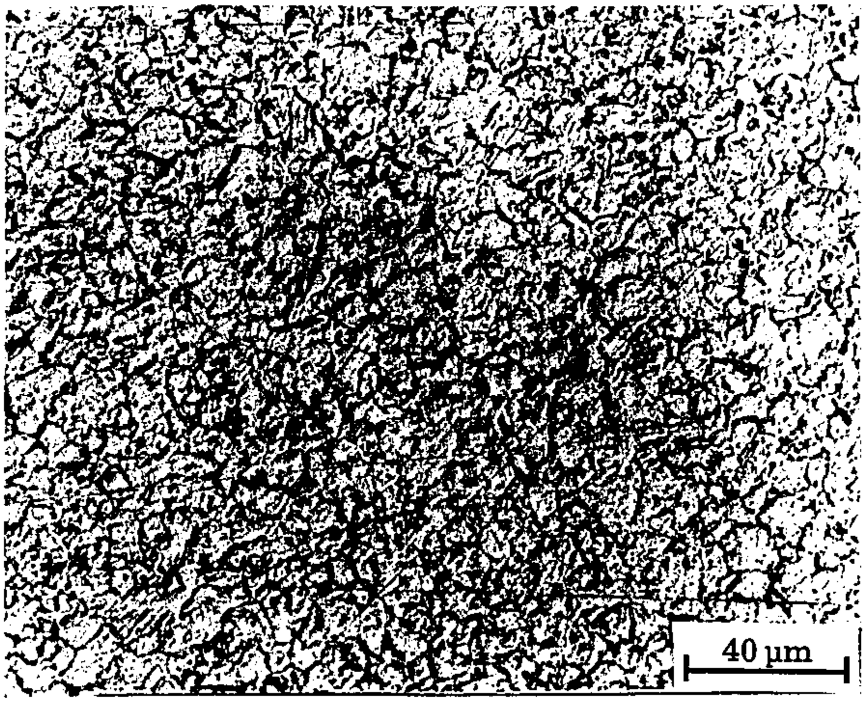

Fig. 4.59: Austenite grain size at 900°C, steel B.

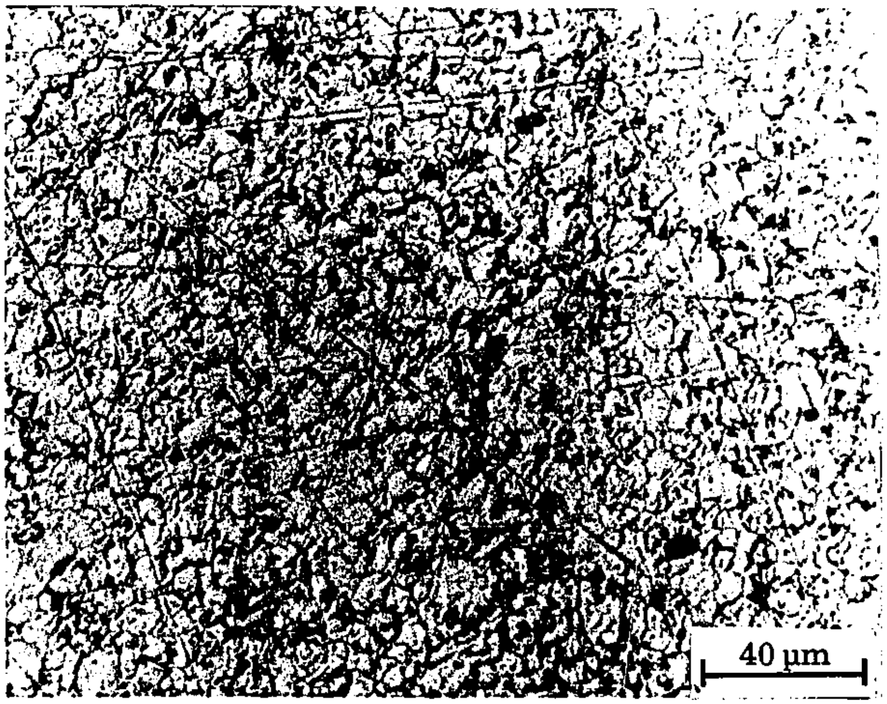

Fig. 4.60: Austenite grain size at 1000°C, steel B.

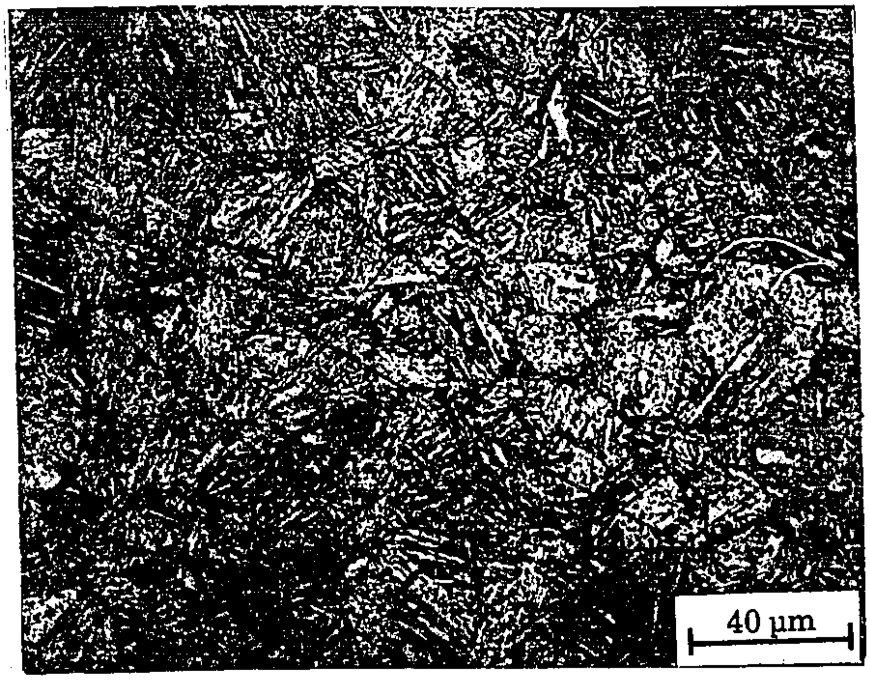

Fig. 4.61: Austenite grain size at 1190°C, steel B.

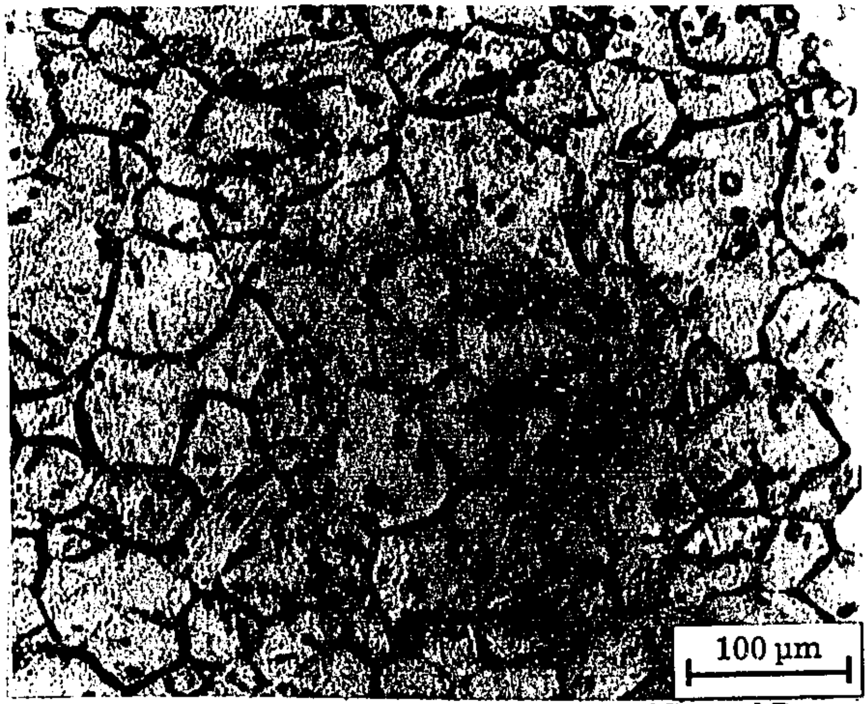

Fig. 4.62: Austenite grain size at 1330°C, steel B.

temperatures, Nb and Al also refine the austenite grains size. The full austenite coarsening behaviour from 900 to1330°C is presented in Fig. 4.63 for steel P and 4.64 for all the other grades.

The mean austenite grain size of the C-Mn-Al steel (P) increases slightly from 11.5 to 20 µm in the temperature range 900-1100°C, but rapid grain coarsening occurs between the temperatures of 1100-1200°C, where the mean grain size diameter increases from 20 to 130 µm. At 1300°C the average grain size is 475 µm, which means that the cross section of the tensile specimen is occupied by only six or seven grains.

The mean grain size of steels A, B and C, which contain Ti, Nb and Al, is relatively small at 900°C (between 6 and 8 µm), and the rate of coarsening is low up to 1200°C. Significant grain growth only takes place around 1300°C. The rate of grain coarsening varies slightly with the carbon level, steel B posessing the lowest grain size in the temperature range 900-1200°C, whereas steel A shows the highest grain coarsening rate. Steel S, has the largest grain size after the direct heat treatment, but exhibits the slowest coarsening rate such that the grain size is comparable to the other steels at 1300°C.

4.4 FRACTOGRAPHY

4.4.1 Temperature Range 800-1300°C

In this section, unless otherwise mentioned, results are for specimens deformed at the lowest strain rate in the temperature range 800-1000°C, i.e. generally corresponding to the ductility trough. Some specimens were also sectioned perpendicularly through the fracture surface. The cut face was polished to a metallographic finish, and the sub-fracture surface region examined for details of initial crack formation and propagation.

Fracture surfaces following direct heating :

At 900°C, where the reduction of area is a minimum for all the steels, the fracture surfaces display characteristics which are shown in Fig. 4.65. The fracture surface does not appear to be transgranular since neither dimples or

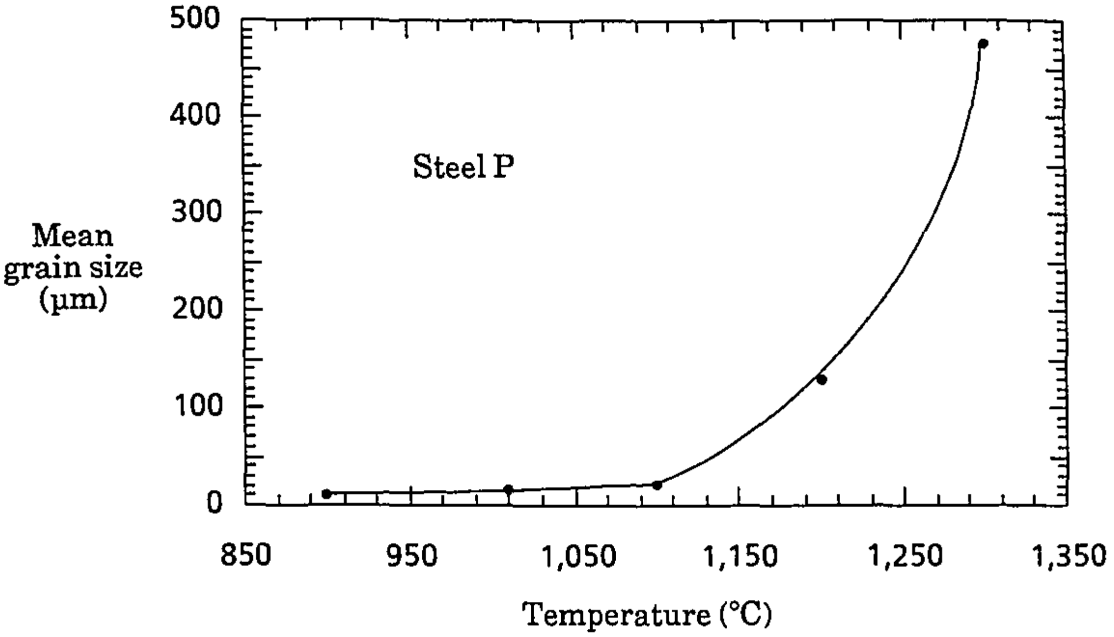

Fig. 4.63: Influence of reheating temperature on the mean austenite grain size. The heat treatment involves reheating at temperature, holding 10 min and water quenching.

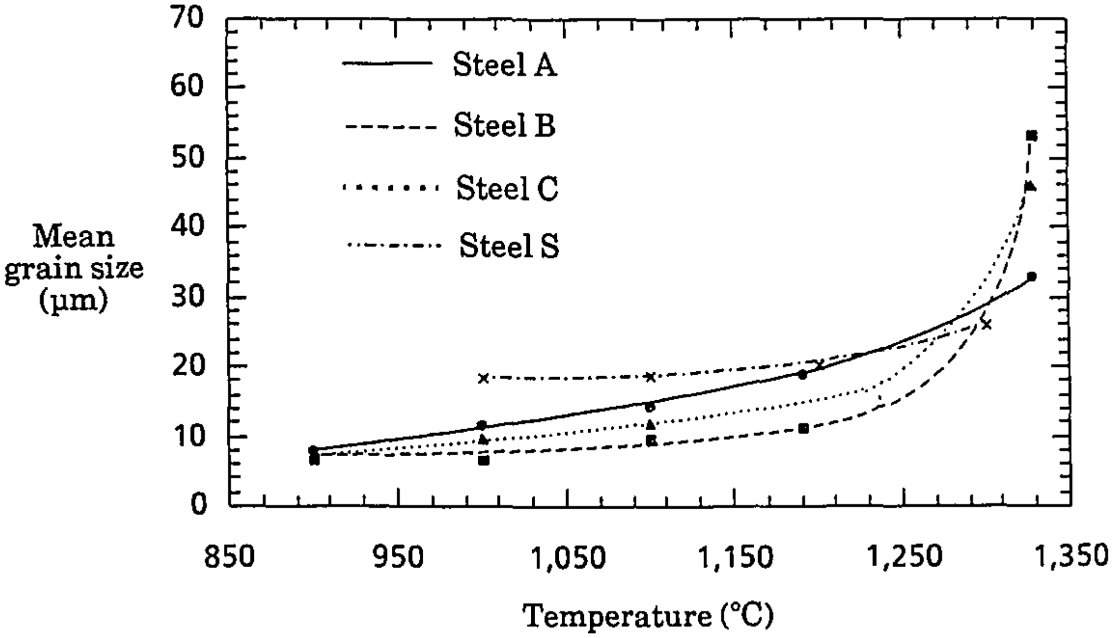

Fig. 4.64: Influence of reheating temperature on the mean austenite grain size. The heat treatment is as for Fig. 4.63.

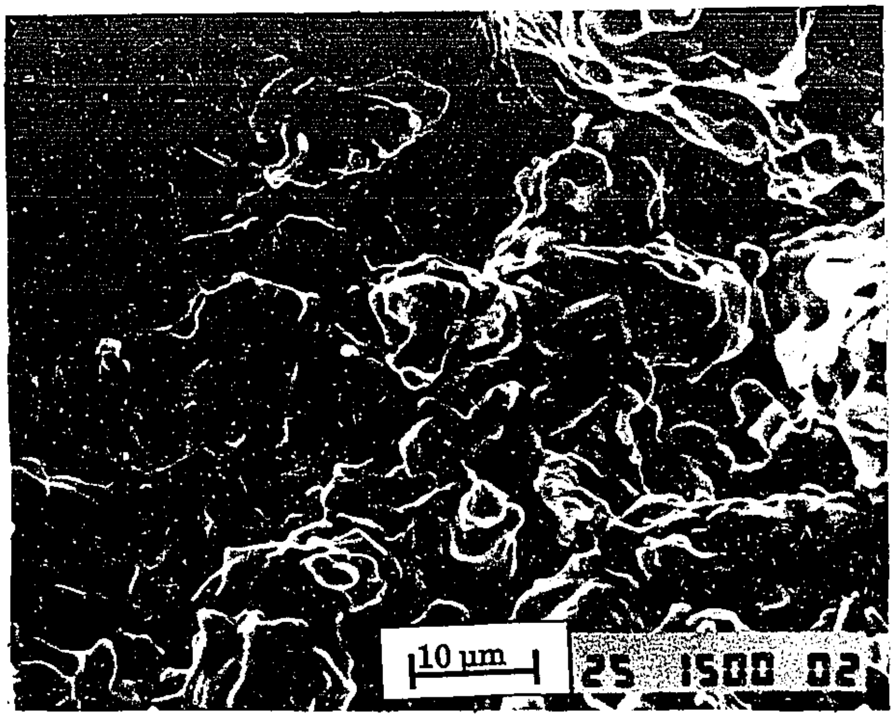

Fig. 4.65: Fracture surface of steel P, tested at 900°C following direct heating (RA = 36%).

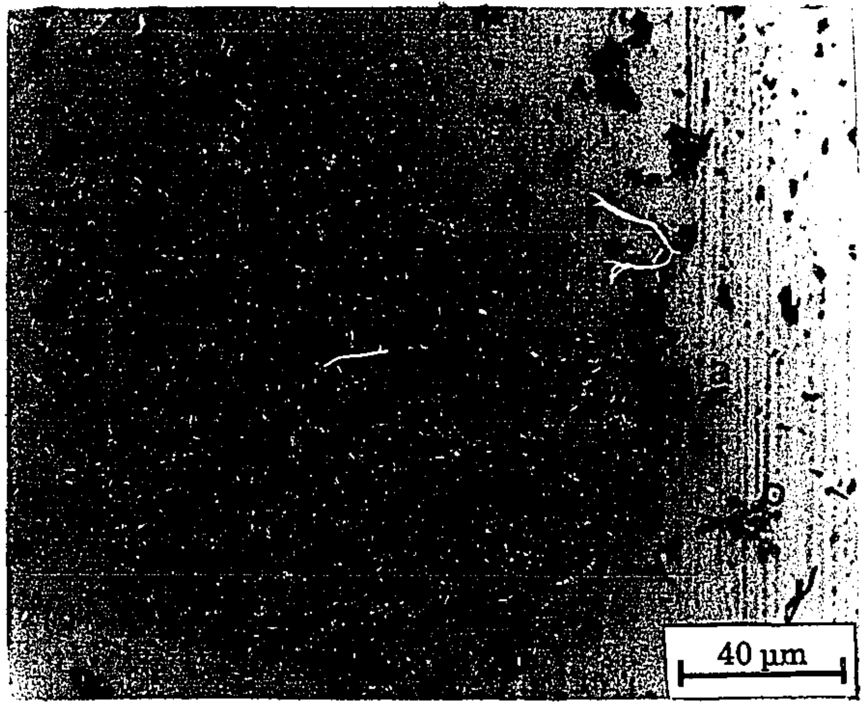

Fig. 4.66: Micrograph of a transverse section of steel A tested at 900°C following direct heating (RA = 62%).

cleavage facets are observed. The fracture mode is therefore probably intergranular. This is confirmed by noting that the size and shape of many of the features in Fig. 4.65 (shown by the arrows) are comparable to those of the austenite grains seen at 900°C (Figs. 4.57 and 4.58). In Fig. 4.65 the mean size of the 'grains' is about 12 µm; the austenite grain size at 900°C prior to deformation is between 6 and 8 µm.

Furthermore, the austenite grain morphology is generally rounded as are the features in Fig. 4.65, and examination of the fracture sub-surface shows evidence of intergranular separation (Fig. 4.66 regions a and b). An intergranular fracture mode under these test conditions is in agreement with the observations of Mintz et al [96].

At 1000°C, where dynamic recrystallization starts to occur, the reduction of area is greater than 60%. However, the appearance of the fracture surface is similar to the low ductility fracture, although some rounded voids can be seen in Fig. 4.67. The subsurface region reveals intergranular decohesion (Fig. 4.68, region a), but the density of the cracks is much lower than at 900°C. The rounded shape of some holes (region b) suggests the occurence of void dilatation, as opposed to intergranular separation.

As a result of the large ductility at 800°C for all the steels (RA>80%), the fracture surface could not be readily examined.

Fracture surfaces following annealing:

At 900°C, the appearance of the fracture surface (Fig, 4.69) of steels A, B and C is generally similar to the direct heating case. However, at this magnification individual grains cannot clearly be observed. At lower magnification features resembling grains can be identified, e.g. the arrowed regions of Fig. 4.70 indicate possible intergranular decohesion. Again the surface rougheness (Fig. 4.69) suggests some intergranular deformation prior to rupture. The examination of the polished section through the fracture surface of steel A (Fig. 4.71) shows that the fracture is still intergranular.

Since the ductility of steel S is high at 900°C, some fractographic differences were expected. The fracture surface is shown in Fig. 4.72. In this

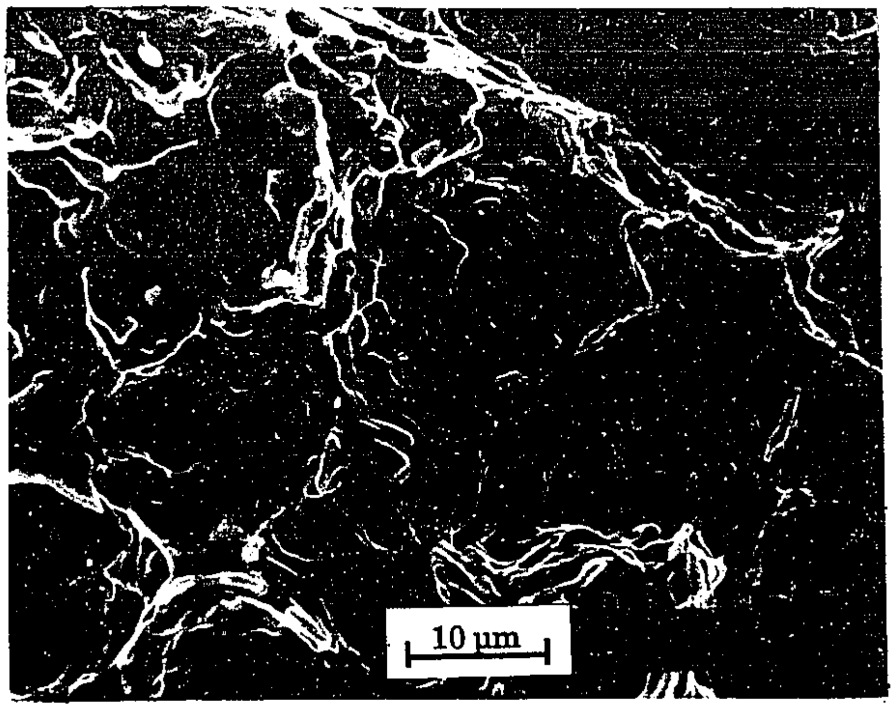

Fig. 4.67: Fracture surface, steel B deformed at 1000°C following direct heating (RA = 73%).

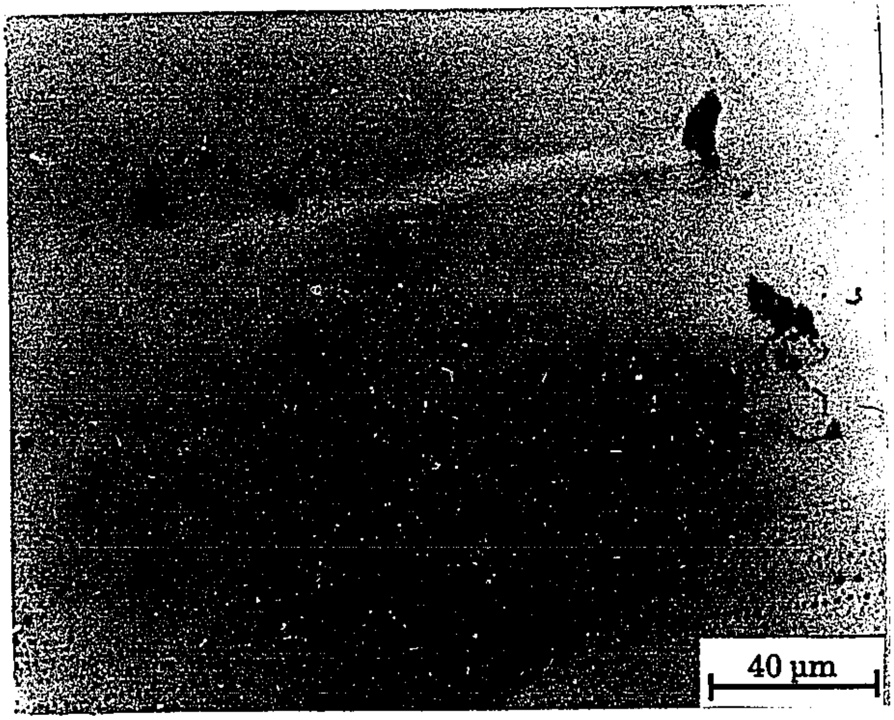

Fig. 4.68: Micrography of a transverse section of steel B tested at 1000°C following direct heating (RA = 73%).

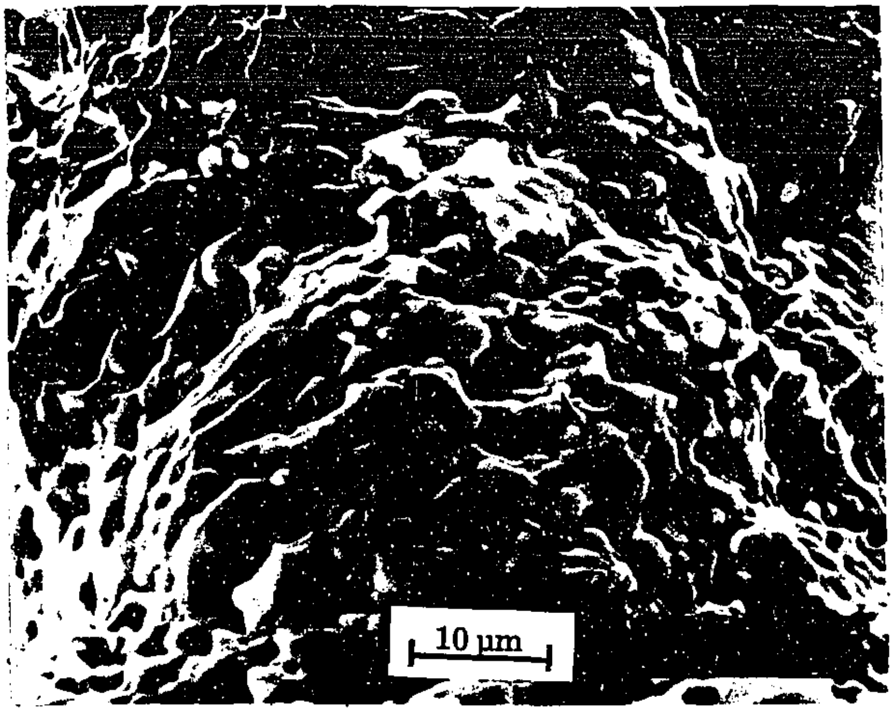

Fig. 4.69: Fracture surface, steel B deformed at 900°C following annealing, (RA = 54%).

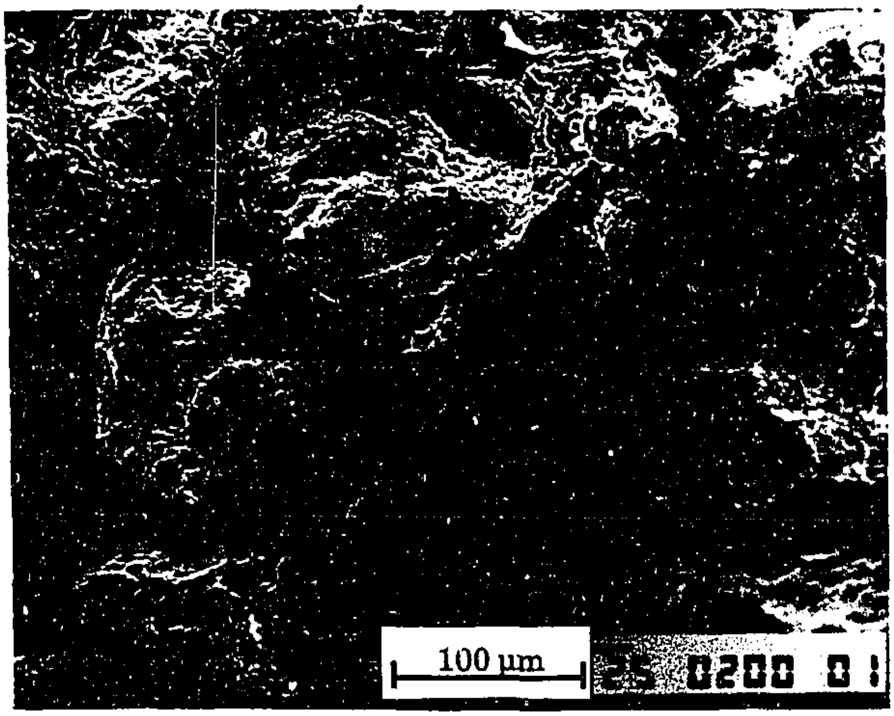

Fig. 4.70: Fracture surface, steel B deformed at 900°C following annealing, (RA = 54%) (lower magnification).

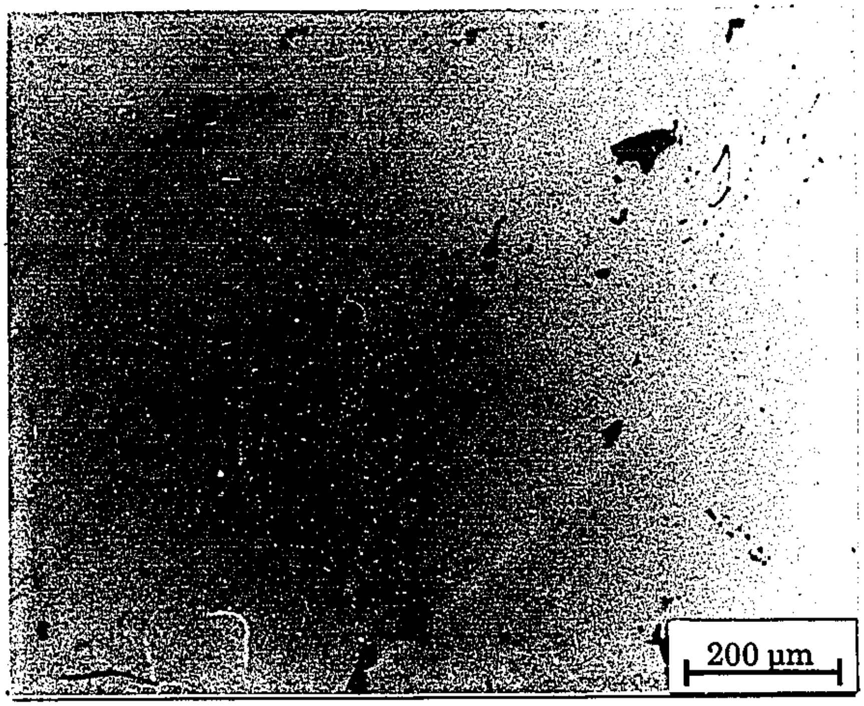

Fig. 4.71: Micrograph of a transverse section of steel A tested at 900°C following annealing (RA = 62%).

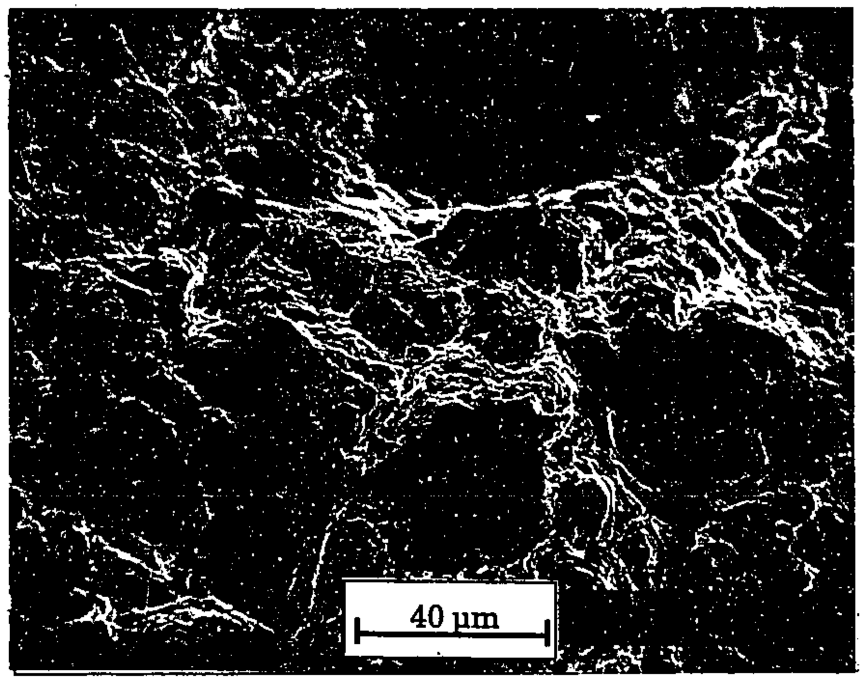

Fig. 4.72: Fracture surface of steel S tested at 900°C after annealing, (RA = 83%).

figure, intergranular cracks cannot be seen, but many shallow circular regions are observed, and, occasionally deeper voids are observed (Fig. 4.73). Sub-fracture surface examinations reveal a low density of intergranular cracks (Fig. 4.74), but there are indications that the dilatation of these cracks is greater than for steel A (Fig. 4.72). Thus for grade S, both intergranular decohesion and transgranular ductile fracture mechanisms appear to be operating.

At 800°C, for all the steels the fracture is still intergranular (Fig. 4.75), but, at higher magnification many shallow dimples are observed on surface of the grains (Fig. 4.76).

No observations were carried out on steel P since the ductility was very high in the temperature range investigated.

Fracture surfaces following sensitizing

It can be seen from Figs. 4.77 to 4.80 (corresponding to steels A, B, C, and S respectively) that sensitizing leads to a facetted fracture surface, indicative of intergranular rather than transgranular fracture. The sensitizing temperature is well above the grain coarsening temperature shown in Fig. 4.64. This corresponds well to the extremely large facet size (>100 μm) apparent in all these steels. It is also notable that grain coarsening is accompanied by an increasing tendency towards a facetted grain morphology (e.g. compare Figs. 4.59 to 4.62). These latter observations confirm the hypothesis of intergranular fracture.

The effect of C level on the fracture surface is illustrated by comparing Figs. 4.77 and 4.78 (steels A and B) with Figs. 4.79 (steel C). It can be seen that, steel C displays a much larger average facet size than grades A or B. An approximate measure of the mean diameter of the facets, using the method described in section 3.7, gives values of 150, 170, and 325 μm for steels A, B, and C, respectively. No other clear differences are apparent.

The plain C-Mn steel (P) exhibits high ductility throughout all test temperatures. The addition of Nb-Ti (steel A) as shown in Fig. 4.77, leads to large cleavage facets on the fracture surfaces at 900°C. The presence of Ni-Cr-V

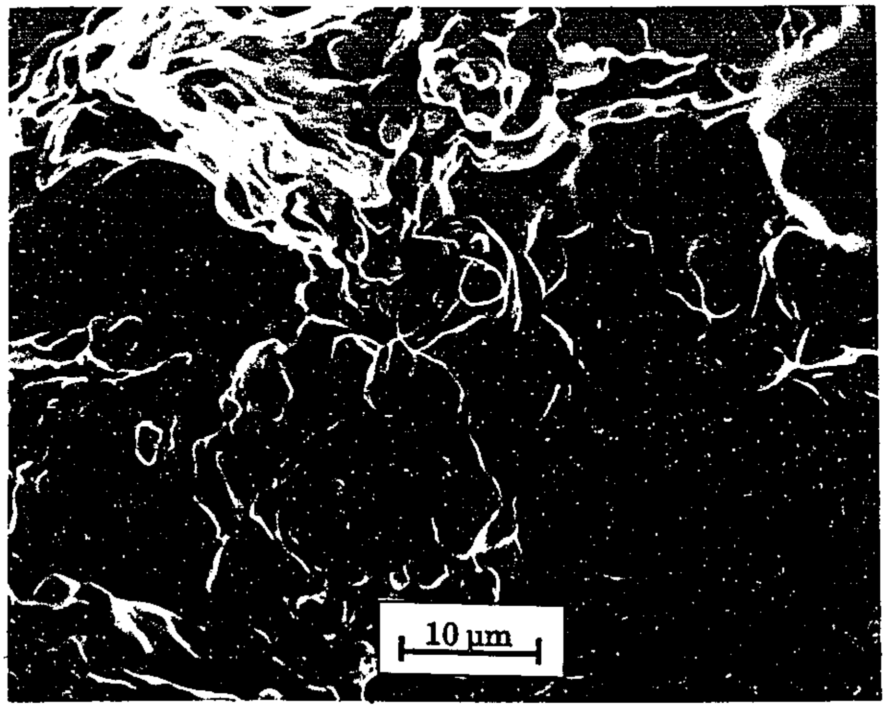

Fig. 4.73: Fracture surface of steel S tested at 900°C after annealing (RA = 83%).

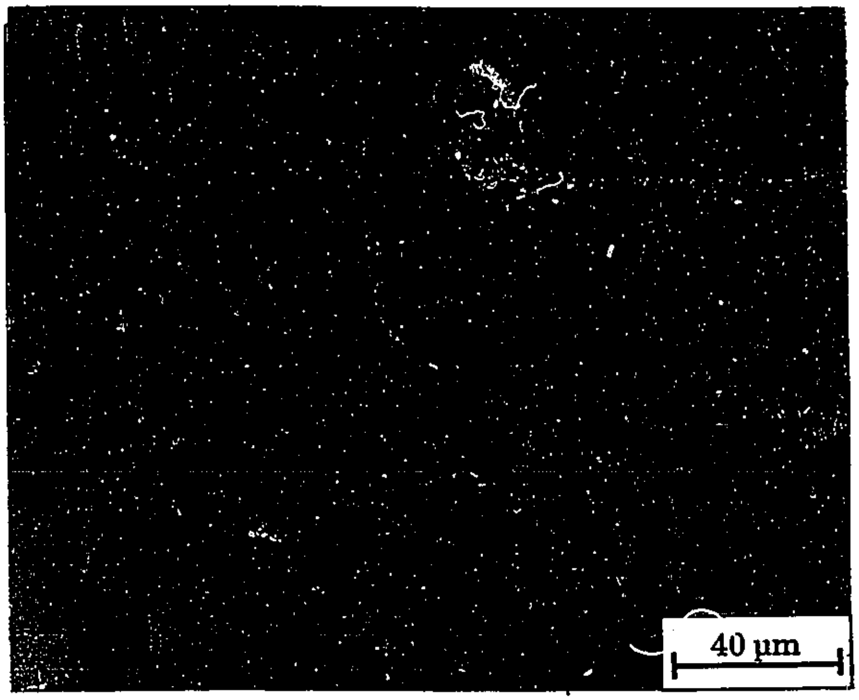

Fig. 4.74: Micrography of a transverse section of steel S tested at 900°C following annealing (RA = 83%).

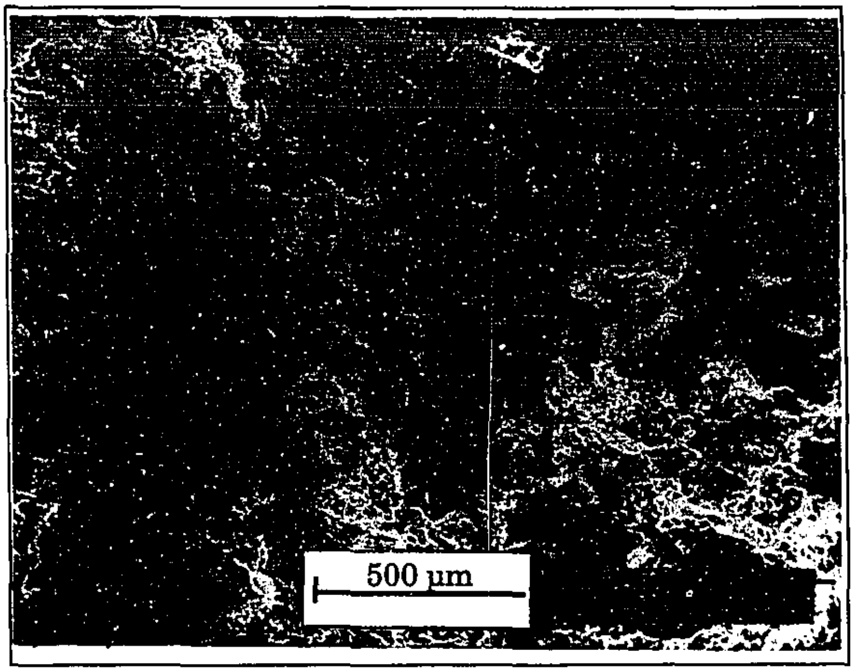

Fig. 4.75: Fracture surface of steel C at 800°C after annealing (RA = 48%).

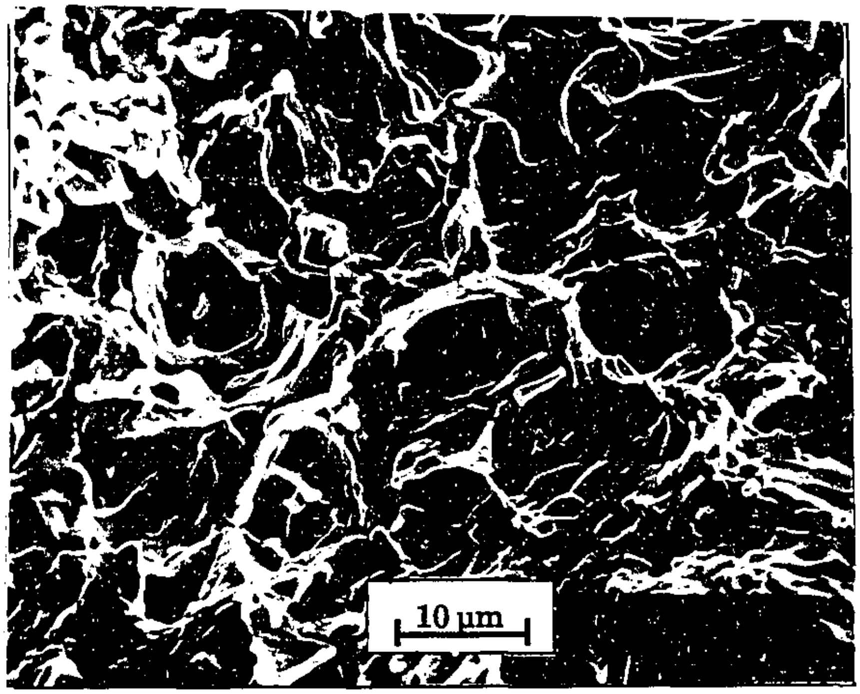

Fig. 4.76: Fracture surface of steel C at 800°C after annealing (RA = 48%) (higher magnification).

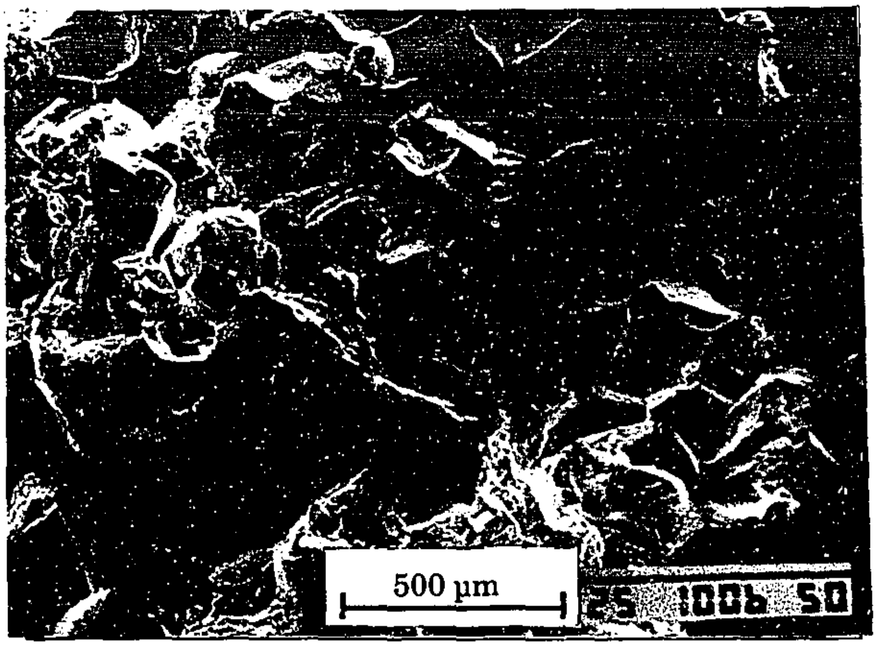

Fig. 4.77: Fracture surface of steel A, tested at 900°C following sensitization (RA = 37%).

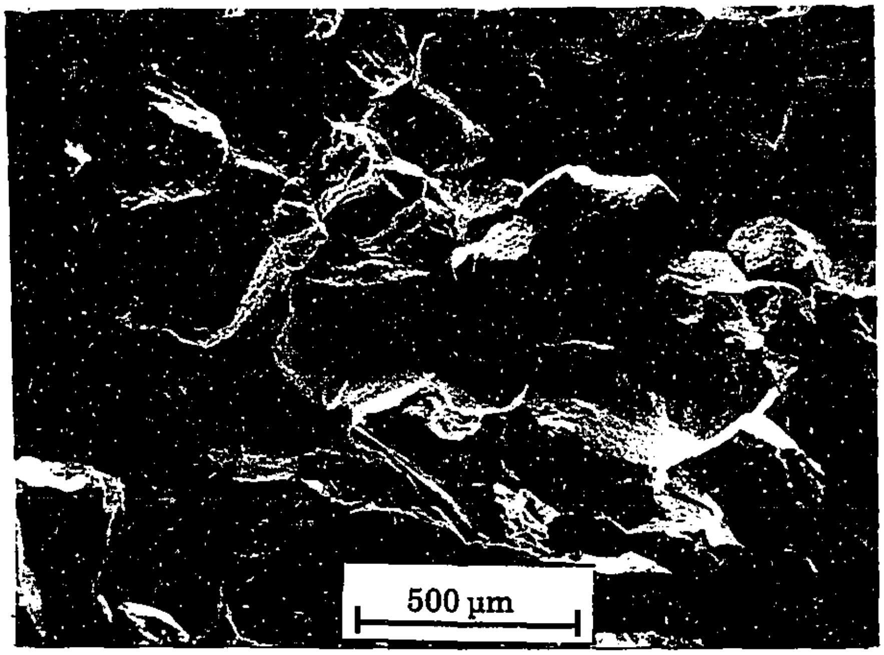

Fig. 4.78: Fracture surface of steel B, tested at 900°C following sensitization (RA = 42%).

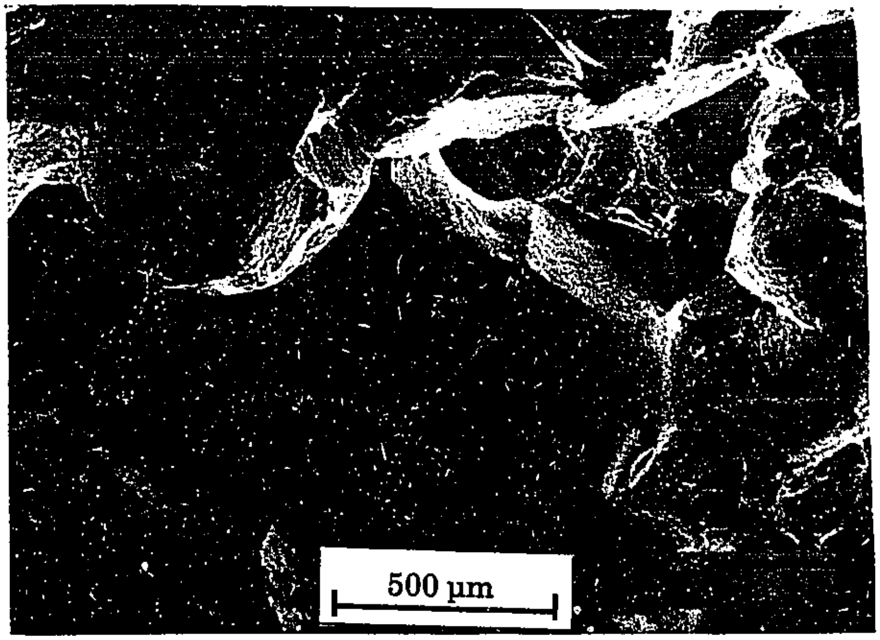

Fig. 4.79: Fracture surface of steel C, tested at 900°C following sensitization (RA = 34%).

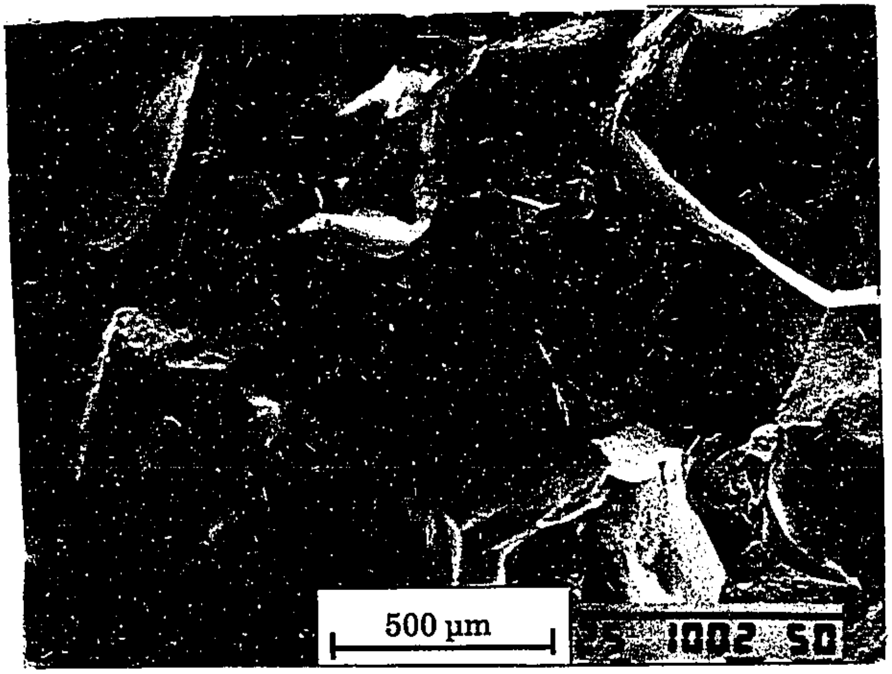

Fig. 4.80: Fracture surface of steel S, tested at 900°C following sensitization (RA = 56%).

along with NbTi (Fig. 4.80) reveals still larger facets (335 µm) at the same test temperature.

Examination of the fracture surface at higher magnification of steel B deformed at 900°C reveals two types of facet surface. The first one (Fig. 4.81), which is predominant, comprises many small voids or dimples at the surface of the grain. There are similarities between this and the fracture surface at 900°C following annealing (Fig. 4.69), but it is clear that the latter has much coarser features. The second type of facet surface (Fig. 4.82) is generally smoother, but some cracks can be observed along with relatively few fine voids.

At 800°C, the fracture surfaces of steels B and C (Figs 4.83 and 4.85, respectively) still display essentially intergranular features, but, compared to the specimens fractured at 900°C, dimples can be clearly seen, even at low magnification (Figs. 4.84 and 4.86). Finally, at 1000°C, the fracture mode (Fig. 4.87) is still intergranular but without dimpling.

4.4.2 Temperature Range 1400°C-Solidus

Fractography was conducted on all the specimens displaying brittle behavior below the measured solidus temperature. The morphologies of the fracture surfaces are shown in Figs. 4.88-4.89 (steel P) 4.90-4.93 (steel A), 4.94-4.97 (steel B), 4.98-4.101 (steel C) and 4.102-4.103 (steel S). Intergranular fracture is exhibited for all the steels and the smoothness of the surface is indicative of a solidified liquid film. In fact, features can be seen in Fig. 4.93, (arrowed) that appear to be solidified liquid film at intergranular interfaces. Examinations were carried out on samples displaying a reduction of area greater than 50%, i.e. in specimens in which a certain amount of deformation has taken place before rupture. A typical example is shown (steel B) in Figs. 4.94-4.95 revealing indications of deformation compared to those associated with lower ductility (Figs. 4.96-4.97).

The influence of carbon content on the facet size is followed in the series of fractographs, Figs. 4.90 to 4.101. The grain size remains approximately constant when the C level is increased from 0.07 (steel A) to 0.10 wt% (steel B).

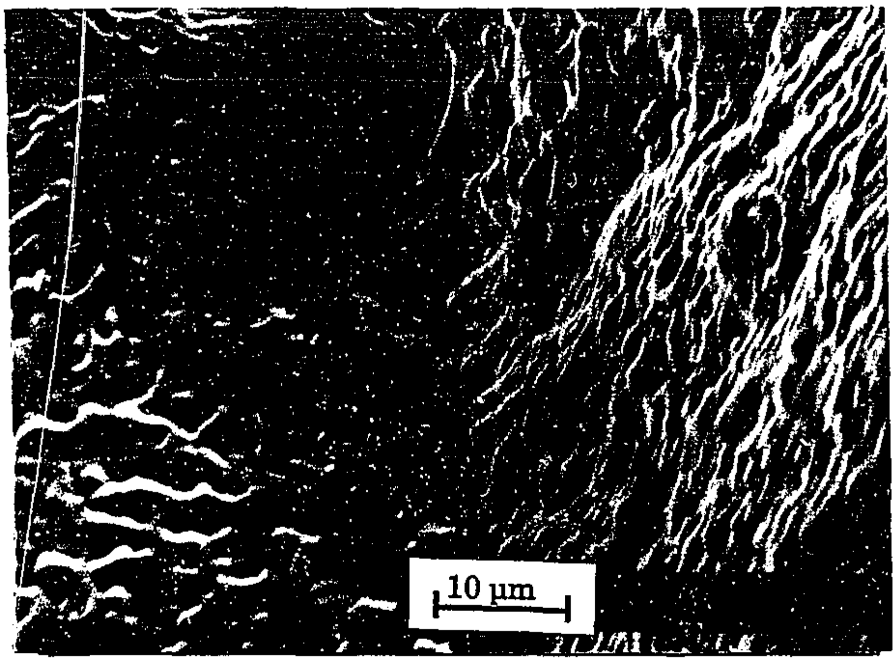

Fig. 4.81: Fracture surface of steel B, tested at 900°C following sensitization (RA = 42%).

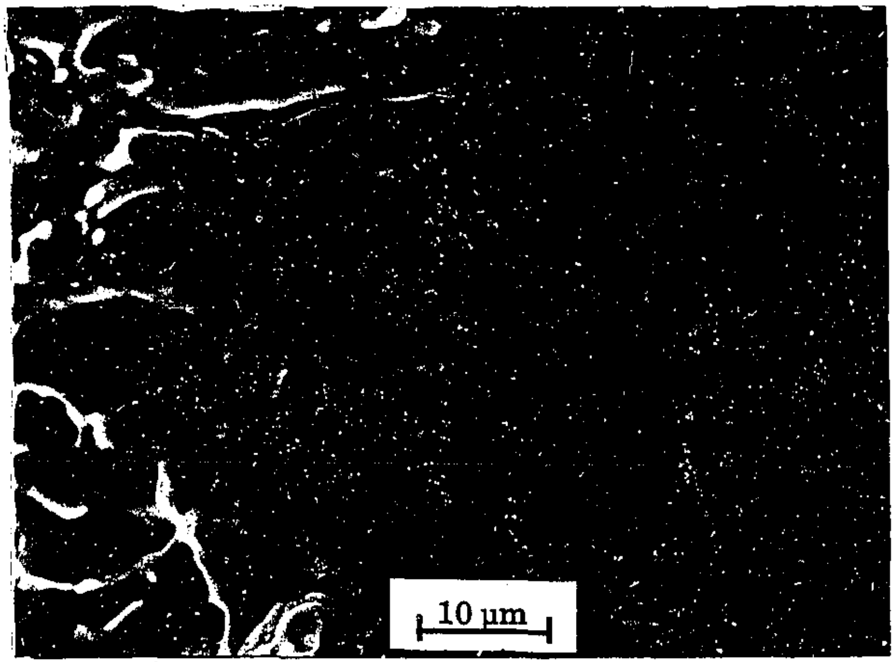

Fig. 4.82: Fracture surface of steel B, tested at 900°C following sensitization (RA = 42%).

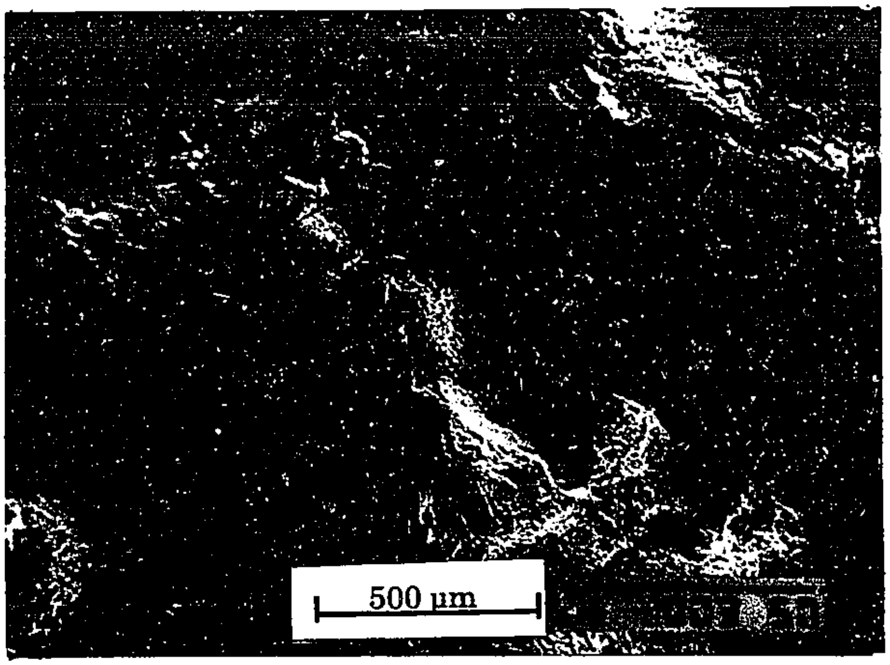

Fig. 4.83: Fracture surface of steel B, tested at 800°C following sensitization (RA = 55%).

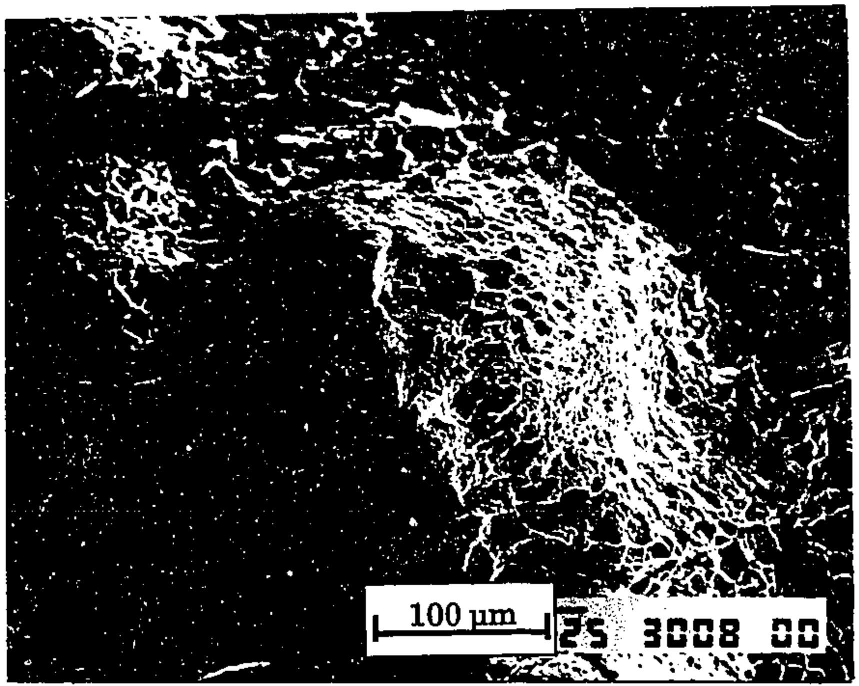

Fig. 4.84: Fracture surface of steel B, tested at 800°C following sensitization (RA = 55%) (higher magnification).

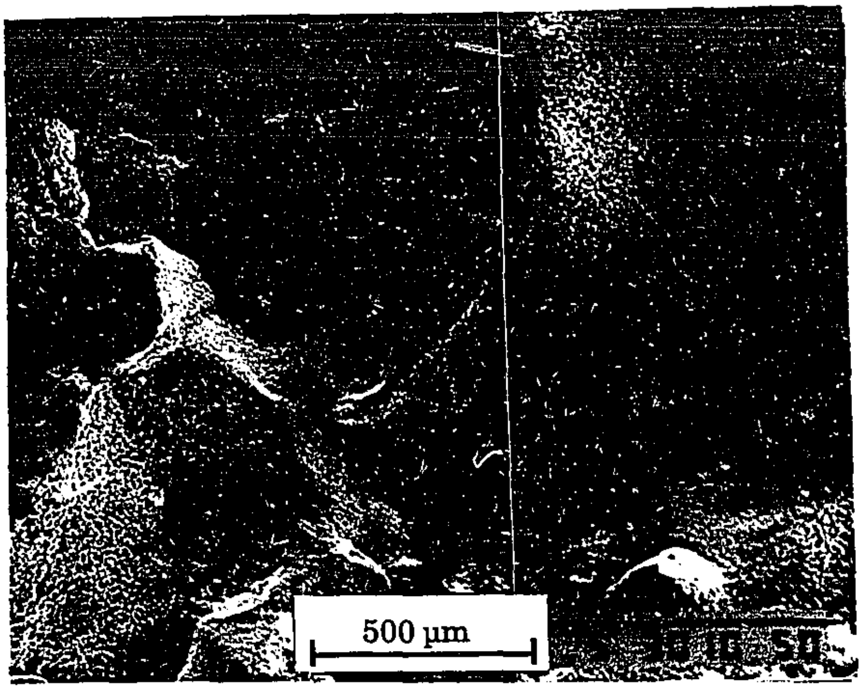

Fig. 4.85: Fracture surface of steel C, tested at 800°C following sensitization (RA = 28%).

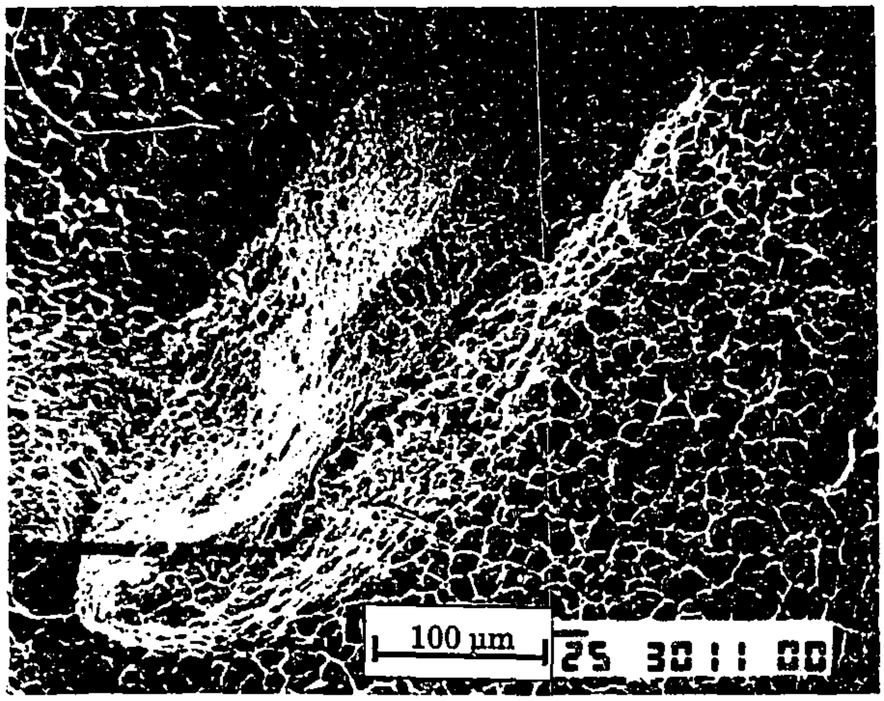

Fig. 4.86: Fracture surface of steel C, tested at 800°C following sensitization (RA = 28%) (higher magnification).

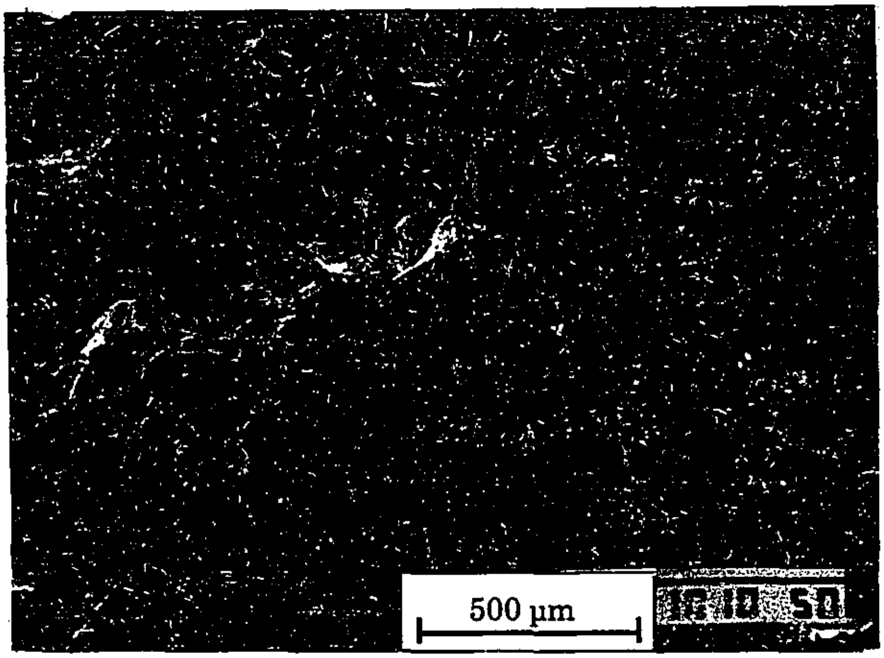

Fig. 4.87: Fracture surface of steel A, tested at 1000°C following sensitization (RA = 66%).

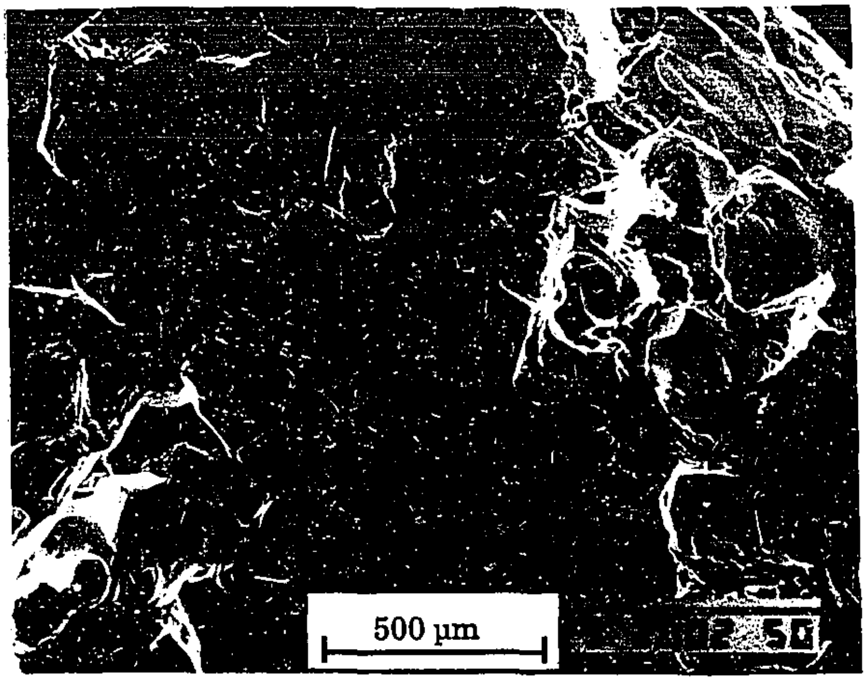

Fig. 4.88: Fracture surface of steel P, tested at 1487.5°C (RA=72%).

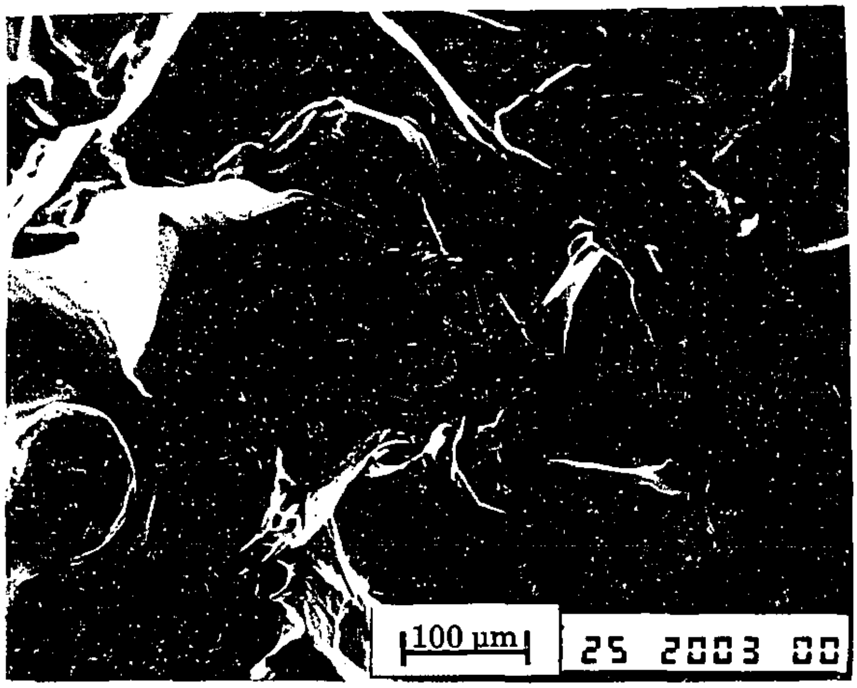

Fig. 4.89: Fracture surface of steel P, tested at 1487.5°C (RA=72%) (higher magnification).

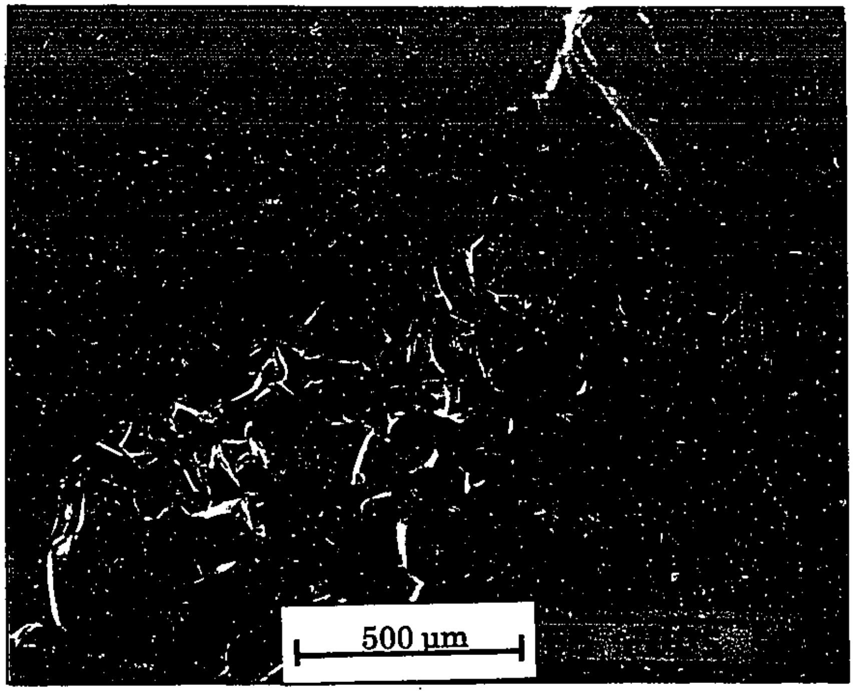

Fig. 4.90: Fracture surface, steel A deformed at 1485°C (RA = 62%).

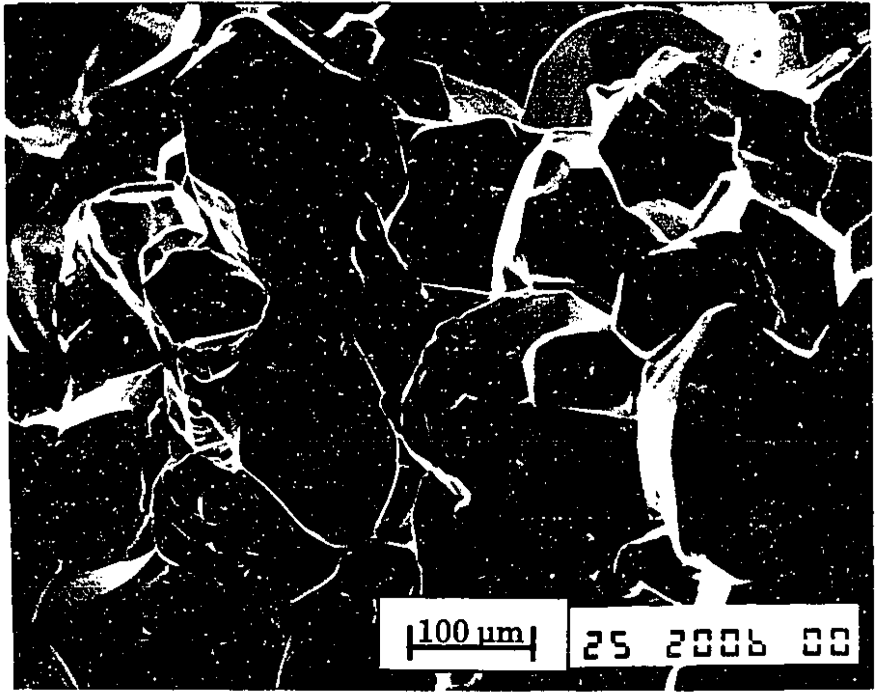

Fig. 4.91: Fracture surface, steel A deformed at 1485°C (RA = 62%) (higher magnification).

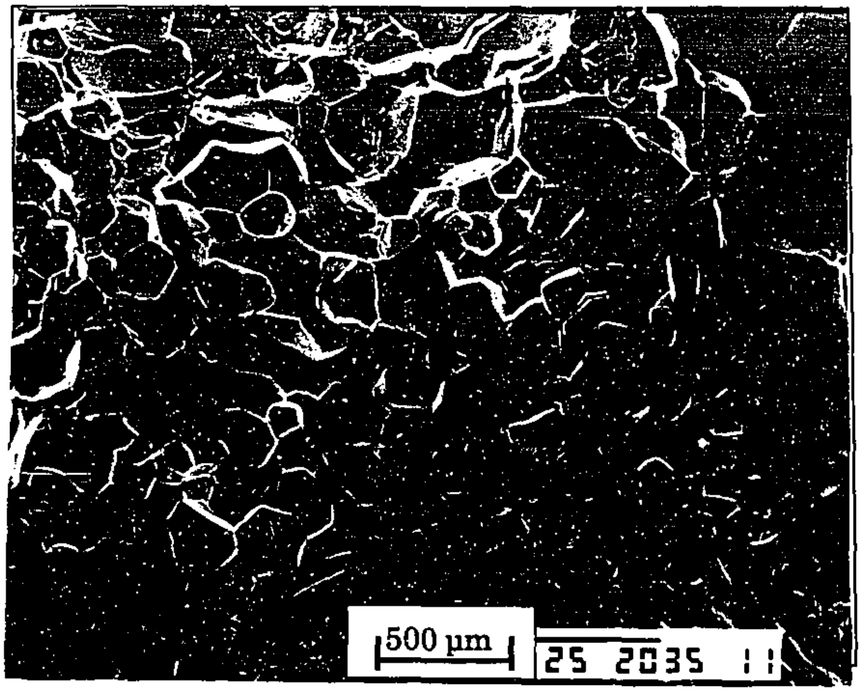

Fig. 4.92: Fracture surface, steel A deformed at 1495°C (RA=10%).

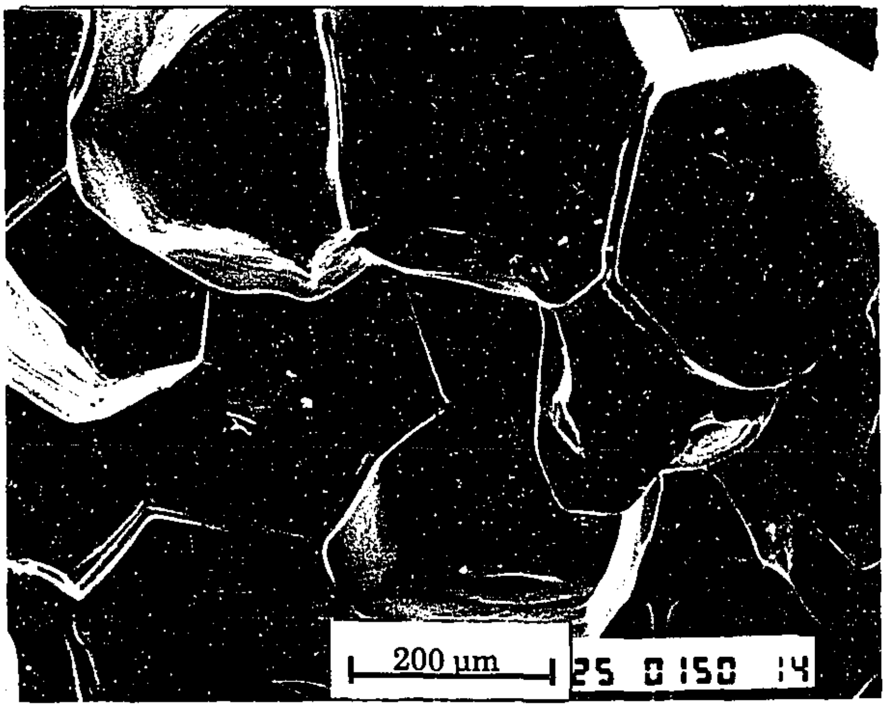

Fig. 4.93: Fracture surface, steel A deformed at 1495°C (RA=10%) (higher magnification).

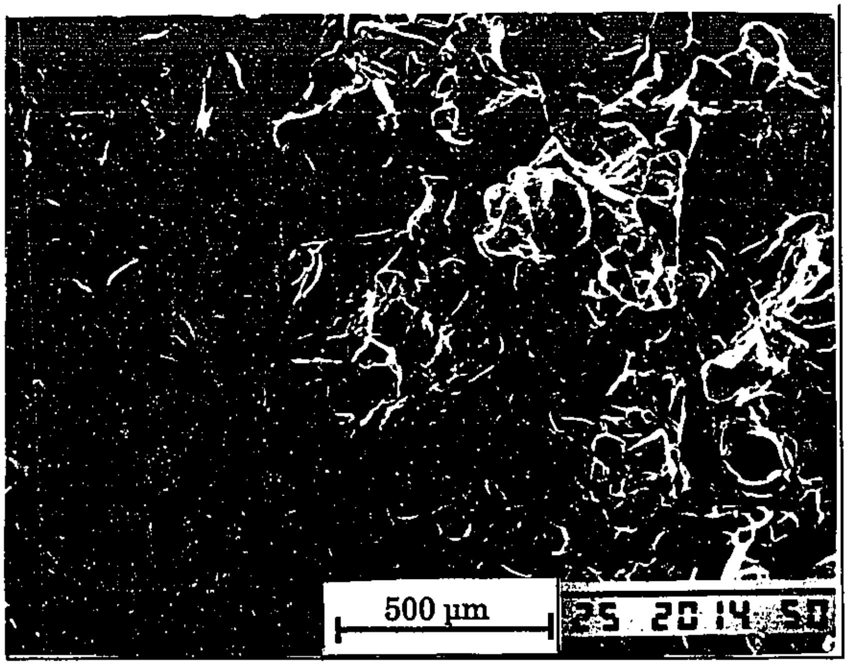

Fig. 4.94: Fracture surface, steel B deformed at 1485°C (RA = 69%).

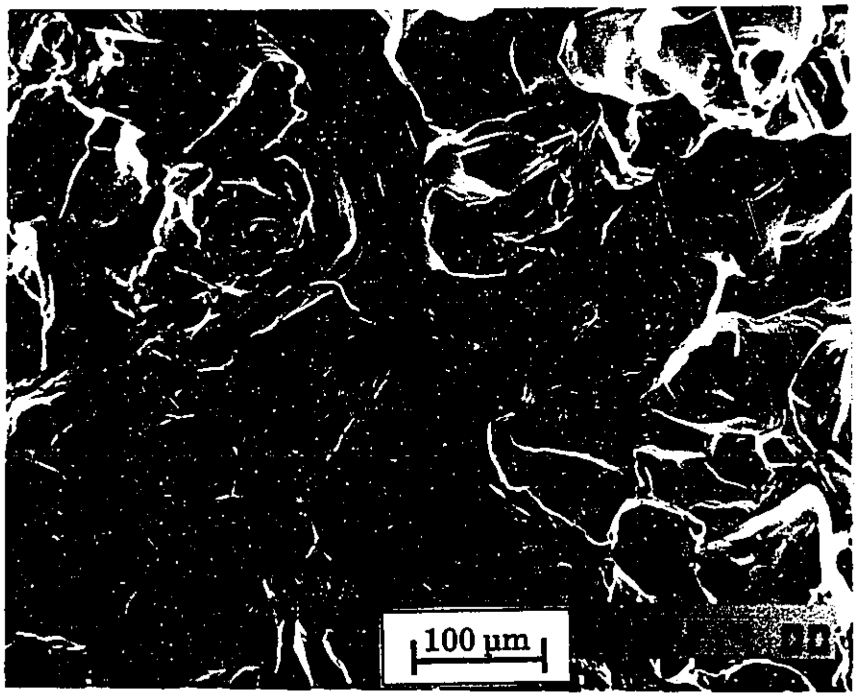

Fig. 4.95: Fracture surface, steel B deformed at 1485°C (RA = 69%) (higher magnification).

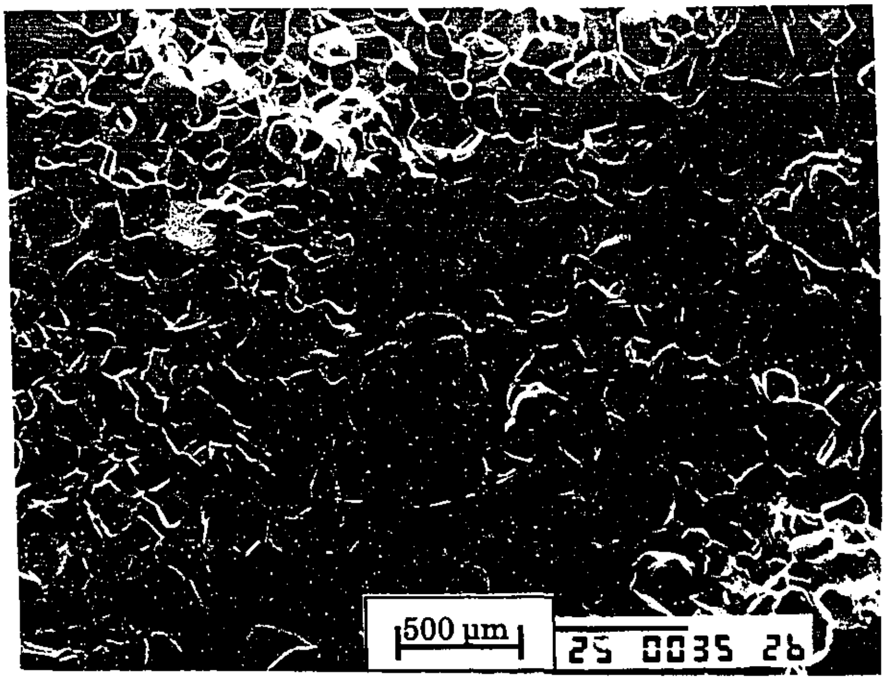

Fig. 4.96: Fracture surface, steel B deformed at 1490°C (RA = 28%).

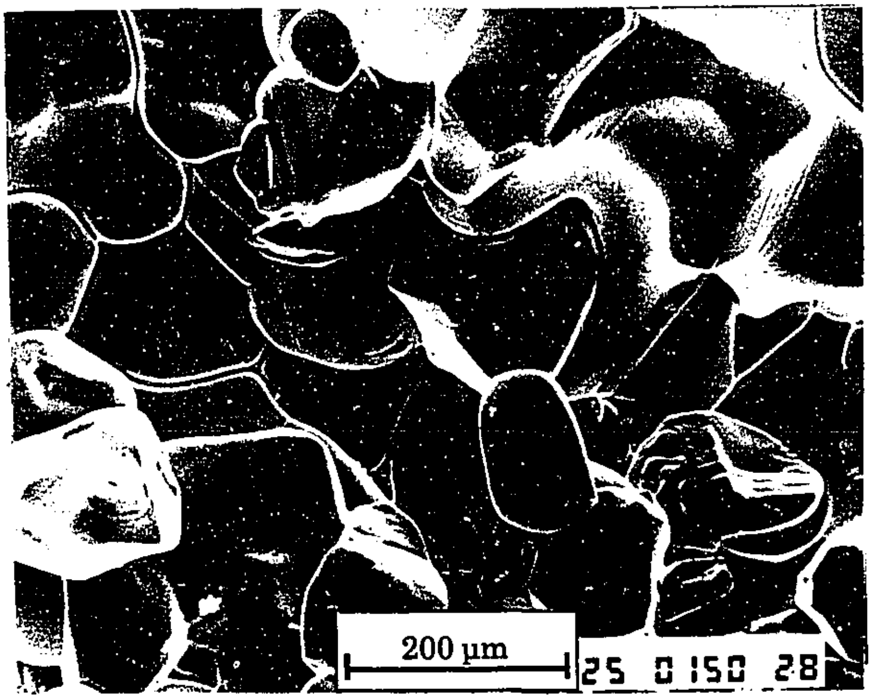

Fig. 4.97: Fracture surface, steel B deformed at 1490°C (RA = 28%) (higher magnification).

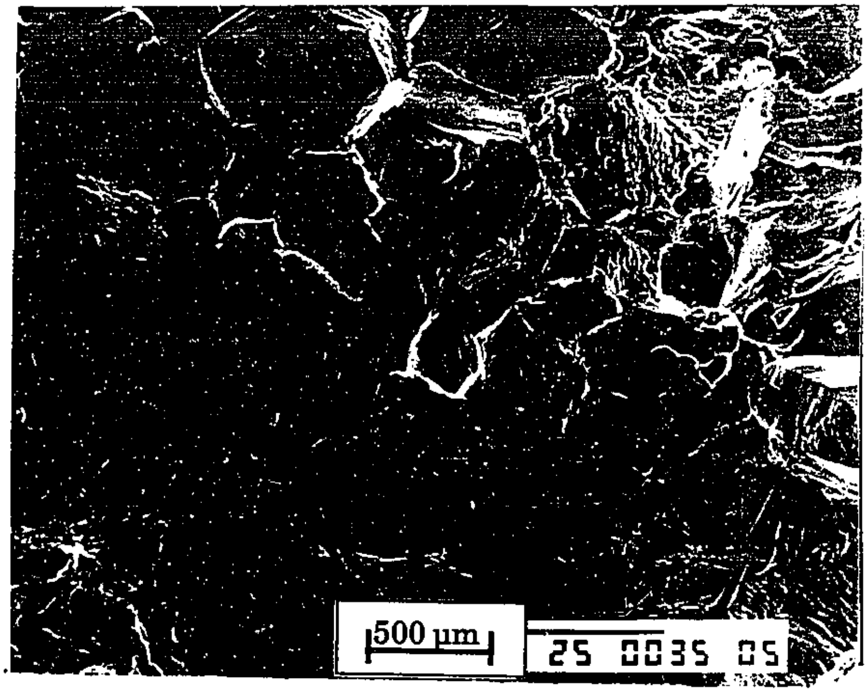

Fig. 4.98: Fracture surface of steel C, tested at 1475°C (RA = 72%).

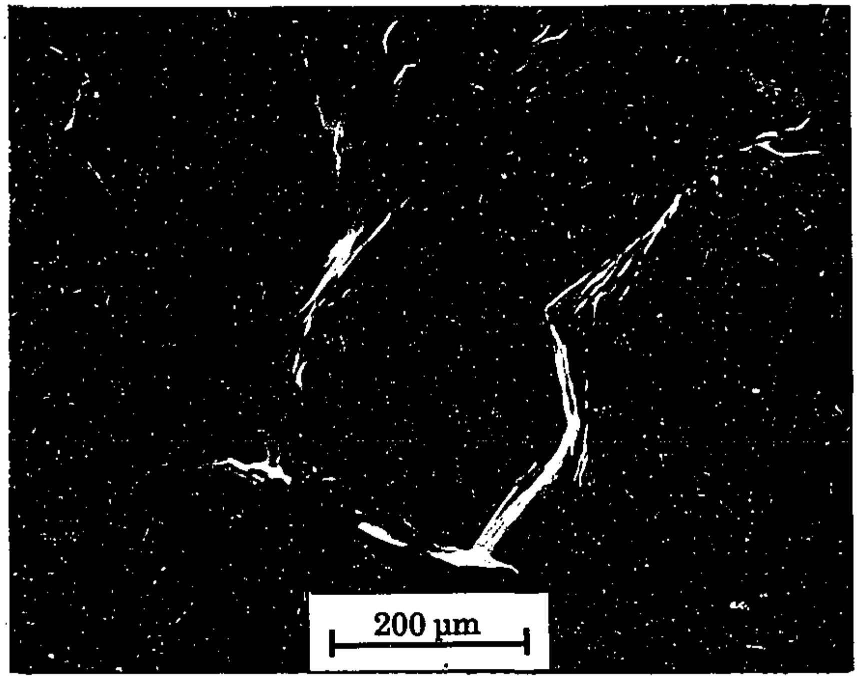

Fig. 4.99: Fracture surface of steel C, tested at 1475°C (RA = 72%) (higher magnification).

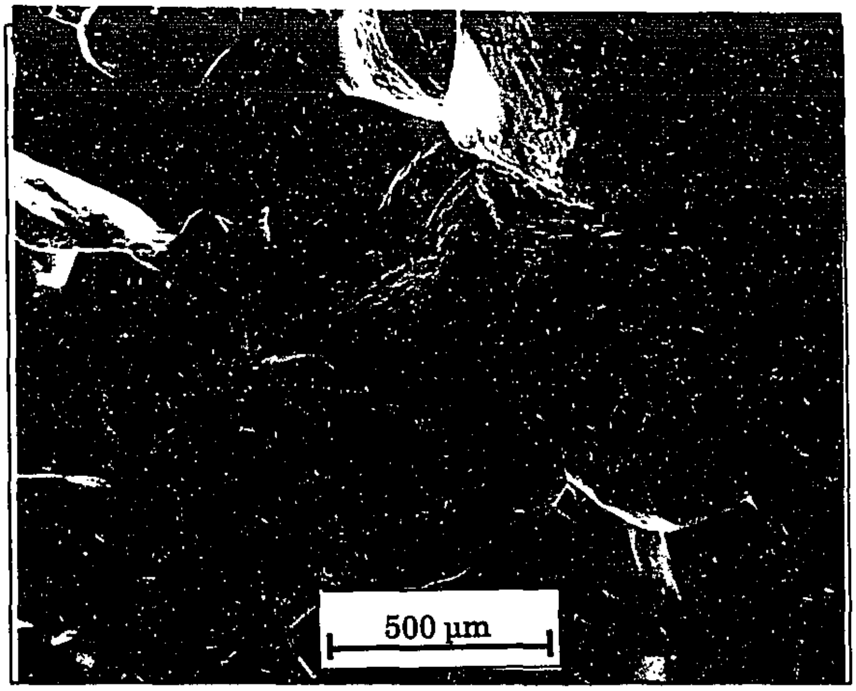

Fig. 4.100: Fracture surface of steel C, tested at 1480°C (RA = 0%).

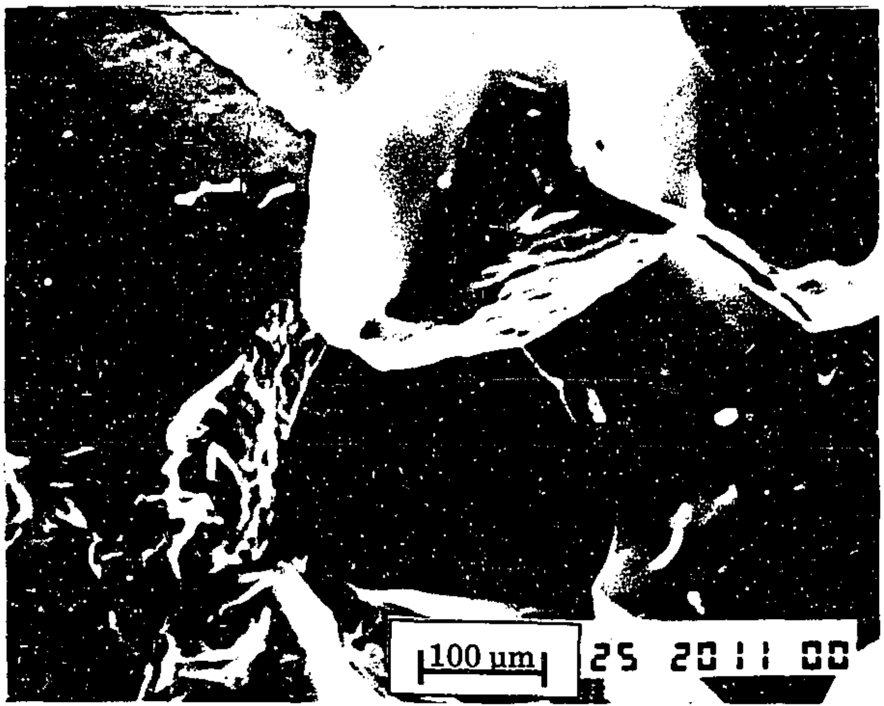

Fig. 4.101: Fracture surface of steel C, tested at 1480°C (RA = 0%) (higher magnification).

For steel A (Figs.4.90-4.93) the diameters of the facets are between 110 - 185 µm and 110 µm for steel B (Figs. 4.94-4.97). For grade C (0.14 wt%), the diameters were found to be between 275 and 350 µm (Figs. 4.98-4.101). These values are comparable to those observed in the fracture surfaces of the sensitized specimens tested at 900°C. Note that, steel C is the only material where the fracture facets display both rough and smooth surfaces (regions a and b of Fig. 4.99).

The only significant influence that microalloying elements have on the fracture surface characteristics is facet size. The addition of Nb-Ti to steel P (Figs. 4.88-4.89) appears to have a small influence on the facet size (Figs .4.90-4.93) which remains approximately constant between and 110 - 185 µm. However, the addition of Ni/Cr/V and/or the lower sulfur level in steel S leads to an increase of the grain size to approximately 250 µm, (Figs. 4.102-4.103).

4.5 AUGER ELECTRON SPECTROSCOPY

Auger electron spectra can be presented either by the energy distribution function N(E) versus E or by the differential curve dN(E)/dE versus E, where E is the energy of the Auger electrons emitted from the surface and N(E) is the intensity of the Auger signal for the energy E. The 'derivative' mode (dN(E)/dE versus E) is preferred because the Auger peaks are more clearly revealed. An example of a spectrum generated by the 'derivative' mode for steel C after 10 minutes of ion sputtering is given in Fig. 4.104

The fracture surface of steel C (Fig. 4.100) deformed at high temperatures (1480°C) revealed the presence of iron (matrix), oxygen, carbon and sulfur (Fig. 4.104). The carbon peak can be attributed either to the general atmospheric contamination or to segregation. The oxygen peak, which can be seen even after long etching times, was probably due to sample oxidation during storage. The fact that a relatively intense oxygen peak was detected even after long ion sputtering times could be ascribed to the strong affinity of this element with iron, i.e. the oxygen was not sputtered away, but tended to immediately reform as some iron-oxygen 'compound'. Nitrogen was also detected and can be due to a micro leak in the apparatus.

A semi-quantitative method was used to calculate the approximate atomic concentration of the elements which are present at the surface, i.e.:

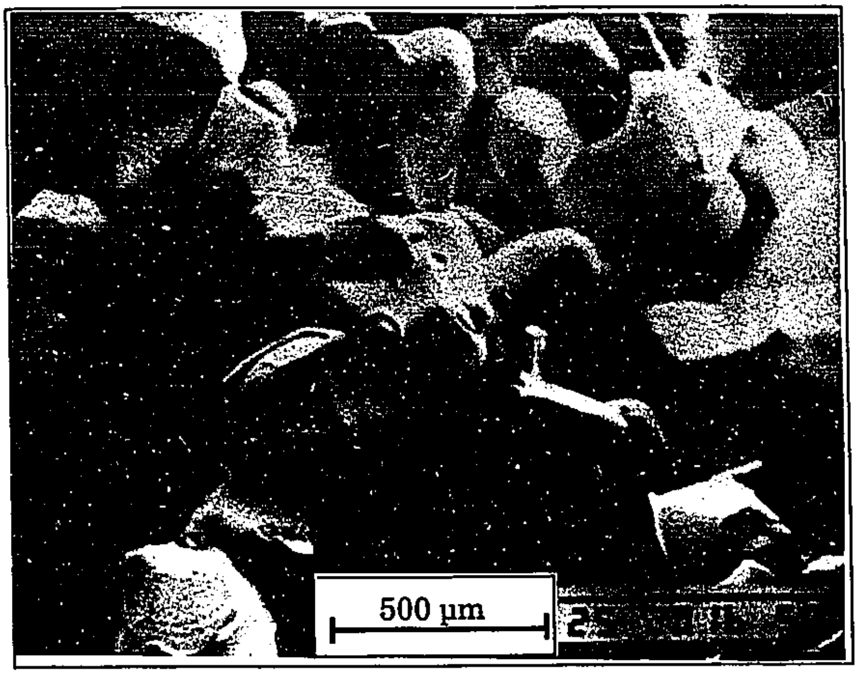

Fig. 4.102: Fracture surface of steel S, tested at 1500°C (RA=0%).

Fig. 4.103: Fracture surface of steel S, tested at 1500°C (RA=0%) (higher magnification).

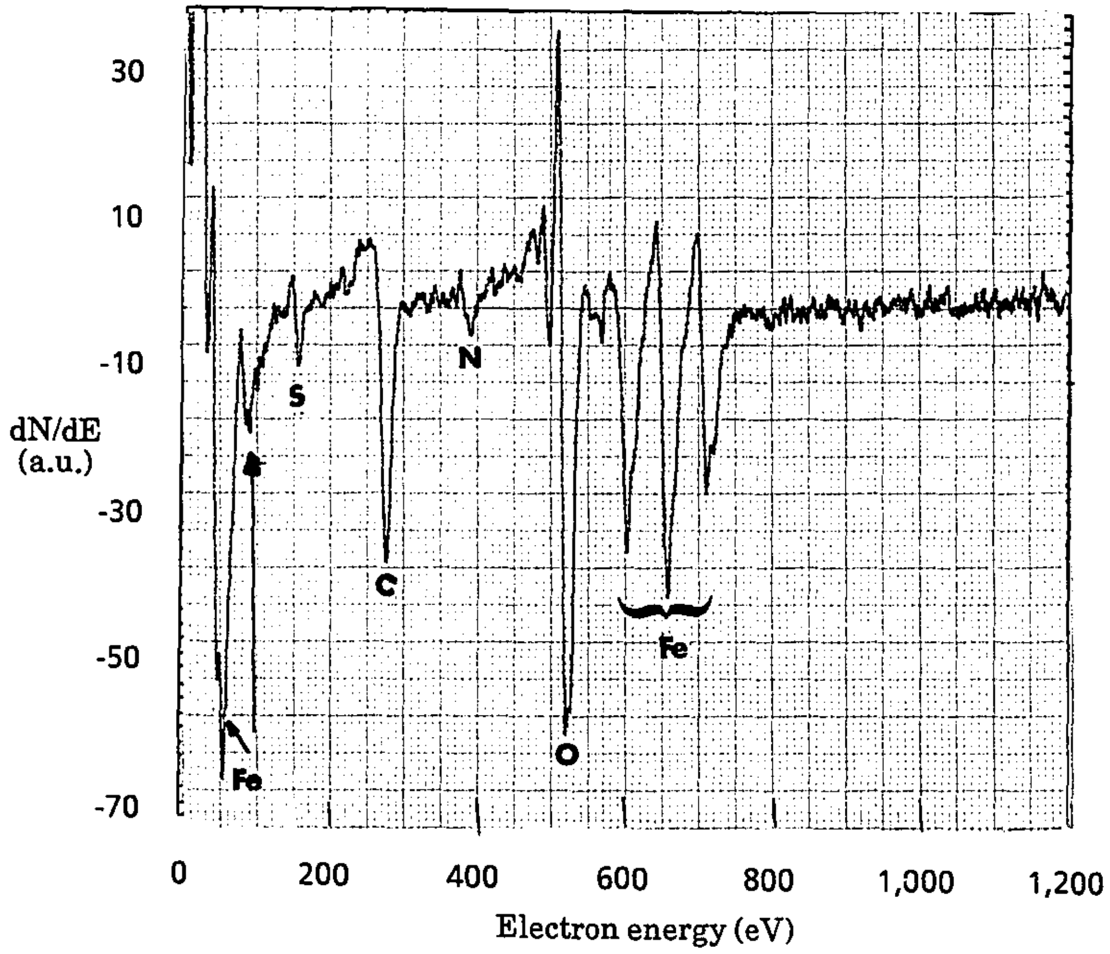

Fig. 4.104 : Typical Auger electron spectra obtained after 8 min. of Argon ions sputtering. Steel C.

$$C_x = I_x / S_x / (\Sigma_i (I_i / S_i)) \qquad (4.4)$$

where S_x is a relative elemental sensitivity factor, measured from a pure elemental standard and I_x is the peak-to-peak height (i.e. the total height of the signal, including the parts which are above and below the baseline) of element x in the differential curve [107,108]. The S_x values are available in the literature [108]. The summation is done for all the elements, but for one peak per element, as specified in the literature [108]. The approximate concentrations of the elements detected on fracture surface of steel C were calculated on this basis. The change of the atomic concentrations of sulfur and carbon with increasing ion sputtering times are presented in Figs. 4.105-a and 4.105-b, respectively. Due to the general atmospheric contamination (C,O and N) the sulfur peak is not immediately seen. However, it is evident that for both sulfur and carbon, maximum concentrations are reached after 10 min. of ion etching; approximately 3.8% of the atoms of the surface are sulfur atoms and 46% are carbon atoms. The presence of carbon cannot be attributed only to the atmosphere contamination because, even after 69 min. of etching the peak is detectable and the concentration has been estimated to be a relatively high 13%.

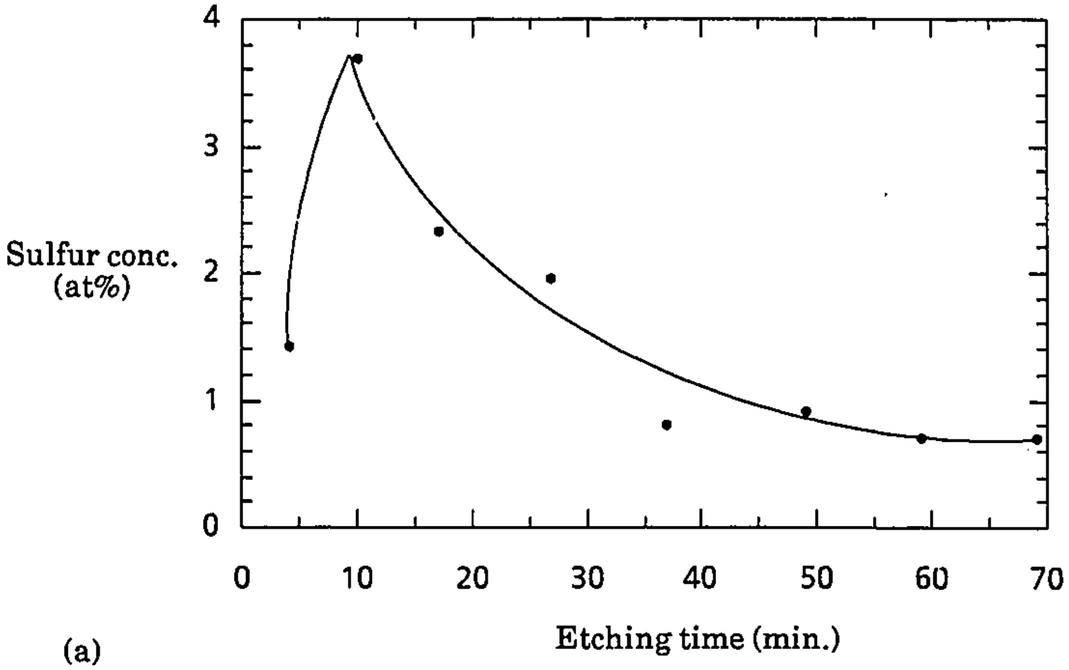

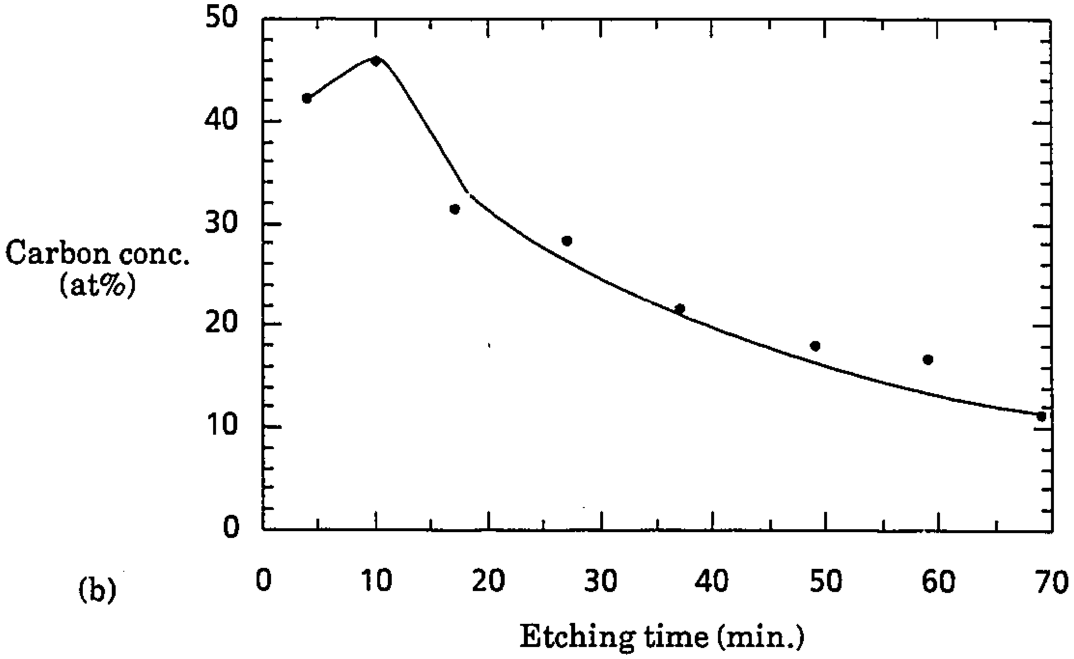

Fig. 4.105: Influence of ion sputtering time on the surface concentration of (a) sulfur, (b) carbon on steel C.

CHAPTER 5

DISCUSSION

HOT DUCTILITY BETWEEN 1400°C AND SOLIDUS TEMPERATURE

Differential thermal analysis (DTA) has shown that the temperature at the onset of melting in the investigated steels remains more or less constant at around 1500°C. However, the hot ductility tests have shown that incipient melting (as indicated by the ductility drop start temperature, DDS) occurs at the grain boundaries, at temperatures between 0 and 36°C lower than those measured by DTA. In other words, in contrast to the DTA results, the ductility drop start temperature (DDS) is dependent on the chemical composition. This dependence can be summarized as follows:

(i) when C is increased from 0.07 wt% to 0.14 wt%, the difference (ΔT_1) between the DDS and the solidus temperature measured by DTA increases from 24 to 35.5°C, and

(ii) steel S which contains Ni-Cr-V and has a lower sulfur level than the other grades (0.005 and 0.009 wt%, respectively), exhibits practically the same solidus and DDS temperatures ($\Delta T = 0°C$).

However, the addition of Nb and Ti (steel A) to the C-Mn-Al steel (steel P) does not affect ΔT_1, the value for both steel A and P being 24°C.

Essentially, then, it appears that the onset of melting detected by the DTA corresponds to the "bulk" solidus, whereas the DDS of the hot ductility tests is a grain boundary melting phenomenon. Accordingly, it will be shown in this chapter that the DTA findings correspond directly to changes in bulk composition, whereas the hot ductility results are indirectly linked to the bulk composition via grain boundary segregation. At this point it is worth noting that, although many workers [25,33,56,115-118] have stated that embrittlement occurs at a temperature below the solidus, their findings are based only on calculated solidus temperatures. The fact that the solidus temperature of each steel was not actually measured is a limitation. An accurate determination of the solidus temperature of the bulk material is of a critical importance, since it is the *difference* between the bulk solidus temperature and the characteristic ductility drop temperatures (DDS, DDE), which enables a critical analysis of segregation to be undertaken.

However, before proceeding with the analysis, it is worth pointing out that steels C and S display much bigger grains at fracture than the grades P, A and B. In the following analysis, incipient melting at grain boundaries does not depend on grain size and is therefore not a factor in this temperature range. Grain size does, however affect the behaviour in zone III as will be seen in chapter 6.

The elements which are commonly cited as segregants in steel are S, C and P. Indeed, in this work the presence of segregated sulfur and carbon has been detected on the fracture surface of steel C. However phosphorus was not detected, confirming the observations of Bailon and Weinberg [119] and indicating that P may not be a factor.

Figure 5.1, which includes the results from a number of papers as well as from this study, illustrates the effect of C on ZDT. Here, the numbers identifying each point refer to the *sulphur* level and the literature reference. All these results pertain to experiments that were carried out following a *direct heating* treatment without prior melting, and can therefore be compared with the present results. The results of this work generally concur with those found in the literature. Despite a relatively high scatter, it can be seen that for C levels lower than about 0.12 wt%, the effect of increasing the carbon content is to slightly decrease the ZDT. However, between 0.12 and about 0.19 wt% the ZDT decreases sharply. This is also in agreement with hot ductility tests performed after melting and solidification (Fig. 2.8 of the literature survey), where it has been clearly observed that, when the carbon level is increased to the peritectic composition, a sudden decrease of ZDT is observed.

Although the sulfur levels were not systematically varied in the investigation, the influence of increasing sulfur concentration on the zero ductility temperature can be assessed by replotting Fig. 5.1 in terms of S, as

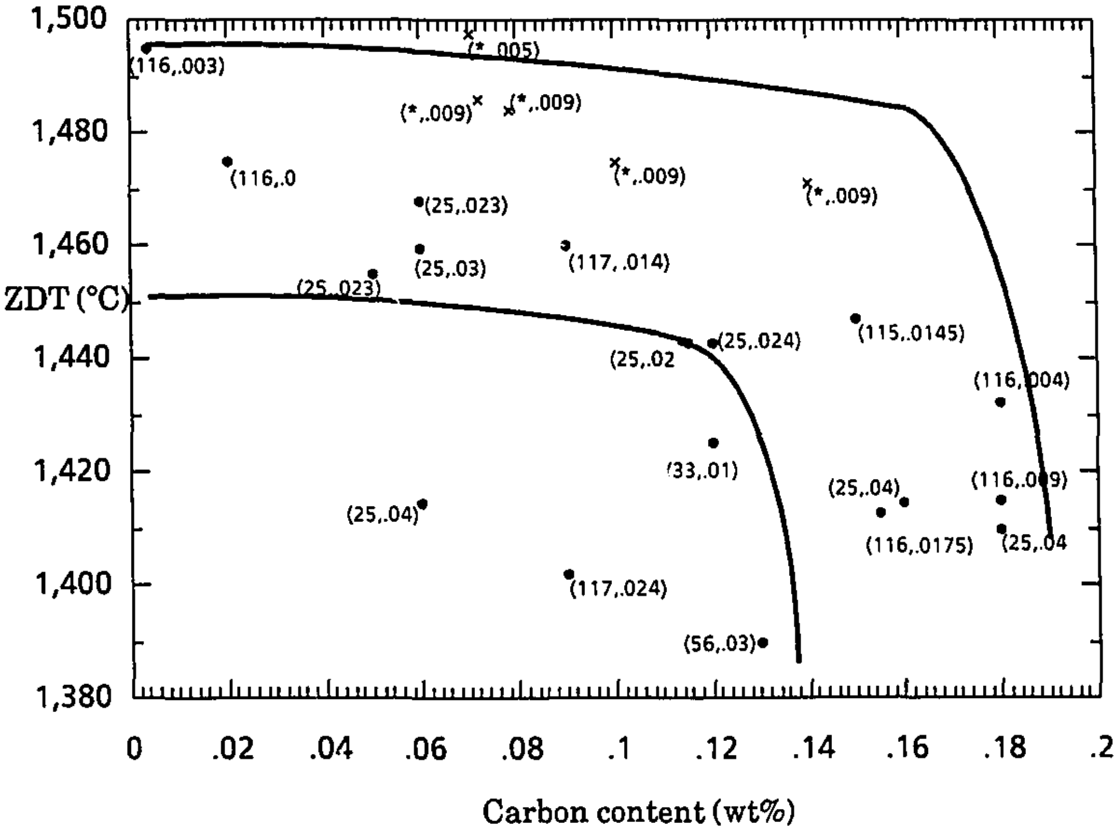

Fig. 5.1: Influence of carbon content on ZDT for different sulfur levels, first number in parentheses is literature survey, second is sulfur level (wt%). (*results from the present investigations).

shown in Fig.5.2. Thus, each point on the graph is identified by first the carbon level (in wt%) and second the reference from which the data point was taken. Here, the two C ranges of 0.05 to 0.12 wt% and 0.12 to 0.18 wt% are clearly observed. For a given carbon level, increasing the sulfur level decreases the ZDT.

There is little published data concerning the effect of phosphorus. Weinberg [25] did not observe any influence of this element on ZDT of 0.07-0.09 wt% C steels, even at phosphorus levels as high as 0.09 wt%. However, Adams has detected the presence of phosphorus at the grain boundaries of steels with carbon levels greater than 0.16 wt% and displaying embrittlement [56].

There is general agreement in the literature that the intergranular failure of steels at temperatures just below the solidus is due to incipient melting at grain boundaries [25,33,56,115-118]. On direct heating from room temperature, the embrittlement is attributed to the formation, at the grain boundaries, of an alloy having a lower melting temperature than the matrix. Of course, segregation of carbon, sulfur and phosphorus at the grain boundaries appears to be the cause of this incipient melting. This must be distinguished from the segregation which occurs on cooling from the melt. As will be discussed below, the former refers to an *equilibrium* process, whereas the latter is due to *non equilibrium* segregation. Other elements such as B, Sn, Sb etc, are known to segregate in iron [120], but there are no reported data in the literature concerning their influence on grain boundary melting.

Despite the fact that C, S and P have been frequently singled out as the cause of incipient melting in steels, a quantitative or even semi-quantitative analysis of the segregation behaviour of these elements in relation to incipient melting has, to the knowledge of the present author, not been performed. This will be addressed in the following sections.

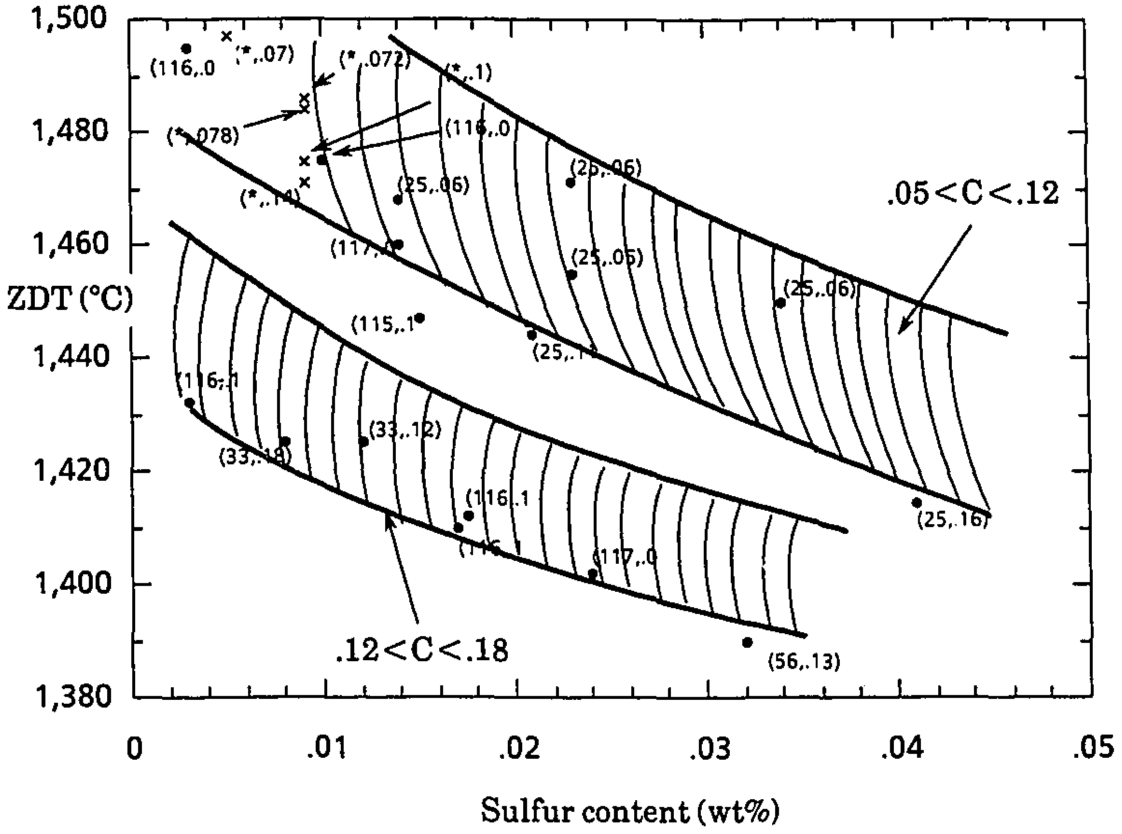

Fig. 5.2: Influence of sulfur content on ZDT for different carbon levels as for Fig. 5.1 (*results from the present investigations).

5.1 EFFECT OF COMPOSITION ON BULK SOLIDUS TEMPERATURE

The results of the differential thermal analysis presented in Table 4.2 are compared with those of the Fe-C phase diagram (Fig.4.8) in Table 5.1. It can be seen that the correspondance between the steels investigated and the pure Fe-C diagram is quite good, especially with respect to the temperature at $\delta \rightarrow \delta + L$. This reflects the rather low alloying additions used.

The DTA results are also comparable with other solidus temperatures of steels with similar compositions. The solidus temperatures quoted by Kinoshita [115] fall in the range 1456-1467°C for an average composition of 0.15 wt% C, 0.23 wt% Si, 0.9 wt% Mn, 0.02 wt% P, 0.014 wt% S and 0.02 wt% Al. Data from the work of Weinberg, presented in Table 5.2, are in a good agreement with the present experimental results, i.e. when the carbon concentration increases from 0.05 to 0.12 wt% C when the solidus temperature decreases from 1507 to 1495°C. The important point to note here is that, in the carbon range investigated, the solidus temperature varies only slightly. Note that in both the above cases, the solidus temperatures were *calculated*, but in neither case was the method reported.

An attempt was made in this study to calculate the solidus temperatures using the method of Kagawa and Okamoto [121]. The details of the calculations are described in Appendix IV. Unfortunately, the solidus temperatures calculated with this model are between 20 and 30°C below the experimental values, indicating significant deficiencies in the model, as discussed in appendix IV.

Nevertheless, it seems, then that the DTA values pertain to "bulk" behaviour, rather than grain boundary melting. This is emphasised by performing a simple calculation to determine the volume fraction of liquid present at the grain boundaries at the DDS temperature. Consider a DTA sample of volume V where the grains are assumed to be spherical with a mean radius R, and are surrounded by a boundary of thickness e. The volume of the grain boundary is given by:

Table 5.1

Comparison between experimental phase transformation temperatures of the steels P, A, B, C, and S with the corresponding temperatures in the pure Fe-C phase diagram [122]. The experimental values are shown in parentheses.

STEEL		A	B	C
STEEL P	Temperature (°C)	1440 (1456)	1470 (1473)	1501 (1500)
	Transformation	$\gamma \rightarrow \gamma + \delta$	$\gamma + \delta \rightarrow \delta$	$\delta \rightarrow \delta + L$
STEEL A	Temperature (°C)	1432 (1455)	1464 (1469)	1504 (1500)
	Transformation	$\gamma \rightarrow \gamma + \delta$	$\gamma + \delta \rightarrow \delta$	$\delta \rightarrow \delta + L$
STEEL B	Temperature (°C)	1453.5 (1455)	1492.5 (1475)	1492.5 (1500)
	Transformation	$\gamma \rightarrow \gamma + \delta$	$\gamma + \delta \rightarrow \delta + \gamma + L$ $(\gamma + \delta \rightarrow \delta)$	$\gamma + \delta + L \rightarrow \delta + L$ $(\delta \rightarrow \delta + L)$
STEEL C	Temperature (°C)	1479 (1469.5)	1492.5 (1497.5)	1492.5 (1509)
	Transformation	$\gamma \rightarrow \gamma + \delta$	$\gamma + \delta \rightarrow \gamma + \delta + L$	$\gamma + \delta + L \rightarrow \delta + L$
STEEL S	Temperature (°C)	1434.5 (1461.5)	1462 (1488)	1504.5 (1503.5)
	Transformation	$\gamma \rightarrow \gamma + \delta$	$\gamma + \delta \rightarrow \delta$	$\delta \rightarrow \delta + L$

Table 5.2

Chemical composition and corresponding calculated solidus temperature [25].

Steel	C	Mn	Si	P	S	Sol. (°C)
1	.05	1.93	.03	.012	.023	1507
2	.06	2.38	0.1	0.014	0.034	1509.5
3	.06	.34	.013	.008	.014	1505
4	.115	1.13	0.09	0.010	.021	1489.5
5	.12	.62	-	.0003	.024	1495
6	0.16	.89	0.26	0.025	0.041	1478.5

$$V_{gb} = \frac{4}{3}\pi(R+e)^3 - \frac{4}{3}\pi R^3 \approx 4\pi(R+e)Re \qquad (5.1)$$

The number of grains inside the sample is given by the ratio of the total volume of the sample over the volume of one grain. Thus, the grain boundary volume fraction, is given by:

$$\frac{V_{gb}}{V} \approx \frac{3(R+e)Re}{(R+e)^3} \approx \frac{3e}{R} \qquad (5.2)$$

Assuming a grain boundary thickness of 10^{-9} m and grain boundary radius of $55\text{x}10^{-6}$ m (estimation of the mean fracture facet size in section 4.4.2), the grain boundary volume fraction, and hence the liquid volume fraction when incipient melting occurs, is $5.5\text{x}10^{-5}$. It is unlikely that the DTA technique will detect such a small volume fraction of liquid, further indicating that the temperatures measured by this technique correspond to the onset of melting of the *bulk* alloy.

Acccording to the DTA results and the above calculations, the bulk solidus temperatures vary little with the compositional changes of the steels investigated. The DDS and DDE values, however, clearly show an effect of composition. As will be shown below, this is due to differences in the grain boundary incipient melting temperatures, which in turn, are due to changes in segregation at the grain boundaries brought about by bulk compositional variations.

5.2 THEORY OF GRAIN BOUNDARY SEGREGATION

Segregation at the grain boundaries, which is a particular case of adsorption at an interface [120], can be classified into two broad categories: equilibrium and non-equilibrium segregation. Non-equilibrium segregation (which occurs, for example, during solidification) depends on kinetics [120], and in general disappears after long hold times as a result of diffusional processes.

A further important distinction between these two classifications is that, in the non-equilibrium case, the concentration gradient between the interface and the bulk can extend up to several microns, whereas, for equilibrium segregation, it is localized to one or two atomic layers at the interface [120].

Equilibrium segregation occurs because defects (i.e. the grain boundaries) in the solid provide sites in which solute atoms have a lower free energy [123]. At very high temperatures, close to the solidus, it may be assumed that equilibrium conditions are attained. This assumption has been employed sucessfully by several workers in the analysis of segregation in α and γ iron [109,124-130].

The following analysis is based on the model due to McLean [123]. It is first assumed that there are N *undistorted* lattice sites with P solute atoms distributed among them and n *distorted* sites (i.e. grain boundary sites) with p solute atoms distributed among them. The free energies associated with one solute atom in the *undistorted* and *distorted* sites are (E-TS) and (e-Ts), respectively, where E and S (or e and s) refer to the enthalpy and entropy associated with the undistorted (or distorted) sites, and T is the temperature. Thus the total free energy due to the solute atoms reads:

$$G=p(e-Ts)+P(E-TS)-kT\{ln(n!N!)-ln(n-p)!p!(N-P)!P!\} \qquad (5.3)$$

where the last term of the r.h.s. of equation 5.3 represents the configurational entropy. Equilibrium occurs when G is at a minimum. Thus by equating dG/dp to zero and noting that the sum of solute atoms remains constant (i.e. p+P=const) we obtain:

$$(e-Ts)-(E-TS)=kTln(\frac{n-p}{p}\times\frac{P}{N-P}) \qquad (5.4)$$

Writing C_{gb}=p/n for the concentration of solute in the distorted region, C=P/N in the undistorted region, and ΔG=(E-TS)-(e-Ts), equation 5.4 becomes:

$$\frac{C_{gb}}{1-C_{gb}}=\frac{C}{1-C}exp(-\frac{\Delta G}{RT}) \qquad (5.5)$$

In this model, the following assumptions are made [120]:

(i) there is no interaction between solute atoms at the grain boundaries, and

(ii) segregation is restricted to one monolayer

Using the notation of Hondros and Seah [120] where the grain boundary concentration of solute i is X^i_{gb} and the bulk concentration is X^i, equation 5.5 becomes:

$$\frac{X^i_{gb}}{X^{i0}_{gb}-X^i_{gb}}=\frac{X^i}{1-X^i}exp(-\frac{\Delta G^i}{RT}) \qquad 5.6$$

where ΔG^i is the change in free energy accompanying segregation, and X^{i0}_{gb} is the fraction of grain boundary monolayer which can accomodate segregating atoms at saturation. X^{i0}_{gb} replaces unity in the denominator of the l. h. s. of equation 5.5, i.e. it was implicitly assumed in the McLean's analysis that $X^{i0}_{gb}=1$. Although there is experimental evidence that, for phosphorus segregation in α iron, the entire grain boundary monolayer can accomodate segregating atoms (i.e. $X^{i0}_{gb}=1$) [127], Hondros and Seah [131] claim that Xi^0_{gb} may be as low as 0.5. However, for simplicity in the following analysis X^{i0}_{gb} is considered to be unity. Thus, equation 5.6 can re-written as:

$$X^i_{gb}=\frac{X^i exp(-\frac{\Delta G^i}{RT})}{1-X^i+X^i exp(-\frac{\Delta G^i}{RT})} \qquad (5.7)$$

Finally, for $X^i<<1$:

$$X^i_{gb}=\frac{X^i exp(-\frac{\Delta G^i}{RT})}{1+X^i exp(-\frac{\Delta G^i}{RT})} \qquad (5.8)$$

Analysis of equation 5.8 leads to the following key points:

- the more negative the free energy (ΔG^i), the higher the segregation tendency;
- the concentration of solute at the grain boundaries increases with increasing bulk concentration; and
- the concentration at the grain boundaries increases with decreasing temperature.

This approach has been applied to steels, but (with the exception of ref. 131) only in the α-ferrite [125-140] or in the austenite phases [109,141]. In order to extend this treatment to solidus temperatures, knowledge of the free energies of segregation for the elements C, S and P are required. However, only values pertaining to the γ and α ferrite phases are available in the literature. Therefore, the free energies of segregation of carbon, sulfur and phosphorus in δ-ferrite at 1480°C (i.e. in the region of DDS) were estimated from those of the α-ferrite as shown in Appendix V. Then, for grades P, A, B and S, grain boundary concentrations of carbon, sulphur and phosphorus were calculated for δ-ferrite. For steel C, which, as revealed by the DTA results, displays a γ+δ duplex structure at embrittlement, the calculation was done separately for the austenite and δ phases.

5.2.1 Carbon segregation

The carbon solubility in austenite is higher than in α and δ ferrite phases. This arises because the size of the interstitial spaces in the austenite phase is more than twice as large as those in α ferrite, leading to much lower lattice distortion in the austenite. Thus, the strain energy component of the free energy segregation of carbon is correspondingly smaller in the austenite, i.e. ΔG is much less negative for austenite than δ ferrite [109]. Consequently, C should exhibit a considerably lower segregation in γ than in α (and by extension in δ ferrite) at the same temperature. This was also the conclusion of McLean who calculated several values for the free energy of C in α by considering the elastic distortion caused by C atoms in the α ferrite [123]. This postulate is further supported by comparing the ΔG values found in the literature

(Appendix V), the mean values of which are listed in Table 5.3. Unfortunately, only a single value of ΔG for austenite was found in the literature, this being associated with the temperature range 850-1100°C, (i.e. no temperature dependence of ΔG was observed over this range). Taking this value to be certainly correct at the middle of this temperature range, i.e. 975°C, a corresponding ΔG for "δ ferrite" can be calculated at this temperature using the equation generated in Appendix V. The calculated value at 975°C assuming δ ferrite is ≃-87 KJ/mole compared to -30 KJ/mole quoted in the literature for austenite. It is therefore highly probable that the negativity of ΔG at 1480°C is much greater in δ ferrite than in austenite. Thus, the segregation of carbon is correspondingly higher in δ ferrite than in austenite (Table 5.4).

5.2.2 Sulfur segregation

Sulfur, although a substitutional element, is one of the strongest segregants in iron [128,138].. At low temperatures (900-1200°C), it forms a sulfide with any Mn addition and is not available as segregant. Above 1200°C there is a significant dissolution of the MnS precipitates. The amount of sulfur in solution at any temperature can be estimated by the solubility product of MnS [142]:

$$K_S = \frac{(\%Mn)(\%S)f_S^{Mn}}{A_{MnS}} = 2.93 - \frac{9020}{T} \tag{5.9}$$

where f_s^{Mn} is the activity coefficient of dissolved sulfur in the presence of manganese, and A_{MnS} is the activity of MnS which is equal to 1 if manganese in solution is greater than 0.3 wt%. The change in f_s^{Mn} with temperature and Mn content is given by:

$$Log f_S^{Mn} = \left(\frac{-215}{T} + 0.097\right)(\%Mn) \tag{5.10}$$

The calculated increase in the amount of sulfur in solution with increasing temperature is presented in Fig. 5.3 for the steels used in this

Table 5.3

Enthalpy and entropy of segregation of carbon, sulfur and phopsphorus in α and γ phases and calculated free energy of segregation at 1480°C in the δ and γ phases.

Element	ΔH^{α} (KJ/mol.)	ΔS^{α} (KJ/mol.)	ΔG^{δ} (1480°C) (KJ/mol.)	ΔH^{γ} (KJ/mol.)	ΔS^{γ} (KJ/mol.)	ΔG^{γ} (1480°C) (KJ/mol.)
C	-50	-0.0294	-101.5	6.7	-0.0294	-44.83
S	-51	-0.0231	-91.49	-31.1	-0.0231	-71.6
P	-33.5±6.5	-0.0231	-74±6.5	14±4	-0.0272	-61.7±4

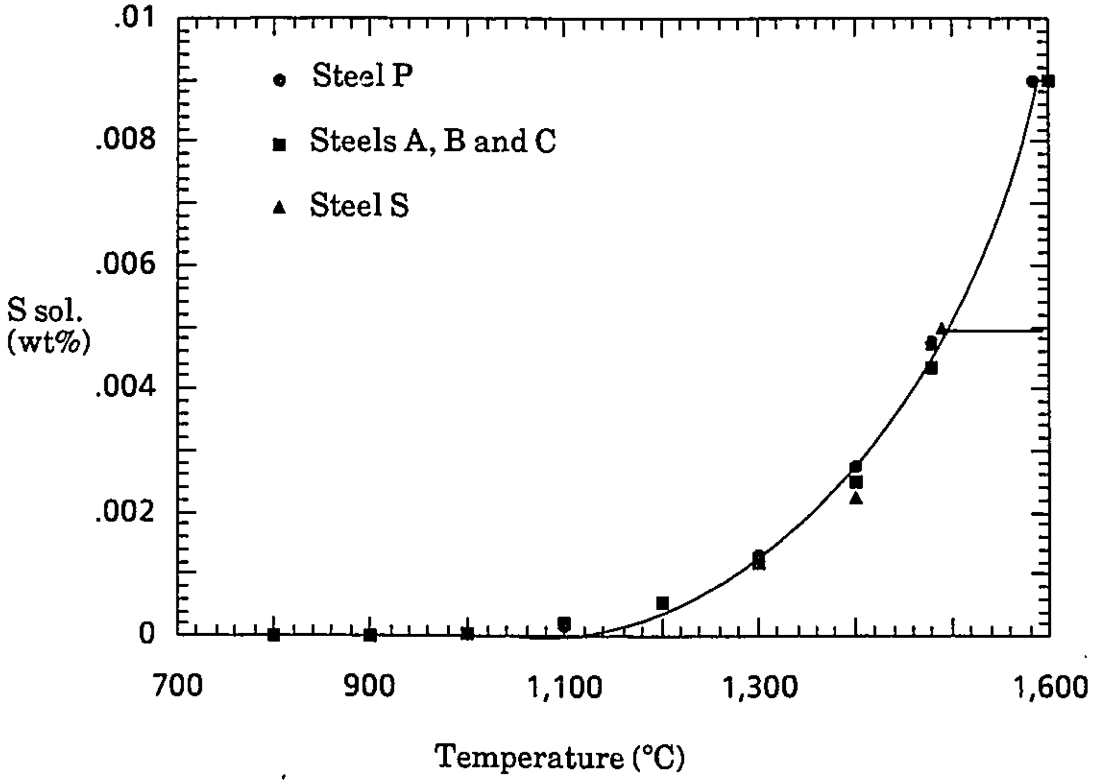

Fig. 5.3: Calculated equilibrium variation of the sulfur in solution with increasing temperature for steels P, A, B, C and, S.

investigation. At 1480°C the amount of dissolved sulfur is about 0.0045 wt% for all the steels, and will segregate to the grain boundaries.

Using the method presented in Appendix V, the free energy of segregation in δ ferrite was found to be -91.5 kJ/mole at 1480°C, compared to -71.9 kJ/mole at the same temperature in the austenite (Table 5.4). Using equation 5.8, the grain boundary sulfur concentration in the δ phase, is 4.21 at% for steel P, 3.8 at% for steels A, B and C and 4.15 at% for grade S (Table 5.5). As for carbon segregation the most significant result concerns steel C, where the calculated grain boundary concentration in the γ phase is much lower than in the δ phase: 0.99 versus 3.8 at%, respectively.

5.2.3. Phosphorus segregation

From investigations of temper embrittlement in steels, phosphorus (which is substitutional in iron) is known to segregate in α-ferrite [127-130,137,139,143] and in austenite [109]. For these phases, the free energies of segregation have been determined as shown in Appendix V. As for C and S, the ΔG value is more negative for the δ ferrite than for the austenite phase (Table 5.3).

The free energy of segregation of P is not negligible, and therefore some P segregation is expected as can be seen in Table 5.4. However, the absolute value of ΔG is much lower than that for carbon and sulfur which may partly explain the absence of P segregation in the present Auger examinations. Moreover, although phosphorus is known to segregate at the grain boundaries of α ferrite [127-130,137,139,143] and austenite [109], the literature suggests that it may not affect the ZDT under certain circumstances. In directly heated specimens, a high P concentration at the grain boundaries of steels containing 0.13 wt% of C and above (i.e. grades in which the very high temperature phase is austenite) has been observed [25,56]. However Suzuki et al. claim that in directly heated relatively high carbon steels (i.e. $C > 0.14$ wt%) there is no effect of phosphorus, but it is not stated whether the results refer to temperature zone I [36]. Other experiments confirm that there is no influence of P on the ZDT of 0.07-

Table 5.4

Calculated grain boundary concentration of carbon, sulfur and phosphorus in the δ phase for steels P, A, B, C and S at 1480°C (and in the austenite for steel C).

Element	X^{δ}_{gb} (at%) Steel P	X^{δ}_{gb} (at%) Steel A	X^{δ}_{gb} (at%) Steel B	X^{δ}_{gb} (at%) Steel C	X^{γ}_{gb} (at%) Steel C	X^{δ}_{gb} (at%) Steel S
Carbon	79.4	77.3	83	87.2	12.3	77.3
Sulfur	4.21	3.8	3.8	3.8	0.99	4.15
Phosphorus	1.8-4.3	2.2-5.1	2.2-5.1	2.2-5.1	1.1-1.9	1.1-2.6

0.09 wt% C steels (i.e. grades exhibiting a δ phase) for P levels between 0.015 to 0.09 wt% [25].

The conclusion from the literature, then, is that there appears to be segregation of P in the austenite and not in δ ferrite, which is actually the *opposite* of what is expected from the single segregation model.

However, it has been demonstrated, that on cooling from the melt, P decreases the ZDT of electrolytic iron (i.e. the primary phase is the δ ferrite) [33]. In other words, where P is the only segregant, the single segregation model is valid. In the presence of other segregants, cosegregation must be considered.

5.2.4. Summary of single component segregation calculations

The key conclusion of this analysis is that carbon, phosphorus and sulfur show a higher tendency to segregate in the δ-ferrite than in the austenite, this being most marked in the case of carbon which is the main segregant regardless of phase. One further point to note is that, in general, the calculated grain boundary concentrations are at least 2 orders of magnitude greater than the bulk concentration. The high grain boundary concentration of carbon in delta ferrite is due to the relatively high C content in the steels investigated and to the very high segregation energy of carbon in the δ phase. (In contrast, in the austenite phase, because of the low ΔG, the C grain boundary concentration is strongly decreased). The calculated grain boundary concentrations seem rather high, but are actually of the same order of magnitude of the values detected by Auger analysis, e.g. max C concentration = 46 at% (Fig. 4.105).

To reiterate the observation made in section 5.1, as embodied in Figs. 5.1 and 5.2: when the C level is increased to the peritectic composition, there is an abrupt decrease in the ZDT. At C contents lower than that corresponding to the peritectic region, only the δ phase is present, and, from the single segregation model, the C grain boundary concentration is about 80%. In the peritectic region, both δ and γ are present and the *austenite* grain boundary concentration is about 12%. An obvious conclusion is that the incipient melting temperature associated with an Fe-80% alloy is much higher than that of a Fe-12%C composition. This is a reasonable assumption, even though the melting point of a Fe-80% C alloy is not known. However, the Fe-12%C solidus temperature is 1150°C [122] which is well below the observed DDS. Quantitatively there is a large discrepancy between experiment and theory, which is probably due to the following:

(i) the inaccuracy in the measurements of the free energy of segregation of C, S and P in austenite, and the lack of data in the δ ferrite ,

(ii) the assumption that the maximum grain boundary segregant that is possible is 100% (i.e. $X^{i0}_{gb} = 1$ in equation 5.6), and

(iii) the model adopted for the grain boundary structure (e.g. a monolayer thick) may be oversimplified. In other words it appears unlikely that the grain boundary behaviour corresponds directly to the bulk behaviour. Thus, for example, the addition of 12% C to Fe will lower the bulk melting point to 1150°C, but it is doubtful that 12% C at the grain boundary will lead to a grain boundary melting temperature of 1150°C.

In qualitative terms, though, the behaviour of C on the ZDT appears to be well explained by the single segregation model. Note also that the differences in the grain boundary melting temperature between γ and δ explain the observation in steel C that the fracture surface is comprised of a "duplex" structure, i.e. fracture facets that are either completely smooth or completely rough (Figs. 4.98-4.101). The higher incipient melting temperature at the δ grain boundaries corresponds to the rough facet surface. Rogberg [118] has also observed such a "duplex" fracture surface in a high carbon (0.51 wt%) steel and has attributed this to variations in grain boundary segregation, but via crystallographic considerations [118,120]. However, the crystallographic assumption should apply for all grades, and not only for steel C, as was observed in this work.

Up to now, carbon, sulphur and phosphorus have been considered to segregate singly, but since these elements are all present in the materials investigated their co-segregation behaviour must be examined. This is presented in the next section.

5.3 THEORY OF GRAIN BOUNDARY CO-SEGREGATION

Two models are discussed which consider interdependance of the segregating elements. In the first one, the "competition" model, co-segregation of carbon, sulfur and phosphorus occurs and there is competition for grain boundary sites, but no chemical interaction between the three segregating species. In the second, the "chemical interaction" model, the analysis is based on the assumption that a chemical interaction exists between carbon, sulfur, and phosphorus, but there is no competition.

5.3.1 Competition model

In his original treatment of co-segregation based on the adsorption theory, Guttmann [144] has considered the general case of a multicomponent system with 1 to n components (1 to n-1 solutes, the nth being the solvent). At the thermodynamic equilibrium, the chemical potentials of element i both in the bulk (μ^i) and at the grain boundaries ($\mu_{gb}{}^i$) are equal:

$$\mu^i_{gb}=\mu^i \qquad (5.11)$$

μ^i and $\mu_{gb}{}^i$ can be written as:

$$\mu^i=\mu^{i0}+RTlna^i=\mu^{i0}+RTln(f^iX^i)) \qquad (5.12)$$

$$\mu^i_{gb}=\mu^{i0}_{gb}+RTlna^i_{gb}=\mu^{i0}_{gb}+RTln(f^i_{gb}X^i_{gb}))-\sigma \qquad (5.13))$$

where and X^i ($X_{gb}{}^i$) is the bulk (grain boundary) fractional concentration of element i, a^i is the chemical activity, f^i is the activity coefficient, and σ is a term associated with surface tension at the grain boundaries. The sums of all the components in the matrix and at the grain boundary are equal to unity, i.e.:

$$\sum_{i=1}^{n} X^i_{gb} = \sum_{i=1}^{n} X^i = 1 \tag{5.14}$$

Thus, by combining equations 5.11 to 5.14, the grain boundary concentration of element i reads:

$$X^i_{gb} = \frac{X^i exp(-\Delta G^i/RT)}{1 + \sum_{j=1}^{n-1} (X^j(exp(-\Delta G^j/RT) - 1))} \tag{5.15}$$

where the summation in the denominator includes the solutes only. ΔG^i represents the free energy for segregation of element i and, in the analysis of Guttmann, includes a chemical interaction coefficient, which will be discussed in the next section [144]. In this section, it is assumed that there is no chemical interaction between i and j, and the segregation free energy ΔG^i is that of the binary system Fe-i used in the initial segregation analysis (i.e. ΔG^i values given in Table 5.3) [128]. Clearly, equation 5.15 is the same as that for a single component (equation 5.8) but extended to include all segregants, in this case carbon, sulfur and phosphorus.

The assumption that an equilibrium can be attained by mutual displacement (i.e. competition) without any chemical interaction between the segregating species, has been used several times in the case of the cosegregation of P and C in α ferrite [109,127,130,136,137]. Other workers [127,138,140] have also suggested that competition could occur between S and C, again in α ferrite. Equation 5.15 (or an equivalent one) has been extensively used for the cosegregation of P and C in the the α ferrite, but (to the author's knowledge) it has never been used for the quaternary system Fe-C-S-P. However, the extension of this model to the latter case is quite straightforward. In the present work, at high temperatures (1480°C), the grain boundary concentrations of carbon, sulfur and phosphorus were calculated using equation 5.15 and the ΔG^i values listed in Table 5.3. Rewriting equation 5.15, the carbon, sulfur and phosphorus concentration at the grain boundaries are given by equations 5.16, 5.17 and 5.18, respectively:

$$X_{gb}^{C}=\frac{X^{C}exp(-\Delta G^{C}/RT)}{1+X^{C}(exp(-\Delta G^{C}/RT)-1)+X^{S}(exp(-\Delta G^{S}/RT)-1)+X^{P}(exp(-\Delta G^{P}/RT)-1)} \quad (5.16)$$

$$X_{gb}^{S}=\frac{X^{S}exp(-\Delta G^{S}/RT)}{1+X^{C}(exp(-\Delta G^{C}/RT)-1)+X^{S}(exp(-\Delta G^{S}/RT)-1)+X^{P}(exp(-\Delta G^{P}/RT)-1)} \quad (5.17)$$

$$X_{gb}^{P}=\frac{X^{P}exp(-\Delta G^{P}/RT)}{1+X^{C}(exp(-\Delta G^{C}/RT)-1)+X^{S}(exp(-\Delta G^{S}/RT)-1)+X^{P}(exp(-\Delta G^{P}/RT)-1)} \quad (5.18)$$

The terms in the denominator for S and P are very small relative to the one for C because of the concentrations and ΔG values. This means that the grain boundary carbon concentration in both phases is not going to differ markedly from the single segregation model, but the S and P results will be significantly decreased by the C term because the S and P levels depend strongly on the carbon segregation. With respect to sulphur and phosphorus segregation in austenite, the large decrease in carbon segregation in the austenite will offset the lower ΔG values of sulphur and phosphorus in the numerator. In other words the segregation of S and P in austenite is *higher* than for delta ferrite, if a co-segregation mechanism is active.

Thus, as can be seen from Table 5.5, the carbon segregation differs little from that predicted by the single segregation model, and the S and P levels are generally between 5 and 7 times lower, due to the influence of carbon segregation. In contrast to the findings of the single segregation model, the segregation of both sulphur and phosphorus in the austenite phase of steel C is *higher* than in the delta ferrite. In the case of sulphur, the segregation is almost doubled; for P there is about a 3 fold increase over the segregation in the δ phase. However, note that the amount of sulfur at grain boundaries of the δ of steel A is the same as that at the grain boundaries of austenite in steel C. Compared to steel A, the amount of phosphorus is slightly higher at the grain boundaries of steel C. Thus, a consideration of cosegregation completely changes the behaviour of S and P with respect to the effect of segregation in γ vs δ phases. However, the S and P segregation does not vary significantly in

Table 5.5

Calculated grain boundary concentrations for steels P, A, B, C and S. For comparison the bulk composition is also given.

	P (δ)	A (δ)	B (δ)	C (δ)	C (γ)	S (δ)
X^C (at%)	0.364	0.323	0.462	0.645	0.645	0.323
X^C_{gb} (at%)	78.2±.2	76.4±.3	82.3±.2	86.65±.15	12.1	76.75±.15
$X^S_{tot.}$ (at%)	0.0156	0.0156	0.0156	0.0156	0.0156	0.0087
$X^S_{sol.}$(at%)	0.0083	0.0750	0.0750	0.0750	0.0750	0.00819
X^S_{gb} (at%)	0.90	0.885	0.665	0.5	0.88	0.95±.2
X^P(at%)	0.0179	0.0215	0.0215	0.0215	0.0215	0.0108
X^S_{gb} (at%)	0.6±.3	0.85±.35	0.6±.3	0.5±.2	1.3±.35	0.45±.15

grades A, B and C. Thus, with respect to effect of C concentration the explanation based on the single segregation model still holds.

It is important to note that, although C is the dominant segregant, any additional segregation of S and P to the grain boundaries will affect the grain boundary melting. The effect of increasing S concentration is noted in Fig. 5.2. Furthermore, the observations of Weinberg [25] and Adams [56], concerning the effect of phosphorus, can be explained by the cosegregation theory. Weinberg has observed no effect of phosphorus on ZDT in the δ phase, whereas Adams has attributed the incipient melting of the grain boundaries of austenite to the presence of phosphorus. According to the co-segregation model in the delta phase carbon has displaced more phosphorus atoms than in the austenite, i.e. P segregation is much higher in the γ that in the δ.

Although the competition and single segregation models adequately explain the behaviour of steels P, A, B and C, the difference between steel S and the other grades is not addressed. Also, for steel S, the differences between the solidus and the DDE and DDS temperatures are negligible (Table 4.3), suggesting that the composition at the grain boundaries is similar to that of the matrix. Here the explanation must lie with the presence of Ni, Cr and V. However, since the free energies of segregation of Cr and Ni are small ($\Delta G_{Cr} \simeq 0$ kj/mole, $\Delta G_{Ni} \simeq -3$kJ/mole) [128], and V does not segregate in iron [120], the possible effect of these elements cannot be considered using the competition model. A possible explanation of non segregating elements in steel S can be furnished using "the chemical interaction" model, as outlined below.

5.3.2 Influence of chemical interaction on segregation

From the analysis of Guttman [128,145,146], in a ternary Fe-i-j solution, the intergranular concentration is given by equation 5.15 as before. To account for any chemical interaction between i and j, the free enthalpy of segregation of element i (or j) is expressed as a function of the matrix and intergranular concentration of element j (or i), as shown in the following equation:

$$\Delta G^{i} = \Delta G_{0}^{i} + \alpha_{ij} X_{gb}^{j} + \alpha_{ij}^{'} X^{j} \tag{5.19}$$

where α_{ij} and α'_{ij} are the interaction energies between elements i and j at the interface and in the matrix, respectively, and ΔG^{i}_{0} (ΔG^{j}_{0}) is the free energy of segregation of element i (j) in the Fe-i (Fe-j) system. The other terms have the same meaning as before. If i (or j), are at low levels, the last term of the r.h.s. of equation 5.19 is always negligible, because $X^{j} << X_{gb}^{j}$, i.e the general form of the equation will have terms for grain boundaries only. Depending on the magnitude and the sign of α_{ij}, the absolute value of ΔG^{i} can be decreased or increased. When the interaction is *attractive* ($\alpha_{ij} > 0$) the absolute values of ΔG^{i} and ΔG^{j} increase and the segregation of elements i and j are mutually enhanced, provided that the difference between ΔG^{i} and ΔG^{j} is relatively small. However, where one of the elements is a weak segregant ($\Delta G^{i}_{0} \simeq 0$), and the other is a strong segregant (i.e. the difference between ΔG values is large), there are two possibilities:

(i) the strongly segregating element is removed from the grain boundaries by a "scavenging" effect of the weakly segregating element, or

(ii) the weakly segregating element can be attracted to the grain boundary by the strong segregant.

Case (i) has been observed for the Fe-i-j system where i is a transition metal ($\Delta G^{i}_{0} \simeq 0$) and j is either carbon, phosphorus or sulfur [128]. The precipitation of an intermetallic compound (Fe-i)j, thereby reducing the amount of solute j both in the matrix and at the grain boundaries, can be considered as an extreme example of case (i).

Such a model has been used to explain 'temper embrittlement' of steels, which is due to phosphorus segregation at α-ferrite grain boundaries [127]. Increasing carbon decreases temper embrittlement because of the replacement of P atoms by C atoms at the grain boundaries (according to the competition model). However, the addition of Cr to a Fe-C-P alloy strongly scavenges C by carbide formation [127,145] leading to a large increase in the P segregation, therefore, increasing the tendency to embrittlement. However, whether the decrease in carbon concentration at the grain boundaries is due solely to a decrease of C level in the matrix and/or to the attraction of C atoms by Cr has not been ascertained. No example of case (ii) has been found in the literature, to date.

If a *repulsive* interaction exists between i and j ($\alpha ij<0$), and if the difference between ΔG^i and ΔG^j is not too large, the absolute values of ΔG^i and ΔG^j decrease and the segregation of both elements is reduced. If one solute is a weak segregant, the repulsive interaction leads to an increase of the segregation of the strong segregant (i.e. the weak segregant repels the strong one *towards* the grain boundary).

A quantitative determination of the segregation pattern using equation 5.19 is not possible, primarily because of the scarcity of interaction coefficient data. A qualitative approach can be taken using the formalism of Darken and Simkovitch [147], which is a very general treatment of high temperature adsorption of two solutes on the surface of a solvent (a metal), and can therefore be applied to the particular case of segregation at grain boundaries. Using the same notation of these workers, if '1' is the solid surface and '2' the solute, the Gibbs adsorption relation states that:

$$\Gamma_2^0 = -\left(\frac{\delta\sigma}{\delta\mu_2}\right) = -\frac{1}{RT}\left(\frac{\delta\sigma}{\delta ln a_2}\right) \qquad (5.20)$$

where Γ_2^0 is defined as "the excess concentration of component 2, with respect to component 1, adsorbed at the interface", which can be interpreted as the difference in concentration between the interface and the matrix. Thus, according to the above expression, segregation is a function of σ, the surface free energy of the system, and μ_2 and a_2, which are the chemical potential and activity coefficient, respectively, of component 2. The addition of a low level of a third element, 3, to the system leads to the following change in the "excess concentration" of component 2:

$$\Gamma_2 \simeq \Gamma_2^0 - y_2 \frac{\varepsilon_{32}}{1+y_2\varepsilon_{22}} \Gamma_3 \qquad (5.21)$$

where y_2 is the ratio of the number of moles of solute 2 in the bulk over the number of moles of solvent 1 and ε_{32} is the Wagner interaction coefficient between the elements 3 and 2, and ε_{22} is the Wagner *self* interaction coefficient of element i (j). Note that the latter two coefficients are equivalent, but not the same as, the interaction energy (i.e α_{ij} in equation 5.19) in Guttmann's model. Equation 5.21 also holds for component 3, provided that the concentration of solute 2 is low.

In the ternary Fe-i-j system (using the notation of Seah and Hondros), the excess of concentration of components i (j) adsorbed at the grain boundaries is therefore given by:

$$\Delta X^{i}_{gb} \simeq \Delta X^{i0}_{gb} - \frac{X^{i}}{X^{Fe}} \frac{\varepsilon_{ij}}{1 + \frac{X^{i}}{X^{Fe}} \varepsilon_{ii}} \Delta X^{j}_{gb} \qquad (5.22)$$

where ΔX^{i0}_{gb} (or ΔX^{j0}_{gb}) is the excess of concentration of component i (j) in the Fe-i (Fe-j) binary system. Analysis of this equation leads to essentially the same conclusions as Guttmann's model. If the interaction between the elements i and j is attractive, ε_{ij} is negative and there is a mutual enhancement of the segregation of both elements, provided that the difference between ΔX^{i0}_{gb} and ΔX^{j0}_{gb} is not too large. If the latter occurs, the stronger segregant attracts the weaker segregant away from the grain boundaries. In the case where there is a repulsion between i and j (the interaction coefficient is positive) the segregation of both elements is reduced, if they are both strongly surface active. If one is a weak segregant, the interaction repels the strong one towards the grain boundaries, increasing the grain boundary concentration of the strong segregant.

Values for ε_{ji} exist in the literature although mainly for liquid iron at 1600°C [148]. Guttmann [128] has used such values qualitatively in the α-ferrite phase. He has argued that, in spite of large differences that must exist between ε_{ji} in the liquid phase and in the α-ferrite, the *sign* of these interactions (i.e. their repulsive or attractive character) is the same, especially if the magnitudes of the coefficients are large in the liquid phase.

In the present chapter, following in the work of Kagawa and Okamoto [121] (discussed in Appendix IV), it is assumed that the Wagner interaction coefficients in the δ phase are equal to those in the liquid phase. This may be regarded as being an extension of the assumption that liquid phase values have the same sign as for α-ferrite, and it is possibly a better assumption, because the temperatures associated with liquid and δ phases are much closer. The interaction coefficients of S, P and C with Cr, Ni and V are presented in Table 5.6. It can be seen that, both Cr and V exhibit attractive interaction coefficients with these elements, the V/C interaction being particularly strong. Consequently, since the free energy of segregation of carbon and sulfur is much higher than those of Cr and V, S and C will show a tendency to be attracted away from the grain boundaries by Cr and V. In fact it has recently been observed that the addition of 0.1 wt% Cr in α ferrite greatly reduces the amount of sulfur in solution by precipitation of chromium sulfides, leading to a decrease in grain boundary segregation [149]. Also Weinberg [25] has observed a grain boundary melting temperature close to the solidus for a 0.38 wt% C steel containing 0.88 wt% Cr. Ni exhibits a weak tendency for segregation, which, together with a repulsive interaction coefficient, could *enhance* segregation of C and S. However, Ni exhibits (in absolute terms) a lower interaction coefficient compared to both C and S. It is thus likely that any effect of Ni on C and S is largely negated by the combined influence of V and Cr. The Wagner interaction coefficient between phosphorus and Ni is negligible (the effect of V on phosphorus is unknown since no interaction coeffcients are available).

Thus, the experimental observation that steel S exhibits a ZDT very close to the solidus temperature (i.e. Solidus-DDE $\simeq 0$) can be qualitatively explained by the suppression of grain boundary segregation of P, S and C due to scavenging of these elements by Cr and V.

Although the behaviour of steels A, B and C were semi-quantitatively explained by the single segregation model, it is interesting to apply the interaction concept to these steels. This can be done with the help of the interaction coefficients of the elements C, S and P (Table 5.7) together with their free energies of segregation (Table 5.3). In the δ ferrite phase, the interaction between the three elements is highly repulsive, therefore, since the energy of segregation of C is the highest (Table 5.4), C will have a tendency to repel S and P from the grain boundaries. In the austenite phase, the interaction coefficients are still repulsive, but, sulphur is the most powerful segregant, followed by P.

Table 5.6

Wagner interaction coefficients of C, S and P with Cr, Ni and V. Superscript numbers refer to references.

ε_{ij}	Cr	Ni	V
Carbon	-5.05 [148] -4.59 [121]	2.85 [148] 3.36 [121]	-16 [148]
Sulfur	-2.28 [148]	0.85 [148]	-3.26 [148]
Phosphorus	-6.32 [148]	-.005 [148]	?

Table 5.7

Wagner interaction coefficients of carbon, sulfur and phosphorus and self interaction coefficients. Superscript numbers refer to references.

ε_{ij}	C		S		P	
	γ	δ or L	γ	δ or L	γ	δ or L
C	7.07 [121]	8.09 [121] 7.7(40)	11.1 [148]	12.0 [121] 6.47 [148]	5.48[121]	5.93[148] 6.95[121]
S	11.1 [121]	12.0 [121] 6.47 [148]	?	-3.11 [148]	?	4.1 [148]
P	5.48[121]	5.93(40) 6.95[148]	?	4.1 [148]	?	8.34 [148]

Therefore, C will be reduced from the austenite grain boundaries by the repulsive interaction with S.

To summarize, in the single segregation and co-segregation models the important factors which decide whether or not an element will segregate at the grain boundaries are the intrinsic free energy of segregation of each element and the matrix composition. In the case of the interaction model, both the free energy and the interaction coefficient (or interaction energy) must be considered. Applied to the present steels, the essential features of these approaches are the following:

i) In δ ferrite, when competition between C, S and P is considered, it is shown that C segregation predominates.

ii) In austenite, C segregation is much reduced, but still predominates, and segregation of S and P are increased when compared to the δ ferrite.

iii) The behaviour of steel S (i.e. the observation that Solidus-DDS$\simeq$0) can be explained by the presence of Cr and V which attracts C, S and P from the grain boundaries, thus increasing the DDS temperature.

5.4 RELATIONSHIP BETWEEN STRENGTH AND DUCTILITY IN THE TEMPERATURE RANGE DDS AND ZST

From Table 4.5, it can be seen that the strength corresponding to the zero ductility temperature (σ_{DDE}) is greater than zero. Since the fracture surface of all the steels but C are completely smooth at the DDE temperature, it is assumed that the grain boundaries at fracture are liquid. Therefore, for a reduction of area of zero, the stress corresponds to the surface tension between the liquid film and the facets of the grains [118]. The maximum stress can be identified as the stress to overcome the surface tension:

$$\sigma_{max}=\frac{2\Gamma}{d} \qquad (5.23)$$

where σ_{max} is the maximum stress correponding to the DDE temperature, Γ is the surface tension and d is the liquid film thickness. For pure iron, $\Gamma = 1.8$ j/m^2 and decreases with increasing alloying additions [118]. Following the work of Rogberg [118], a value of 1 J/m^2 is used to calculate the thickness of the liquid film of steels P, A, B and S. It can be seen from Table 5.8 that the film thickness varies between 0.5 and 8 µm, which is of the same order of magnitude as the thickness range of 0.25-2µm evaluated by Rogberg [118]. In the present study, no systematic influence of chemical composition on the calculated liquid film thickness was observed. (For steel C, the duplex structure $\delta + \gamma$ contains solid δ grain boundaries and therefore equation 5.23 cannot be applied.)

Table 5.8
Mean thickness of grain boundary liquid film at the grain of steels P, A, B and S at the DDE temperatures and σ_{DDE}.

Steels	σ_{DDE} (MPa)	d (µm)
P	3.5	.57
A	.25	8
B	4	.5
S	1	2

Equation 5.23 also demonstrates that with a decreasing liquid film thickness the stress due to surface tension can exceed the stress at the DDS temperature. It is generally considered that equilibrium segregation extends over few monolayers [120]. Hence, the thickness of the liquid film at the DDS temperature should be very small. If, as noted in section 5.1, a grain boundary thickness of 10^{-9} m is estimated (which corresponds approximately to three times the diameter of an iron atom), the stress necessary to overcome the surface tension is 2000 MPa. This calculation is certainly an overestimate for the following reasons:

i) The model employed to represent the grain boundaries is very simple: 2 disks separated by a layer of liquid.

ii) The surface tension Γ used for the calculation of σ_{max} was chosen to be closed to pure iron, whereas the grain boundary composition is very different from the bulk.

iii) Although much smaller than in the non equilibrium case, the actual grain boundary thickness could be larger than that estimated here [120].

Nevertheless, this simple calculation indicates that the temperature at the onset of the grain boundary melting (i.e. at very thin liquid film thicknesses) may be lower than that measured by the simple tensile test.

To summarize, at temperatures below the DDS, the grains are deformed preferentially because the surface tension due to liquid film at the grain boundaries is higher than the flow stress of the solid phase. Between the DDS and DDE deformation of the grains occurs before the surface tension of the liquid is exceeded. This is observed in steels P, A and B where fractographic analysis reveals that all the grain boundaries (i.e. fracture surfaces) are smooth indicating melting, but the grains themselves appear to be deformed. This is especially clear in steel B when comparing the fracture surfaces due to a RA of 69% (Figs. 4.94 and 4.95) with those corresponding to a reduction of area of 28% (Figs. 4.96 and 4.97)). In steel C, however, this is not observed (Fig. 4.98); the reason for this is probably that the behaviour of the $\gamma+\delta$ region (i.e. melting preferentially at the grain boundaries) masks the above effect. Finally, in the temperature range between DDE and the zero strength only surface tension contributes to the flow (fracture) strength.

CHAPTER 6

DISCUSSION

HOT DUCTILITY BETWEEN 800-1300°C

In the temperature zone 800-1300°C, the depth and width of the ductility trough is related to nitride and carbonitride dissolution and precipitation processes, carbon content, grain size, and the γ/α transformation. The discussion will therefore be centered on the influence of chemical composition and prior heat treatment on microstructural evolution and precipitation behaviour. In the next section, the mechanisms of embrittlement of low carbon microalloyed steels in the solid phase is first presented and the influence of microstructure is outlined. The effect of prior heat treatment on the hot ductility of each steel is then analysed in terms of dissolution, precipitation of the carbonitrides and nitrides as well as austenite grain growth. The role of chemical composition (i.e. carbon content and microalloying additions) is treated in detail with respect to microstructural changes and their effect on hot ductility.

6.1 MECHANISMS OF EMBRITTLEMENT IN THE SOLID PHASE

As pointed out in the literature survey, poor hot ductility due to intergranular failure is observed at low strain rates in microalloyed steels because of the following embrittling mechanisms:

Grain boundary sliding: This takes place at low strain rates, which favour grain boundary sliding. As a consequence deformation is localised at the grain boundary [28].

Intergranular precipitation: This process is the main cause of poor ductility in the single austenite phase because the precipitates act as stress concentration sites during grain boundary sliding, therefore allowing void nucleation by decohesion at the grain boundary-precipitate interface. Intergranular fracture is essentially completed by void growth and coalescence. Apart from acting as void initiation sites, precipitates inhibit grain boundary movement, thus facilitating void nucleation.

As will be shown below, with respect to the steel grades used in this work, the types of precipitates associated with these effects are nitrides (AlN), carbides (NbC) or carbonitrides (Nb(C,N)). In the case of precipitation of Nb(C,N) away from the grain boundaries, matrix hardening occurs and precipitation free zones are observed in the vicinity of the grain boundary. These regions of relatively low flow strength will lead to strain concentration.

Ferrite film nucleation: On cooling from a solution temperature to the γ/α two phase region, ferrite nucleates at the austenite grain boundary, and grows as a thin grain boundary film. Since ferrite is the softer of the two phases, strain concentration occurs in the ferrite. Thus, ductility is at its lowest when the ferrite film around the grain boundaries is continuous; a thin ferrite film thickness leads to embrittlement. Failure occurs by nucleation and coalescence of voids, generally at the MnS inclusions. Grain boundary precipitation will aggravate the problem and, in fact precipitation is enhanced because precipitate solubilities are lower in ferrite. As the temperature decreases, the ferrite film thickness increases, reducing the strain concentration and increasing ductility. Ductility is completely recovered, i.e. 100% reduction of area is attained, generally well before the end of the $\gamma \rightarrow \alpha$ transformation.

In both the single austenite phase and duplex $\gamma+\alpha$ regions, ductility is decreased by an increase of grain size. In the former, this occurs because:

1) there is an increase in the amount of grain boundary sliding [150,151]
2) triple points are obstacles to crack propagation, therefore crack propagation is easier in coarse grained material [152],
3) the crack aspect ratio is high in the case of a coarse grain size leading to an overall high stress concentration at the crack tip, which produces a higher crack growth rate [153]
4) a given volume fraction of intergranular precipitates is spread over a smaller area in coarse grained material, thus decreasing the mean interparticle spacing [154].

A similar reasoning applies to the duplex structure, but in addition, the smaller grain boundary surface area results in a decrease in the rate of ferrite nucleation. This will tend to widen the trough.

In the single austenite phase, ductility, recovers with increasing test temperature because of the absence of precipitation and/or the occurrence of dynamic recrystallisation. Dynamic recrystallization is a restoration process which takes place during deformation of the austenite at high temperatures [155]. Grains free of dislocations nucleate at the grain boundaries of the initial structure, thereby isolating the cracks at the grain boundaries, preventing coalescence. Thus, the occurence of dynamic recrystallization is generally accepted as being beneficial to ductility [155-157].

6.2 PRECIPITATION AND DISSOLUTION IN MICROALLOYED STEELS

6.2.1 Maximum Stress and Precipitation

No direct observation of precipitates was performed in this work, but an indirect analysis is possible from flow stress. With respect to precipitate behaviour, the main difference between direct heating and annealing or sensitizing is that, in the latter two conditions, precipitation is likely to occur during deformation. In directly heated specimens, precipitates are present, but it may be assumed that they are too coarse to contribute to the flow stress [96].

In Figs. 6.1 to 6.6, $\Delta\sigma$, the difference between the maximum flow stress after the sensitizing (or annealing) and direct heating treatments is plotted against test temperature.

For steel P (C-Mn-Al), AlN precipitation is a possibility. However, it can be seen in Fig. 6.1 that the difference between the maximum stress after sensitizing and direct heating is smaller than 3 MPa and can even be negative. This indicates that there is probably no precipitation taking place in this steel.

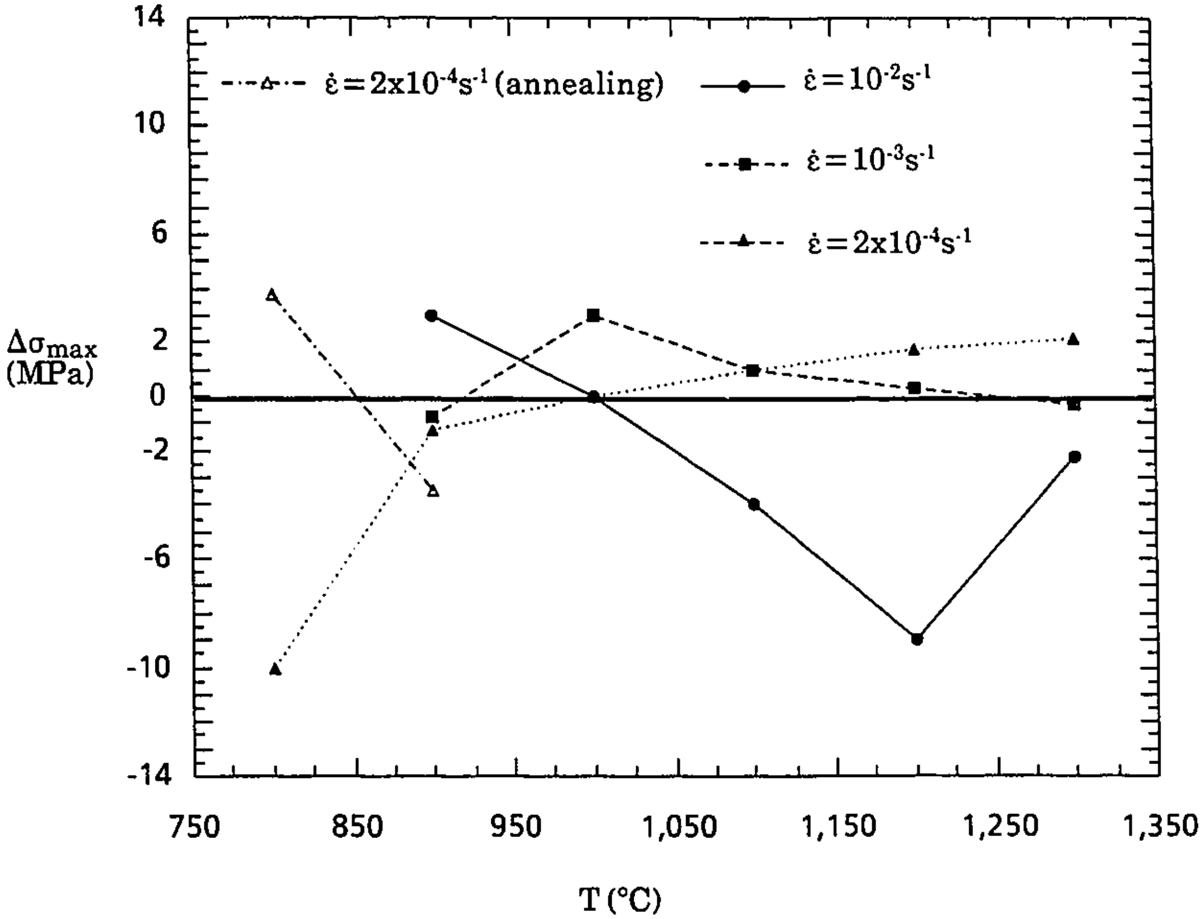

Fig. 6.1: $\Delta\sigma_{max}$ versus temperature curve, steel P. All results refer to sensitizing, unless otherwise labelled.
$\Delta\sigma_{max} = \sigma_{max}$(sensitizing or annealing)-σ_{max}(direct heating).

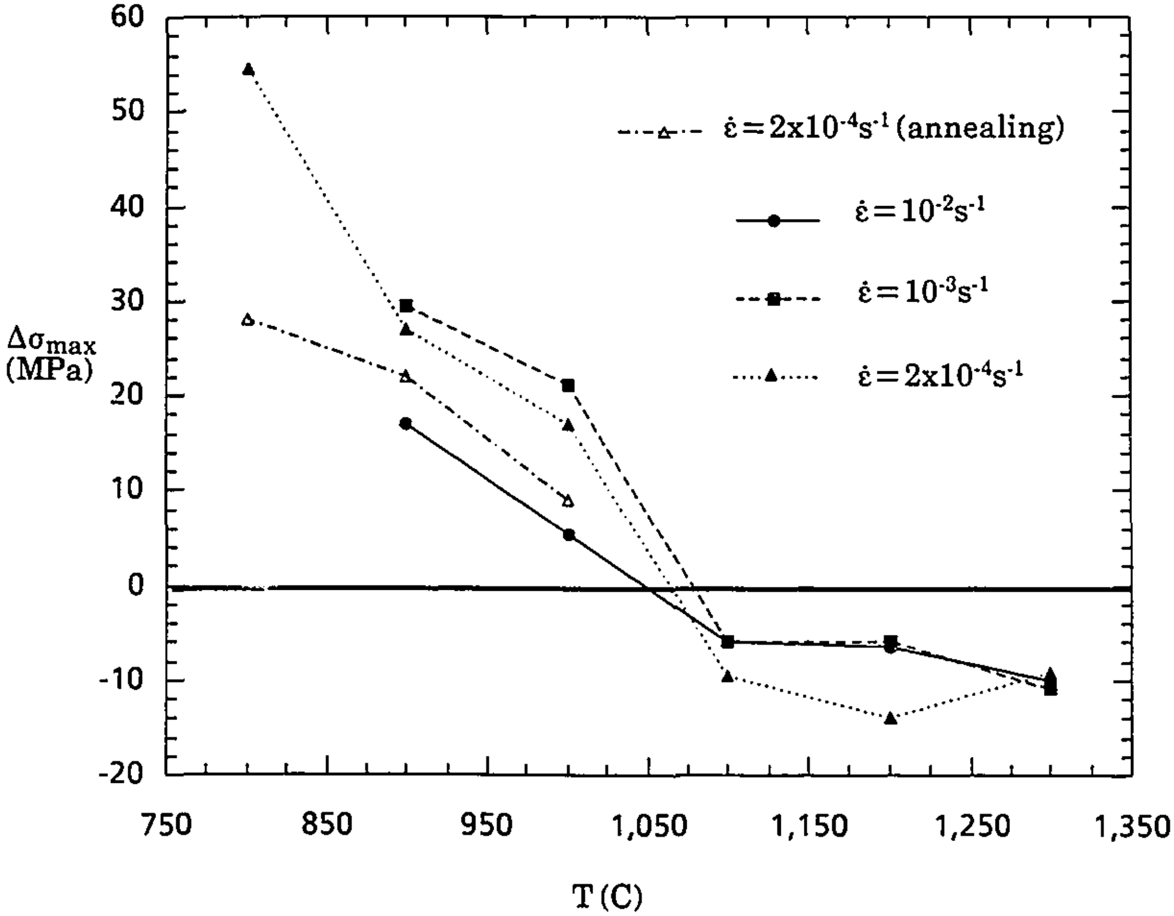

Fig. 6.2: $\Delta\sigma$ versus temperature curve, steel A. All results refer to sensitizing, unless otherwise labelled.
$\Delta\sigma_{max} = \sigma_{max}$(sensitizing or annealing)-σ_{max}(direct heating).

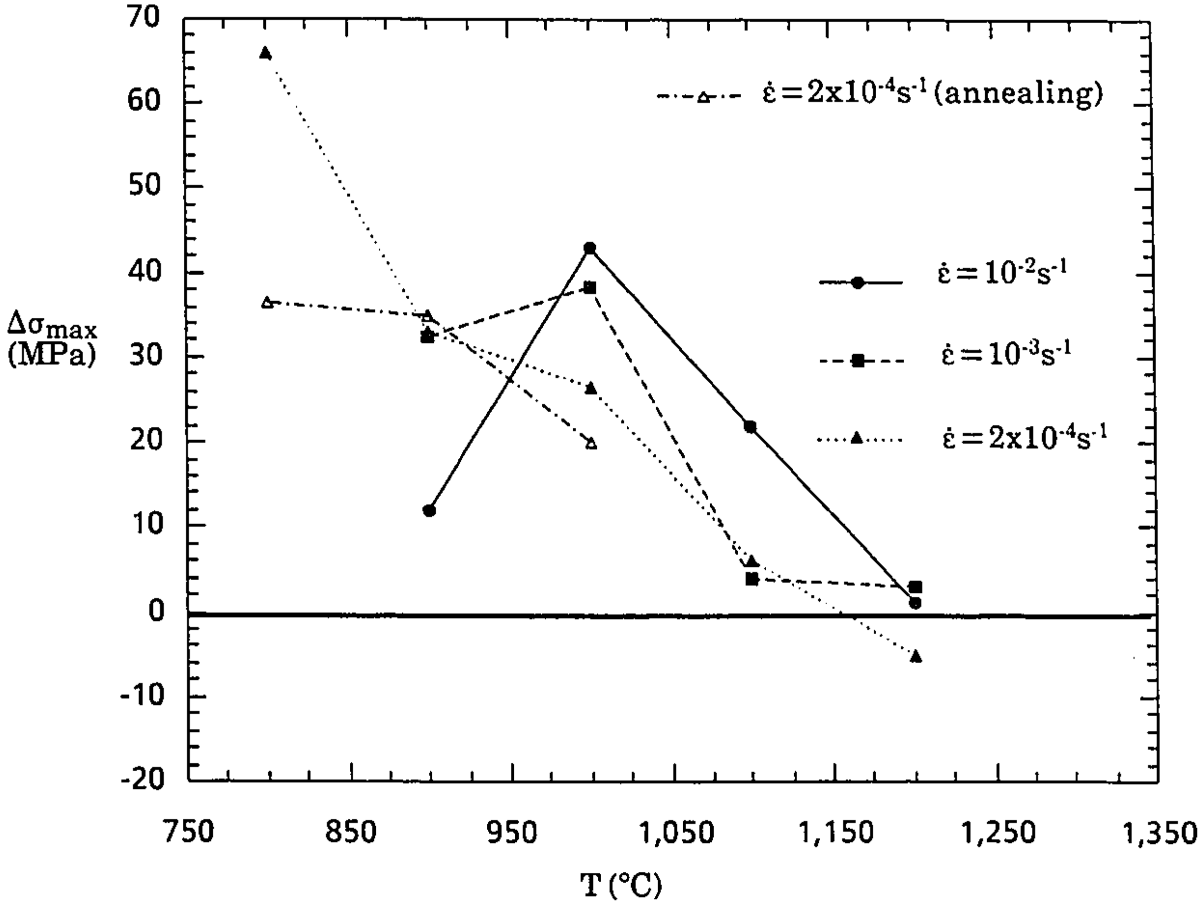

Fig. 6.3: $\Delta\sigma_{max}$ versus temperature curve, steel B. All results refer to sensitizing, unless otherwise labelled.
$\Delta\sigma_{max} = \sigma_{max}$(sensitizing or annealing)-σ_{max}(direct heating)

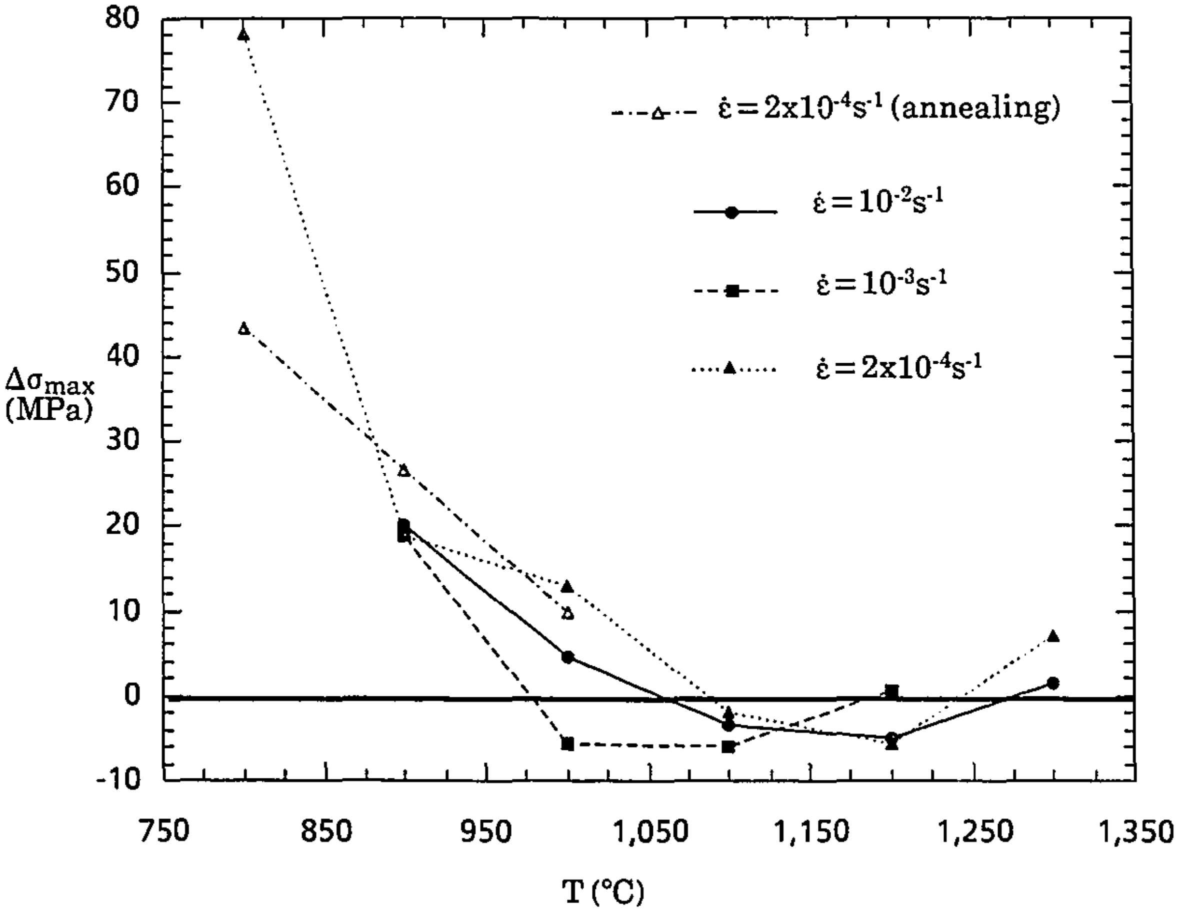

Fig. 6.4: $\Delta\sigma$ versus temperature curve, steel C. All results refer to sensitizing, unless otherwise labelled.
$\Delta\sigma_{max}=\sigma_{max}$(sensitizing or annealing)-σ_{max}(direct heating).

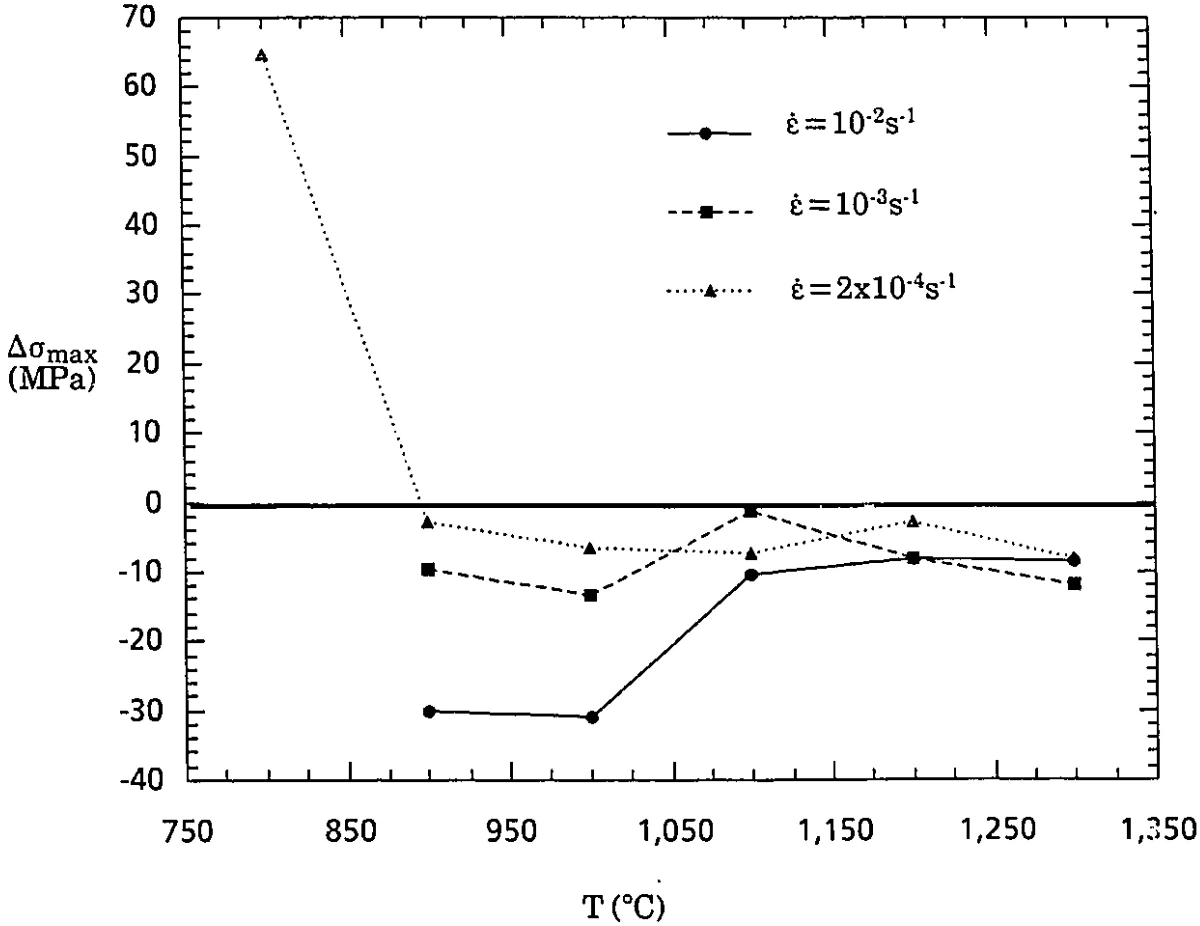

Fig. 6.5: $\Delta\sigma$ versus temperature curve, steel S. Sensitizing. $\Delta\sigma_{max} = \sigma_{max}$(sensitizing)-$\sigma_{max}$(direct heating).

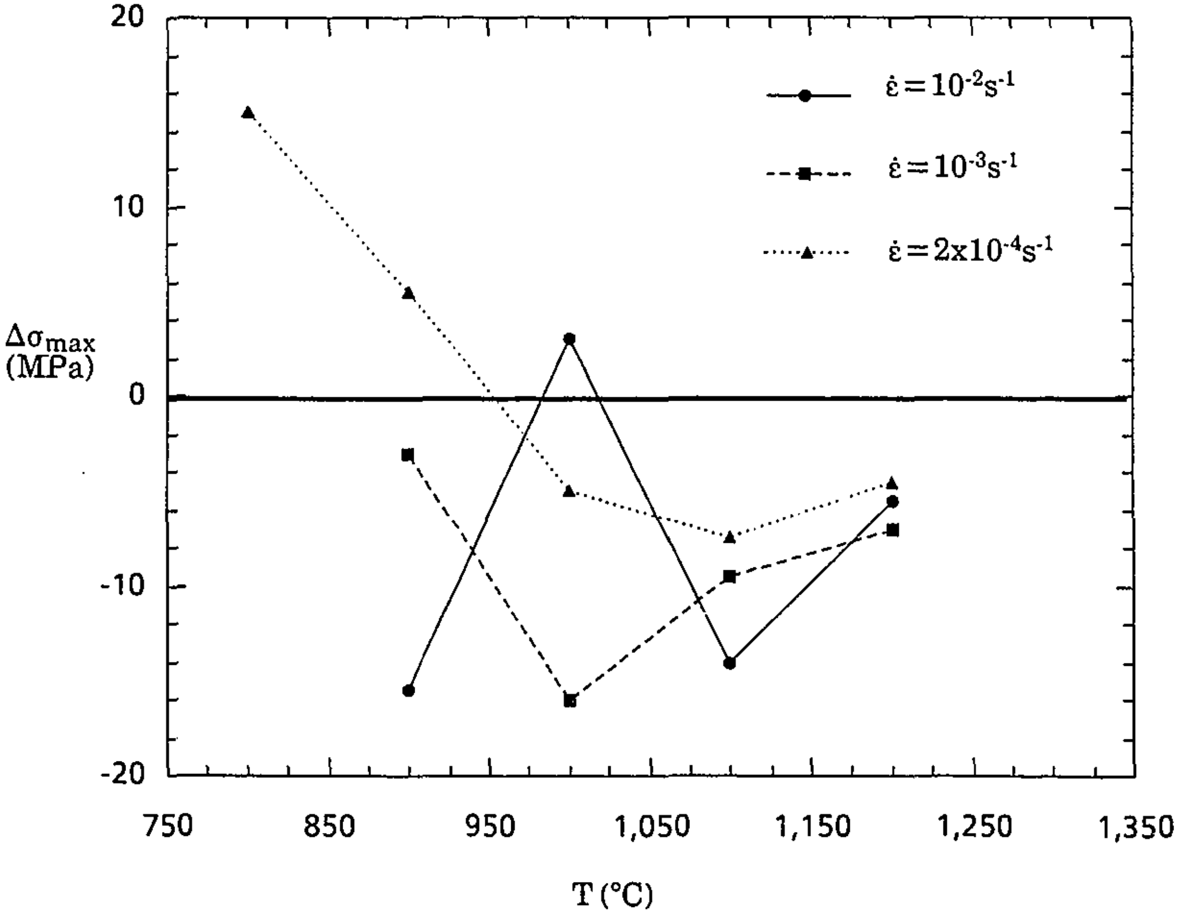

Fig. 6.6: Δσ versus temperature curve, steel S. Annealing. $\Delta\sigma_{max}=\sigma_{max}$(annealing)-$\sigma_{max}$(direct heating).

For steels A, B and C (Figs. 6.2 to 6.4), it can be seen that, in general, $\Delta\sigma$ increases quite markedly at the lower temperatures, probably due to the dynamic precipitation of Nb(C,N) in the sensitized specimens. For these three grades, at the strain rate of $2x10^{-4}$ s^{-1} (where the lowest ductility is seen) the stress difference becomes positive below the temperature range 1050-1100°C. At strain rates of 10^{-2} and 10^{-3} s^{-1}, the temperatures at which the stress difference becomes positive is more scattered, varying in the range 1050-1200°C for the strain rate of 10^{-2} s^{-1} and between 975 and 1100°C for the strain rate of 10^{-3} s^{-1}. The reason for this increased scatter is unclear.

The highest stress differences between direct heating and sensitizing are seen at 800°C. This is due to the large amount of ferrite formed in direct heating leading to a structure with a relatively low flow strength. For this heat treatment, the temperature of 800°C is between the calculated Ac_1 and Ac_3 temperatures (Table 4.1), and a large amount of ferrite remains untransformed. On cooling from the solution temperature, the austenite-to-ferrite transformation begins at the Ar_3, a temperature which is well below 800°C [69]. Note that, for steels A, B and C, the stress difference at 800°C between sensitizing and direct heating is higher than between annealing and direct heating. This probably arises because the amount of NbCN available for precipitation in a fine form is greater in the sensitizing treatment because some NbCN remains undissolved after the annealing treatment. The presence of ferrite in the direct heating case complicates the analysis, but it is clear that once the Ac_3 temperatures have been exceeded (Table 4.1), then any contribution from transformation induced ferrite can be disregarded and the stress differences must be due solely to precipitation.

The most interesting observation concerns grade S where, at temperatures higher or equal to 900°C, $\Delta\sigma$ for sensitizing is negative, indicating an absence of precipitation hardening (Fig.6.5). Only at 800°C is a very high stress differential noticed, this being due to ferrite, as explained above. The stress difference between annealing and direct heating shows a similar trend (Fig. 6.6), although the temperature at which the stress difference becomes positive is higher and the maximum stress difference is lower than after sensitizing.

6.2.2 Activation Energy Calculations

Several workers have established that the relationship between stress, strain rate and temperature follows the equation [53,96,117,158-161]:

$$\dot{\varepsilon}=A\sigma^{n}exp(\frac{-Q}{RT}) \qquad (6.1)$$

where σ is the stress, $\dot{\varepsilon}$ the strain rate, Q the activation energy for deformation in austenite (T>900°C), T is the temperature and A and n are constants. The activation energy was calculated using the following two methods:

i) rewriting equation 6.1:

$$ln\sigma = ln(A^{-1/n}\dot{\varepsilon}^{1/n})+\frac{Q}{nRT} \qquad (6.2)$$

Q/nR is obtained from a plot of lnσ vs 1/T, and n is calculated from the linear plot between lnσ and ln$\dot{\varepsilon}$ at constant temperature, which leads to a slope of Q/R, i.e.:

$$ln\sigma = ln(A^{-1/n})+\frac{Q}{nRT}+\frac{1}{n}ln\dot{\varepsilon} \qquad (6.3)$$

ii) plotting (from the σ-T curves) ln$\dot{\varepsilon}$ against 1/T at constant stress, i.e.:

$$ln\dot{\varepsilon}=ln(A\sigma^{n}) - \frac{Q}{RT} \qquad (6.4)$$

Both methods were employed to calculate Q for steels P, A, B, C and S after the direct heating and sensitizing treatments. For example, for steel B, the lnσ versus 1/T curves at the three strain rates and two heat treatments investigated are presented in Fig. 6.7. In Table 6.1 the mean Q values obtained from both methods are given, together with n values and the reduction of area at 900°C at the lowest strain rate.

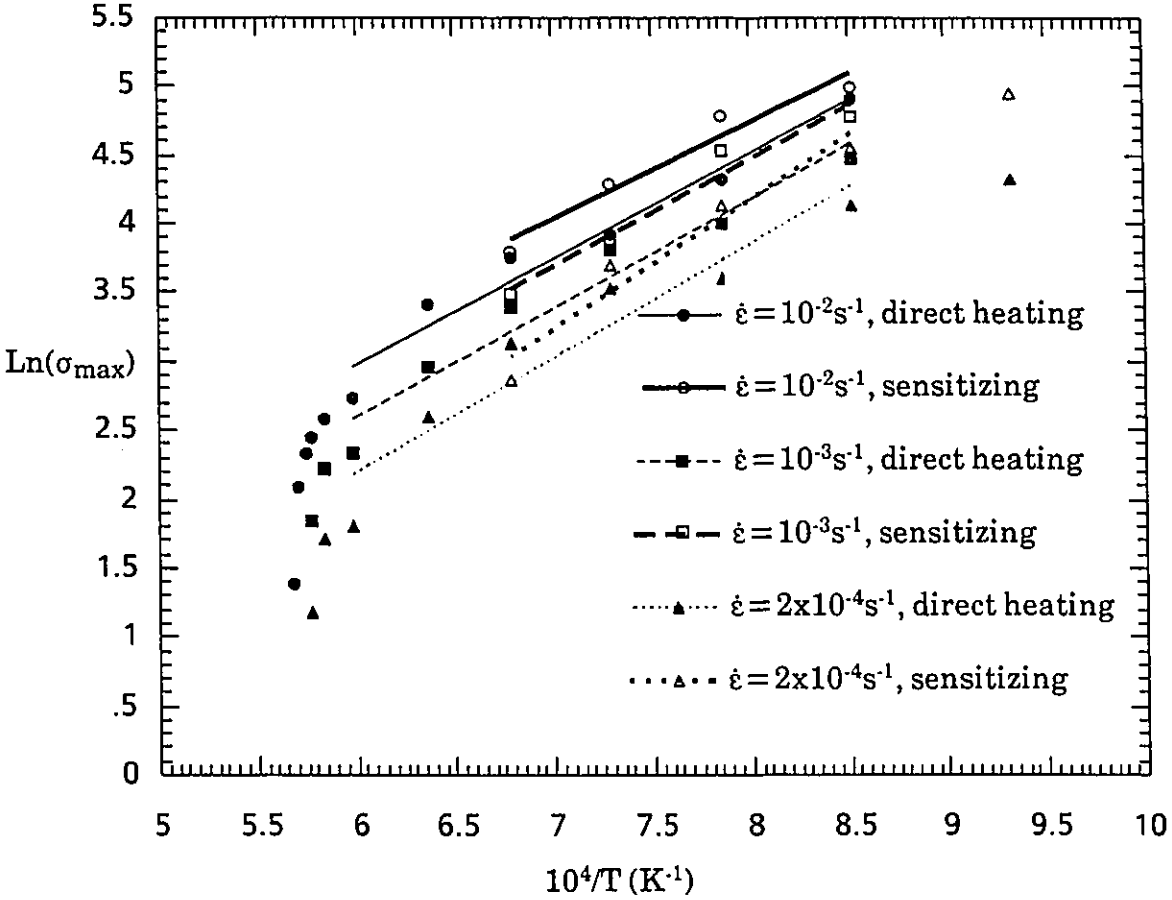

Fig. 6.7: Logarithm of the maximum true stress versus 1/T curve, steel B.

Table 6.1

Q and n coefficients of steels P, A, B, C and S after direct heating, sensitizing and annealing treatments. The reduction of area at 900°C after deformation at the strain rate of $2x10^{-4}$/s are also shown.

Steel	Direct heating			Sensitizing			Annealing		
	n	Q (kJ/mole)	RA (%) 900°C, $2x10^{-4}$/s	n	Q (kJ/mole)	RA (%) 900°C, $2x10^{-4}$/s	n	Q (kJ/mole)	RA (%) 900°C, $2x10^{-4}$/s
P	5.05	379	36	6.39	364.5	96	-	-	-
A	6.54	376.5	62	6.1	533.5	37	-	-	-
B	5.88	383	54	5.56	422.5	42	-	-	-
C	6.58	454	54	6.33	404	34	-	-	-
S	6.41	447	66	5.92	511	56	7.14	492.5	84

It can be seen that there is no clear relationship between either Q or n values and the existence of a ductility trough. For example, steel P has approximately the same Q values for both direct heating and sensitizing, but a marked trough was observed on direct heating whilst excellent ductility occurred after sensitizing. Nevertheless, there is a noticeable increase in Q for steels A and B after any condition in which marked precipitation occurs. However, steel C, which would also show marked precipitation after sensitizing, gives a lower value of Q. Hence, these calculations show, as other researchers have noted, that the Q values do not generally relate to the ductility [96]. Note also that steels with similar n values have very different reductions of area (Table 6.1).

6.2.3 Precipitation Analysis of Previous Hot Ductility Investigations

A systematic survey of the published data concerning precipitation in hot ductility studies was performed in order to determine the types of precipitates likely to be present in the steels in this work. Of particular interest is the size and distribution of the precipitates.

6.2.3.1 C-Mn-Al steels

Table 6.2 summarises the data on precipitation found in the literature for C-Mn-Al steels. The chemical composition is given, together with the prior thermomechanical treatment undergone by the sample, i.e., solution temperature, cooling rate to the test temperature, predeformation between the solution temperature and test temperature (if any), and the testing conditions (test temperature, holding time prior to deformation and strain rate). Finally, the results of the precipitate analysis (type and size of the precipitates, and the interparticle spacing) at the grain boundaries and within the matrix are presented. From these published results it appears that AlN particles have been observed in Al bearing steels, depending on the chemical composition and thermomechanical history.

Table 6.2

Type, size and interparticle spacing of precipitates in C-Mn-Al steels for different chemical compositions and thermomechanical treatments. ST, PT, TT and HT stand for Solution Temperature, Predeformation Temperature, Test Temperature and, Holding Time, respectively. Data taken from the literature.

	Chemical Composition (wt%)				Thermomechanical Treatment											Precipitate Analysis				
					Solutionizing			Predeformation				Testing				Grain Boundaries			Matrix	
Ref	C	Al	Ti	N	ST °C	HT min	C.R. °C/mn	PT °C	HT (min)	ε %	ε s^{-1}	TT °C	HT (min)	ε s^{-1}	RA %	type	size nm	inter. nm	type	size nm
					850										65	AlN	35	-	none	-
					1000										88	AlN	55	-	none	-
70	.151	.017	-	.004		5	60	-	-	-	-	850	5	3x10^{-3}						
					>1000										>90	none	-	-	none	-
96	.15	.017	-	.006	850	15	-	-	-	-	-	850	15	3x10^{-3}	46	AlN	39	32		
					1050	15	-	-	-	-	-	1050	15	3x10^{-3}	80	AlN	51	84		
66	.15	.032	.002	.004	1350	5	60	-	-	-	-	750	?	5x10^{-3}	38	none	-	-	none	-
						5	60	1050	-	?	5x10^{-3}	750	?	5x10^{-3}	80	none	-	-	none	-
31	.175	.017- .03	.0004	.006- .02	1350	.3	45	900	3	0	0	1020	?	1.4x10^{-3}	100	none	-	-	none	-
								900	10	0	0	1020	?	1.4x10-3	100	none	-	-	none	-
								900	120	0	0	1020	?	1.4x10^{-3}	43	AlN	100*	few	TiAlCN	100
19	.21	.03	-	.012	1300	10	140	-	-	-	-	800	1	.83x10^{-3}	50	AlN	~100	250	none	-
									-			800	120	.83x10^{-3}	42.5	AlN	~200	500	none	-
								1100	120			800	1?	.8310^{-3}	95	AlN	~500	-	none	-

*Length of the AlN dynamically precipitated.**Some coarse AlN particles were also found.

Direct heating

AlN precipitates have been generally detected at the austenite grain boundaries and not in the matrix [71,96]. Thus, in steel P, the ductility trough in the austenite phase is caused by the AlN precipitates inherited from hot rolling, preventing the grain boundaries from moving and providing sites for nucleation of cavities. In the temperature range 950-1000°C, precipitate coarsening allows the grain boundaries to migrate, thus restoring the ductility.

Annealing and sensitizing

Annealing and sensitizing, although coarsen the grain size, improve hot ductility because the sluggish kinetics of AlN precipitation lead to grain boundaries which are relatively precipitation free [19-21,24,30,31,35,38-40,46,51,66,68-71,76]. This is consistent with the analysis of the previous section, where the low stress difference between the maximum stress after direct heating and sensitizing (or annealing) is an indication that no precipitation has occured. For these two heat treatments, a ductility trough would be expected to occur on phase transformation, which occurs at temperatures below the range examined.

6.2.3.2 C-Mn-Al-Nb steels

For C-Mn-Al-Nb steels, the precipitation data taken from the literature is presented in Table 6.3. The type of particles detected in these steels are mainly Nb(CN).

Direct heating

On direct heating, at 850°C, AlN particles have been observed at the grain boundaries and NbCN in the matrix and at grain boundaries. For both the AlN and NbCN particles at the grain boundaries, the particle size is typically 10 to 35 nm and, in the case of Nb(CN), between 5 and 10 nm in the matrix [71].

Annealing

As can be seen in Table 6.3, niobium carbonitrides precipitate both within the matrix and at the grain boundaries, but because of sluggish kinetics,

Table 6.3

Type, size and interparticle spacing of precipitates in C-Mn -Nb-Al steels for different chemical compositions and thermomechanical treatments. ST, PT, TT and HT stand for Solution Temperature, Predeformation Temperature, Test Temperature and, Holding Time, respectively. Data taken from the literature.

	Chemical Composition (wt%)					Thermomechanical Treatment										Precipitates Analysis					
						Solutionizing			Predeformation			Testing				Grain Boundaries			Matrix		
Ref	C	Al	Nb	Ti	N	S.T. °C	H.T. min	C.R. °C/mn	P.T. °C	ε %	$\dot{\varepsilon}$ s^{-1}	T.T. °C	H.T. (min)	$\dot{\varepsilon}$ s^{-1}	RA %	type	size nm	inter. nm	type	size nm	inter. nm
30	.1	.036	.026	-	.0075	1560	5	100	-	-	-	900	5	5x10^{-3}	42	NbCN	25	50	NbCN	20	-
												1050	5	5x10^{-3}	92	none	-	-	NbCN	45	-
169	.14	.025	.038	-	.0024	1300	10	120	-	-	-	800	1	5x10^{-4}	14	NbC	coarse	-	NbC	~nm	-
																NbCN	coarse	-	NbCN	~nm	-
						1300	10	120	800	10	4x10^{-4}	800		.8x10^{-1}	20	NbC	coarse		NbC	~nm	-
																NbCN	coarse		NbCN	~nm	-
						1300	10	120	800	10	4x10^{-4}	1100		.8x10^{-1}	70	NbC	coarse		NbC	500	-
																NbCN	coarse		NbCN	500	-
71	.12	.017	.034	-	.010	850	5	60	-	-	-	850	5	3x10^{-3}	52	NbCN	35	-	NbCN	5-10	-
																AlN	35				
						1100	5	60	-	-	-	850	5	3x10^{-3}	80	-	-	-	NbCN	70	-
						1200-1360	5	60	-	-	-	850	5	3x10^{-3}	25	NbCN	10	-	NbCN	<10	-
38	.14	.038	.04	-	.006	1560	-	60	-	-	-	950	-	1.3x10^{-2}	70	NbCN	10-20	-	NbCN	10-20	-
66*	.14	.039	.039	.004	.006	1350	5	60	-	-	-	850	-	5x10^{-3}	32	NbCN?	5	-	NbCN?	5	-
							5	60	1050	?	5x10^{-3}	850		5x10^{-3}	70	NbCN	20-150	-	NbCN	20-150	-
47	.12	.015	.035	-	.010	1330	10	60	-	-	-	870	5	3x10^{-3}	25	NbCN	15	60	NbCN	7	
								cycl**	-	-	-	870	5	3x10^{-3}	18	NbCN	15	60	NbCN	7	
								60	-	-	-	1050	5	3x10^{-3}	95	NbCN	45	150	NbCN		few
								cycl**	-	-	-	1050	5	3x10^{-3}	25	NbCN	35	80	NbCN		few

*These workers do not mention if the precipitates are intergranular or within the matrix, **Cyclic cooling.

Table 6.3 (continued)

Type, size and interparticle spacing of precipitates in C-Mn -Nb-Al steels for different chemical compositions and thermomechanical treatments. ST, PT, TT and HT stand for Solution Temperature, Predeformation Temperature, Test Temperature and, Holding Time, respectively. Data taken from the literature.

	Chemical Composition (wt%)					Thermomechanical Treatment										Precipitates Analysis					
						Solutionizing			Predeformation			Testing				Grain Boundaries			Matrix		
Ref	C	Al	Nb	Ti	N	S.T. °C	H.T. min	C.R. °C/mn	P.T. °C	ε %	$\dot{\varepsilon}$ s^{-1}	T.T. °C	H.T. (min)	$\dot{\varepsilon}$ s^{-1}	RA %	type	Size nm	inter. nm	type	Size nm	inter. nm
19	.21	.012	.055	-	.0027	1300	10	140	-	-	-	800	120	$.83x10^{-3}$	25	NbCN	50-100	200	NbCN	3-9	-
38	.16	-	.032		.009	1330	10	60	-	-	-	850	-	$3x10^{-3}$	35	NbCN	19	300	NbCN	?	?
44	.14	.022	.038	-	.006	1330	5	60	-	-	-	850	-	$3x10^{-3}$	35	NbCN	14	300	NbCN	?	
		.072	.035	-	.0057	1330	5	60	-	-	-	850	-	$3x10^{-3}$	20	NbCN	9	60	NbCN	?	
49	.16	-	.032		.009	1330	10	60	-	-	-	850	-	$3x10^{-3}$	35	NbCN	19	300	NbCN	?	?
49	.16	.049	.042	-	.0062	1330	5	60	-	-	-	850	-	$3x10^{-3}$	35	NbCN	~9	~60	NbCN	fine	-
								1500	-	-	-	850	-	$3x10^{-3}$	21	NbCN	6	30	NbCN	fine	-
96	.12	.015	.034	-	.010	850	15	-	-	-	-	850	-	$3x10^{-3}$	43	AlN-	45	64	NbCN	30	-
						1050	15	-	-	-	-	1050	-	$3x10^{-3}$	55	NbCN	58	127		35	-

*These workers do not mention if the precipitates are intergranular or within the matrix, **Cyclic cooling no AlN precipitates have been detected. Typically, for cooling rates in the range 60-120°C/min, the grain boundary particle size varies between 10 and 50 nm. This particle size range is associated with a reduction of area values between 25 and 40% for a strain rate of $10^{-3}s^{-1}$ and for the temperature range 800-900°C. Under the same testing conditions, the size of the particles in the matrix is very fine, in the range 5-15 nm. Again, this confirms that the $\Delta\sigma$ increase seen earlier may be due to precipitation.

Sensitizing and melting

On cooling from the melt a particle size of 25 nm was measured for NbCN at the grain boundaries and 20 nm within the grains, this value is comparable to those observed after annealing [30]. No AlN was detected.

6.2.3.3 C-Mn-Al-Nb-Ti steels

Precipitation data from hot ductility work on Nb-Ti bearing steels is sparse. For these chemical compositions, two types of precipitates are expected: NbCN and TiN, but mixed precipitates of NbTiCN and NbCN particles are actually observed, as can be seen in the compiled data presented in Table 6.4.

Several publications exist where NbTiCN precipitates were analysed in continuously cast [162-165,167] or rolled [162,166,167] products. These investigations are relevant for the direct heating treatment because steels A, B and C were received as rolled, and grade S as cast. Thus, the precipitates in the temperature range 800-900°C are inherited from the prior thermomechanical treatment (i.e. hot rolling for steels A, B, and C, as cast for steel S). Furthermore, included in Table 6.4 is precipitation data from one investigation [166] which examined the precipitates present after a thermal cycle treatment simulating the heat affected zone (HAZ) during welding, where the annealing temperature and cooling rate were similar to the annealing treatment used in the present investigation.

Direct heating

In as cast (CC conditions) material containing 0.075 wt% C, 0.011 wt% Ti, 0.04 wt% Nb and, 0.006 wt% N, four types of precipitates have been found at

Table 6.4

Type, size and interparticle spacing of precipitates in C-Mn-Nb-Al-Ti steels for different chemical compositions and thermomechanical treatments. ST, PT, TT and HT stand for Solution Temperature, Predeformation Temperature, Test Temperature and, Holding Time, respectively. Data taken from the literature.

	Chemical Composition (wt%)					Thermomechanical Treatment										Precipitates Analysis					
						Solutionizing			Predeformation			Testing				Grain Boundaries			Matrix		
Ref	C	Al	Nb	Ti	N	S.T. °C	H.T. min	C.R. °C/mn	P.T. °C	ε %	$\bar{\varepsilon}$ s^{-1}	T.T. °C	H.T. (min)	$\dot{\varepsilon}$ s^{-1}	RA %	type	Size nm	inter. nm	type	Size nm	inter. nm
30	.115	.023	.023	.02	.008	1560	5	100	-	-	-	900	5	5×10^{-3}	48	NbTiCN 80% Nb	l=100 e=40	130	NbTiCN	15	-
30	.115	.023	.023	.02	.008	1330	5	100	-	-	-	850	5	5×10^{-3}	69	none	-	-	TiN	40	-
169	.14	.036	.034	.019	.0012	1300	10	120	800	10	4×10^{-4}	900	10	$.83 \times 10^{-1}$	60	NbC	fine	-	NbC TiN	fine coarse	
44	.14	.035	.04	.04	.0043	1330	10	60	-	-	-	750	-	3×10^{-3}	43	NbC	16	60	?	?	?

room temperature, all of which are mixed Nb-Ti particles. They can be classified in terms of shape and diameter [164]:

(i) $d<20$ nm, small TiNbCN (Nb rich) carbonitride particles, roughly spherical
(ii) $20<d<50$ nm, polyhedral or cuboidal Ti rich TiNbCN particles located at prior austenite grains;
(iii) $50<d<200$ nm, cuboidal, small dendritic or angular; Ti rich TiNbCN particles
(iv) $d>200$ nm, dendritic or angular Ti rich TiNbCN particles).

Type (i) nuclei are believed to form in the lower part of the austenite range, the spherical shape strongly suggesting a Nb rich phase mixed with some Ti. Another analysis performed on as cast steels with similar compositions confirms these observations except that only precipitates larger than 20 nm were detected [165]. The regular solution model used by these workers predicts that precipitation starts with TiNbCN in the high temperature range followed by epitaxial growth of NbCN on TiNbCN particles in the low temperature range.

The evolution from as-cast precipitates to precipitates in hot rolled steel occurs via the transformation of the particles to a Ti rich compound of the form $Ti_xNb_{(1-x)}N$ during soaking. This is followed by the precipitation of Nb rich particles during controlled rolling, either epitaxially on the TiNb(N) particles [168] or independently [162]. The result is a particle distribution of cuboidal TiNb(N), between 20 and 200 nm and spheroidal precipitates ($d<20$ nm) which are predominantly Nb(C,N) but containing some Ti.

Annealing

In general the presence of a fine intergranular network of NbC particles [44,169] with a fine NbC and coarse TiN precipitation within the matrix [169] is observed after annealing and deformation (Table 6.4). However, it should be mentioned that in one study [30] no NbC particles were detected at the grain boundaries but TiN was observed in the matrix.

A study of the heat affected zone (HAZ) after a weld thermal cycle similar to that used during annealing [166], shows that the mixed TiNbCN particles inherited from the as-cast or as-rolled structure evolve towards an equilibrium composition, which can be predicted using the model of Houghton et al. [162,167,170]. With increasing annealing temperature the precipitates are enriched in Ti and show the cuboidal morphology characteristic of Ti-rich precipitates. On subsequent cooling to the test temperature and deformation, NbCN particles precipitate either epitaxially [168] on the existing TiNbCN, or independently.

Sensitizing and melting

Only one study has been carried out on C-Mn-Al-Ti-Nb steels following prior melting and deformation at 900°C [30]. Here, there is evidence of complex NbTi(CN) precipitates with 80% Nb, both at the austenite grain boundaries and within the matrix. The intergranular precipitates were found to be elongated in shape (100 nm length and 40 nm width), i.e. coarser than those found in Nb bearing steel (Table 6.2) [30], leading to improved ductility. Particle analysis of the fusion line of a weld has also revealed the presence of large cuboidal Ti rich precipitates (~45nm), with some spheroidal Nb particles which have grown on TiN [168].

As noted earlier, melting and sensitizing treatments differ in that the former leads to non-equilibrium segregation during solidification, therefore producing coarse particles, as observed as-cast material [162,164,165]. Although there is no precipitation analysis of specimens of Nb-Ti bearing steel available, it can be assumed that sensitizing will lead to an homogeneous solute distribution. The fast cooling to the test temperature used in the present work is likely to lead to fine precipitation of TiN particles on which NbCN grows epitaxially or precipitates independently [168].

From this survey, the type of precipitates likely to be present in the grades used in this work are listed in Table 6.5. Knowing the compositions of each steel, and the solubility products for the precipitates present, solution temperatures can be calculated as shown in the next section.

Table 6.5

Precipitates present in the investigated steels after direct heating, annealing and, sensitizing treatments.

Steel	Direct heating (900°C)	Annealing		Sensitizing	
		1330°C	900°C	1480°C	900°C
P	AlN	none	none	none	none
A	TiNb(CN) NbC	TiNbCN	TiNb(CN) NbC	few large TiN	TiN NbC
B	TiNb(CN) NbC	TiNbCN	TiNb(CN) NbC	few large TiN	TiN NbC
C	TiNb(CN) NbC	TiNbCN	TiNb(CN) NbC	few large TiN	TiN NbC
S	TiNb(CN) NbC VC	TiNbCN	TiNb(CN) NbC	few large TiN	TiN NbC

6.2.4 Solubility Products and Precipitation Kinetics of Carbides, Nitrides, and Carbonitrides

6.2.4.1 Simple precipitates

In the absence of solubility equations concerning complex precipitates such as NbTiCN, those equations established for simple precipitates (i.e TiN, NbC, NbCN, VC) could be used to calculate precipitate dissolution temperatures. The solubility products of the carbonitrides which can be observed in the present steels are given in Table 6.6.

The following should be noted:

$NbC_{0.87}$ and NbC_xN_y

In Nb bearing steels, NbCN precipitates are observed in preference to NbC, but, because of the presence of Ti, most of the nitrogen is combined with Ti and NbC may form. However, since some N remains in solution, NbCN can eventually precipitate. Therefore, the dissolution temperatures of both NbC and NbCN are calculated for comparison (section 6.2.4.3). Liu [171] has compiled different formulae for dissolution of NbC_x precipitates, but only the equation relating to austenite alloyed with manganese [172], has been used here. Both equations of Irvine et al. [173] and Mori et al. [174] were employed for NbC_xN_y (Table 6.6).

TiN

Of the solubility products available for TiN [171], that of Matsuda and Okamura [175] was regarded as being the most appropriate. It is applicable up to 1450°C for steels containing 1.5 wt% Mn and 0.3 wt% Si.

6.2.4.2 Complex precipitates

Experimental evidence shows that Ti, Nb, C and N form a continuous solid solution with Ti and Nb on substitutional sites and C and N in the interstitial sites in the structure (NaCl) [176] of the carbonitride [162-167,177]. The formation of such a precipitate can be expressed as follows:

Table 6.6

Solubility products of Al, Nb, Ti, and V nitrides, carbides, carbonitrides.

Precipitates	Temp. range (°C)	$\log(M)(I)^x = A + B/T$			Ref
		x	A	B	
AlN	900-1350	1	1.03	-6770	178
NbC_x	900-1200	0.87	3.11	-7520	172
Nb(C+12/14N)	900-1300	1	2.26	-6770	173
$NbC_{0.7}N_{0.2}$	1000-1300	0.7	4.12	-9454	174
TiN	1250-1450	1	0.32	-8000	175
VC_x	920-1150	0.75	4.24	-7050	178

$$(1-x)Nb+xTi+(1-y)N+yC=Ti_xNb_{1-x}C_yN_{1-y} \qquad (6.5)$$

Here, homogeneous equilibria both within and between isolated precipitates in Fe solution, and a regular solution are required in order to evaluate the solubility. The calculation incorporates the influence of the free energy of mixing of the precipitate into the solubility relationships.

The cumulative precipitation sequence of a steel of chemical composition close to steel A (0.05 wt% C, 0.01 wt% N, 0.05 wt% Nb and 0.01 wt% Ti) is illustrated in Fig. 6.8 [170]. For example at 1000°C the mole fraction of Ti is a, the mole fraction of N is (a + b), the mole fraction of Nb is (b + c) and finally, the mole fraction of C is c. In the mixed compound $Ti_xNb_{1-x}(C_yN_{1-y})$, the atom fraction x of Ti is given by the ratio a/(a + b + c), and y, the atom fraction of carbon, is c/(a + b + c). Therefore, with this method the composition of the mixed carbonitride is known at any temperature.

As seen in Fig. 6.8, the precipitation of the complex compound $Ti_xNb_{1-x}(C_yN_{1-y})$ initiates at extremely high temperatures due to the high stability of TiN. It can thus be considered that TiN essentially acts as a "stabilizing" agent for $Nb(C_y,N_{1-y})$, which will not normally precipitate at temperatures greater than 1200°C. Thus, on subsequent cooling from any annealing temperature, since the mole fraction of TiN changes little, the precipitation reaction effectively involves only Nb(C,N). Above 1400°C, the amount of Nb combined with Ti can be considered as negligible and the precipitates are basically TiN. The influence of C and Nb on the Fe-Nb-Ti-N-C system with 0.01 wt% Ti and 0.01 wt% N, is displayed in Figs. 6.9 and 6.10, respectively. Increasing the carbon and niobium content increases the stability of $Ti_xNb_{1-x}(C_yN_{1-y})$ precipitates i.e. Nb goes into solution at a higher temperatures.

6.2.4.3 Precipitate dissolution temperatures and volume fraction

With the help of the solubility products given in section 6.2.4.1 it is possible to calculate the temperature of dissolution of the precipitates present in

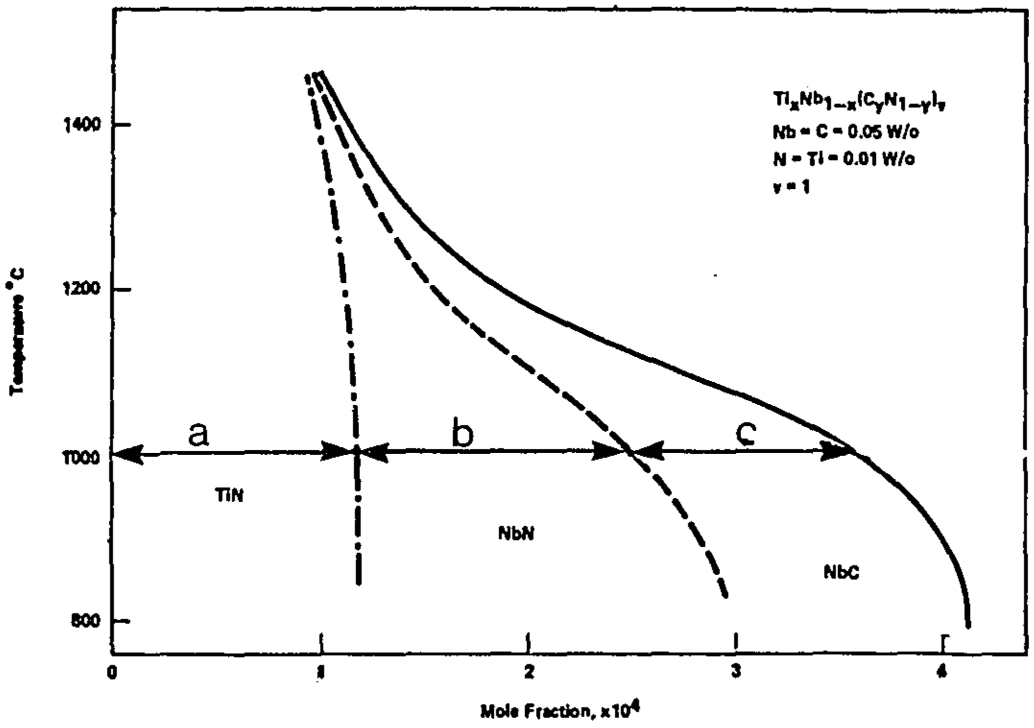

Fig. 6.8: Cumulative mole fraction and precipitation sequence in Fe-Ti-Nb-C-N and in Fe-Nb-C-N of nominal composition: 0.01 wt% Ti, 0.05 wt% Nb, 0.01 wt% N, 0.05 wt%C [170].

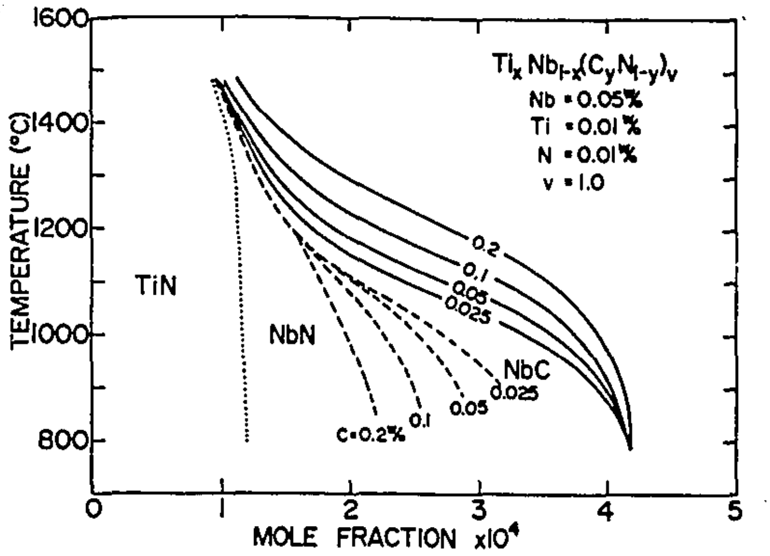

Fig. 6.9: Influence of the carbon content on the precipitation profile of the Fe-Ti-Nb-C-N system [170].

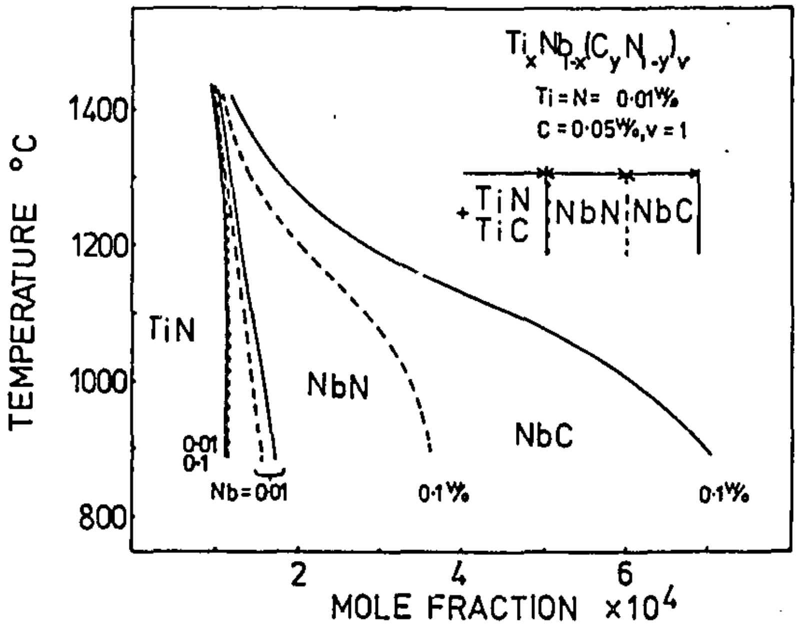

Fig. 6.10: Influence of the niobium content on the precipitation profile of the Fe-Ti-Nb-C-N system [170].

the investigated materials. In addition, the volume percent (VP) of XY precipitates (X=metal, Y=non-metal) at 900°C was calculated using the following equation [178]:

$$VP=\frac{\rho_{Fe}M_{XY}}{\rho_{XY}M_{X}}[\%X]=A[\%X] \qquad (6.6)$$

Where ρ is the density, M the molecular mass, and [%X] is the concentration of metal precipitated in mass percent. The proportionality factors, A, for AlN, NbC_x, TiN and VC_x are reported in Table 6.7. For $Ti_xNb_{1-x}C_yN_{1-y}$ precipitates, the density is not available in the literature, but can be calculated in the following way: $Ti_xNb_{1-x}C_yN_{1-y}$ has the same crystallographic structure as NbC, NbN, TiC and TiN and because of this it is assumed here that Vegart's law can be applied to density (see Appendix VI), i.e:

$$\rho_{Ti_xNb_{(1-x)}C_yN_{(1-y)}}=xy\rho_{TiC}+y(1-x)\rho_{NbC}+x(1-y)\rho_{TiN}+(1-x)(1-y)\rho_{NbN} \qquad (6.7)$$

Thus, for example, when x=0 and y=1 then $\rho_{TixNb1\text{-}xCyN1\text{-}y}=\rho_{NbC}$. The coefficient A in equation 6.6 for $NbC_{0.7}N_{0.2}$ was also calculated with the method described above and is reported in Table 6.7.

Having determined the precipitates that are likely to be present in the various heat treated conditions and their respective solubility products, these data are used, below, to examine how the precipitates behave under the different thermal cycles. The dissolution temperatures for the precipitates are given in Table 6.8, along with their volume percent at 900°C, i.e. in the ductility trough.

Steel P

According to Table 6.5, only AlN precipitates can be present in steel P following the direct heating treatment. Since the dissolution temperature is calculated to be 1126.5°C, the AlN particles should be completely dissolved after annealing or sensitizing. On cooling to the test temperature, according to the literature, it appears that, in the C-Mn-Al steel (P), the holding time (3 min) prior to deformation is too short to allow static precipitation [83,179] of AlN. Moreover the Al level is too low for the occurrence of dynamic precipitation of

Table 6.7

A coefficents for AlN, NbC, NBCN, TiN, and VC precipitates.

Precipitates	A	Ref
AlN	3.66	178
NbC$_x$	1.15	178
Nb(C+12/14N) NbC$_{0.7}$N$_{0.2}$	- 1.12	- -
TiN	1.87	178
VC$_x$	1.60	178

Table 6.8

Dissolution temperatures (°C) and volume percent of Al, Nb, Ti, and V nitrides, carbides, and carbonitrides.

Precipitates	P	A	B	C	S
AlN	1126.5	-	-	-	-
VP of AlN (900°C)	0.0402	-	-	-	-
NbC$_x$	-	1063.5	1094	1126	1020.5
VP of NbC$_x$ (900°C)	-	.0286	.0301	.0322	.0170
Nb(C+12/14N) NbC$_{0.7}$N$_{0.2}$	- -	1110 1100.5	1149 1120.5	1192 1142	1057 1059.5
VP (900°C) NbC$_{0.7}$N$_{0.2}$	- -	.0312	.0317	.0321	.0200
TiN	-	1629	1629	1629	1571
VP of TiN (900°C)	-	.0242	.0242	.0242	.0242
VC$_x$	-	-	-	-	863
VP of VC$_x$ (800°C)	-	-	-	-	.0905

AlN in the austenite [180,181]. Therefore AlN will not reprecipitate at the test temperature or during the test.

Steels A, B and C

According to the literature, the particles likely to be seen following a direct heating treatement are TiNbCN (i.e. cuboidal Ti rich precipitates) and NbC (Table 6.5). However, the dissolution temperatures and volume fraction of precipitates in these steels were calculated assuming the presence of single precipitates (i.e. only NbCN and TiN are present) or complex precipitates TiNbCN for comparison.

i) simple precipitates

From Table 6.8 it can be seen that all the Nb is in solution at the temperature of 1200°C. Thus, according to this model, all the NbCN particles are dissolved at the annealing and sensitizing temperatures.

The dissolution temperature of TiN predicted by the solubility product of Matsuda and Okamura [175] is much higher than the upper limit of the temperature range of their studies. For such temperatures, Turkdogan [178] claims that the solubility product of an XY_n compound in the δ (or α) ferrite (K_δ) phase can be determined from the solubility product in the austenite (K_γ) through the following equation:

$$K_\delta = K_\gamma \frac{[\%X]_\delta [\%Y]_\delta^n}{[\%X]_\gamma [\%Y]_\gamma^n} \tag{6.8}$$

where $[\%X]_\delta/[\%X]_\gamma$ is given in the work of Turkdogan [178] for Ti and N. The solubility product becomes:

$$Log\,K_\delta = Log\,K_\gamma + 0.180 - 2020/T + 0.93 = -10020/T + 1.43 \tag{6.9}$$

When applied to steels A, B and, C, the dissolution temperature of TiN in these materials is 1614°C and 1566°C for grade S, temperatures which are not very different to those calculated with the solubility product of Matsuda and Okamura [175] (Table 6.8). These values are above the solidus of steel, and therefore indicate that in the present experimental work, the TiN particles are never fully dissolved even at the sensitizing temperature.

The amount of nitrogen remaining in solution after combining with Ti, rather than the total nitrogen, was used to determine the dissolution temperature of NbC_xN_y particles. The solubility product of TiN (Table 6.6) gives values for N in solution of 0.00625 wt% for steels A, B and C, and 0.0045 wt% for grade S. These can be considered as constant in the temperature range 800-1100°C. For steels A, B and C, NbCN precipitates out at about 50°C higher than NbC_x. From Table 6.8 it can be seen that, for all the grades, Nb is completely in solution at the temperature of 1200°C. Thus, according to this model, at the annealing and sensitizing temperatures all the NbCN particles are dissolved.

In contrast to AlN, NbC_xN_y will reprecipitate after annealing or sensitizing. NbC_xN_y precipitation in undeformed austenite has been found to be sluggish [182,183] requiring an incubation time of approximately 30 min at 900°C in a 0.04 Nb wt% steel [183]. Therefore, the holding time prior to deformation is too short to allow static precipitation of NbC_xN_y in steels A, B, C and S.

In deformed austenite, the precipitation start time has been found to occur between 10 and 50 s at 900°C [184,185]. Thus, it is expected that the decrease in ductility observed in steels A, B and C after annealing or sensitizing is due to the dynamic precipitation of NbC_xN_y.

ii) complex precipitates

According to Table 6.5, TiNbCN and NbC precipitates are present following a direct heating treatment. An estimation of the chemical composition, mole fraction and volume percent of the $Ti_xNb_{1-x}C_yN_{1-y}$ precipitates can be done graphically (Fig. 6.8) based on the work of Houghton [170] at 900 and 1330°C (annealing temperature). The results, presented in Table 6.9, show that at 1330°C not all the Nb is in solution, in contrast to the predictions of the non mixing model. For example, this model predicts the following composition for steel C at the temperature of 1330°C: $Ti_{0.89}Nb_{0.11}C_{0.06}N_{0.94}$. This observation is important with respect to the annealing treatment, i.e. not all the Nb is available for reprecipitation at the

Table 6.9

Estimated chemical composition, mole fraction (MF) and, volume percent (VP) of $Ti_xNb_{1-x}C_yN_{1-y}$ precipitates at 900 and 1330 °C. Steels A, B and C.

Steel	900°C				1330°C			
	x	y	MF (10^{-4})	VP	x	y	MF (10^{-4})	VP
A	0.49	0.221	3.07	0.054	0.89	0.06	1.60	0.026
B	0.47	0.285	3.19	0.0565	0.87	0.08	1.64	0.0265
C	0.47	0.32	3.22	0.0565	0.83	0.13	1.72	0.029

test temperature, because it is combined with some TiN. Although the model of Houghton cannot predict the composition of the complex above 1400°C, it can be seen in Fig. 6.8 that above 1400°C, the composition of the precipitate is very close to pure TiN. To the author's knowledge no data concerning the precipitation kinetics of $Ti_xNb_{1-x}C_yN_{1-y}$ are available.

Steel S

Finally, in steel S, the same types of precipitates as grades A, B and C are expected. In addition, $VC_{0.75}$ particles are present on the direct heating treatment, and can reprecipitate out at 865°C after annealing and sensitizing [186,187].

6.3 AUSTENITE GRAIN GROWTH IN MICROALLOYED STEELS

Austenite grain size in the temperature range 900-1400°C

The austenite grain size of rolled samples of the C-Mn-Al steel (grade P, Fig. 4.63) and C-Mn-Nb-Al-Ti steel (steels A, B and C, Fig. 4.64) after direct heating to 900°C is between 7 and 8 µm. In microalloyed steels the so-called grain coarsening temperature corresponds to partial dissolution and growth of precipitates, which renders them less effective in pinning the grain boundaries [188]. The grain coarsening temperature of the C-Mn-Al steel is between 1100 and 1200°C (Fig. 4.63), compared to 1050°C observed by Cuddy and Raley for a steel having the same AlxN product [188]. The difference could be due to the smaller initial grain size in the present study, (7-8 µm compared to 15-20 µm), which implies a smaller AlN particle size and/or a higher precipitate density [188]. The longer annealing time employed by these workers (30 min. compared to 10 min.) may also explain the higher grain coarsening temperature via precipitate coarsening [189].

Due to the pinning effect of the Ti rich precipitates, grain coarsening takes place at temperatures greater than 1330°C for grades A, B, C and S. This temperature is also higher than other values reported in the literature [167,188], but may again be explained by the shorter holding times in the present examination.

Following the direct heating treatment, the initial larger austenite grain size of steel S compared to grades A, B and C is probably due to the fact that the size of the precipitates is likely to be smaller and their density larger in the as-rolled structures [162,166] than in the as cast structure [164].

In its simplest form the relationship between grain diameter (D), particles diameter (d) and, volume fraction (f_v) of precipitates according to the Zener model is given by [188]:

$$D=\zeta\frac{d}{f_v} \tag{6.10}$$

where ζ is between 2/3 [183] and 1/6 [190]. Knowing the volume fraction of precipitates at a given temperature and the mean austenite grain size, the mean particle size can be estimated. For example, applied to steel P (C-Mn-Al), using the data given in Table 6.8, the corresponding AlN particles size at 900°C is between 7 and 28 nm. In the case of grades A, B and C the calculated diameter of the precipitates falls in the range 6 and 24 nm which emcompasses the 8 nm of $Ti_xNb_{1-x}C_yN_{1-y}$ precipitates observed in rolled plates by Suzuki et al. [166]. These calculations show that the precipitate size is very fine at 900°C (in the region of the trough).

Austenite grain size in the temperature range 1400°C-ZDT

From the grain size measurements performed at 1300°C (Fig. 4.63), the high temperature grain size (i.e. above 1400°C) of steel P is expected to be large, between 400-500 µm. Therefore, it is also expected that at the DDS temperature, the grain facets on the fracture surface should be also large. However, the grain size measurements of Fig. 4.63 were performed only in the single γ phase. When the γ transforms to δ, the δ grain size at the end of the transformation will be smaller than the prior γ, because there is more than one δ nucleation site per austenite grain. Note that Anger and Dubé [191] have observed a grain refinement of austenite after the transformation of a coarse α ferrite structure to austenite. Thus, on the fracture surface of all the steels (e.g. Figs 4.88 and 4.89) many small grains can be seen.

The appearance of these smaller grains on the fracture surface could also be due to the onset of dynamic recrystallization occuring just before rupture. However this is not likely to occur because:

(i) At the time of rupture the grain boundaries are melted, and

(ii) Wray (82) claims that no dynamic recrystallization occurs in the δ phase; this is supported by examination of the flow curve between 1480-1490 (Fig. 4.44) where no peak is observed.

Similarly, although no grain size measurements between 1400 and 1500°C were carried out on steels A, B and C, a grain size of about 450 μm would be expected in Nb-Ti steels [167,192] since above the grain coarsening temperature the pinning effect of TiN precipitates is relieved [188]. However, as for steel P, steel A (Figs. 4.90-4.93), and steel B (Figs. 4.94-4.97), clearly show smaller grains than might be expected.

The grain growth of steel C in the proximity of the DDS temperature, after a direct heating treatment, is much higher than for grades A and B (Figs. 4.91, 4.95 and 4.98). The γ/δ transformation start temperature in grade C is 10 to 15°C higher than the other steels (Table 4.2), allowing more grain coarsening than in grades A or B. There is also a possible pinning effect of γ grain growth by δ in steels [20]. According to the Fe-C phase diagram (Fig. 4.8) the proportion of γ /δ phases can be estimated at 1475°C using the lever rule. For a carbon level of 0.1 wt% (grade B), the percentage of γ and δ is 55 and 45 %, respectively, compared to 92 and 8 % for a C concentration of 0.12 wt% (grade C), very close to the peritectic composition. This lower amount of δ implies a lower pinning effect, thus allowing much greater grain growth in the γ+δ two phase region prior the completion of the γ to δ transformation. Therefore, the higher temperature of the γ/δ transformation together with the lower amount of δ phase can explain the larger grains observed in steel C.

The above arguments could also explain the grain coarsening behaviour of steel S, because the presence of Ni/Cr/V, has increased the onset of the γ/δ transformation by 6.5°C compared to steel A (Table 4.2). This difference would seem rather small to explain this grain coarsening behaviour, although

Weinberg has observed that grain coarsening could take place in an 0.06 wt% C steels over a temperature range of 8°C [25].

Alternatively, Lucke and Detert [193] have developed a theory of the grain boundary motion in the presence of impurities, based on grain boundary segregation, which can be summarized as follows. For a high solute level at the grain boundaries, the grain boundaries are held back by the solutes and their rate of migration is controlled by the speed of diffusion of the foreign atoms. For low concentrations, the grain boundaries cannot be held by the solutes, breakaway occurs and the interface moves much faster. Since steel S has been shown to have a much lower grain boundary solute concentration (section 5.2.2), grain growth is relatively easy.

6.4 INFLUENCE OF HEAT TREATMENT ON HOT DUCTILITY

On the basis of the previous sections the hot ductility behaviour of each steel following the three heat treatments employed (direct heating, annealing and, sensitizing) is analysed.

Steel P

In the 800-1300°C test temperature range, an increase of prior heat treatment temperature (i.e. going from direct heating, through annealing and up to the sensitizing treatment) increases the ductility of steel P (Fig. 4.22).

The microstructural characteristics associated with the direct heating treatment are:

(i) the precipitates are inherited from the previous thermomechanical treatment (i.e. hot rolling), and

(ii) the microstructure transforms *from* the α-ferrite phase *to* γ, as opposed to transforming *to* α-ferrite from austenite.

Because the transformation is from ferrite to austenite, the embrittlement based on the presence of thin film of ferrite at austenite grain boundaries will not occur. Nevertheless, the decrease in ductility at the low temperature side of the ductility trough appears to be associated with the final stages of the α-γ transformation (837°C). In the *early* stages of the α-γ transformation, where austenite presumably exists at ferrite grain boundaries, the duplex microstructure is able to accomodate the deformation, even if, as anticipated, a dense network of fine precipitates is present within the material. This occurs because ferrite is softer than austenite and is *not* present as a grain boundary film. As a consequence the deformation is localized mainly within the ferrite grains. Thus, at 800°C ductility of steel P is good because there is approximately 78 % of ferrite according to the Fe-C-1.5 Mn diagram [194]. Furthermore, according to investigations in the intercritical regions, austenite never forms continuous thin layers around ferrite grains but rather forms isolated islands [195-197]. Therefore, even if deformation leads to the nucleation of cracks at the austenite grain boundaries the coalescence is not possible because the austenite grains are isolated from each other. This is in contrast to what is observed on cooling from the single austenite phase, where a small amount of ferrite is extremely deleterious to ductility.

With increasing temperature, between 800°C and Ac_3, the ductility decreases because the ferrite volume fraction decreases and the deformation cannot be accomodated by the ferrite grains. During the transformation the existing network of AlN precipitates pins the austenite grain boundaries. Thus, after the completion of the α→γ transformation, in the single γ phase, embrittlement is due to austenite grain boundary precipitates, leading to the minimum in reduction of area which is observed at 900°C. The ductility increases with increasing temperature due to precipitate coarsening.

Annealing at 1330°C leads to complete dissolution of AlN precipitates, according to Table 6.5, and produces a coarse austenite grain size (475 μm). On cooling to the test temperature the ductility is excellent at and above 900°C,in agreement with Cardoso [114]. As noted in section 6.2.3, the holding time prior to deformation is too short to allow static precipitation, and the level of Al and N is too low for the occurrence of dynamic precipitation. Thus no embrittlement is expected to take place. However, below 900°C Cardoso [114] has shown that steel P displays a ductility trough in which the higher temperature side of the trough corresponds to the Ae_3 temperature, and is associated with the nucleation of strain induced film of ferrite at the austenite grain boundaries. Ductility starts to recover at the Ar_3 temperature.

As for annealing, the sensitizing treatment leads to a complete dissolution of AlN nitride precipitates. Grain boundary melting and the partial dissolution of MnS (leaving approximately half of the S level in solution) also occurs, but does not cause embrittlement in the low temperature austenite range (900-1000°C) at the strain rate used. This latter observation is important with respect to the results observed for the other steels in that any ductility trough observed in the other grades is unlikely to be attributable to the partial MnS dissolution at 1480°C and MnS reprecipitation during cooling. (However, it may be argued that MnS precipitation may only be effective in reducing hot ductility when the boundaries are pinned by the microalloy precipitates. Again in the case of sensitizing, because no AlN has precipitated, ductility remains high throughout the temperature range examined.

Ductility is high at or above 900°C after sensitizing. However, dynamic recrystallization occurs at and above 1000°C following sensitizing, indicating that dynamic recrystallization is not in itself a necessary requirement for a high ductility. This conclusion has been recently confirmed by Cardoso [114]. He quenched steel P after fracture from a temperature of 900°C, a temperature giving high ductility when strained at 10^{-3} s^{-1}. No evidence for dynamic recrystallization except in the final stage of necking, could be found on microexamination and there was no evidence of dynamic recrystallization from the tensile curve.

Sulphur segregation has been put forward as another explanation to account for the ductility trough. The works of Tacikowski [23] and Osinkolu et al. [198] have shown that the simultaneous presence of segregated sulfur and precipitated AlN can cause severe intergranular embrittlement, whereas the presence of AlN alone does not. However, the calculations for steel P show that the amount of sulfur in solution, and available for segregation at 900°C, is less than 1 ppm (Fig.5.3), a level well below the minimum required to lower the ductility [198]. In steel P the presence of segregated phosphorus may be equivalent to sulfur, but it has been shown that in the case of NbCN precipitates the presence of phosphorus does not cause any ductility trough [24,199].

Steels A, B and C

The analysis of these three Nb-Ti-Al steels have been grouped together because the influence of prior heat treatment is very similar, although there are qualitative differences. In the 800-1300°C test temperature range, an increase of prior heat treatment temperature (i.e. going from direct heating, through annealing and up to the sensitizing treatment) decreases the ductility of these steels (Figs. 4.23 to 4.25).

As suggested earlier (Table 6.5) in the direct heating treatment TiNb(CN) type cuboidal particles and spheroidal NbC precipitates occur in the as hot rolled plate of these steels [162]. The mechanism of embrittlement following direct heating is the same as for steel P. Above 1000°C NbC particles start to grow and dissolve and the ductility is improved. From Table 6.8, if it is assumed that all the Nb has precipitated only as NbC particles, the dissolution temperatures vary between 1100 and 1192°C for grades A, B and C. However, since some Nb is in the form of (Ti,Nb)N complete dissolution of the NbC particles occurs at 1100°C corresponding to almost 100% RA. The relatively fine austenite grain size ($\geqq 20$ µm) at 1200°C indicates that the network of TiNb(CN) particles persists to much higher temperatures. This confirms that, even if the size of Ti-rich particles is small and their density large, as suggested by the grain size measurement, these are not deleterious to ductility, probably because they are generally precipitated randomly in the matrix rather than at the grain boundaries.

After annealing at 1330°C, all the Nb rich precipitates are dissolved and only cuboidal TiNb(CN) particles remain undissolved. As seen previously, in steels containing only Nb, no static precipitation is expected to occur during cooling or holding prior to deformation. However, in Ti-Nb bearing steels it may be possible that TiNb(CN) particles act as nucleation sites for NbC particles, perhaps leading to some static precipitation of NbC. In any case, since cuboidal TiNb(CN) particles are not deleterious to hot ductility, NbC precipitated on the Ti rich particles will likewise cause no embrittlement. Thus the observed ductility trough is most likely due to dynamic precipitation of NbC at the grain boundaries and within the matrix.

After sensitizing, all precipitates are completely dissolved, except for large TiN cuboids, which play no role in hot ductility, apart from reducing the amount of Ti available for reprecipitation during cooling. Due to the fairly high cooling rate, TiN is likely to reprecipitate as a fine dispersion which again would probably act as nucleation sites for NbC precipitation. Thus the ductility starts to drop at 1100°C (100°C higher than after annealing) for steels A and B, and between 1150-1200°C for grade C. Compared to the annealing treatment, sensitizing leads to a wider and deeper trough. This may be due to:

(i) the larger amount of Nb available for precipitation after sensitizing because of the almost complete dissolution of (TiNb)N particles, and

(ii) the coarser austenite grain size after sensitizing which leads to a lower ductility and lower Ar_3 (leading to trough widening).

The differences between steels A, B and C are discussed in the next section.(6.5.1).

Steel S

Since this steel was received as cast, the precipitation pattern differs significantly from the as rolled grades. Verger-Gaugry et al. have shown that the minimum diameter of the precipitates is likely to be around 20 nm, but the size and shape of the particles can vary widely [164]. This relatively coarse particle size is in accord with the grain size of steel S, which is larger than for the rolled samples after the direct heating treatment. The ductility trough in the case of annealing is less deep than that obtained on direct heating (Fig. 4.26) suggesting a low amount of reprecipitation on cooling from the annealing temperature. This is in agreement with the analysis of the strength differential after annealing and direct heating (section 6.2.1), and is probably due to the presence of vanadium, as discussed in the next section.

After sensitizing, precipitation starts in the temperature range 1000-1100°C, and again analysis of the strength data suggests that the amount of precipitates is low (section 6.2.1). However, the ductility trough is wider and deeper than that due to direct heating. This behaviour can again be explained by the very coarse structure which is obtained after sensitizing (Fig. 4.80).

6.5 INFLUENCE OF CHEMICAL COMPOSITION ON DUCTILITY

6.5.1 Role of Carbon

The effect of increasing the carbon content up to the peritectic composition (steel C) on the hot ductility of Nb-Ti-Al steels (grades A, B and C) is to increase the depth and width of the ductility trough (Figs. 4.27-4.29). This influence of carbon is seen mainly after the sensitizing treatment (Fig. 4.29). In steel C, the steel grade with the highest C level (0.14 wt% C), the very poor ductility can be related to the much larger fracture facets observed on the fracture surfaces compared to those observed on steels A or B. The influence of carbon on hot ductility is discussed with respect to the various heat treatments.

Direct heating

Increasing the carbon content from 0.07 wt% to 0.10 wt% leads to a slight deepening of the trough (Fig.4.27). Since there is practically no difference in the austenite grain size of steels A, B and C (Fig. 4.64), the reduced ductility of steels B and C cannot be attributed to this factor. However, the estimated volume percent of $Ti_xNb_{1-x}C_yN_{1-y}$ precipitated at 900°C is slightly higher in steels B and C than in grade A (Table 6.6), which may explain the small reduction in the depth of the trough.

Annealing

After annealing, an increase of the carbon content slightly deepens the ductility trough, the explanation is essentially the same as for the direct heating treatment.

The higher carbon levels of steels B and C also widen the trough to lower temperatures because of an decrease in the Ar_3 (due to carbon). This effect is more pronounced in steel B than steel C, even though steel C has the higher C content. The reason for this is unclear.

On the low temperature side of the ductility trough, the ductility recovery occurs at higher temperatures than in previous experiments [21,200]. This effect is believed to be due to the finer grain size in grades A, B, C which raises the transformation temperature.

Sensitizing

The effect of carbon after sensitizing differs significantly from that of the other heat treatments (Fig. 4.29). While the minimum in reduction of area is only slightly changed by an increase of the carbon content, the ductility trough is widened to both higher *and* lower temperatures. This behaviour can be explained by the austenite grain size difference (Figs 4.77-4.79). For the reasons explained in the previous section, the sensitizing treatment leads to much coarser grains in the steel with the peritectic composition (steel C). The coarser structure in steel C influences the ductility by:

(i) increasing the temperature of the higher side of the trough because the ductility in the single austenite phase decreases with increasing grain size [20],

(ii) decreasing the Ar_3 temperature. In plain carbon steel with coarse grains (290-350 µm) the high temperatureside of the trough can be as high as the Ae_3, because of the production of thin films of strain induced ferrite around the grain boundaries. The trough will move to lower temperatures in response to decreases in Ar_3 [70].

Above the Ae_3 temperature embrittlement is due to the precipitation of the Nb carbonitride either epitaxially on the the TiN nitrides or independently in the matrix and at the grain boundaries.

Thus, the variation of the C level has a marked effect on the hot ductility of Nb-Ti-Al bearing steels only after the sensitizing treatment. The direct heating and annealing treatments reveal only small differences between the steels, because the precipitation characteristics of $Ti_xNb_{1-x}C_yN_{1-y}$ particles are only slightly affected by an increase of the carbon content.

To summarize, the influence of the carbon content on the hot ductility of Nb-Ti steels after sensitization is depicted in Fig. 6.11. Considering two C level ranges, one between 0.12 and 0.16 wt% (i.e. the peritectic composition) and the other between 0.07 and 0.10 wt%, the reduction of area versus temperature graph can be divided in four regions. Above 1300°C (region 1), some Ti rich

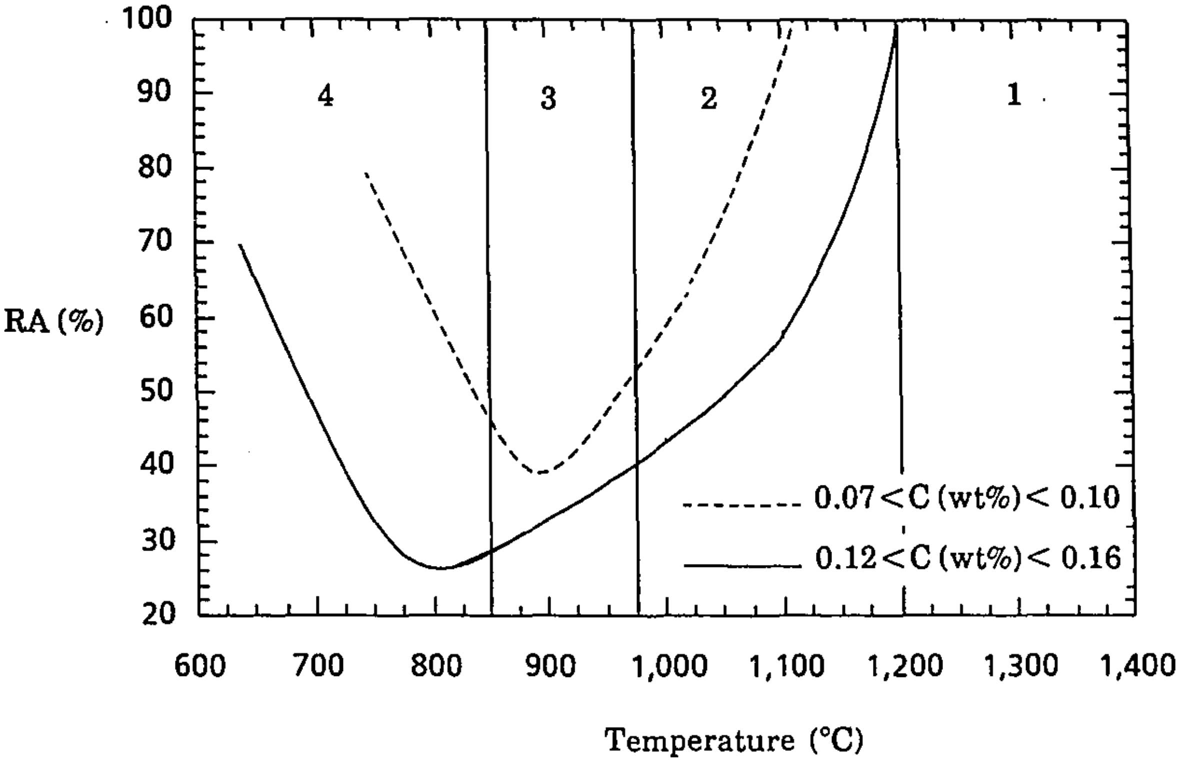

Fig. 6.11: Schematic diagram showing the influence of carbon content after sensitization of a microalloyed steel.

particles can precipitate but they are not deleterious to ductility. In temperature zone 2 (975-1200°C), the coarse structure together with the onset of precipitation leads to a decrease of the ductility; the peritectic composition exhibits a lower ductility because of a coarser grain size. In zone 3 (850-975°C) precipitation dominates the ductility and increasing the C level gives rise to a coarser grain size and a small increase in precipitation [201], leading to a further small deterioration in ductility. Ductility now is so low that changes in grain size can only have a small influence on the reduction area values. Temperature range 4 ($T<850°C$) corresponds to the nucleation of ferrite at the austenite grain boundaries at temperatures below the Ae_3. Here the higher carbon steels exhibit lower Ar_3 temperatures because of the carbon content and the coarser grain size, thus decreasing the temperature at which the ductility recovers.

6.5.2 Role of Microalloying Elements

6.5.2.1 Nb and Ti additions to C-Mn-Al steel

Direct heating

In the case of direct heating, where dissolution and not precipitation takes place, the addition of Nb and Ti to the C-Mn-Al steel was found to increase the ductility over the temperature and strain rate ranges investigated (Fig.4.30). This can be explained by considering the effects of separate additions of Nb and Ti to the C-Mn-Al steel. Although not specifically investigated here, the effect of Nb and Ti separately can be determined by comparing results from our work with those of Crowther and coworkers [96].

They found that, following a direct heating treatment, a Ti addition to a C-Mn-Al steel strongly improves the ductility, the ductility being better than that of plain carbon manganese steel. Here the explanation is straightforward; TiN precipitates at a high temperature and prevents AlN precipitation because most of the nitrogen is combined with TiN. TiN also grain refines the steel without precipitating at the boundaries.

Comparing our results to the above, the addition of Nb is clearly deleterious to the ductility of a Ti bearing C-Mn-Al steel, this effect being due to the presence of NbC precipitates (inherited from hot rolling) either in the matrix and within the grain boundaries. However, as already noted, the net effect of the joint presence of Nb and Ti is an *improvement* in the hot ductility of a C-Mn-Al steel. This can be explained by considering that the volume percent of AlN present at 900°C is much higher than that of NbC particles, according to Table 6.7. Furthermore, it has been shown that, for direct heating, AlN precipitates are seen mainly at the austenite grain boundaries whereas NbC particles are observed in the matrix as well as at the austenite grain boundaries [96]. There thus appears to be a higher volume fraction of precipitates at the austenite grain boundaries in the C-Mn-Al steel. Another cause of the ductility increase is the presence of TiNbCN on which NbC particles nucleate, thus reducing the amount of Nb available for precipitation as simple NbC.

Alternatively, it may be that the ductility improvement observed by the Nb addition may be due to NbC particles coarsening during the time of the experiment. When the particle coarsening is controlled by the volume diffusion of the slowest diffusing species (Nb in the present case), the size, r, of any precipitate of initial radius r_0 at time t is given by [189]:

$$r^3 - r_0^3 = \frac{8\sigma_p V_m C_0 t}{9kT} D_0 exp(-\frac{Q}{RT}) = Kt \qquad (6.11)$$

where σ_p is the surface energy between the particle and the matrix, C_0 the density of precipitates per unit volume, V_m molecular volume of the particle, k the Boltzmann constant and $D_0exp(-Q/RT)$ is the diffusion coefficient (of Nb in the austenite for the present case) at temperature T. Applied to NbC particles, the numerical values for σ_p, and V_m were taken from reference 202; D_0 and Q for niobium are given in reference 166, and C_0 was estimated from the interparticle spacing given in reference 96:

$\sigma_p = 15 x 10^{-7}$ J/cm^2
$V_m = 200$ nm^3
$D_0 = 4.92$ cm^2/s
$C_0 = 2.45\ 10^{-5}$ particles/nm^3

$Q = 285$ kJ/mole
$k = 1.38 \times 10^{-23}$/s
$T = 1123$°K
At 850°C, equation 6.11 reads:

$$r^3 - r_0^3 = 0.12t \tag{6.12}$$

where r and t are expressed in nm and second, respectively. For an experiment of 1h duration, the final size of a particle with an initial radius of 45 nm will be 45.07 nm. Particle coarsening during the time of experiment is therefore negligible.

Annealing and sensitizing

According to the present result (Fig. 4.31), in the austenite phase (i.e. at temperatures equal or greater than 900°C), and in contrast to direct heating, the addition of Nb and Ti to a C-Mn-Al grade is deleterious to ductility. This occurs because NbC can reprecipitate whereas AlN is sluggish to precipitate in austenite.

Continuing the comparison between our work and the results of Crowther et al. [96], it can be seen that after annealing, the addition of Nb to a C-Mn-Al-Ti steel is clearly deleterious to hot ductility at temperatures above 900°C, regardless of the strain rate (Fig. 4.31). Here the explanation is very simple; dynamic precipitation of NbCN takes place, whereas only TiN precipitation occurs in the C-Mn-Al-Ti steel. Examination of the present results with other research work indicates that the *combined* effect of Nb and Ti increases the RA values compared to the single addition of Nb [21]. The explanation of this behaviour arises from the presence of TiNbCN (Ti rich particles), which decreases the amount of Nb available for precipitation (section 6.4).

The C-Mn-Al steel ductility below 900°C, after annealing, was recently investigated by Cardoso [114]. His work shows that the ductility drops to 35% at 800°C at the strain rate of 10^{-3} /s, compared to 74% for steel A (C-Mn-Al-Nb-Ti) at the strain rate of 2×10^{-4} /s. (The lower strain rate used in the latter would be expected to reduce hot ductility, so the ductility improvement due to the Ti and Nb addition is very high.) Basically, there is a difference in the A_{r3} due to differing austenite grain sizes. After annealing, the austenite grain size in the C-Mn-Al steel is one order of magnitude larger than the C-Mn-Al-Ti-Nb steel (Figs. 4.63 and 4.64). In the latter, the larger grain boundary surface area raises the Ar_3 temperature. Thus, at 800°C, the austenite-to-ferrite transformation has just initiated in the C-Mn-Al steel and ductility is poor, whereas it has advanced significantly enough in the C-Mn-Al-Ti-Nb steel for recovery to have occurred.

However, in contrast to the annealing treatment, after sensitization the ductility of the C-Mn-Al steel at 800°C is *higher* than that of the Nb-Ti bearing steel (Fig. 4.32). In fact, the basic problem here is that no ductility trough is observed in the C-Mn-Al steel after sensitization. It could be argued that the ductility trough has moved to a temperature lower than 800°C. However, the austenite grain size after annealing is certainly larger than after sensitization because, on heating to the sensitizing temperature, the $\gamma \rightarrow \delta$ transformation leads to grain refinement as explained in section 6.3, then, on cooling, the $\delta \rightarrow \gamma$ transformation produces additional refinement, (assuming limited grain growth occurs after transformation). Thus, the ductility trough in steel P after sensitization can be expected to be seen at *higher* temperatures than after annealing. The fact that it does not appear in Fig. 4.32 may be explained if the width of the trough is very narrow due to the smaller grain size, as observed elsewhere [114], the trough falling somewhere between 800 and 900°C.

6.5.2.2 V adddition to Al-Nb-Ti steel

Direct heating

Compared to grade A (C-Mn-Al-Nb-Ti), the presence of V in steel S does not significantly affect the hot ductility behaviour (Fig. 4.30). However, in the case of direct heating, a comparison between the two steels is not possible because steel S is an as-cast material and grade A was hot rolled. Hot rolling leads to a significantly finer and more homogeneous precipitation than the as cast material [162,166,167]. This is reflected by the difference between the austenite grain size which is smaller in the rolled material (7-8 µm in steel A compared to 18-20 µm for grade S).

Annealing

Significant ductility improvement is seen when V is added to a Nb-Ti-Al bearing steel in that the RA increases from 56% for steel A to 83% in steel S at the temperature of 900°C. This behaviour can be explained on the basis of retardation of NbCN precipitation by the addition of V. Following the work of Akben and co-workers [186,187], the addition of V to Nb bearing steel retards the precipitation of NbCN, and the "nose" of the precipitation C curve drops to lower temperatures. This effect has been attributed to a decrease in the activity coefficient of carbon and nitrogen brought about by the V addition [186,187].

Sensitizing

Above 900°C, the ductility improvement due to V addition is also observed following sensitizing (Fig. 4.32), and the same explanation holds here. Furthermore, the more copious precipitation in steel A is more deleterious than the coarse structure of steel S, which, as explained previously, was inherited from the sensitizing treatment. Below 900°C, ferrite nucleation occurs, and in this case ductility is lower in coarse grained material because of a lower surface to volume ratio and because NbC precipitation takes place at lower temperatures in the V containing steel.

CHAPTER 7

CONCLUSIONS

In the present work the hot ductility behaviour of five microalloyed steels was investigated by tensile testing between 800°C and the solidus temperature. Deformation to fracture was carried out at strain rates in the range 10^{-2}-$2x10^{-4}$ s^{-1}, following three prior heat treatments: direct heating to test temperature, sensitizing at 1480°C and annealing at 1330°C. For testing above 1400°C, only the direct heating treatment was employed.

In agreement with previous studies, it has been found that microalloyed steels with high Mn:S ratio display two temperature ranges of embrittlement. The first one occurs at a temperature between 10 or 35°C below the solidus, and is caused by incipient melting at the grain boundaries. The second is in the temperature range 800-1200°C, and is associated with the presence of carbonitride precipitation at the grain boundaries and/or the austenite-to-ferrite phase transformation.

As a result of the investigations of the first embrittlement range, above 1400°C, the following conclusions can be drawn for the steels investigated:

1) With increasing carbon content or increasing microalloying addition level, the bulk solidus temperatures remain constant at about 1500°C.

2) For the Nb-Ti steels with a carbon content between 0.07 and 0.10 wt%, embrittlement occurs by incipient melting at the grains of the δ phase. Calculations of the grain boundary segregation have shown that, in this phase, the main segregating species is carbon.

3) For Nb-Ti steel with the peritectic composition (~0.14 wt% carbon) embrittlement occurs at a lower temperature than the low carbon steels, and in the duplex $\delta+\gamma$ phase region. Furthermore, incipient melting occurs at the grain boundaries of the austenite phase. Theoretical considerations have shown that much less carbon segregates to the austenite grain boundaries because of a less negative free energy of segregation. This apparently lowers the grain

boundary melting temperature of the austenite and consequently decreases the temperature of embrittlement.

4) There is no influence of Nb and Ti on the incipient melting temperature, but the addition of Cr leads to an increase of the grain boundary melting temperature by reducing the amount of segregated phosphorus and sulfur.

5) The coarse microstructure observed in the 0.14 wt% steel is explained by (according to the DTA results) the higher temperature of the austenite-to-δ ferrite phase transformation which allows more austenite grain coarsening to occur

6) The coarse grains which are observed in the low carbon steel containing Ni/Cr is attributed to high grain boundary migration rate because the retardation caused by segregated elements is diminished by the reduction of segregation.

In the temperature range 800-1300°C, it has been found that the influence of microalloying addition and carbon content in Nb-Ti steels depends strongly on the prior heat treatment. With respect to the direct heating treatment, the analysis of the experimental results leads to the following conclusions:

1) The C-Mn-Al steel displays a ductility trough in the temperature range 800-1100°C, which is caused by the presence of AlN precipitates (inherited from the rolled plates) at the grain boundaries.

2) The addition of Nb and Ti to C-Mn-Al steel *decreases* the depth of the ductility trough, through one or a combination of the following mechanisms:

(i) The absence of AlN particles at the grain boundaries via the formation of complex $Ti_xNb_{1-x}C_yN_{1-y}$ precipitates which have scavenged the nitrogen. Such precipitates are not deleterious to ductility.

(ii) The formation of $Ti_xNb_{1-x}C_yN_{1-y}$ particles also reduces the amount of Nb available for precipitation of NbCN particles at the grain boundaries.

(iii) In contrast to AlN particles, Nb precipitates are observed both in the matrix and at the grain boundaries, the latter precipitates being more deleterious to hot ductility.

(iv) The volume percent of AlN precipitates is higher in the C-Mn-Al steel than the volume percent of $Ti_xNb_{1-x}C_yN_{1-y}$ in the Nb-Ti steels.

3) The addition of V, Ni and Cr or an increase of the carbon content up to 0.14 wt% in the Nb-Ti bearing steel have no influence on the hot ductility following the direct heating treatment.

The findings and analysis of the effect of annealing and sensitizing on hot ductility in the temperature range 800-1300°C can be summarized as follows:

1) Embrittlement in the C-Mn-Al steel is suppressed in the temperature range 900-1100°C. This is due to AlN particle dissolution during the prior heat treatment, and the absence of AlN reprecipitation because the rate of AlN precipitation in austenite is very sluggish.

2) In the Nb-Ti steels, the annealing treatment increases the depth of the ductility trough, compared to the direct heating treatment, but the upper temperature side of the trough is slightly lowered. This is believed to be due to dissolution of Nb rich $Ti_xNb_{1-x}C_yN_{1-y}$ particles, and reprecipitation of finer particles at temperatures below 1000°C during cooling. For this thermal treatment only a slight influence of the carbon content were found.

3) The ductility trough of the Ti-Nb steels after the sensitizing treatment is wider and deeper than after annealing at 1330°C. This behaviour is associated with the grain coarsening that occurs during the sensitizing treatment.

4) In contrast to the other two prior heat treatments, after sensitization an increase of the carbon level up to 0.14 wt% increases the width of the ductility trough. The 0.14 wt% C steel also exhibits a coarser austenite structure inherited from the annealing at 1480°C, which decreases the ductility.

5) By comparing the present work with published literature it has been confirmed that the addition of Ti to a Nb bearing steel improves the

ductility. As before this is attributed to the combination of some Nb with Ti rich particles, reducing the level of Nb available for precipitation.

6) The addition of V, Ni and Cr to the Al-Nb-Ti steel increases the ductility in the temperature range of the trough because of the retardation of Nb precipitation due to the presence of vanadium. After sensitizing, the improvement due to V addition is seen in the temperature range 900-1100°C only. However, at 800°C the ductility of this grade is lower due to the coarser austenite structure inherited from the sensitizing at 1480°C and precipitation of NbCN. Since ferrite nucleates at the austenite grain boundaries, coarser grains decrease the rate of ferrite nucleation because of a lower surface to volume ratio, thus reducing ductility.

7) Analysis of the hot strength versus temperature curves for the different heat treatments has confirmed the absence of precipitation in the C-Mn-Al and V bearing steels after annealing and sensitizing. In addition, the difference between the maximum stresses after the direct heating and sensitizing treatments has shown that precipitation in the Nb-Ti steels occurs in the temperature range 1000-1100°C.

STATEMENT OF ORIGINALITY AND CONTRIBUTIONS TO KNOWLEDGE

With respect to investigations above 1400°C, the present thesis includes the following original contributions:

1) It is the first time that the solidus temperature has been *measured* (by DTA) and compared with the incipient melting temperatures following a direct heating treatment.

2) It has been shown that for a steel with a carbon level close to the peritectic composition, the fracture surface after rupture at the incipient melting temperature reveals larger grains than grades with a lower carbon content. This behaviour has been explained from the DTA results which show that for the peritectic composition the $\gamma \rightarrow \delta + \gamma$ transformation occurs at a higher temperature than the low carbon steels.

3) In this work, the theory of equilibrium segregation at the grain boundaries has been applied qualitatively to incipient melting for the first time. In order to calculate the free energy of segregation, it has been assumed that the α phase is an extension of the δ phase, in terms of segregation behaviour. On the basis that C, S and P are the main segregating species, these calculations lead to the following findings:

(i) At the grain boundaries of the δ ferrite phase, carbon is the major segregating element (80 at%), because it has the highest free energy of segregation and is present at concentrations levels *two* orders of magnitude higher than S or P.

(ii) In the austenite phase, the grain boundary concentration of carbon is much diminished (12 at%). Thus in steels with C concentration close to the peritectic, in which both δ and γ phases are present at the start of embrittlement, incipient melting occurs first at the γ phase, leading to a lower zero ductility temperatures. This in turn explains why the fracture surface for this grade displays fracture facets which are either smooth (austenite) or rough (δ ferrite).

5) It has been demonstrated qualitatively that the addtion of Cr decreases the amount of grain boundary segregation of phosphorus and sulfur, thus increasing the zero ductility temperature and possibly allowing more grain coarsening.

6) It has been shown that, following the $\delta \rightarrow \gamma$ transformation the δ ferrite grains are smaller than austenite grains.

In the temperature zone 800-1300°C, the influence of carbon on the hot ductility of Al-Nb-Ti bearing steels has been investigated following various heat treatments. Although the sensitizing treatment has been used in the past for the investigations of the effect of S and Mn on hot ductility, it has never been employed to study the ductility behaviour of microalloyed steels prior to the start of this study. With this respect it has been shown that:

1) the wider ductility trough of the 0.14 wt% C steel is due to a coarser austenitic structure inherited from the senzitizing treatment.

2) The improved ductility resulting from the addition of Ti to Nb containing steels has been attributed to the formation of complex Ti rich carbonitrides $Ti_xNb_{1-x}C_yN_{1-y}$ which are not deleterious to hot ductility, and reduce the amount of Nb available for precipitation as Nb rich particles.

3) The addition of V to a Nb-Ti bearing steel has been found to increase the ductility after the annealing treatment. This is explained by the retardation of Nb precipitation by V. The same effect is observed after sensitization in the temperature range 900-1000°C, however, at 800°C the ductility of the V containing steel is lower because of the coarser grains inherited from the sensitzing treatment and the precipitation of NbCN.

4) Hot strength data have been used to assess the onset of precipitation during hot ductility testing.

REFERENCES

1. H. Bessemer, J. of Iron and Steel Inst., 2, (1891), p. 23.
2. Junghans, German patent, cited in Ref.6.
3. A. Etienne and W.R. Irving, Proc of the 1985 international conference on continuous casting, "Continuous casting 85", October 1985, the Institute of Metal, London, England, October 22-24, (1985), p. 1.1.
4. D. Jaffrey, I. Dover and L. Hamilton, Metals Forum, 7, (1984), p. 67.
5. Amer. Iron & Steel Institute, 84th general meeting, "Energy conservation in the steel industry", (1976), p. 75.
6. R. Alberny, Revue de Métallurgie-CIT, 7, (1980), p. 581.
7. Y. Morita, H. Kawashima, M Nakamura, The Sumitomo Search, 30, (1985), p. 19.
8. G. Hollis, H. Bumberger, T. Fastner, F. Hirschmanner and K. Schwaha, Proc. of the 1985 international conference on continuous casting, "Continuous Casting 85", October 1985, The Institute of Metal, London, England, p. 46.1.
9. J. K. Brimacombe and K. Sorimachi, Met. Trans. B, 8B, (1977), p. 489.
10. G. Van Drunen, J. K. Sorimachi and F. Weinberg, Ironmaking and Steelmaking Quaterly, 2, (1975), p. 125.
11. S. Kojima, T. Matsukawa and M. Kadama, Third Process Technology Conf., Pittsburgh, Pensylvania, (1982), p. 255.
12. T. Matsumiya, M. Ito, H. Kajioka, S Yamaguchi and Y Nakamura,Trans. I.S.I.J., 26, (1986), p. 540.
13. H. Vom Ende and G. Vogt, J. Iron and Steel Institute, 210, (1972), p. 889.
14. M. H. Kamdar, 4th International Conf. on Fracture (ICF4), Waterloo, Canada, June 19-24, (1977), p. 387.
15. G. Bernard, J. P. Birat, B. Conseil, J. C. Humbert, Revue de Métallurgie, 7, (1978), p. 479.
16. W. J. Lankford, Met. Trans., 3, (1972), p. 1333.
17. G. A. Wilber, R. Batra, W.F. Savage, and W. J. Childs, Met. Trans. A, 6A, (1975), p.1727.

18. R. J. Gray, A. Perkins and B. Walker, Sheffield International Conference on Solidification and Casting, The Metals Society, London, (1977), p.967.

19. Y. Maehara and Y. Ohmori, Mat. Sciences and Eng., 62, (1984), p.109.

20. Y. Maheara, K. Yasumoto, Y. Sugitani and K. Gunji, Trans. I.S.I.J., 25, (1985), p. 1045.

21. N. E. Hannerz, Trans. I. S. I. J., 25, (1985), p.156.

22. D. N. Crowther and B. Mintz, Mat. Sciences and Techno., 2, (1986), p. 1099.

23. M. Tacikowski, Ph. D. thesis, Ecole des Mines de St Etienne, (1986), St Etienne, France.

24. P. Yi and A. Kobylanski, "Proc. of the International Symposium Simulation of Welding, Hot Forming and Continuous casting", May 2-4, (1988), Ottawa, Canada, in press.

25. F. Weinberg, Met. Trans., 10B, 1979, p. 219.

26. L. Ericson, Scand. J. of Metallurgy, 6, (1977), p. 116.

27. K. Yasumoto, Y. Maehara, S. Ura, Y. Ohmori, Mat. Sciences and Techno., 1, (1985), p. 111.

28. C. Ouchi and K. Matsumoto, Trans. I.S.I.J., 22, (1982), p. 180.

29. A. Norstrom and B. Johansson, Scand. J. of Metallurgy, 11, (1982), p. 139.

30. B. Mintz, Z. Mohamed, "Proc. of the International Symposium Simulation of Welding, Hot Forming and Continuous casting", May 2-4, 1988, Ottawa, Canada, in press.

31. B. Chamont, P. Chemelle, H. Biausser, "Proc. of the International Symposium simulation of Welding, Hot Forming and Continuous casting", May 2-4, 1988, Ottawa, Canada, in press.

32. H.G. Suzuki, S. Nishimura and S. Yamaguchi, Trans. I.S.I.J., 22, (1982), p. 48.

33. H. G. Suzuki, S. Nishimura and S. Yamaguichi "Proc. of the International Symposium simulation of Welding, Hot Forming and Continuous casting", May 2-4, (1988), Ottawa, Canada, in press.

34. H.G. Suzuki, S. Nishimura, J. Imanura, Y. Nakamura, Trans. I.S.I.J., 24, (1984), p.169.

35. T. H. Coleman and J. R. Wilcox, Mat. Sciences and Techno., 1, (1985), p. 80.

36. H.G. Suzuki, S. Nishimura, Y. Nakamura, Trans. I.S.I.J., 24, (1984), p. 54.

37. P. J. Wray, Metal Techno., 12, (1981), p.466.

38. B. Mintz, J. R. Wilcox, D. N. Crowther, Mat. Sciences and Techno., 2, (1986), p. 589.

39. J. R. Wilcox and R. W. K. Honeycombe, Mat. Sciences and Techno., 3, (1987), p. 849.

40. C. Nagasaki, A. Aizawa and J. Kihara, Trans. I.S.I.J., 27, (1987), p.512.

41. G. Bernard, Revue de Métallurgie, 77, (1980), p.307.

42. G. D. Funnel and R. J. Davies, Metals Techno., 9, (1978), p. 151.

43. G. D. Funnel, Heat Treatment and Forming Processes of Steels, Sheffield, The Metals Society, Ed. by C. M. Sellars and G. J. Davies, 1980, p. 104.

44. B. Mintz andJ. M. Arrowsmith, Heat Treatment and Forming Processes of steels, Sheffield, The Metals Society, Ed. by C. M. Sellars and G. J. Davies, 1980, p. 99.

45. K. Yamanaka, F. Terasaki, H. Ohtani, M. Oda, and M. Yamashima, Trans. I.S.I.J., 20, (1980), p. 810.

46. J. R. Wilcox and R. W. K. Honeycombe, Metals Techno., 11, (1984), p.217.

47. B. Mintz, J. M. Steward and, D. N. Crowther, Trans. I.S.I.J., 27, (1987), p. 959.

48. C. Nagasaki, A. Azawa and J. Kihara, Trans. I.S.I.J., 22, (1982), p. 132.

49. B. Mintz and J. M. Arrowsmith, Metals Techno., 1, (1979), p.24.

50. C. Offerman, C. A. Dacker and C. Enstrom, Scand. J. Met., 10, (1981), p.115.

51. T. Sakai and M Ohashi, "International Conference on Physical Metallurgy of Thermomechanical Processing of Steels and Other Metals (Thermec 88)", June 6-10, 1988, Tokyo, Japan, Ed.I. Tamura, The Iron and Steel Institute of Japan, p.162.

52. P. J. Wray, Met. Trans. A, 6A, (1975), p.1379.

53. P. J. Wray, Met. Trans. A, 7A, (1976), p.1621.

54. H. Fuji, T. Ohashi and T. Hiromoto, Trans. I.S.I.J. , 18, (1978), P.510.

55. M. Wolf and W. Kurz, Met. Trans. B, 12B, (1981), p. 85.

56. C. J. Adams, Proc. of the Nation. Basic Open Hearth, The Metallurgical Society, 54, (1971), p.290.

57. R. P. Sopher, Welding Journal Supplement, 11, (1958), p. 481.

58. A. Guessier and R. Castro, Revue de Metallurgie, 57, (1960), p.117.

59. E. Schmidtmann and L. Pleugel, Arch. Eisenhuttenweis, 51, (1980), p.49.

60. E. Schmidtmann and F. Rakovski, Arch. Eisenhuttenweis, 54, (1983), p.358.

61. L. I. Morozenkii, O. A. Mitenev and V. K. Kritirov, Stal., 4, (1965), p.272.

62. W. R. Irving and A. Perkins, Ironmaking and Steelmaking, 5, (1977), p. 292.

63. A. Grill and J. K. Brimacombe, Ironmaking and Steelmaking, 3, (1976), p. 177.

64. S. N. Singh and K. E. Blazek, J. Metals, 26, (1974), p. 17.

65. L. Schmidt and A. Jossefsson, Scand. J. of Metallurgy, 3, (1974), p. 193.

66. D. P. Rizio, R. B. Oldland and D. W. Borland, "International Conference on physical Metallurgy of Thermomechanical Processing of Steels and Other Metals (Thermec 88)", June 6-10, 1988, Tokyo, Japan, Ed. I. Tamura, The Iron and Steel Institute of Japan, p. 178.

67. J. F. Reynolds and T. Gladman, Heat Treatment and Forming Processes of steels, Sheffield, Ed by C. M. Sellars and G. J. Davies, 1980, p. 171.

68. B. G. Thomas, J. K. Brimacombe, and I. V. Samarasekera, I.S.S. Transactions, 7, (1987), p. 7.

69. D. N. Crowther and B. Mintz, Material Sciences and Technology, 2, (1986), p. 671.

70. D. N. Crowther and B. Mintz, Mater. Sciences and Technology, 2, (1986), p.951.

71. D. N. Crowther and B. Mintz, Mater. Sciences and Technology, 2, (1986), p. 1099.

72. J. K. Brimacomb eand E. B. Hawbolt, Met. Trans. B, 10B, (1979), p. 279.

73. E. Schmidtmann and L. Pleugel, Arch. Eisenhuttenwes, 51, (1980), p. 55.

74. E. Schmidtmann and F. Rakovski, Arch. Eisenhuttenwes, 54, (1983), p. 363.

75. A. Josefsson, J. Koeneman and G. Langerberg, J. Iron and Steel Institute, 3, (1959), p. 240.

76. K. Yasumoto, Y. Maheara, S. Ura and Y. Ohmori, Mater. Sciences and Technology, 1, (1985), p. 116.

77. R. P. Messmer and C. L. Briant, Acta Met., 30, (1982), p. 457.

78. M. Tacikowski, G. A. Osinkolu and A. Kobylanski, Mat. Sciences and Technology, 2, (1986), p.154.

79. A. Galibois, M. R. Krishnadev and A. Dubé, Met. Trans. A, 10A, (1979), p.985.

80. B. Chamont, P. Chemelle and H. Biausser, "Proc. of the International Symposium simulation of Welding, Hot Forming and Continuous casting", May 2-4, 1988, Ottawa, Canada, in press.

81. S. Hasebe, Tetsu-to Hagane Overseas, 3, (1963), p. 200.

82. H. Watanabe, Y. E. Smith and R Pehkle, "The Hot Deformation of the Austenite", Ed.J. B. Ballance, The Metallurgical society of AIME, (1977), p. 140.

83. D. N. Crowther, Z. Mohamed and B. Mintz, Met. Trans. A, 18A, (1987), p. 1929.

84. T. Nozaki, J. Matsumo, K. Murata and H. Ooi, Trans.I.S.I.J., 18, (1978), p. 330.

85. Y. Maehara, K. Yasumoto, H. Tomonov and Y. Ohmori, Trans. I.S.I.J., 27, (1987), p. 222.

86. J. R. Wilcox and R. W. K. Honeycombe, Heat Treatment and Forming Processes of steels, Sheffield, The metals Society, Ed by C. M. Sellars and G. J. Davies, (1980), p. 108.

87 W. C. Leslie, R. L. Rickette, C. L. Dotson and C. S. Walton, Trans. ASM, 46, (1954), p.1470.

88. S. C. Desai, J. Iron and Steel Inst., 191, (1959), p.250.

89. B. C. Woodfine, A. G. Quarrell, J. Iron and Steel Inst., 192, (1960), p.409.

90. G. A. Osinkolu and A. Kobylanski, Scripta Met, 21, (1987), p. 243.

91. G. A. Osinkolu and P. Yi, A. Kobylanski, to be published.

92. P. Opel and S. Wagner, Arch. Eisenhuttenw., 35, (1964), p. 1113.

93. B. Mintz, J. R. Wilcox and J. M. Arrowsmith: Proc. Riso. Int'l Conf. on Recrystallization and Grain Growth of Multiphase and Particle containing Materials, Riso natinal Lab., Denmark, (1980), p. 303.

94. M. Tanino, H. G. Suzuki and K Aoki, Supplement to Trans. JIM, 9, (1968), p. 393.

95. M. G. Akben, I. Weiss and J. J. Jonas, Acta Met., 29, (1981), p. 111.

96. D. N. Crowther, Z. Mohamed and B. Mintz, Trans. I.S.I.J., 27, (1987), p.366.

97. ASTM E 8M-85, p.146.

98. A. Salinas Rodriguez, Masters thesis, McGill University, Montreal, 1986.

99. J. Z. Briggs and R. Q. Barr, High Temp.- High Press., 3, (1971), p.363.

100. R. W. Burman, J. Metals, 29, (1977), p.12.

101. O. Kubaschewski, Iron binary phase diagram, 1982, New York, Springer Verlag, p.5.

102. M.I. Pope and P. Judd, Differential Thermal Analysis, Heyden, 1977.

103. W.P. Brennan, Thermal Analysis Application Study, Perkin Elmer Company, Instrument Division, March 1973.

104. Metals Handbook, 9th edition, Metallography and Microstructures, American Society for Metals, Vol. 9, (1985).

105. ASTM E112-82, p.135.

106. Metals Hanbook, 9th edition, Metallography and Microstructures, American Society for Metals, Vol. 10, (1985).

107. L. E. Davis "Modern Surface Analysis", TMS-AIME short course, Las Vegas, Nevada, Feb 23-24, 1980.

108. L. E. Davis, N. C. MacDonald, P. W. Palmberg, G. E. Riach, R. E. Weber, "Handbook of Auger electron spectroscopy", 2nd edition, 1977, Physical Electronics Industries Inc., Eden Prairie, Minessota.

109. M. Paju, H. Viefhaus, and H.J. Grabke, Steel Research, 59, (1988), p.336.

110. K. W. Andrews, J. of Iron and Steel Inst., 227, (1965), p.721.

111. M. Hansen, "Constitution of binary alloys", McGraw Hill, New York, 1959.

112. P.J Wray, Met. Trans. A, 15A, (1985), p.2009.

113. I.Weiss, T. Sakai and J.J. Jonas, Metal Science, 18, (1984), p.77.

114. G. Cardoso, McGill University, personal communication.

115. K. Kinoshita, G. Kasai and T. Emi, Solidification and casting of metals conf., September, 18-21, (1977), The Metals Society, p.268.

116. H. Fuji, M. Oda, T. Ohashi, K. Kawamura and K. Asano, Tetsu-To-Hagane, 64, (1978), p.24.

117. A. Palmers, Metals Reports C.R.M., 53, (1978), p.23.

118. B. Rogberg, Scand. J. of Metallurgy, 12, (1983), p.51.

119. J.P. Bailon and F. Weinberg, Can. Met. Quat., 19, (1980), p.251.

120. E.D. Hondros and M.P. Seah, Physical Metallurgy, R. W. Cahn and P. Hansen Editors. North-Holland Publishing, 1983, p. 878.

121. A. Kagawa and T. Okamoto, Materials Sciences and Technology, 2, (1986), p.998.

122. M. Hansen, Constitution of binary alloys, Mc Graw Hill, (1958) p.1266.

123. D. McLean, Grain boundaries in Metals, (1957), Clarendon Press.

123. M. P. Seah and E. D. Hondros, Proc. Roy. Soc. Lond. A, 335, (1973), p.191.

125. P. V. Ramasubramanian and F. Stein, Met. Trans., 4, (1973), p.1735.

126. C. L. Briant and S. K. Baneji, Inter. Metals review, 4, (1978), p.164.

127. H. Erhrat and H. J. Grabke, Metal Science, 15, (1981), p.401.

128. M. Guttman, Ph. Dumoulin and M. Wayman, Met. Trans. A, 13A, (1982), p. 1693.

129. H. Erhart, H. J. Grabke and R. Moller, Arch. Eisenhuttenwes, 54, (1983), p.285.

130. S. Suzuki, M. Obata, K. Abiko and H. Kimura, Scripta Met., 17, (1983), p.1325.

131. E. D. Hondros and M. P. Seah, Met. Trans. A, 8A, (1977), p.1363.

132. D. Gupta, Met. Trans. A, 8A, (1977), p.1431.

133. C. L. White and W. A. Coghlan, Met. Trans. A, 8A, (1977), p. 1403.

134. M. Guttman, Met. Trans. A, 8A, (1977), p.1383.

135. R. Moller and H. J. Grabke, Scripta Met., 18, (1984), p.527.

136. C. L. Briant, Acta. Met., 33, (1985), p.1241.

137. H. Hansel and Hans Jurgen Grabke, Scripta Met., 20, (1986), p.1641.

138. H. J. Grabke, Steel Research, 57, (1986), p.178.

139. W. Y. Qing, Mat. Sciences and Technology, 3, (1987), p.207.

140. K. S. Shin and B. H. Tsao, Scripta Met., 22, (1988), p.585.

141. J.B. Bradley, H. I. Aaranson, K. C. Russel and W.C. Johnson, Met. Trans. A, 8, (1977), p.1955.

142. W.C. Leslie, IS.S. Trans., 2, (1983), p.1.

143. H. Hansel, L. Stratmann, H. Keller and H. J. Grabke, Acta Met, 33, (1985), p.659.

144. M. Guttmann, Surface Science, 53, (1975), p. 213.

145. M. Guttman and D. McLean, "Interfacial segregation", W.C. Johnson and J. M. Blakeley Eds, ASM, (1977), p.261.

146. M. Guttmann, Metal Science, 10, (1976), p. 337.

147. L.S. Darken and G. Simkovitch, Scripta Met., 13, (1979), p. 431.

148. G.K. Sigworth and J. F. Elliot, Metal Science, 8, (1974), p.298.

149. C.L. Briant, Acta Met., 7, (1988), p. 1805.

150. F. Garofalo, "Fundamentals of Creep and Creep rupture in Metals", McMillan Series in Materials Science, (1965), p.242.

151. R. G. Fleck, G.J. Cocks and D.M.R. Taplin, Met. Trans., 1, (1970), p.3445.

152. K.A. Bywater and T. Gladman, Metals Technology, 3, (1976), p.358.

153. V. Kutumba Rao, D. M. R. Taplin and P. Rama Rao, Met. Trans. A, 6A, (1975), p.77.

154. J.Y. Fu, C.I. Garcia, S. Pytel and A.J. Deardo, "Processing, Microstructure and Properties of HSLA Steels", Proc. Conf., Nov 3-5, 1987, A.J. Deardo Ed., p.27.

155. H.J. McQueen and J.J. Jonas, Treatise on Material Science, Vol.2, 1976, p.393.

156. W. Roberts, Deformation, Processing and Structure, ASM seminar, 1982, Ed. G. Krauss, p.109.

157. B. Mintz, S. Yue, and J.J. Jonas, "Recrystallisation'90 Conference, Wollongong, Australia, (1990).

158. A. Grill and K. Schwerferger, Ironmaking and steel making, 3, (1979), p.131.

159. T. Matsumya, H. Kajioka and Y Nakamura, Nippon Steel Tech. Report, 21, (1985), p.347.

160. J. Y. Lamant, M. Larreq, J. P. Birat, J. L. Hensgen, J.D. Weber and J. C. Dhuyvetter, Continuous casting 1985, p. 37.1.

161. C.M. Sellars and W.J. Tegart, Mémoires Scientifiques de la Revue de Métallurgie, 63, (1966), p.731.

162. D.C. Houghton, G.C. Weatherly, and J.D. Embury, "Advances in the Physical Metallurgy and applications of steels", Proc. of an Int. Conf., The Met. Soc., Liverpool, 1982, p.136.

163. G. Ocampo, T. Castillo, V.S. Raghunathan and, J.D. Embury, Metallography, 16, (1983), p.287.

164. J.L. Verger-Gaugry, G. Ocampo, and J.D. Embury, Metallography, 18, (1985), p.18.

165. S. V. Subramanian, S. Shima, G. Ocampo, T. Castillo, J. D. Embury and, G.R. Purdy, "HSLA Steels, Metallurgy and Applications", Proc. of an Int. Conf., The Chinese Soc. of Metals, Beijing, (1985), p. 151.

166. S. Suzuki, G.C. Weatherly and D.C. Houghton, Acta Met., 35, (1987), p.341.

167. D.C. Houghton, "Thermomechanical Processing of Microalloyed Austenite" AIME Proc. Conf., Pittsburgh, 1981, A.J. DeArdo, G.A. Ratz and P.J. Wray, p. 267.

168. J. T. Bowker and J. NG Yelin, T.F. Malis, CANMET Report N° MTL 89-9 (OP-J).

169. Y. Maheara, K. Nakai, K. Yasumoto and T. Nishima, T.I.S.I.J., 28, (1988) p.1021.

170. D.C. Houghton, to be pubished in Acta Met.

171. L. Weije, PhD Thesis, McGill university, Montreal, 1987.

172. H. Nordberg and B. Aronsson, JISI, 206, (1968), p.1263.

173. K.J. Irvine, F.B. Pickering and T. Gladman, JISI, 205, (1967), p.171.

174. T. Mori, M. Tokizane, K. Yamaguchi, E. Sunani and Y. Nokazina, Tetsu-to-Hagane, 54, (1968), p.763.

175. S. Matsuda and N. Okamura, Trans. of ISIJ, 18, (1978), p.198.

176. H.J. Goldschmidt, "Interstitial Alloys", 1967, Plenum Press, New York.

177. J. Strid and K.E. Easterling, Acta Met., 33, (1985), p.2057.

178. E. T. Turkdogan, Steelmaking Conference Proceedings, Pittsburgh, 70, (1987), p.399.

179. F. Vodopivec, J. of ISI, 211, (1973), p.664.

180. G. Wang, Masters Thesis, McGill University, Montreal, 1986.

181. J.P. Michel and J.J. Jonas, Acta Met, 29, (1980), p.513.

182. R. Simoneau, G. Begin and, A.H. Marquis, Metal Science,39, 1978, p.381.

183. A. Lebon, J. Rofes Vernis and C. Rossard, Metal Science, 36, (1975), p.36.

184. J.J. Jonas and M.G. Akben, Metals Forum, 4, (1981), p.92.

185. B. Dutta and C.M. Sellars, Materials Science and Technology, 3, (1987), p.198.

186. M.G. Akben, PhD Thesis, McGill University, 1980.

187. M.G. Akben, B. Bacroix and, J.J. Jonas, Acta Met., 31, (1983), p.161.

188. L.J. Cuddy and J.C. Raley, Met. Trans. A, 14A, (1983) p.1989.

189. H. Gleiter, "Physical Metallurgy", R. W. Cahn and P. Haansen Eds., 1983, p.649.

190. P. R. Rios, Acta Met.,35, (1987), p.2805.

191. R. Angers and D. Dubé, Met. Trans.,18A, (1987), p.1151.

192. A. Kern and W. Reif, Steel Research, 57, (1986), p.377.

193. K. Lucke and K. Detert, Acta Met., 5, (1957), p.628.

194. D.K. Matlock, F.Z. Ebrahimi, and G. Krauss, "Deformation, Processing and Structure", ASM Materials Science Seminar, 23-24 october 1982, St Louis, Ed. G. Krauss, p.47.

195. C. I. Garcia and A.J. deArdo, Met. Trans., 12A, (1981), p.521.

196. G. R. Speich, V. A. Demarest, and R.L. Miller, Met. Trans., 12A, (1981) p.1419.

197. D. Z. Yang, E.L. Brown, D.K. Matlock and G. Krauss, Met. Trans., 16A, (1985) p.1523.

198. G. A. Osinkolu, M. Tacikowski and A. Kobylanski, Material Sciences and Technology, 1, (1985), p.520.

199. P. H. Yi, Doctoral Dissertation, Ecole des Mines de St Etienne, France, 1988.

200. B. Mintz, personal communication.

201. B. Mintz and Z. Mohamed, Proc. of the 7th Int. Conf. on Fracture, Houston, Texas, March, 1989, Eds. Salama, Ravi-Chandoz, Taplin, Rama Rao, Vol. 4, p. 2545

202. I. Weiss and J.J. Jonas, Met. Trans., 11A, (1980), p.403

203. Z. Morita and T. Tanaka, T.I.S.I.J., 23, (1983), p.824

204. Y. Ueshima, S. Mizoguchi, T. Matsumiya and, H. Kajioka, Met Trans B, 17B, (1986), p. 845.

205. R.C. Sharma, V. K. Lakhshmanan and J. S. Kirkaldy, Met Trans., 15A, (1984), p. 545.

206. M. P. Seah and C. Lea, Phil. Mag., 31, (1975), p.627.

207. M. Paju and H.J. Grabke, Mat. Sciences and Techno. 5, (1989), p.248.

APPENDIX I

LISTING OF PROGRAM FOR MONITORING TENSILE TEST AT CONSTANT TRUE STRAIN RATE

TENSION MTS BASIC VO1B-02D

```
10   REM-------------------------------------------------------------------------------
20   REM-REAL TIME PROGRAM: CONTINUOUS CONSTANT TRUE
     STRAIN RATE TENSILE TEST
30   REM-------------------------------------------------------------------------------
40   CNTR(3)
50   DIM X(500), D(550), M(7), R(7), F1(50), D1(50)
60   DIM S(550), S1(550), X2(2)
70   M(0)=0\M(1)\R(1)=7
90   M(2)=2\R(2)=6
100  M(3)=5\R(3)=5
110  M(4)=10\R(4)=4
120  M(5)=20\R(5)=2
120  M(6)=50\R(6)=1
120  M(7)=100\R(7)=0
130  PRINT “ENTER THE FOLLOWING DATA:”\PRINT
140  PRINT “TEST NUMBER AND MATERIAL:”\INPUT N$,M$\PRINT
150  PRINT “TRUE STRAIN AND STRAIN RATE:”\INPUT E,E1\PRINT
160  PRINT “HEAT TREATMENT:”\INPUT T1$\PRINT
170  PRINT “TEST TEMPERATURE:”\INPUT T$\PRINT
180  PRINT “SPECIMEN HEIGHT AND DIAMETER:”\INPUT
     H0,D0\PRINT
190  D1=H0*(EXP(E)-1)
200  PRINT “MINIMUM DISPLACEMENT OF THE
     ACTUATOR:”,D1\PRINT
210  PRINT “STROKE (MM) AND LOAD (LBS) RANGES:”\INPUT
     R1,R2\PRINT
220  C=2048
230  C2=9.81
240  T=E/E1
250  K1=C/R1
260  K2=C/R2/.4536/C2
270  A0=PI*(D0/2)^2
280  QUIT
290  REM-------------------------------------------------------------------------------
300  REM---HARDWARE SEGMENT GENERATORS PARAMETERS
310  REM-------------------------------------------------------------------------------
320  IF T<200 THEN 350
330  N=100\F1=1\F2=7
340  GO TO 2400
350  R3=5.00E-3*R1/2
360  N=INT(D1/R3+0.5)
370  FOR I=0 TO 6
380  F3=M(I)
390  F4=M(I+1)
```

```
400   FOR J=F3 TO F4
410   M1=J*T
420   IFN<=M1 THEN 460
430   NEXT J
440   NEXT I
450   F1=100\N=INT(F1*T)\GO TO 480
460   F1=F4
470   F2=R(I+1)
480   X(1)=INT(C*N/T/F1)\X1=INT(F1*X/C+0.5)\CNTR(3)
490   S1=E/N
500   PRINT “THE HSG PARAMETERS ARE:”\PRINT
510   PRINT “NUMBER OF LEVELS:”,N\PRINT
520   PRINT “MAXIMUM FREQUENCY:”,F1\PRINT
530   PRINT “FREQUENCY RANGE:”,F2\PRINT
540   PRINT “FREQUENCY (MU):”,X(1)\PRINT
550   PRINT “FREQUENCY (HZ):”,X1\PRINT
560   T8=X(1)*F1/4095
570   T9=1/2/T8
580   PRINT “TIME/LEVEL (SEC.):”,T9\PRINT
590   REM-------------------------------------------------------
600   REM---DATA ACQUSITION PARAMETERS
610   REM-------------------------------------------------------
610   IF T>=1 THEN 650
620   A1=10\A4=T*10\N1=100
630   PRINT “THE NUMBER OF POINTS TO BE ACQUIRED IS 100”
640   GO TO 720
650   N1=500
660   PRINT “THE NUMBER OF POINTS TO BE ACQUIRED IS 500”
670   IF T>400 THEN 700
680   A1=T*10
690   A4=2\GO TO 720
700   A1=T
710   A4=20
720   INPUT F$\CNTR(3)
730   REM-----------------------------------
740   REM---SET UP THE SYSTEM
750   REM-----------------------------------
760   MSW1(2)
770   FG1(0)
780   PRINT “CHECK THE FOLLOWING”
790   PRINT “DC ERROR=0”
800   PRINT “REMOTE/LOCAL SWITCH IN REMOTE POSITION”
810   PRINT “SPAN 1 IS AT ZERO POSITION”
820   PRINT “STROKE CONTROL LED ON”
830   PRINT “PRESS RETURN TO CONTINUE”\INPUT F$\PRINT
840   PRINT “TURN ON THE HYDRAULICS”\PRINT
850   PRINT “SET SPAN 1 TO 10”
860   PRINT “PRESS RETURN TO CONTINUE”\INPUT F$\CNTR(3)
870   REM-------------------------
880   REM---DUMP CHECK
890   REM-------------------------
900   EDMP
910   SDMP(1,A)\IF A=0 THEN 950
920   PRINT “DUMP CARD PROBLEM, UNABLE TO FINISH THE TEST”
```

```
930   PRINT “TURN OFF THE HYDRAULICS”
940   STOP
950   REM-----------------------------------------------------------------
960   REM--AUT0MATIC POSITIONING OF THE PISTON
970   REM-----------------------------------------------------------------
980   QUIT
990   CNTR(3)\GOSUB 1680
1000  PRINT “THE PISTON IS AT “S” MACHINES UNITS”
1010  PRINT “THE LOAD IS AT “Q” MACHINES UNITS”
1020  PRINT “DO YOU WISH TO POSITION THE PISTON
      AUTOMATICALLY?”
1030  INPUT F$\ IF F$ = “YES” THEN 1680
1040  PRINT “PRESS RETURN WHEN THE PISTON IS IN THE PROPER
      POSITION”
1050  PRINT “IS POSITION OK?”\INPUT F$
1060  IF F$ < > “YES” THEN 1040
1070  S5 = S
1080  FOR I = 1 TO 600
1090  I2 = S5 + I
1100  FG1(I2)
1110  GOSUB 1680
1120  IF Q < > -5 THEN 1170
1130  NEXT I
1140  GOSUB 1680
1150  PRINT “CHECK THE SAMPLE”\STOP
1160  GOSUB 1680
1170  PRINT “THE PISTON IS AT “S” MACHINES UNITS”
1180  PRINT “THE LOAD IS AT “Q” MACHINES UNITS”
1190  PRINT“ “IS THE PISTON OK? (Y/H/L)”INPUT F$
1200  IF F$ = “Y” THEN 1270
1210  IF F$ = “H” THEN 1220\ IF F$ = “L” THEN 1230\ GO TO 1160
1220  I2 = I2-1\GO TO 1240
1230  I2 = I2 + 1
1240  FG1(I2)
1250  GO TO 1160
1260  S0 = S
1270  REM------------------------------------------
1280  REM-THE EXPERIMENT START
1290  REM------------------------------------------
1300  PRINT “IS THE PISTON IN THE RIGHT POSITION”;\INPUT F$
1310  IF F$ < “Y” THEN 1190
1320  DACQ(0,S0,2,0)
1330  FOR I = 2 TO N + 1
1340  X(I) = S0 + K1*H0*(EXP(S1*(I-1))-1)\ X(I) = INT(X(I) + 0.5
1350 NEXT I
1360  X2 = 2
1370  X2(I) = C/2
1380  X2(2) = X(N + 1) + 50
1390  X = N + 1
1400  DACQ(0,F0,0,0)\ PRINT “EXPERIMENT UNDER WAY!!!”
1410  TIME(A1,A2)\ DACQ(3,D,2,A4)\ DACQ(6,F,0,0)
1420  FG1(X,1,7,2)\ STAR
1430  BUF1(Z1)\ IF Z1 > -1 THEN 1430
1440  QUIT
```

```
1450  FOR I=X2(2) TO 0
1460  FG1(I)
1470  NEXT I
1480  D(D+I)=D(I)
1490  F(D+I)=F1(I)
1500  NEXT I
1510  P=D+D1
1520  PRINT "EXPERIMENT FINISHED, TURN OFF HYDRAULIC AND
      ELECTRIC POWER"
1530  INPUT F$\ CNTR(3)
1540  REM------------------------------------------------------------------
1550  REM----STORE THE DATA IN A FLOPPY DISK
1560  REM------------------------------------------------------------------
1570  PRINT "DO YOU WANT TO SAVE THE DATA";\ INPUT F$
1580  IF F$<"Y" THEN 1670
1590  FOR I=P+2 TO 3 STEP -1
1600  D(I)=D(I-2)
1610  NEXT I
1620  D(2)=S0
1630  d(1)=P
1630  OPEN "DX1:"&N$ FOR OUTPUT AS FILE #1
1640  AOUT(D,1,0,E2)
1650  AOUT(F,1,3,E3)
1660  CLOSE #1
1670  STOP\ END
1680  Q=0/S=0
1690  FOR J=1 TO 15
1700  DACQ(0,Q0,0,0)\ DACQ(0,S0,2,0)
1710  Q=Q+Q0\ S=S+S0
1720  NEXT J
1730  Q=Q/15\ S=S/15
1740  RETURN
1750  STOP\ END
```

APPENDIX II

LISTING OF PROGRAM FOR DATA ANALYSIS

```
ANALYSIS   MTS BASIC VO1B-02D

10      REM---------------------------
20      REM-DATA ANALYSIS
30      REM---------------------------
40      CNTR(3)
50      QUIT
60      DIM X(550), F(550), S1(550), S(550), F1(550), F(550), D1(550), L(550),
        E(550)
70      PRINT “ENTER THE FOLLOWING DATA:”\PRINT
80      PRINT “TEST NUMBER AND MATERIAL:”\INPUT N$,M$\PRINT
90      PRINT “TRUE STRAIN AND STRAIN RATE:”\INPUT E,E1\PRINT
100     PRINT “HEAT TREATMENT:”\INPUT T1$\PRINT
110     PRINT “TEST TEMPERATURE:”\INPUT T$\PRINT
120     PRINT “SPECIMEN HEIGHT AND DIAMETER:”\INPUT
        H0,D0\PRINT
130     OPEN “DX1:”&N$ FOR INPUT AS FILE #1
140     AINP(D,1,0,B1)
150     S0=D(2)
160     P=D(1)
170     FOR I=1 TO P
180     D(I)=D(I+1)
190     NEXT I
200     AINP(F,1,3,B2)
210     CLOSE #1
220     X1$=“TRUE STRAIN”
230     Y1$=“TRUE STRESS (MPA)”
240     Z1$=“TENSION FLOW CURVE”
250     W1$=“STRAIN RATE”
260     W3$=“TEST NUMBER”
270     FOR I=1 TO P
280     F1(I)=F(I)
290     D1(I)=D(I)
300     NEXT I
310     FOR I=1 TO P
320     F(I)=F1(I)
330     D(I)=D1(I)
340     NEXT I
350     A0=PI*(D0/2)^2
360     C1=2048
370     C2=9.81
380     T=E/E1
390     K1=C1/R1
400     K2=C1/R2/0.4536/C2
410     PRINT “DO YOU WANT THE DATA LISTED”\ INPUT F$
420     IF F$<“Y” THEN GO TO 510
430     CNTR(3)
```

```
440    PRINT “S0 = ”, S0, “P = ”,P
450    PRINT “I”, “F(I)”, “D(I)”
460    FOR I = 1 TO 100
470    PRINT I, F(I), D(I)
480    NEXT I
490    PRINT\PRINT
500    FOR I = 450 TO 350 STEP -1
510    PRINT I, F(I), D(I)
520    NEXT I
530    PRINT “N1 = ”; \INPUT N1
540    PRINT “P1 = ”; \INPUT P1
550    U = 0
560    FOR I = N1 TO P1
570    IF D(I) = 0 GO TO 610
580    H = H0 + (D(I)-ABS(S0)-D(N1-1))/K1
580    S(I) = (ABS(F(I)-F(1))/K2)*H/A0/H0
590    S1(I) = LOG(H/H0)
600    IF U < S(I) THEN U = S(I)
610    NEXT I
620    PRINT “MAX STRESS = ”;U\PRINT
630    PRINT “MAX STRESS FOR GRAPH”; \INPUT U
640    PRINT “MAX STRAIN FOR GRAPH”;\INPUT E3
650    PRINT “ENTER STRAIN AND STRESS INCREMENT FOR GRAPH”
660    INPUT X1, Y1
670    PRINT “I”, “P”, “DEL”,“SIG”, “EPS”
680    FOR I = 1 TO 70
690    PRINT I, L(I), E(I), S1(I), S(I)
700    NEXT I
710    PRINT “ENTER THE TYPE OF SCALE; LINEAR S4 = 0, LOG-LOG
       S4 = 3”\INPUT S4
720    IF S4 = 0 GO TO 760
730    PRINT “N1 = ”;\INPUT N1
740    PRINT “P1 = ”;\INPUT P1
750    GO TO 770
760    E5 = 0\U1 = 0
770    CNTR(0)\CNTR(3)
780    PHYL(100,900,100,700)
790    SCAL(S4,E5,E3,U1,U)
800    AXES(E5,U1)
810    AXES(E3,U)
820    LABL(X1$,Y1$,X1,Y1,1)
830    IF S4 = 3 THEN XXX
840    LABL(“ ”,“ ”,X1*0.1,Y1*0.5,3)
850    FOR I = N1 TO P1
860    MARK(“ + ”,S(I),S1(I))
870    NEXT I
880    CPOS(X3,Y3)
890    COMM(W3$,X3,Y3)\PRINT N$
900    COMM(M$,X3,0.96*Y3)
910    COMM(W1$,X3,0.92*Y3)\PRINT E1
920    COMM(T$,X3,0.94*Y3)
930    COMM(Z1$,X3,0.84*Y3)
940    CNTR(2)\INPUT F$
```

```
950   PRINT “DO YOU WANT TO TRY ANOTHER
      MAGNIFICATION”;\INPUT F$
960   IF F$<“Y” GO TO 1000
970   CPOS(X3,Y3)
980   E3=X3
990   GO TO 770
1000  REM-----------------------------------------
1010  REM--REMOVING THE SCATTER
1020  REM-----------------------------------------
1030  PRINT “DO YOU WANT TO REMOVE THE SCATTER?”;INPUT F$
1040  IF  F$<“Y” GO TO 1160
1050  PRINT “CHOOSE THE LIMIT FOR THE SCATTER?\INPUT L1
1060  FOR I=N1 TO P1
1070  IF D(I)=0 GO TO 1120
1080  IF ABS(ABS(F(I))-ABS(F(I-1)))<L1 THEN 1120
1090  IF ABS(ABS(F(I+1))-ABS(F(I)))<L1 THEN 1120
1100  F(I)=0
1110  D(I)=0
1120  NEXT I
1130  PRINT “DO YOU WANT TO PLOT THE RESULT?”;\INPUT F$
1140  IF  F$<“Y” GO TO 1150
1150  GO TO 410
1160  PRINT “DO YOU WANT TO THE LOAD VS STRAIN?”;\INPUT F$
1170  IF  F$<“Y” THEN STOP
1180  PRINT “ MAX STRESS (KG/MM**2)?;\INPUT M
1190  M=F*A0
1200  PRINT “THE MAX LOAD IS:”,F,“KG”
1210  PRINT “ENTER THE LOAD LIMIT (KG)”;\INPUT F1
1220  PRINT “MAX TRUE STRAIN”;\INPUT E3
1230  PRINT “ENTER STRAIN AND LOAD INCREMENT FOR GRAPH”
1240  INPUT X1,Y1
1250  CNTR(0)\CNTR(3)
1260  Y2$=“LOAD (KG)
1270  X2$=“DELTA H (MM)”
1280  SCAL(0,0,E3,F1)
1290  AXES(0,0)
1300  AXES(E3,F1)
1310  LABL(X2$,Y2$,X1,Y1,1)
1320  LABL(“ ”,“ ”,X1*0.1,Y1*0.5,3)
1340  K3=C1/R2/0.4536
1350  FOR I=N1 TO P1
1360  L(I)=S(I)*A0/EXP(S(I))
1370  E(I)=H0*EXP(S(I))-H0
1380  MARK(“+”,E(I),L(I))
1390  NEXT I
1400  CPOS(X3,Y3)
1410  COMM(W3$,X3,Y3)\PRINT N$
1420  COMM(W1$,X3,0.92*Y3)\PRINT E1
1430  COMM(T$,X3,0.88*Y3)
1440  COMM(Z1$,X3,0.84*Y3)
1450  CNTR(2)\INPUT F$
1460  PRINT “DO YOU WANT TO TRY ANOTHER
      MAGNFICATION”;\INPUT F$
1470  IF F$<“Y” GO TO 1510
```

```
1480  CPOS(X3,Y3)
1490  E3=X3
1500  GO TO 1250
1510  STOP\END
```

APPENDIX III

LISTING OF PROGRAM FOR PLOTTING SEVERAL CURVES ON THE SAME GRAPH

```
CURVE   MTS BASIC VO1B-02D

10 REM------------------------------------------------------------------------------
20 REM--PRGM TO PLOT SEVERAL CURVES ON THE SAME GRAPH
30 REM------------------------------------------------------------------------------
40 DIM F2(300), D2(300), S(6,300), S1(6,300), H$(6), P(6)
50 DIM  N$(7),M$(7),E$(7),R1(7),R2(7), T$(7),D0(7),H0(7),K1(7),K2(7),A0(7)
60 PRINT “HOW MANY CURVES DO YOU WANT TO RECALL”\INPUT C
70 V=0
80 FOR I=1 TO C
90 PRINT “INPUT I”\INPUT I
100    U=0\L=0
110    PRINT “SAMPLE NUMBER”\INPUT N$(I)
120    PRINT “MATERIAL”\INPUT M$(I)
130    PRINT “TRUE STRAIN RATE”\INPUT E$(I)
140    PRINT “STROKE AND LOAD (PDS) RANGE”\INPUT R1(I),R2(I)
150    PRINT “SPECIMEN DIAMETER AND HEIGHT (MM)”\INPUT
       D0(I),H0(I)
160    PRINT “TEST TEMPERATURE”\INPUT T$(I)
170    PRINT “HEAT TREATMENT” \INPUT H$(I)
180    PRINT “INPUT P”\INPUT P(I)
190    Q$=N$(I)
200    OPEN “DX1:”&Q$ FOR INPUT AS FILE #1
210    AINP(D2,1,0,B1)
220    AINP(F2,1,3,B2)
240    CLOSE #1
250    PRINT “DO YOU WANT TO LIST THE VALUES?”\INPUT F$
260    IF F$<“Y” GO TO 300
270    FOR L=1 TO P+20
280    PRINT L,F2(L),D2(L)
290    NEXT L
300    PRINT “INPUT STRAIN START”\INPUT O1
310    PRINT “INPUT STRESS START”\INPUT O2
320    REM-------------------------------------------------------
330    REM--CALCULATION OF THE FLOW CURVE
340    REM-------------------------------------------------------
350    A0(I)=PI*(D0(I)/2)**2
360    C1=2048
370    C2=9.81
380    K1(I)=C1/R1(I)
390    K2(I)=C1/R2(I)/0.4536/C2
400    FOR K=1 TO P(I)
410    H=H0(I)+(D2(K)-O1)/K1(I)
420    S(I,K)=((ABS(F2(K))-O2)/K2(I)*H/A0(I)/H0(I)
430    S1(I,K)=LOG(H/H0(I))
440    IF U<S(I,K) THEN U=S(I,K)
```

```
450   IF V<S(I,K) THEN V=S(I,K)
460   NEXT K
470   PRINT “DO YOU WANT TO PLOT THE GRAPH” \INPUT F$
480   IF F$<“Y” GO TO 830
490   PRINT “MAX STRESS=”, U
500   PRINT “ENTER MAX STRESS FOR GRAPH” \INPUT U1
510   PRINT “ENTER MAX STRAIN FOR GRAPH”\INPUT E3
520   PRINT “ENTER STRAIN AND STRESS INCREMENT FOR GRAPH”
530   INPUT X1,Y1
540   X1$=“TRUE STRAIN”
550   Y1$=“TRUE STRESS MPA”
560   Z1$=“TENSION FLOW CURVE”
570   W1$=“STRAIN RATE:”
580   W3$=“TEST NUMBER”
590   CNTR(0)\CNTR(3)
600   PHYL(100,900,100,700)
610   SCAL(0,0,E3,0,U1)
620   AXES(0,0)
630   AXES(E3,U1)
640   LABL(X1$,Y1$,X1,Y1,1)
650   LABL(“ ”,“ ”,X1*0.1,Y1*0.5,3)
660   FOR K=1 TO P(I)
670   MARK(“+”,S1(I,K),S(I,K))
680   NEXT K
690   CPOS(X3,Y3)
700   COMM(W3$,X3,Y3)\PRINT N$(I)
710   COMM(M$,X3,0.96*Y3)
720   COMM(W1$,X3,0.92*Y3)\PRINT E$(I)
730   COMM(T$(I),X3,0.88*Y3)
740   COMM(Z1$,X3,0.84*Y3)
750   CNTR(2)\PRINT K$
760   PRINT “DO YOU WANT TO TRY ANOTHER
      MAGNIFICATION”\INPUT F$
770   IF F$<“Y” GO TO 820
780   CPOS(X3,Y3)
790   E3=X3
800   CNTR(3)
810   GO TO 590
820   IF L<P(I) THEN L=P(I)
830   NEXT I
840   REM---------------------------------------------------------------------------
850   REM--PLOT OF SEVERAL CURVES ON THE SAME GRAPH
860   REM---------------------------------------------------------------------------
870   PRINT “IS IT A TEMP. (1), STRAIN RATE (2), HEAT TREAT. (3),
      CHEM. COMP. (4) GRAPH?”
880   INPUT X1,Y1
890   CNTR(0)\CNTR(3)
900   PHYL(100,900,100,700)
910   SCAL(0,0,V3,0,V1)
920   AXES(0,0)
930   AXES(V3,V1)
940   LABL(X1$,Y1$,X1,Y1,1)
950   LABL(“ ”,“ ”,X1*0.1,Y1*0.5,3)
960   FOR I=1 TO C
```

```
970   FOR J=1 TO P(I)
980   MARK("+",S1(I,J),S(I,J))
990   NEXT J
1000  NEXT I
1010  IF G=1 GO TO 1050
1020  IF G=2 GO TO 1170
1030  IF G=3 GO TO 1280
1040  IF G=4 GO TO 1400
1050  FOR I=1 TO C
1060  CPOS(X3,Y3)
1070  COMM(T$(I),X3,Y3)
1080  NEXT I
1090  I=C
1100  E$(C)="0.01/S"
1110  CPOS(X3,Y3)
1120  COMM(M$(I),X3,Y3)
1130  COMM(W1$,X3,Y3*0.96)\PRINT E$(I)
1140  W4$="HEAT TREATMENT:"
1150  COMM(W4$,X3,0.92*Y3)\PRINT H$(I)
1160  GO TO 1510
1170  FOR I=1 TO C
1180  CPOS(X3,Y3)
1190  COMM(E$(I),X3,Y3)
1200  NEXT I
1210  CPOS(X3,Y3)
1220  COMM(M$(I),X3,Y3)
1230  W4$="HEAT TREATMENT:"
1240  COMM(W4$,X3,0.92*Y3)\PRINT H$(I)
1250  W5$="TEMPERATURE:"
1260  COMM(W5$,X3,0.96*Y3)\PRINT T$(I)
1270  GO TO 1510
1280  FOR I=1 TO C
1290  W4$="HT:"
1300  FOR I=1 TO C
1310  CPOS(X3,Y3)
1320  COMM(W4$,X3,0.92*Y3)\PRINT H$(I)
1330  NEXT I
1340  W5$="TEMPERATURE:"
1350  CPOS(X3,Y3)
1360  COMM(M$(I),X3,Y3)
1370  COMM(W5$,X3,0.96*Y3)\PRINT T$(I)
1380  COMM(W1$,X3,0.92*Y3)\PRINT E$(I)
1390  GO TO 1510
1400  FOR I=1 TO C
1410  CPOS(X3,Y3)
1420  COMM(M$(I),X3,Y3)
1430  NEXT I
1440  CPOS(X3,Y3)
1450  W1$="STRAIN RATE:"
1460  W4$="HEAT TREATMENT:"
1470  W5$="TEMPERATURE:"
1480  COMM(W1$,X3,Y3)\PRINT E$(I)
1490  COMM(W5$,X3,0.96*Y3)\PRINT T$(I)
1500  COMM(W4$,X3,0.92*Y3)\PRINT H$(I)
```

```
1510 CNTR(2)\INPUT K$
1520 PRINT “DO YOU WANT ANOTHER MAGNIFICATION?”\INPUT F$
1530 IF F$<“Y” THEN GO TO 1570
1540 CPOS(X3,Y3)
1550 V3=X3
1560 GO TO 890
1570 STOP
1580 END
```

APPENDIX IV

DETERMINATION OF THE PHASE TRANSFORMATION TEMPERATURE IN IRON ALLOY MULTICOMPONENT SYSTEMS

Kagawa and Okamoto have proposed the following model to calculate the phase transformation temperatures of dilute multicomponent iron alloys [121]. As shown in the schematic Fe-C phase diagram at high temperatures presented in Fig. IV.1, the addition of a third element I leads to a change in the position of the nodal points D, A and L to D', A' and L', respectively. It is assumed that the slopes of the boundary lines LC, AE, AG, FD and DH are not altered by the addition of element I. The changes in temperature (ΔT^X) and carbon concentration (ΔN_C^X) of points A, D and L brought about by adding 1 at% of element I have been calculated by Kagawa and Okamoto using thermodynamic considerations. In the case of a dilute solution containing many alloying elements, the interaction between the elements can be neglected [203]. Therefore, the changes in temperature and composition at points D, A and L for a multicomponent alloy are calculated by the summation of the contributions of each alloying element i.e.:

$$\Delta T^X = \sum_i x_i \Delta T_i^X \qquad \text{IV.1}$$

$$\Delta N_C^X = \sum_i x_i \Delta N_{C,i}^X \qquad \text{IV.2}$$

where x_i is atomic percentage of element i. $\Delta N_{C,i}^x$ and ΔT_i^x have been calculated previously for Mn, Si, Ni, Cr, P, and S, and are listed in Table IV.1. The technique of Kagawa and Okamoto [121] has been extended to determine these values for N, Al, Nb and V to enable the phase transformation temperatures of these steels to be calculated.

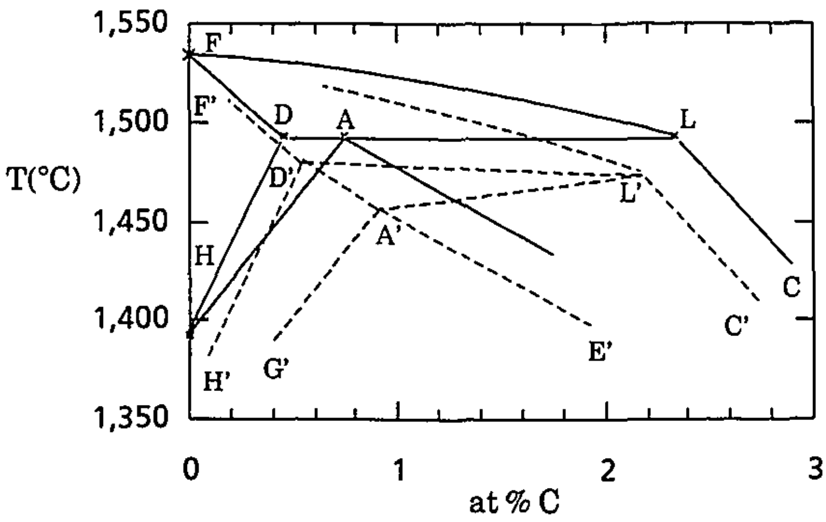

The new equations of the boundaries lines are given by:

A'E': $T(°C) = cI_C\,(at\%) + d' = -32.2I_C\,(at\%) + d'$

A'G': $T(°C) = eI_C\,(at\%) + f' = 101.4I_C\,(at\%) + f'$

D'H': $T(°C) = gI_C\,(at\%) + h' = 126.1I_C\,(at\%) + h'$

F'D': $T(°C) = iI_C\,(at\%) + j' = -89.71I_C\,(at\%) + j'$

Steel	d' (°C)	f' (°C)	h' (°C)	j' (°C)
P	1494.5	1375.5	1416.5	1516
A,B,C	1494	1382.5	1421	1510
S	1492	1375	1430	1500
	d (°C)	f (°C)	h (°C)	j (°C)
Pure Fe-C	1517	1418	1435	1534

Fig. IV.1: Calculated equations of the boundaries lines in the peritectic region for steels P, A, B, C, and S.

Table IV.1

Changes in temperatures and carbon concentration of points L, A and D brought about by adding 1 at.-% of element I [121].

I	ΔT^L (°K/at% I)	ΔT^A (°K/at% I)	ΔT^D (°K/at% I)	ΔN_C^L (at%C/at%I)	ΔN_C^A (at%C/at%I)	ΔN_C^D (at%C/at%I)
Mn	0.5	0.6	0.6	-0.30	-0.15	-0.09
Si	-17.2	-28.6	-21.2	0.67	0.52	0.20
Al	-19.4	-21.75	-23.1	1.75	0.34	-0.012
V	-37.5	-30	-34.1	2.43	0.45	-0.174
Nb	-44.9	-90	-183.18	6.93	0.55	-0.85
Ti	-12.9	-51.7	-39.2	0.33	0.35	0.11
Ni	8.7	9.1	10.8	-0.84	-0.33	-0.23
Cr	-8.7	-11.1	-9.8	0.50	0.21	0.11
N	0	0	0	-0.007	0.004	-0.012
P	-13.4	-149.0	-89.4	-0.16	0.15	-0.11
S	-12.8	-512.2	-200.1	-0.41	-1.27	-0.68

IV.1. CALCULATION OF ΔT_i^x FOR I = N, Al, Nb, AND V

The change in temperature (ΔT^X) values for X = L and D can be determined by using equations IV.3 and IV.4[121]:

$$\Delta T_i^L = \left(\frac{\Delta T_i^A}{N_i^A}\right) P_i^{A/L} N_i^L \tag{IV.3}$$

$$\Delta T_i^D = \left(\frac{\Delta T_i^A}{N_i^A}\right) P_i^{A/D} N_i^D \tag{IV.4}$$

where ΔT^A_i refers to the change in temperature at point A (Fig.IV.1) caused by the addition of 1 at% of an element i, (Table IV.1), N_i^μ is the mole fraction of element i in µ-phase and $P_i^{\mu/v}$ is the partition coefficient for element i between µ-phase and v-phase in the Fe-C-i system diagram, defined as N_i^μ/N_i^v. Knowing the partition coefficient $(P_i^{\mu/v})^*$ of the Fe-i system, $P_i^{\mu/v}$ can be calculated for the equilibrium between austenite (A) and liquid (L) phases, and delta ferrite (D) and liquid phases with the help of equations IV.5 and IV.6, respectively [121]:

$$P_i^{A/L} = (P_i^{A/L})^* exp(\varepsilon_{ii}^L N_i^L + \varepsilon_{iC}^L N_C^L - \varepsilon_{ii}^A N_i^A - \varepsilon_{iC}^A N_C^A) \tag{IV.5}$$

$$P_i^{D/L} = (P_i^{D/L})^* exp(\varepsilon_{ii}^L N_i^L + \varepsilon_{iC}^L N_C^L - \varepsilon_{ii}^D N_i^D - \varepsilon_{iC}^D N_C^D) \tag{IV.6}$$

where ε_{ii}^v is the self interaction coefficient of element i in v phase, and ε_{ic}^v is the interaction coefficient between carbon (c) and element i in v phase. These interaction coefficients have also been taken from different sources as shown in Table IV.2. Because of lack of data concerning the interaction coefficients in the delta phase the following relationships were assumed [121]:

$$\varepsilon_{ii}^D \approx \varepsilon_{ii}^L \tag{IV.7}$$

$$\varepsilon_{ci}^D \approx \varepsilon_{ci}^L \tag{IV.8}$$

Table IV.2

Wagner interaction coefficients for N, Al, V and Nb. Superscript number are literature references.

	ε_{ii}^{L}	ε_{ic}^{L}	ε_{ii}^{A}	ε_{ic}^{A}	ε_{ic}^{D}	ε_{ic}^{D}
N	0 [148,203]	7.18 [148]	6294/T [205]	6.56 [148,203]	0 [148,203]	7.18 [148]
Al	10.16 [148]	5.29 [148]	7000/T + 1.74	4.89 [148,203]	10.16 [148]	5.29 [148]
V	6050/T [203]	30100/T [203]	7900/T [203]	-23400/T [203]	6050/T [203]	30100/T [203]
Nb	-0.664 [148]	-23.61 [148]	-2 [205]	-21.89 [148,203]	-0.664 [148]	-23.61 [148]

Also, there is a linear relationship between the interaction coefficient between element i and carbon in the liquid and in the austenite phases [203]:

$$\varepsilon_{ci}^{A}=0.925\varepsilon_{ci}^{L} \qquad \text{IV.9}$$

The partition coefficient $P_i^{A/D}$ is determined with the following relationship:

$$P_i^{A/D}=1/P_i^{D/A}=(N_i^A/N_i^L)(N_i^L/N_i^A)=P_i^{A/L}/P_i^{D/L} \qquad \text{IV.10}$$

From data given in the literature [203] the partition coefficient $(P_i^{A/L})^*$ and $(P_i^{D/L})^*$ of N, Al, Nb and V are presented in Table IV.3. Where the partition coefficients are given with an error range, the mean value has been used for the calculation.

The calculated partition coefficients, $P_i^{A/L}$, $P_i^{D/L}$ and $P_i^{A/D}$, of element i at 1493°C in the Fe-C-i system for 1at% of addition of element i are displayed in Table IV.4. From these values, the change in temperature at points L and D caused by the addition of 1 at% of element i is calculated for N, Al, V and Nb with the equations IV.3 and IV.4 respectively. The results of the calculations have been incorporated in Table IV.1. Note the strong influence of Nb on the change of the position of point D along the temperature axis, and that nitrogen has no influence on the position of points L and D on the temperature axis.

IV.2 CALCULATION OF ΔN_i^x FOR I = N, Al, Nb, AND V

The move along the C concentration axis, ΔN_C^X, of carbon at points X = A, D and L brought about by adding 1 at% of element i is given by equations IV.11, IV.12 and IV.13, respectively [203]:

$$\Delta N_c^A=(c\Delta N_c^{A(L)}-e\Delta N_c^{A(D)})/(c-e) \qquad \text{IV.11}$$

Table IV.3

Partition coefficient of element i (i = N, Al, Nb and V) between the austenite and liquid and, between delta ferrite and liquid phase [198].

	N	Al	V	Nb
$(P_i^{A/L})^*$	0.48-0.54	0.76 (1)	0.93 (1)	0.76
$(P_i^{D/L})^*$	0.24-0.38	0.6-0.92	0.9-0.96	0.310 (2)

(1) due to the lack of data, estimated to be equal to the mean value $(P_i^{D/L})$.*

(2) Calculated from the Fe-Nb binary phase diagram [111].

Table IV.4

Calculated partition coefficients of element i (i = N, Al, Nb and V) between the austenite and liquid and, between delta ferrite and liquid phase in the Fe-C-I system.

	N	Al	V	Nb
$P_i^{A/L}$	.573	.88	1.25	.522
$P_i^{D/L}$	.33	.83	1.10	.245
$P_i^{A/D}$	1.75	1.06	1.14	2.13

$$\Delta N_c^D = \frac{\Delta T^A}{g} + \Delta N_c^{D(A)} \qquad \text{IV.12}$$

$$\Delta N_c^L = \frac{\Delta T^A}{a} + \Delta N_c^{L(A)} \qquad \text{IV.13}$$

Where the numerical values of a, c, e and g are given in Fig IV.1. $\Delta N_C^{\mu(v)}$ is the change in mole fraction of carbon ($N_C^{\mu(v)}$) in μ phase equilibrating with v phase caused by introducing a third element i at constant temperature, and is a function of mole fraction of element i in μ phase. $\Delta N_C^{A(L)}$, $\Delta N_C^{A(D)}$, $\Delta N_C^{D(A)}$ and, $\Delta N_C^{L(A)}$ are calculated using the following equations:

$$\Delta N_c^{A(L)} = \left\{ \frac{(P_i^{L/A} - P_{Fe}^{L/A}) N_{Fe}^A}{1 - P_c^{L/A}} - \varepsilon_{ci}^A N_c^A \right\} \frac{N_i^A}{1 + \varepsilon_{cc}^A N_c^A} \qquad \text{IV.14}$$

$$\Delta N_c^{A(D)} = \left\{ \frac{(P_i^{D/A} - P_{Fe}^{D/A}) N_{Fe}^A}{1 - P_c^{D/A}} - \varepsilon_{ci}^A N_c^A \right\} \frac{N_i^A}{1 + \varepsilon_{cc}^A N_c^A} \qquad \text{IV.15}$$

$$\Delta N_c^{D(A)} = \left\{ \frac{(P_i^{A/D} - P_{Fe}^{A/D}) N_{Fe}^D}{1 - P_c^{A/D}} - \varepsilon_{ci}^D N_c^D \right\} \frac{N_i^D}{1 + \varepsilon_{cc}^D N_c^D} \qquad \text{IV.16}$$

$$\Delta N_c^{A(L)} = \left\{ \frac{(P_i^{A/L} - P_{Fe}^{A/L}) N_{Fe}^L}{1 - P_c^{A/L}} - \varepsilon_{ci}^L N_c^L \right\} \frac{N_i^L}{1 + \varepsilon_{cc}^L N_c^L} \qquad \text{IV.17}$$

The partition coefficients for $P_i^{\mu/v}$ are shown in Table IV.4 for N, Al, V and Nb, and in Table IV.5 for carbon and iron. The various interaction coefficients are given in Table IV.3 and the calculations at 1493°C have been performed for the addition of 1 at% of element i. Once $\Delta N_C^{A(L)}$, $\Delta N_C^{A(D)}$, $\Delta N_C^{D(A)}$ and, $\Delta N_C^{L(A)}$ are calculated for N, Al, V and Nb, it is possible to determine the change in carbon composition at points D and L with the help of equations IV.11, IV.12 and IV.13. The results are reported in Table IV.1.

Table IV.5

Partition coefficient $P_X^{\mu/\nu}$ of iron and carbon for a dilute solution of a third element [121].

	X = C	X = Fe
$P_X^{L/A} = 1/P_X^{A/L}$	3.125	0.98
$P_X^{D/A} = 1/P_X^{A/D}$	0.625	1

IV.3 CALCULATED PHASE TRANSFORMATIONS TEMPERATURES FOR STEELS P, A, B, C AND, S

Using equations IV.1 and IV.2, together with the data of Tables IV.1, the change in temperature and composition at points A, D and L caused by the alloying elements present in steels P, A, B, C and S was calculated. Only one calculation was necessary for steels A, B and C, which have the same level of microalloying elements. With the new coordinates of the points A, D and L (Table IV.6), the equations of the boundary lines A'G', A'E', D'H' and F'D' can be calculated (Fig. IV.1). From these equations or phase diagram, the temperatures of the onset and end of the phase transitions have been calculated and are presented in Table IV.7, along with the experimental values measured by DTA.

In Table IV.7 it can be seen that the correspondance between calculated and experimental values in the case of the solid/solid transformation (temperatures A) is not as good as for the solidus temperature. In fact, to insure that the DTA values were not at fault, the model was used to calculate the phase transformation temperatures of Schmidtmann and Pleugel, who established the corresponding phase diagram [59]. The discrepancy between experimental and calculated results is shown in Table IV.8. Furthermore, from Schmidtmann and

Table IV.6

New coordinates (temperature and composition) at points A, D and L caused by the alloying elements of steels P, A, B, C and S.

	T^D(°C)	$N_C{}^D$(at%)	T^A(°C)	$N_C{}^A$(at%)	T^L(°C)	$N_C{}^L$(at%)
Fe-C	1493	0.46	1493	0.74	1493	2.33
Fe-C-steel P	1475	0.463	1466	0.894	1480.5	2.432
Fe-C-steels A B or C	1473	0.413	1467	0.834	1481.5	2.488
Fe-C-steel S	1471	0.332	1464	0.877	1483.5	2.684

Table IV.7

Calculated and experimental phase transformation temperatures of the steels P, A, B, C, and S and corresponding phase transformation . In brackets, the experimental values are shown.

STEEL		A	B	C
STEEL P	Temperature (°C)	1393.5 (1456)	1453 (1473)	1483.5 (1500)
	Transformation	$\gamma \rightarrow \gamma + \delta$	$\gamma + \delta \rightarrow \delta$	$\delta \rightarrow \delta + L$
STEEL A	Temperature (°C)	1397.5 (1455)	1454 (1469)	1481.5 (1500)
	Transformation	$\gamma \rightarrow \gamma + \delta$	$\gamma + \delta \rightarrow \delta$	$\delta \rightarrow \delta + L$
STEEL B	Temperature (°C)	1417 (1455)	1472 (1475)	1473.5 (1500)
	Transformation	$\gamma \rightarrow \gamma + \delta$	$\gamma + \delta \rightarrow \gamma + \delta + L$ $(\gamma + \delta \rightarrow \delta)$	$\gamma + \delta + L \rightarrow \delta + L$ $(\delta \rightarrow \delta + L)$
STEEL C	Temperature (°C)	1441 (1469.5)	1470 (1497.5)	1474.5 (1509)
	Transformation	$\gamma \rightarrow \gamma + \delta$	$\gamma + \delta \rightarrow \gamma + \delta + L$	$\gamma + \delta + L \rightarrow \delta + L$
STEEL S	Temperature (°C)	1388 (1462)	1471.5 (1488)	1471.5 (1503)
	Transformation	$\gamma \rightarrow \gamma + \delta$	$\gamma + \delta \rightarrow \delta$	$\delta \rightarrow \delta + L$

Pleugel [59], the slope of D'H' is 230°C/at%C and 149.25°C/at%C for the boundary line A'G'. This can be compared with 126°C/at%C and 101.4°C/at%C for the boundary lines DH and AG in the pure iron carbon phase diagram. Thus, the assumptions that these slopes are not changed by an alloy additions is clearly erroneous.

Table IV.8

Comparison between experimental values of coordinates of points A and D [59] with calculated values [121].

	Point D		Point A	
	N_C^D(at%)	T_C^D(°C)	N_C^D(at%)	T_C^D(°C)
Exper. values	0.369	1479.5	0.608	1477.5
Calculated values	0.584	1457.5	0.862	1457.5

The reasons for the discrepancy between experiment and model is no doubt contained in the basic assumptions and simplifications of the model. The key constraint is that equations IV.1 and IV.2 are applicable for *dilute* solutions, in order to ensure the non interaction of alloying elements i and j. No upper limit for the concentration, above which the equations are invalid, is given. But for example, a steel with a manganese level of 1.6 wt% may not be considered as "dilute". The further assumption that the slopes of the boundary lines LC, AE, AG and DH (Fig. IV.1) are not altered by alloying elements additions has been shown to be invalid. Finally, the calculation of ΔN_i^x and ΔT_i^x requires the knowledge of the Wagner interaction coefficients between carbon and the alloying element i (see appendix IV) in the *delta* phase, but, due to the lack of data, the values pertaining to those of the *liquid* phase have been used.

Other much simpler empirical equations exist to predict phase changes at high temperature. For example, the following expression has been used to calculate the end of the γ/δ transformations for plain carbon steels [204]:

$$T = 1392 + 1122C - 60Si + 12\,Mn - 140P - 160S \qquad \text{IV.18}$$

all values expressed in wt%. Applied to steel P, which contains all these elements plus aluminum, the result gives a temperature of 1472.5°C, which is in good agreement with the measured value (1473.5°C), (Table 4.2). Unfortunately, this equation cannot be used to calculate the end of the γ/δ transformation of the other steels since they contain Nb, Ti (steels A, B, C) and Ni, Cr and V (steel S).

APPENDIX V

DETERMINATION OF THE FREE ENERGY OF SEGREGATION OF CARBON, SULPHUR AND PHOSPHORUS IN DELTA FERRITE AND AUSTENITE

The value of the free energy of segregation, ΔG^i, depends on the degree of distortion in the matrix due to the presence of a solute atom. For example carbon (which is an interstitial solute) shows a higher segregating tendency in the α ferrite rather than in the γ phase, because of the smaller interstitial spacing in α [123]. In the absence of values for the free energy of segregation of phosphorus, carbon and sulfur in the δ phase, it is assumed here that δ, in terms of segregation behaviour, is an extension of the α phase and not of the γ phase. This may be justified purely on the basis that the crystallographic structure of both α and δ phases is b.c.c. In the case of carbon, this is further reinforced by a consideration of solubility in the three phases. Solubilities imply a degree of distortion of the lattice, i.e. a small distortion is associated with a high solubility (if no other effects are considered). In the pure Fe-C system, the solubility of C in α is 0.0022 wt% at 727°C, and in δ at 1493°C it is 0.1 wt%. Since the maximum solubility of carbon in austenite is about 2% at 1150°C, it is clear, on the basis of solubility, that δ is more similar to α. This in turn implies a less negative ΔG^i for segregation in austenite. Therefore, it can be argued that, in the case of carbon, the ΔG^i for δ ferrite may be extrapolated to higher temperatures from values found at lower temperatures for α ferrite.

For sulphur, the Fe-S phase diagram shows that, for both α and γ phases, the solubility of sulphur in Fe is low, but the solubility difference between the two phases (α and γ) is not as large as for carbon [122]. In the case of phosphorus, the Fe-P diagram reveals a closed loop in the austenite domain and the maximum solubility is around 0.25 wt% at 1150°C. Above a P level of 0.57 wt%, there is a continuity between the lattice parameter of α and δ phases, which further validates the assumption which considers the δ as an extension of the α phase. Both the Fe-S and Fe-P phase diagrams show that the solubility of S and P increases with increasing temperature [122], suggesting that ΔG could be less negative than predicted by assuming that ΔG values for δ can be extrapolated from α, rather than γ values. Therefore the free energy calculated here must be considered as an *upper limit* for the free energy of segregation. This is especially clear in the case of Fe-S where the maximum solubility in the α phase is 0.02 wt% at 910°C, compared to 0.18 wt% in the δ phase at 1365°C suggesting that the free energy of segregation should be lower in δ.

With the knowledge of the variation of ΔG^i in the α-ferrite with temperature, it is thus possible to extrapolate a ΔG^i value of a solute in the δ phase using the basic relationship between free energy (ΔG), enthalpy (ΔH) and entropy (ΔS):

$$\Delta G = \Delta H - T\Delta S \qquad \text{V.1}$$

where T is the temperature, and ΔH and ΔS are independant of temperature [128].

The ΔG values of carbon, sulfur and phosphorus reported in the literature are given in Tables V.1, V.2, and V.3, respectively. From these results ΔH and ΔS of equation V.1 were determined for each element (C, P and, S) by a linear regression on the plot of the ΔG values against temperature in Fig.V.1. If ΔG is expressed in the form of an equation valid over a temperature range, several data points were plotted at different temperatures, and if one value of ΔG referred to a temperature range it was assumed valid for the centre of that range. It can be seen in Fig.V.1 that for carbon the correlation in α is good, except for one point, and the data can be reasonably well fitted with a linear equation. Note also that the only data point for the free energy of segregation of carbon in austenite is well below the values for α ferrite, as was expected from the preceding discussion.

In the case of sulphur, no entropy data were found in the literature, either for the ferrite or austenite, and there was insufficient data to determine a value of entropy from the ΔG versus temperature plot. However, since the vibrational component of the entropy predominates, and because sulfur is very close to phosphorus in terms of mass and size, their vibrational behaviours are assured to be similar [206]. Therefore, the entropy term of sulfur was taken to

Table V.1

Free energy of segregation of carbon in the α and γ phases.

Ref	ΔG (KJ/mol.)	Phase	Remarks
138	-57 -0.0215T	α (500-700°C)	Presented as a "preliminary result"
137	-37.7 -0.0432T	α (500-700°C)	-
130	-80	α (800°C)	$\Delta S \approx 0$
123	-92.4	α (600°C)	-
127	-76	α (600°C)	-
109	-30	γ (850-1100°C)	-

Table V.2

Free energy of segregation of sulfur in the α and γ phases.

Ref	ΔG (KJ/mol.)	Phase	Remarks
136	-51.5	α (550°C)	-
124	-71.1	α (600-700°C)	-
141	-75.2	α (650-800°C)	calculated from data of ref. 124
141	-54.34	γ (850-1300°C)	ΔG constant over the temperature range

Table V.3

<u>Free energy of segregation of phosphorus in the α and γ phases.</u>

Ref	ΔG (kj/mol.)	Phase	Remarks
127	-34.3 -0.0215T	α (450-800°C)	-
130	-50	α (800°C)	$\Delta S \approx 0$
137	-21.2 -0.0373T	α (500-700°C)	error on ΔH: ±10 Kj/mol.
141	-22.8 -0.0192T	α (540-810°C)	-
109	-47	γ (850-1100°C)	-
207	-19.9 - 0.0228T	γ (950-1200°C)	error on ΔG: ±4 kj/mol.

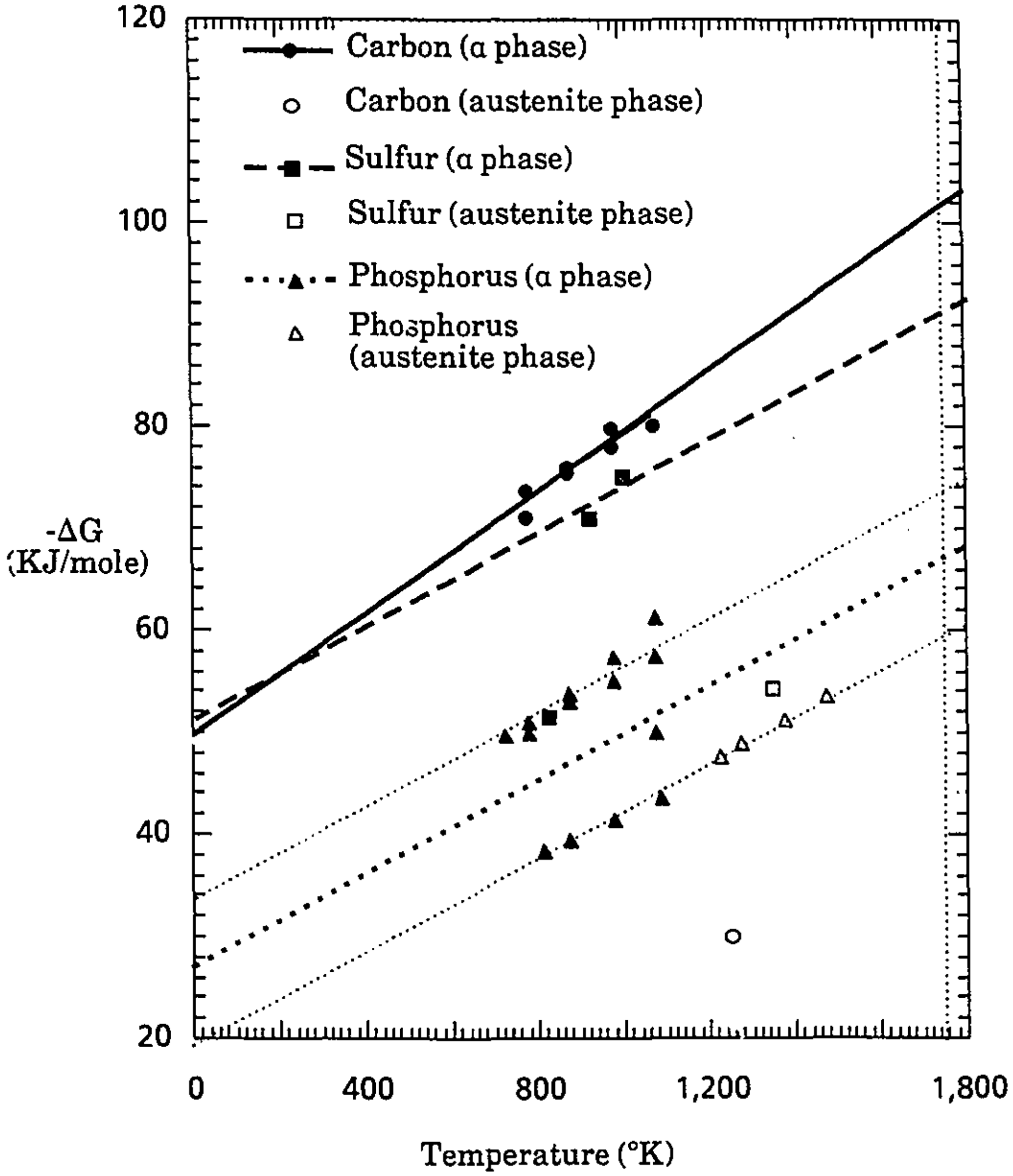

Fig. V.1: Determination of the free energy of segregation of carbon, sulfur and phosphorus in the α phase and austenite.

be the same as that evaluated for phosphorus. The free energy of segregation of phosphorus in α ferrite is given by three equations and one data point at 800°C (Table V.3). As shown in Fig. V.1 for phosphorus the three.equations define two parallel straight lines. The upper line has been established from the equations of references 130 and 127, whereas the lower line is drawn from equation of reference 141. The mean line between these two plots was used to calculate ΔG in this work.

In the austenite only one value for ΔG was found in the literature for carbon and sulphur. Thus, the entropy term in the austenite of both elements was taken to be that for α ferrite. This assumption is supported to a certain degree by the fact that the entropy term of phosphorus in the α ferrite is similar to that in austenite (Table V.3). Note also that the data points in austenite for phosphorus fall approximately on the same lower line defined by the equation of reference 141.

Clearly, some of these assumptions are quite tenuous, especially in the case of sulfur and austenite where the data are very scarce, but it is felt that at least the general trends can be revealed by some degree of quantification.

It should be mentioned that McLean [123] has calculated several values for the free energy of C in α-ferrite by considering the elastic distortion caused by C atoms in the α ferrite. He has found much higher ΔH and ΔS (-83.6 KJ/mole for the enthalpy and -0.044 KJ/mole for the entropy) values than those given in Table V.1 which were obtained by Auger measurements. The difference is certainly due to the basic assumption of the model which considers only the mechanical distortion caused by the solute atoms in the matrix whereas some other electronic effects must also be influential.

APPENDIX VI

CALCULATION OF THE DENSITY OF THE COMPLEX COMPOUND TiNbCN

In order to calculate the volume percent of precipitate for a complex carbonitride of the type of $Ti_xNb_{1-x}C_yN_{1-y}$ one must know the proportionality factor A of equation VI.1:

$$VP=\frac{\rho_{Fe}M_{XY}}{\rho_{XY}M_X}[\%X]=A[\%X] \quad \text{(VI.1)}$$

where $XY=Ti_xNb_{1-x}C_yN_{1-y}$, ρ is the density, M the molecular mass, and [%X] is the concentration of Ti and Nb precipitated in mass percent. The only factor in equation VI.1 which is not readily available in the literature is the density of the compound $Ti_xNb_{1-x}C_yN_{1-y}$. However, knowing that the B1 structure of $Ti_xNb_{1-x}C_yN_{1-y}$ contains 4 atoms per unit cell [176], the density of this precipitate is given by equation 6.2:

$$\rho_{Ti_xNb_{(1-x)}C_yN_{(1-y)}}=\frac{4(xm_{Ti}+(1-x)m_{Nb}+ym_C+(1-y)m_N}{a_{Ti_xNb_{(1-x)}C_yN_{(1-y)}}} \quad \text{(VI.2)}$$

where m_i represents the mass of one atom i, and $a_{Ti_xNb_{1-x}C_yN_{1-y}}$ refers to the lattice parameter of the unit cell. This can be determined from the extension of the Vegart's law [176] which states that there is a linear variation of the lattice parameter of a MC_yN_{1-y} compound (M being Nb or Ti in the present case) between y=0 (pure compound MN) and y=1 (pure compound MC). The same rule is also valid for the variation of the lattice parameter of $Ti_xNb_{1-x}L$ (L being C or N) when x varies between 0 and 1. Therefore, the extension of such law to the dimension of the unit cell in the quaternary system is straightforward, i.e.:

$$a_{Ti_xNb_{(1-x)}C_yN_{(1-y)}}=xya_{TiC}+x(1-y)a_{TiN}+y(1-x)a_{NbC}+(1-y)(1-x)a_{NbN} \quad \text{(VI.3)}$$

However the calculation of of the density of the $Ti_xNb_{1-x}C_yN_{1-y}$ precipitate is more simple if it is assumed that the Vegart's law can be applied to *density* provided that the density of TiC, TiN, NbC, and NbN are known:

$$\rho_{Ti_xNb_{(1-x)}C_yN_{(1-y)}} = xy\rho_{TiC} + y(1-x)\rho_{NbC} + x(1-y)\rho_{TiN} + (1-x)(1-y)\rho_{NbN} \qquad \text{(VI.4)}$$

It can be seen that this equation works when x (or y) equals 0 or 1. In order to check the accuracy of this assumption, computer calculations of the ratio of the density given by equations VI.2 and VI.4 were carried out for sets of x and and y values. In all cases the ratio ranges between 0.998 and 1.011 showing the validity of the assumption.